Synthesis, Surface Functionalization and Application of Group 14 Nanomaterials

by

Morteza JavadiCharani

A Thesis submitted in partial fulfillment of the requirements for the degree of

Doctor of Philosophy

Department of Chemistry
University of Alberta

Abstract

The elements of Group 14 show an extensive range of chemical behaviors. Lying at the boundary between metals and non-metals, some members of Group 14, namely silicon and germanium, are intermediate in their properties. These semiconductors are extremely important in science and technology. Si, Ge, Si_xGe_{1-x}, and corresponding compounds (*e.g.,* oxides and carbides) hold potential for far-reaching modern impacts and numerous optoelectronic applications. The discovery of size-dependent optical responses from nanostructures of these semiconductors has opened new avenues for further studies and enhanced their potential for various uses. Although Si-based nanostructures (*e.g.*, Si nanocrystals and porous-Si) have been widely studied, Ge-based nanostructures have received significantly less attention, presumably because of their complex chemistry and the lack of convenient/predictable methods for their preparation.

In this context, germanium dioxide nanoparticles (GeO_2 NPs) of varied sizes and morphologies were prepared *via* facile sol-gel synthesis without the addition of surfactant (Chapter two). Morphology control was readily achieved by tailoring the water/ethanol ratio in the reaction mixture. Through judicious tailoring of reaction parameters, surfactant-free crystalline GeO_2 nano-cubes and nano-eggs exhibiting currently unparalleled narrow size distributions were obtained. After that, tetraethoxysilane (TEOS) based sol-gel reactions were used to form a robust shell of Stöber SiO_2 around previously prepared GeO_2 NPs and form GeO_2@SiO_2 core-shell nano-cubes or nano-eggs (Chapter three). Subsequently, the core and the shell of these NPs were selectively reduced by 5% H_2/95% Ar and elemental magnesium to yield Ge@SiO_2 and Ge@Si core-shell NPs, respectively.

In the fourth and fifth chapters, we turned our attention to the synthesis of germanium nanocrystals (GeNCs) with well-defined surface chemistry. This research area is of considerable interest because of the attractive optoelectronic properties of GeNCs with sizes smaller than the germanium Bohr-exciton radius (*i.e.*, <24 nm). In the Chapter four, we reported a straight-forward route for synthesizing GeNCs in high-yield and also clarified some chemistry regarding the Ge (II) precursor. Both the precursor and procedure were modified to yield GeNCs of various morphologies.

Modifying and tailoring GeNC surface chemistry was the subject of the fifth Chapter, due to the important role of surface functionalization in solubility and stability of GeNCs. In this context, hydride-terminated GeNCs (H-GeNCs) were freed from their germania matrices by chemical etching of the GeNC/GeO_2 composite and were then derivatized using a series of hydrogermylation approaches (*i.e.*, thermally-activated, radical-initiated, and borane-catalyzed). We found that surface functionalization occurred under all conditions investigated; however, the nature of the surface species (*i.e.*, monolayers *vs.* multilayers) and surface coverage varied depending on the conditions employed.

Application of functionalized NCs is the subject of sixth Chapter. The nanostructures of Group 14 semiconductors are well suited for use in biological systems due to their biocompatibility and fairly low toxicity compared to typical quantum dots such as CdSe. The size/surface dependent optical response of Si nanocrystals (SiNCs) is well-known and more developed than GeNCs. Therefore, we chose acid-functionalized SiNCs as the pioneer for making nano-hybrids with Fe_3O_4 NPs. We demonstrated proof-of-concept confocal cell imaging using these magnetic nano-hybrids.

Finally, Chapter seven summarises what has been achieved for each Chapter of current Thesis. The aim of this Chapter is to provide a summary for synthesize and surface functionalization of Group 14 semiconductors nanomaterials and outline some possible future direction for continuing this Thesis.

Preface

This Thesis is an original work by Morteza JavadiCharani. The research described herein was conducted under the supervision of Professor Jonathan G. C. Veinot in the Department of Chemistry, University of Alberta.

A version of Chapter 2 has been published as M. Javadi, Z. Yang, J. G. C. Veinot, "Surfactant-free synthesis of GeO_2 nanocrystals with controlled morphologies" *Chem. Commun. (Camb).* **2014**, *50*, 6101–6104. I performed all of the research and analysis as well as the manuscript composition. Z. Yang contributed to experimental design, data interpretation and editing the manuscript. J. G. C. Veinot was the supervising author and was involved with experimental design, data interpretation and manuscript composition.

Portions of Chapters 4 and 5 have been published as M. Javadi, D. Picard, R. Sinelnikov, M. A. Narreto, F. A. Hegmann, J. G. C. Veinot, "Synthesis and Surface Functionalization of Hydride-terminated Ge Nanocrystals Obtained from the Thermal Treatment of '$Ge(OH)_2$'" *Langmuir* **2017**, DOI 10.1021/acs.langmuir.7b00358. I performed all of experimental activities and data analysis, as well as first draft manuscript composition. D. Picard was an undergraduate research student who assisted with material synthesis under my supervision. R. R. Sinelnikov from Department of Chemistry, University of Alberta, as well as M. A. Narreto and Professor F. A. Hegmann, from Department of Physics, University of Alberta assisted with PL measurement of Ge nanocrystals (NCs) and edited the final draft of the manuscript. J. G. C. Veinot was the supervising author and was involved with experimental design, data interpretation and manuscript composition.

A version of Chapter 6 has been published as M. Javadi, T. Purkait, L. Hadidi, J. Washington, J. G. C. Veinot, "Synthesis and properties of covalently linked photoluminescent magnetic magnetite nanoparticle-silicon nanocrystal hybrids" *MRS Adv.* **2016**, *1*, 2321. I prepared all materials and performed all material characterization/data interpretation related to material properties, as well as all of the manuscript composition. T. Purkait assisted with synthesizing of acid-functionalized SiNCs. L. Hadidi assisted with surface functionalization of Fe_3O_4 nanoparticles. J. Washington contributed to experimental design and manuscript composition. J. G. C. Veinot was the supervising author and was involved with experimental design, data interpretation and manuscript composition. All data collection and analysis related to cell studies were performed by Van A. Ortega and Professor Greg G. Goss from Department of Biological Sciences, University of Alberta.

I dedicate this thesis to Dad, Mom and my lovely wife. I love you all so much.

تقدیم به دست های پینه بسته پدرم،

دل پرمهر مادرم،

و... یگانه ترینم

Acknowledgment

The Persian poet, Rumi, has a very famous and often quoted line: “what you seek is seeking you." Now, after coming a long way − after spending five years in pursuit of my goal − I truly feel one with what I was seeking. Five years of happiness and sadness, clarity and confusion, upwards and downwards, and great times as well as tough moments is about to be finished. I know that it is not wise to brood on difficult days after they are over, especially during these sweet moments of successful graduation from Ph.D. life. One thing that I am sure about, however, is that overcoming those hurdles was not possible without my wonderful family, supportive supervisor and crazy friends.

Mom and Dad, you never said anything to deter me when I left you alone in Iran and came to Canada, but I could read so many things from your eyes. You have always wished me the best without any complaints, and I know that today you are as happy as I am, if not more. You guys are the biggest reasons for me to push myself to reach as high as possible. Agha joon (Dad), you are the hero of my life. I still remember the days you were working 6 am to 9 pm to keep our life’s wheel rolling. Maman, I am quite sure you could have been a highly-educated professional, but you instead chose to see your kids through to that point. Roghayeh, Somayeh, Samaneh and Parvaneh, your brother is always thinking of you. I love all you guys to the moon and back.

There were so many people in school who helped me a lot in my research. First of all, I would first like to thank my thesis advisor, Professor Jonathan G. C. Veinot, for all of the things he taught me during these last several years that will stay with me forever. Jon, you always kept telling me this: "do not put your name in a thing that does not make you proud." So, thank you for putting your name on my thesis. If I want to make a list of tough or sweet days of my Ph.D.

life, you, for sure, play a big role there. Days that I could not make you happy I would call tough, while conversely you made me extremely proud of myself whenever you heard about my research and praised me for being a great researcher, while today I say that you were the one: an amazing researcher. One of the things I learnt from you was how to balance my personal and family life with my professional and school life without sacrificing the good of either. You consistently allowed my Ph.D. be my own work but steered me in the right direction whenever you thought I needed it. Thank you, Thank you, Thank you for all of the things you have taught me.

I would also like to thank the members of the Veinot team from 2012 to now. First of all, to my officemates, Drs. Lida Hadidi and Christina Gonzalez. Lida and Christina, you were such crazy/awesome friends. We have so many happy and sad memories together. We started our career almost in the same time and passed through the most stressful times of Ph.D. life together: the 502 and the Candidacy. Oh, god! I am happy that we all made it through. I would also like to thank Dr. Melanie Hoffman, who was the very first member of Veinot group to mentor me in starting my own research. Mel, you are a wonderful teacher and a great scientist. Thank you for all things you taught me in such a short time; I used them many times even after you were no longer around. Dr. Dan Krushelnycky, Dr. Muhammad Iqbal, Austin Toresdahl, Darren Picard, Dr. Tapas Purkait, Dr. Rhett Clark, Dr. Md Hosnay Mobarok, Muhammad Islam, Regina Sinelnikov, Maryam Aghajamali, Dr. John Washington, Md Asjad Hossain, Alyxandra Aarbo, Haoyang Yu, Dr. Philipp Kitschke, Christopher Jay Robidillo, Subha Jana, Xiyu (Zach) Zhang, Dr. Angélique Faramus, and many others! I was very lucky to have friends like you.

I spent a couple months of my Ph.D. in Germany as a part of a student exchange program funded by “Alberta/Technische Universität München Graduate School for Functional Hybrid

Materials (ATUMS)". Although two months seems like a flash in my Ph.D. life, the experiences I acquired from living in Munich and researching at TUM are priceless. I would like to thank Professor Bernhard Rieger and his team as well as my amazing friends in Germany for their great hospitality. I especially want to thank Leah Veinot for making this exchange possible through her coordination and follow-ups.

I have also recognized generous continued support from my supervisory committee members: Professors Eric Rivard and Michael Serpe. Thank you for providing me with unfailing support and continuous encouragement throughout my years of study. I must express my very profound gratitude to Professor Richard Tilley from the University of New South Wales and Professors Arthur Mar, Gabriel Hanna and Vladimir Michaelis from the University of Alberta for spending much time and effort in evaluating my Ph.D. thesis. There were also so many supporting staff members from the University of Alberta which helped me a lot with characterizations. Wayne Moffat, Jennifer Jones, Dr. Nathan Gerein, Greg Popowich, and Jing Zheng are some of the names to which I appreciate all of their help. This accomplishment would not have been possible without them. Thank you.

Finally, and most importantly, I would like to thank my wife Yeganeh for her understanding and love during these past few years. Yeganeh, it was just a few days after your own Ph.D. defense that we moved to Canada and I began my own Ph.D. studies. Now I understand how tired you were during that time, but you never told anything. Your support and encouragement were in the end what made this dissertation possible. Thank you for being my best friend. I owe you everything.

Thank you, everyone!

Table of Contents

List of Figures

List of Tables

List of Schemes

List of Symbols, Nomenclature and Abbreviations

Å	Angström (0.1 nm)
°C	degree Celsius
1D	one-dimensional
2D	two-dimensional
3D	three-dimensional
AFM	atomic force microscopy
AIBN	2,2'-azobis(2-methylpropionitrile)
APTMS	(3-aminopropyl)trimethoxysilane
BP	benzoyl peroxide
BF-TEM	bright field transmission electron microscopy
CB	conduction band
cm^{-1}	wavenumber
CMOS	complementary metal-oxide semiconductor
DCC	N,N′-dicyclohexylcarbodiimide
EA	elemental analysis
EDX, EDS	energy-dispersive X-ray spectroscopy
E_g	band gap
eV	electron volt
ε	dielectric constant
FT-IR	Fourier-transform infrared spectroscopy
GC-MS	gas chromatography coupled with mass spectrometry
GeNCs	germanium nanocrystals

GRO	germanium-rich oxide
h	hour(s)
h	Planck's constant ($6.62607004 \times 10^{-34}$ m^2kg/s)
HPLC	High-performance liquid chromatography
HOMO	highest occupied molecular orbital
HRTEM	High resolution transmission electron microscopy
HSQ	hydrogen silsesquioxane
ICP-MS	inductively coupled plasma mass spectrometry
IR	infrared
K	Kelvin
λ	wavelength
LED	light emitting diode
LUMO	lowest un-occupied molecular orbital
NALDI	nanostructured-assisted laser desorption/ionization spectroscopy
m_e	effective mass of an electron
m_h	effective mass of a hole
e	charge of an electron (1.6021×10^{-19} coulombs)
mg	milligrams
min	minute(s)
mmol	millimole
MS	mass spectrometry
MEM	minimal essential medium
NC	nanocrystal
nm	nanometer

NP	nanoparticle
NVMs	non-volatile memories
PBS	phosphate buffered saline
PI	propridium iodide
PL	photoluminescence
pm	picometer
ppm	parts per million
PTFE	polytetrafluoroethylene
QD	quantum dot
R	radius of QD or NP
RBL	rat basophilic mast
rpm	revolutions per minute
SAED	selected area electron diffraction
SEM	scanning electron microscopy
SE-SEM	secondary electron scanning electron microscopy
SEM	standard error on the mean
SiNCs	silicon nanocrystals
T	temperature
TOP	trioctylphosphine
TBP	tributylphosphine
t	time
TEM	transmission electron microscopy
TEOG	tetraethoxygermane
TEOS	tetracthoxy silane

TGA	thermogravimetric analysis
UV	ultraviolet
UV-vis	ultraviolet-visible
VB	valence band
μL	microliter
XP	X-ray photoelectron
XPS	X-ray photoelectron spectroscopy
XRD	X-ray diffraction

Chapter 1:

Introduction

1.1. Quantum Dots and Quantum Confinement

Quantum dots (QDs) are semiconductor nanoparticles (NPs) with diameters smaller than the exciton of the bulk semiconductor (usually in the size range of 2-10 nm) and whose optical and electronic properties differ from their bulk state. Their properties lie between the molecular and bulk semiconductor regimes.[1] The semiconductor material used for making QDs can be an element, such as silicon or germanium, or a compound, such as CdS or CdSe. The term "dot" is connected to their extremely small size, thus resulting in properties different than bulk semiconductors and closer to discrete atoms. This is why they have been called "artificial atoms".[2,3]

Quantum dots are of much interest for their unique electro-optical properties. Multidisciplinary interest in QDs has been largely motivated by the size-dependent properties that they possess.[4] A famous example is different photoluminescent (PL) colors of CdSe QDs as larger QDs (*ca.* 5 – 6 nm) emit longer wavelengths (orange or red) while smaller ones (*ca.* 2–3 nm) emit shorter wavelengths (blue or green, Figure 1-1).[4–6]

How can QDs show such unique properties? The answer is related to a fascinating phenomenon called "quantum confinement,"[7] which was first observed in QDs around three decades ago.[8–11] It is an intrinsic property of semiconductors, which have an electron-filled valence band (VB) and an empty conduction band (CB). It is worth noting that similar analogues exist at the molecular level wherein electrons can transfer from the highest occupied molecular orbital (HOMO) to the lowest unoccupied molecular orbital (LUMO). Lying between the molecular and bulk semiconductor regimes means that by decreasing the size of the nanomaterial (number of atoms), the density of energy states decreases and the energy difference between the

valence and conduction band increases (Figure 1-1).[12,13] As a result, transferring an electron from the conduction band to the valence band and back again releases higher energy photons (hν) and the PL emission wavelength of a QD demonstrates a "blue-shift" due to quantum confinement of its electron.

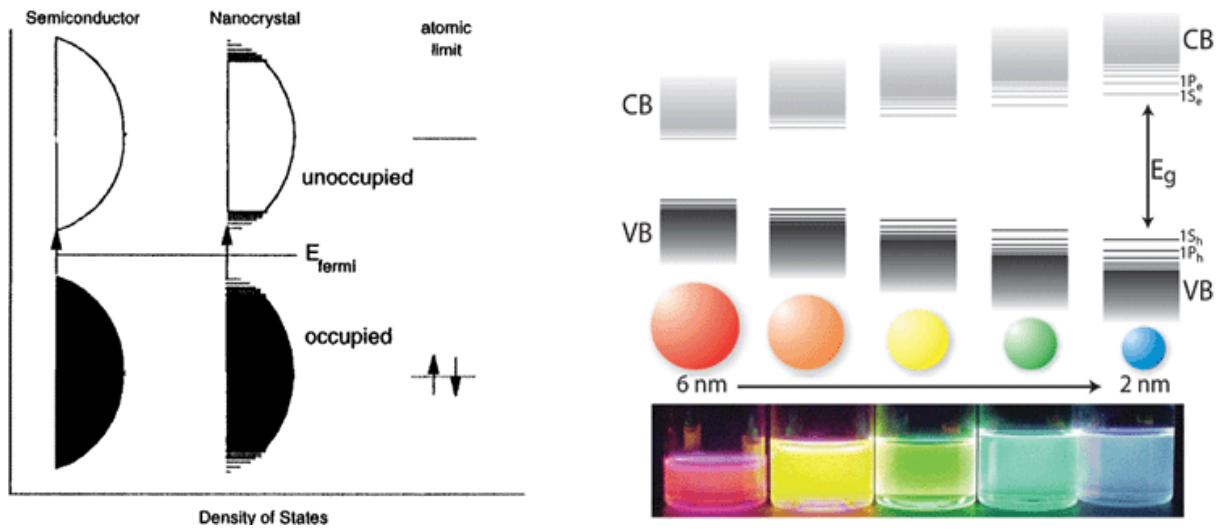

Figure 1-1. Pictorial representation of the changes in optical behaviour of nanoparticles associated with their size. Electronic structure of QDs with a "blue-shift" due to quantum confinement.[12–14]

However, the illustration of the quantum confinement effect shown in Figure 1-1 is only a simplified approximation of what is actually happening in QD systems. A more accurate explanation is possible by accounting both the size and band-gap of the bulk semiconductor. If a semiconductor is irradiated by photon energy (*hν*) greater than the band-gap, electrons will be excited from the valence to the conduction band across the band-gap, leaving a "hole," or absence of an electron, behind. The coulomb-correlated electron (negatively charged) and hole (positively charged) bound pair in a semiconductor material is called an exciton.[15]

The exciton was the basis of several different models attempting to explain the relationship between particle size and band-gap energy of semiconductor quantum dots. *Eq.* 1-1 exhibits one of these models that shows a reasonable similarity to experimental measurements:[15]

$$E_{g.QD} = E_{g.b} + \frac{h^2}{8R^2}\left(\frac{1}{m_e} + \frac{1}{m_h}\right) - \frac{1.786e^2}{4\pi\varepsilon_0\varepsilon R} \qquad Eq.\ 1\text{-}1$$

Where:

$E_{g,QD}$ and $E_{g,b}$ are the band-gap energies of the quantum dot and bulk solid, respectively;

R is the quantum dot radius;

m_e and e are the effective mass and elementary charge, respectively, of an electron;

$\hbar$ is Planck's constant;

m_h is the effective mass of the hole in the solid; and

ε is the dielectric constant of the solid.

Eq. 1-1 describes the outcome of the effective masses of electrons and holes and their electrostatic interactions (terms of the exciton by its definition) as being related to the E_g of the solid. As a result, the E_g of a QD is connected to the size of a QD (R).

QDs have been prepared from various semiconductor systems. Some of them are composed of one element like Si[16,17] or Ge,[18–20] and some are a combination of elements from different periodic groups such as the following:

II-VI: CdS,[21] CdSe,[22,23] CdTe,[21] ZnO,[24] ZnS,[25] ZnSe,[26,27] and ZnTe.[28,29]

II-V: Zn_3N_2.[30]

III-V: InP,[31–33] InAs,[34,35] InSb,[36,37] and GaN.[38]

IV-VI : PbS,[39,40] PbSe,[41] and HgTe.[42]

Other: $AgInS_2$,[43,44] CI(Z)S [CuI(Zn)S].[45–47]

Moreover, different combinations of previously mentioned semiconductor systems have been synthesized in the form of core-shell QDs, which are of much interest.[62–65] In this context, core-shell QDs can be classified into two main types (Figure 1-2):

- Type I (like CdSe/ZnS core-shell QDs)[4]: band-gap of the core smaller than the band-gap of the shell.
- Type II (like CdS/CdSe core-shell QDs)[52]: band-gap of the core larger than the band-gap of the shell.

Confinement behaviours in core-shell QDs are highly dependent on the core and shell materials themselves. For example, Type-I QDs demonstrate higher photoluminescent (PL) efficiency as compared to Type-II QDs. This is because in type-I QDs, the electrons and holes are confined to the core, while in Type-II QDs, the confinement is happening to the shell (for electrons) and to the core (for holes). Therefore, during recombination the charge carriers have to cross the core-shell interface.[52]

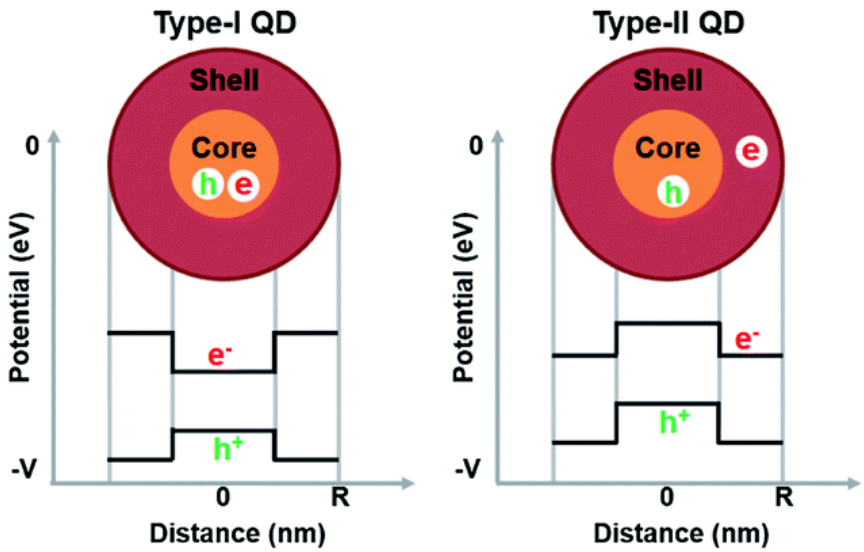

Figure 1-2. Energy level diagrams of Type-I and Type-II QDs.[53]

Thus, there are possibilities for manipulating QD structures to make their emission wavelengths cover a broad range of electromagnetic radiation in the visible and IR (infrared) regions (see Figure 1-3 in next section).[51] QDs also show size dependent, multiple PL wavelengths (*vide supra*), high quantum yields, high stability (chemical and photochemical), narrow and mostly symmetrical emission bands, and have multiple capabilities by possessing various functional groups on their surfaces.[54–56] All of these properties make QDs useful in many different applications such as photovoltaics,[57,58] light emitting diodes (LEDs),[59,60] ultrahigh density data storage,[61] biological imaging,[62,63] and cancer therapy.[64,65]

1.1.1. Group 14-Based Nanostructures

Despite all of the remarkable properties and applications for typical QDs, their theoretical as well as practical utility, especially in biological systems, is very limited. There are huge concerns regarding their application because they include toxic heavy metals, such as cadmium,

along with elements whose reserves are depleting, such as selenium. This has led to, for example, the European Union's Restriction of Hazardous Substances Directive (RoHS), limiting the usage of compounds containing toxic heavy metals.

Figure 1-3 summarizes the emission wavelength range for most QDs mentioned in this Chapter, classified based on their application concerns (toxicity and source).[51] One group is that of materials with no major concerns regarding their toxicity and source (green). The second group is less toxic but contains geographically concentrated elements such as indium (orange). Finally, the last group encompasses QDs that contain toxic elements such as Cd, Pb and Hg.

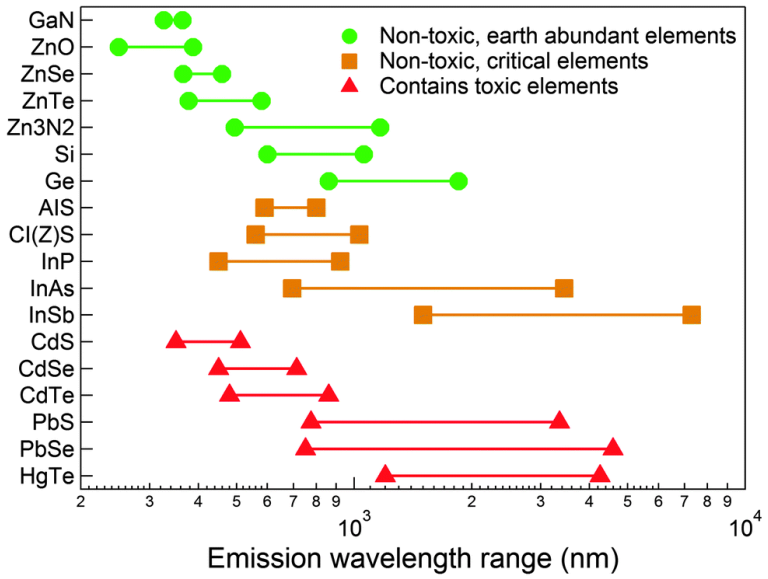

Figure 1-3. Emission tunability of selected semiconductor NCs. In most cases, the range varies from the bulk band-gap down to the shortest confinement-induced, blue-shifted emission.[51] GaN,[38] CdS,[21] CdSe,[22,23] ZnO,[24] ZnSe,[26,27] ZnTe,[28,29] Zn_3N_2,[30] Si,[16,17] Ge,[18–20] $AgInS_2$,[43,44] CI(Z)S [CuI(Zn)S],[45–47] PbS,[39,40] PbSe,[41] CdTe,[21] InP,[31–33] InAs,[34,35] InSb,[36,37] and HgTe.[42]

Therefore, developing less toxic alternatives for typical QDs is necessary for their further use and, indeed, this is becoming a dynamic area of research. Photoluminescence has been

observed for Group 14 semiconductor nanostructures (*i.e.,* Group 14 QDs), and these have thus been introduced as a new class of QDs that lack the toxicity of classic QD examples.[66,67] Canham, in 1990, reported the visible photoluminescence of silicon nanostructures[66] and closely after that, in 1991, Yoshihito *et al.* observed a similar phenomenon for germanium crystals embedded in silica.[67] This was the beginning of a challenge for bulk semiconductor band structure models[10] and a longstanding debate regarding the origin of PL in indirect band-gap materials.

Table 1-2 summarizes different properties for elements of Group 14. These quantities, especially band-gap values, will be frequently cited during this report.

Table 1-2. Selected Properties of the Group 14 Elements

	Carbon (C)	**Silicon (Si)**	**Germanium (Ge)**	**Tin (Sn)**	**Lead (Pb)**
Atomic number, atomic mass (amu)	6, 12.01	14, 28.09	32, 72.64	50, 118.71	82, 207.2
Valence electron configuration	[He] $2s^2 2p^2$	[Ne] $3s^2 3p^2$	[Ar] $4s^2 3d^{10} 4p^2$	[Kr] $5s^2 4d^{10} 5p^2$	[Xe] $6s^2 5d^{10} 6p^2$
Atomic radius (pm)	77	111	125	145	154
Electronegativity	2.6	1.9	2.0	2.0	1.8
M-M Bond dissociation energy (kJ/mole)	346	222	188	146	98
Band-gap (eV, nm)	5.48, 226	1.12, 1107	0.67, 1867	0.1, 12000	N/A

1.2. Germanium Nanoparticles

1.2.1. Properties and Applications

General interest in germanium increased with the realization of semiconductor-based electronics in the second half of the 20th century.[68] Transistors, which are essential components in the electronic devices that modern society relies upon, were first made using germanium. While Ge lost out to ultra-pure silicon in the electronics industry, it remains an important material for optoelectronic applications.[68] As previously mentioned, the early 1990s saw the surprising discovery of visible photoluminescence from germanium nanostructures, which opened many new directions for investigation.[66,67]

Despite being in Group 14, germanium differs substantially from its more frequently studied cousin, silicon. Bulk Ge possesses a smaller band-gap (0.67 eV *vs.* 1.1 eV at 300 K),[69] larger Bohr-exciton radius (24.3 nm *vs.* 4.9 nm),[67,70] higher electron and hole mobility (≤3900 $cm^2/V\cdot s$ compared with ≤1500 $cm^2/V\cdot s$ for Si),[71] as well as greater capacity for and diffusivity of ions (*e.g.,* Li^+).[72] In this context, comparatively large germanium nanocrystals and related structures (*e.g.,* oxide-embedded GeNCs) should possess the favourable optical and electronic properties that will be potentially useful in applications like solar cells,[18] biological imaging,[73,74] Bragg reflectors[18], light-emitting diodes, and non-volatile memory devices.[75–79]

1.2.2. Synthesis of Germanium Nanocrystals

Despite great achievements in the synthesis and morphological control of high quality and extremely monodisperse chalcogenide QDs (such as CdSe) during the last two or three decades, Group 14 QDs (*e.g.,* Si, Ge and SiGe NCs) of such quality have been problematic to produce.

Higher covalent characteristics of elements in Group 14 necessitate harsh reaction conditions (such as high temperatures, long reaction times, *etc.*) as well as adverse reagents (sensitive precursors, strong reducing agents, *etc.*) to prepare highly crystalline Ge or Si nanoparticles (*i.e.,* nanocrystals).

GeNCs, of particular interest in current research, have not been studied and understood as well as their Si counterparts. In the last two decades, a variety of methods have been proposed for their synthesis. Some of these methods have been very well developed and understood (*e.g.,* solution phase reduction) while some others are in even earlier stages of development. Although GeNCs have been prepared through a variety of physical and chemical methods, *via* top-down or bottom-up approaches, herein we bring our attention to some well-established methods that yield colloidal, free-standing GeNCs by focusing on their synthesis and characterization.

1.2.2.1. Solution Phase Reduction of Germanium Halides

Solution-based synthetic methods are probably the most widely reported approaches for preparing GeNCs. In this context, a variety of germanium precursors, like germanium halides ($GeCl_4$, $GeBr_4$ GeI_4, GeI_2), are reacted with several kinds of reducing agents (*e.g.,* NaK, $LiAlH_4$, *n*-BuLi) under various reaction conditions (*i.e.,* different temperatures, applying reverse micelles) to yield GeNCs. Because of the high number of GeNC preparation methods falling into this category, we split this group into two sub-groups based on the type of reducing agent used, namely, A) Organoalkali and alkali metal reduction of germanium salts; and B) Hydride-based reduction of germanium compounds.

A) Organoalkali and Alkali Metal Reduction of Germanium Salts

Some of the earliest reports of GeNC synthesis were based on the reduction of $GeCl_4$ in solution. In the early 1990s, Heath *et al.*[80] made GeQDs of various sizes (*ca.* 6, 11 and 20 nm) based on a method they had developed at first for making Ge quantum wires.[81] Their strategy was based on ultrasonic-mediated high-temperature (275 °C) and high-pressure (200 atm) reduction of chloro-germanes and phenyl-$GeCl_3$ by an ultrafine dispersion of NaK alloy in heptane. Because of the harsh synthetic conditions, the final product was crystalline enough but has limited selectivity over size, shape and surface termination.

$$GeCl_4 + RGeCl_3 + R_2GeCl_2 + NaK \longrightarrow GeNCs + NaCl + KCl \qquad \textit{Eq.}\ 1\text{-}2$$

At around the same time, Weller *et al.* reduced $GeCl_4$ with lithium naphthalide in THF at room temperature and produced amorphous GeNPs around 2 nm in size. The surface of the NPs were functionalized with $(CH_3)_3SiCl$. Due to the amorphous nature of the initial NPs (low temperature synthesis), a ruby laser was used to increase the crystallinity of the particles and thus produce GeNCs. Although large particles were removed by filtration during the synthesis, final particles still demonstrated poor monodispersity (Figure 1-4).[82]

$$nGeCl_4 + 4n\ Li[C_{10}H_8] \longrightarrow Ge_n\ (GeNPs) + 4nLiCl \qquad \textit{Eq.}\ 1\text{-}3$$

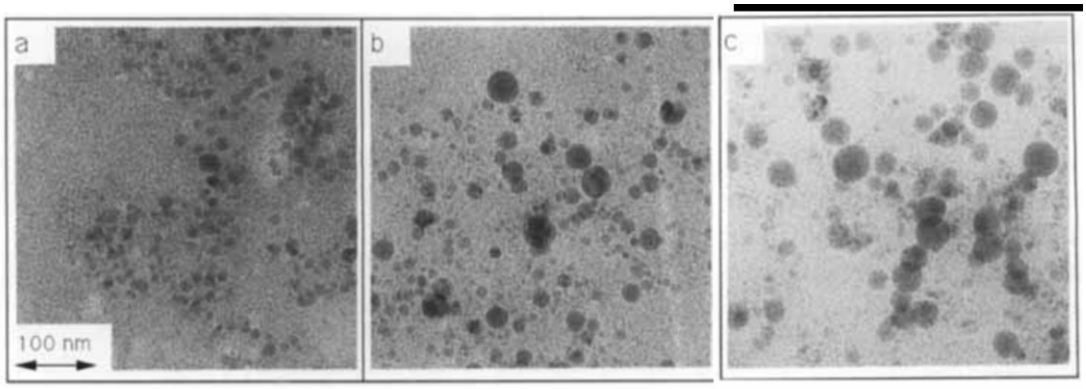

Figure 1-4. TEM images of the particles made by Weller *et al.* (a) 3 nm, (b) 5 nm and (c) 20 nm after flashes with a ruby laser.[82]

One decade later, Kauzlarich *et al.* modified this method to overcome the particle size distribution problem and yield nearly monodispersed GeNCs. They reduced $GeCl_4$ with sodium naphthalide in dimethoxyethane (glyme) at room temperature. Instead of $(CH_3)_3SiCl$ in the previous method, they used n-butylmagnesium chloride (butyl Grignard) to aid in the production of alkyl terminated GeNCs around 4 nm in size (Figure 1-5 a). They also discovered that the particles lost their crystallinity upon heating to 300 ºC under vacuum (Figure 1-5 b). Further recrystallization and growth required temperatures as high as 600 ºC.[83] They modified synthetic parameters such as reductant, stirring time, concentration, and temperature to yield different sizes of photoluminescent GeNCs. As just one example, they synthesized 5 nm Ge NCs by reacting $GeCl_4$ and sodium naphthalide at -40 °C while the same reaction yielded 11 nm particles when carried out at 70 °C.[84]

Some minor modifications were applied to Kauzlarich's method by different groups. For example, Cho *et al.* used n-butyllithium instead of n-butylmagnesium chloride to produce amorphous butyl terminated photo-luminescent Ge particles around 10 nm in diameter (Figure 1-5 c).[85]

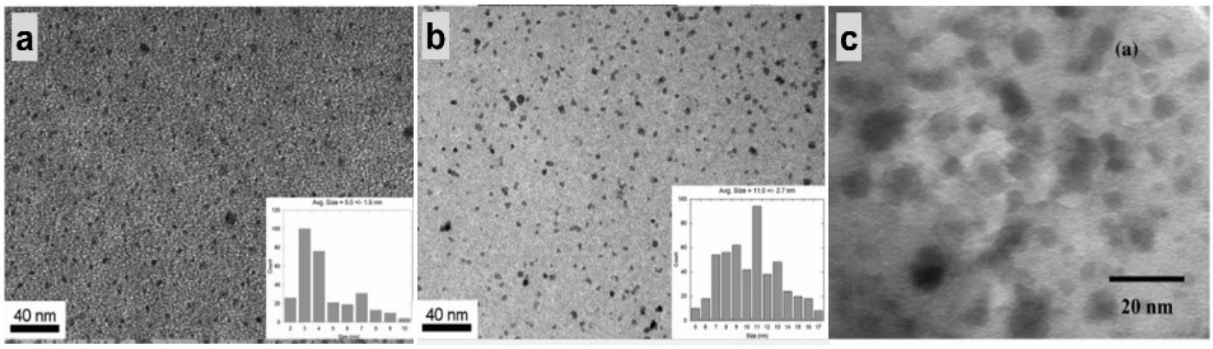

Figure 1-5. a) and b) GeNCs produced from $GeCl_4$ and Na naphthalide before (a) and after (b) annealing at 300 °C under vacuum, made by Kauzlarich *et al.*[83] c) TEM image of butyl-capped Ge nanoparticles made by Cho *et al.*[85]

B) Hydride-Based Reduction of Germanium Salts

Apart from alkali metals being used as reducing agents, a remarkable number of reports of making GeNCs *via* solution based reduction methods used hydride containing reductants, such as lithium aluminum hydride ($LiAlH_4$), sodium borohydride ($NaBH_4$) or even hydrazine (N_2H_4). In this procedure, the Ge precursor is usually a Ge (IV) or Ge (II) halide and the reaction proceeds in presence of adequate surface-stabilizing ligands. Using hydride reducing agents means that the final NPs are expected to be hydride-terminated. Surface-stabilizing ligands further react with hydride-terminated surfaces of GeNCs, leading to functionalized GeNCs with complex surface chemistry.

The first attempt in this category was performed in 2001 by Wilcoxon *et al.* who reduced GeX_4 (where X=Cl, Br, or I) at room temperature with $LiAlH_4$ in an inverse micelle system.[86] They used non-ionic aliphatic polyether or quaternary ammonium cationic surfactant to build up their micelle system. As a result of the inverse micelles, nucleation and growth of the Ge was

restricted to the micelle interior. It is worth noting that because of the entirely anhydrous system they used, simple hydrolysis of GeX_4 to GeO_2 was not possible. Finally, an High-performance liquid chromatography (HPLC) system was used to separate NCs by size and also to separate the surfactant from the NCs. This group made GeNCs 2-5 nm in size and observed PL in the range of 350–700 nm while the larger particles (8–10 nm) showed only weak emission. Later, the authors advised the community for a safety issue that involved the production of highly toxic and pyrophoric germane (GeH_4) gas.[86]

Several groups changed parameters of the Wilcoxon procedure – temperature, surfactant type and precursor – to produce different sizes and morphologies of GeNCs. Jiang and co-workers reduced $GeCl_4$ with $NaBH_4$, $LiAlH_4$, or N_2H_4•H_2O to prepare GeNCs.[87] They claimed that as $GeCl_4$ concentration increased (Figure 1-6 a and b), the nucleation and growth rates also increased; however, surprisingly, as GeNCs became smaller, their size distributions broadened. They used different kinds of reducing agents, reporting average grain sizes of 4.8 ± 0.7 nm, 6.7 ± 0.6 nm or 3.8 ± 0.6 nm for GeNCs prepared with $NaBH_4$, $LiAlH_4$ or $N_2H_4 \cdot H_2O$ as reductants, respectively (Figure 1-6).[87]

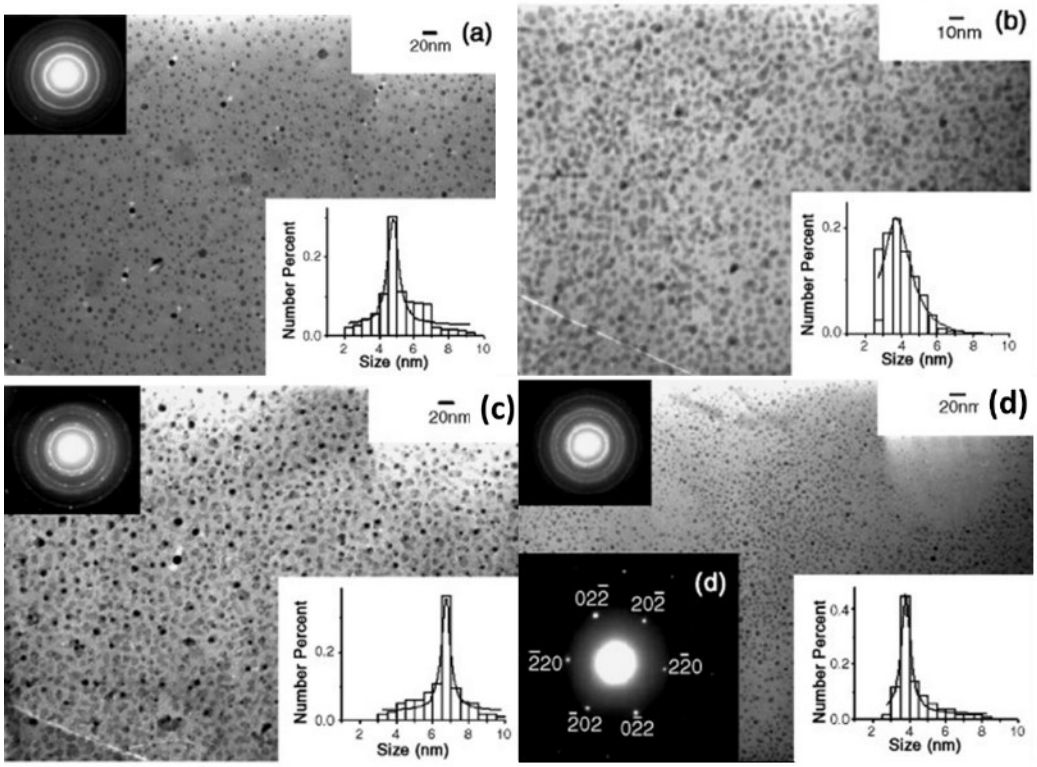

Figure 1-6. TEM images of GeNCs. (a and b) Using $NaBH_4$ as reducing agent. (a) $[GeCl_4] = 2.5 \times 10^{-3}$ mol/l and (b) $[GeCl_4] = 1 \times 10^{-2}$ mol/l. (c) using $LiAlH_4$ as reducing agent ($[GeCl_4] = 2.5 \times 10^{-3}$ mol/l). (d) Using N_2H_4 as reducing agent ($[GeCl_4] = 2.5 \times 10^{-3}$ mol/l). SAED pattern obtained from an individual 4.5 nm Ge nanocrystal, using $NaBH_4$ as reducing agent.[87]

To further address the issues of hydride-based reduction of germanium compounds, Veinot and coworkers used solid GeI_4 instead of volatile $GeCl_4$ and reduced a toluene solution of this in cetyltrimethylammonium bromide (CTAB) with $LiAlH_4$ (Figure 1-7).[19] Refluxing of the produced hydroterminated GeNCs with n-undecene led to n-undecyl terminated GeNCs, which showed PL around 390 nm.

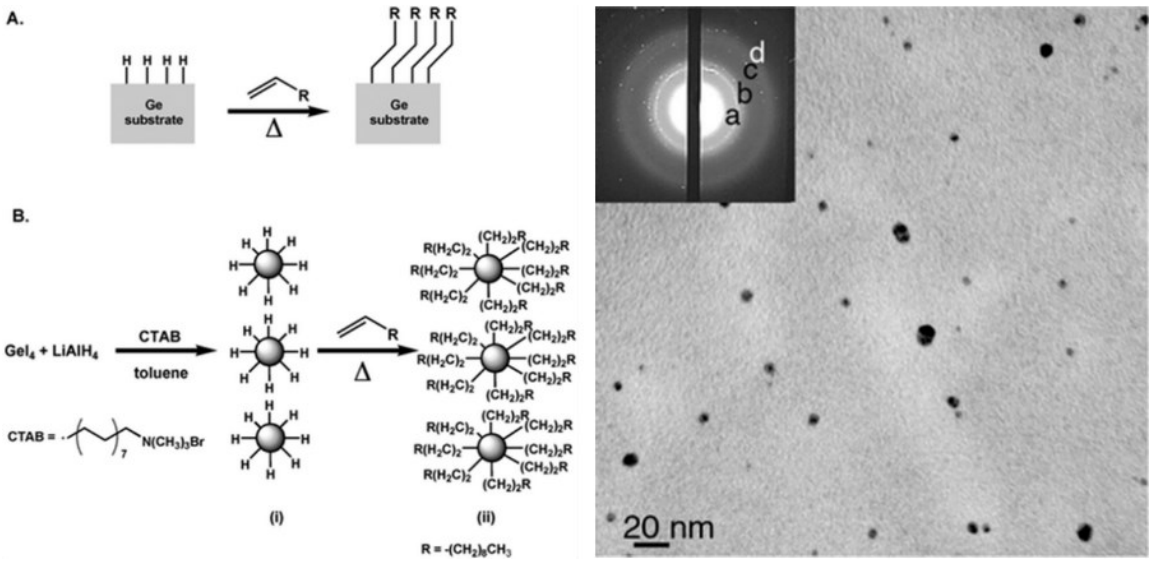

Figure 1-7. A) Hydrogermylation of the surface of hydride terminated Ge. B) The general reaction scheme for the synthesis and surface derivatization of GeNCs. C) Representative TEM image of GeNCs made with this method.[19]

The next factor to study was the type of surfactant, which was done by Korgel and co-workers. This was followed by changing the precursor and temperature.[88] They found that using a coordinating type of surfactant, such as trioctylphosphine (TOP) or tributylphosphine (TBP), with GeI_2 and $LiAlH_4$ while concurrently applying different temperature steps (120 ºC at first and later 300 ºC for 1 h each) led to uniformly-sized GeNCs. GeI_2, with the aid of a coordinating surfactant, can disproportionate into Ge and GeI_4. Using different concentrations of GeI_2 was the key factor in producing different sizes of GeNCs. They reported GeNCs with sizes ranging from 3 to 11 nm, synthesized in TOP at 300 °C and in TBP at 240 °C (Figure 1-8).[88]

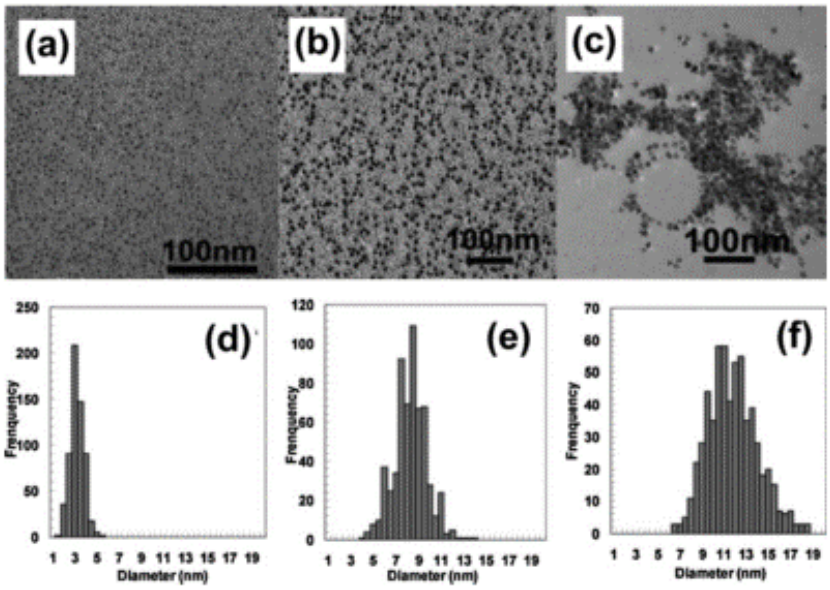

Figure 1-8. GeNCs synthesized from (a) 130, (b) 260, and (c) 520 mM GeI_2 solution in TOP at 300 °C. Particle size distributions are 3.0 ± 0.5, 8.1 ± 1.4, and 11.6 ± 2.2 nm, respectively.[88]

In the case of TBP as the coordinating solvent, GeNCs were bigger and size distributions were broader. Although the NPs made with this method were uniform and nearly monodisperse, the surface chemistry of the NCs unfortunately remained complex and unclear presumably due to using different types of additives like coordinating surfactants.[89]

Correspondingly, in an important work, Tilley and co-workers performed systematic studies to explore the effect of the reducing agent. They investigated GeNC size at room temperature prepared *via* reduction of $GeCl_4$ solution in hexane and pentaethylene glycol monododecyl ether using a series of metal hydrides including $LiAlH_4$, $Li(C_2H_5)_3BH$, $LiBH_4$, and $NaBH_4$. The authors found that the size of the GeNCs was inversely related to the strength of the reducing agent, with stronger reductants producing smaller particles and weaker ones producing larger particles (*e.g.,* $LiAlH_4$ [4.0 ± 0.5nm], $Li(C_2H_5)_3BH$ [4.5 ± 0.5 nm], $LiBH_4$ [5.5 ± 0.5 nm],

$NaBH_4$ [25.0 ± 15.0 nm]).[73] They also performed biological imaging by attaching allylamine to the GeNC surfaces (using H_2PtCl_6 as a catalyst) to render them water soluble (Figure 1-9).[73] This work, along with similar attempts by this group,[90–92] provide a major background on the synthesis and biological applications of GeNCs using hydride-based reducing agents.

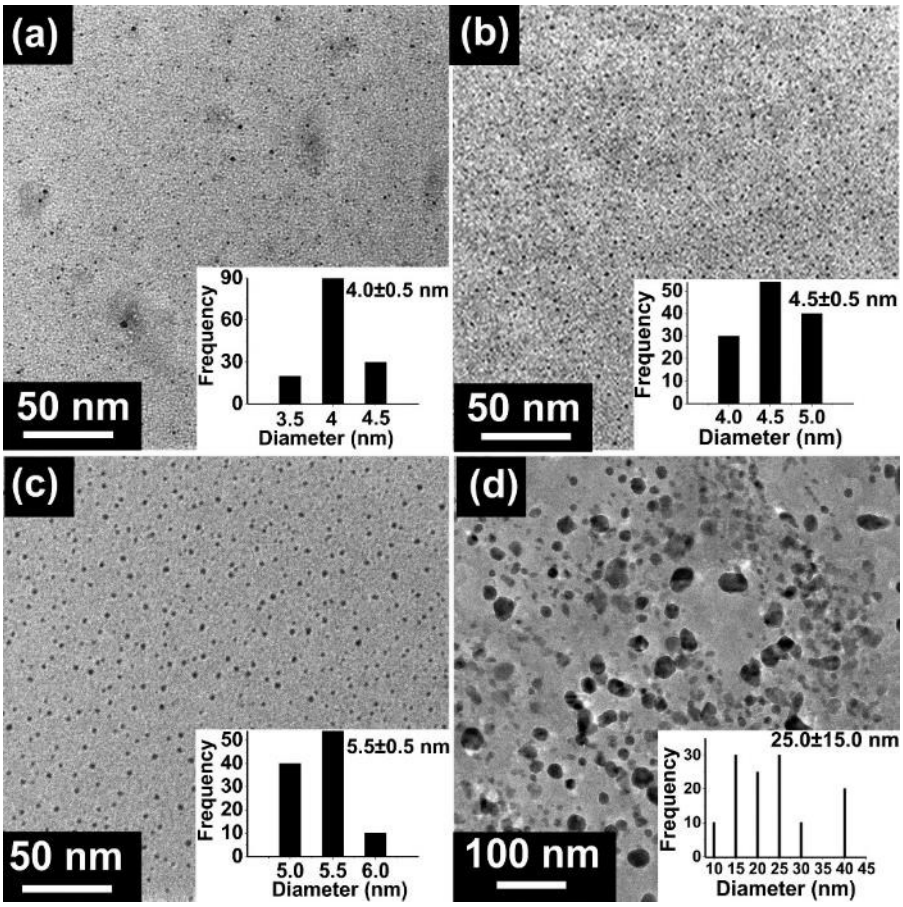

Figure 1-9. TEM images with related particle size distributions of GeNCs obtained from reduction with (a) $LiAlH_4$, (b) $Li(C_2H_5)_3BH$, (c) $LiBH_4$, and (d) $NaBH_4$.[73]

1.2.2.2. Germanium Zintl Salt Metathesis Reactions

A reaction in which two compounds react to form two new compounds, with no changes in oxidation number is referred to as a "metathesis reaction".[93] In metathesis reactions, the ions of two compounds exchange their partners. By definition, Zintl phase is the product of the reaction between alkali metals or alkaline earths and post transition metals or metalloids of groups 13-16.[94] In this context, metathesis reacting Ge Zintl salts such as NaGe, KGe or Mg_2Ge with excess $GeCl_4$ can lead to chloro-terminated GeNCs, which were studied in detail by Kauzlarich and co-workers (Figure 1-10).[84,95–97] They reported particle sizes ranging from 2 to 5 nm by refluxing precursors in glyme or diglyme for 8-120 h. Further reaction of these chloro-terminated GeNCs (Cl-GeNCs) with alkyl lithium or Grignard reagents produced alkyl-terminated NCs that exhibit size-dependent photoluminescence.

For example Cl-GeNCs react with methyllithium, methylmagnesium bromide, or octylmagnesium results in methyl- or octyl-terminated GeNCs.[98] Kauzlarich *et al.* also exploited a metathesis reaction of a germanium Zintl salt with $NaBH_4$ to produce hydride-terminated GeNCs that again showed photoluminescence of various wavelengths (mostly in blue region).[97]

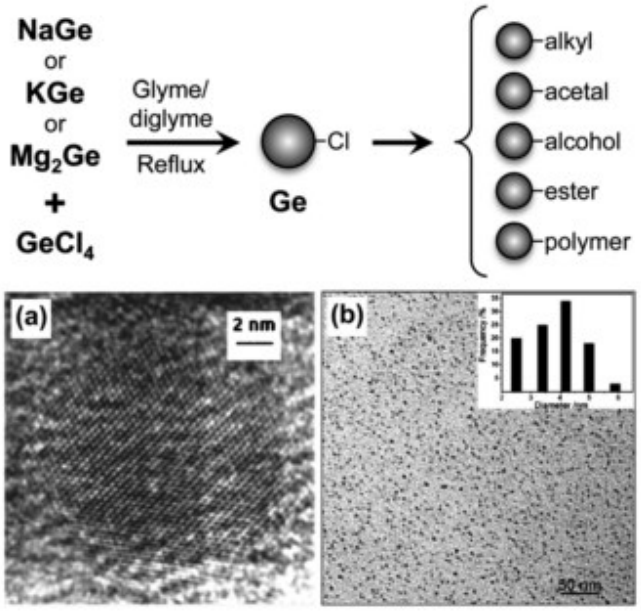

Figure 1-10. The synthesis of GeNCs *via* a metathesis reaction between Ge Zintl salts and $GeCl_4$, with an example TEM image and size distribution histogram for NCs made by reacting NaGe and NH_4Br.[96,97,99]

1.2.2.3. Thermal Decomposition of Organogermane Precursors in High Boiling Solvents

In this class of procedures, instead of using a highly reactive reducing agent as shown in previous methods, high temperatures were used to decompose zero-valent organogermane precursors to elemental germanium in the form of GeNCs. A considerable number of groups reported various sizes of GeNCs synthesized with several types of procedures, Ge precursors, high boiling point solvents, temperatures, pressures.[20,100–103] Generally, these methods produced GeNCs in three ways: single-pot heating, hot-injection, and a super-critical fluid (high pressure) processing methods. In single-pot heating methods, a mixture of reagents and solvents are heated to a desired temperature, while in hot-injection methods the Ge precursor (or precursors) are injected into a preheated solvent/capping agent system. The mechanism of GeNC formation can be understood with classical mechanisms of nucleation and growth used for other NP syntheses

(LaMer model).[104] Explaining all of the details of the LaMer model is beyond the scope of this Thesis.

A) Single Pot Heating Methods

As an example of a single pot heating method, Schaak and co-workers made 6 ± 1, 12 ± 2 and 22 ± 4 nm GeNCs using different concentrations of GeI_4 in oleylamine, oleic acid, and hexamethyldisilazane heated to 260 ºC for 30 min.[100] Similar work has been done by Guo *et al.* to produce GeNCs around 10 nm in diameter by using $GeBr_2$, which is more reactive than the previously used GeI_4 (Figure 1-11).

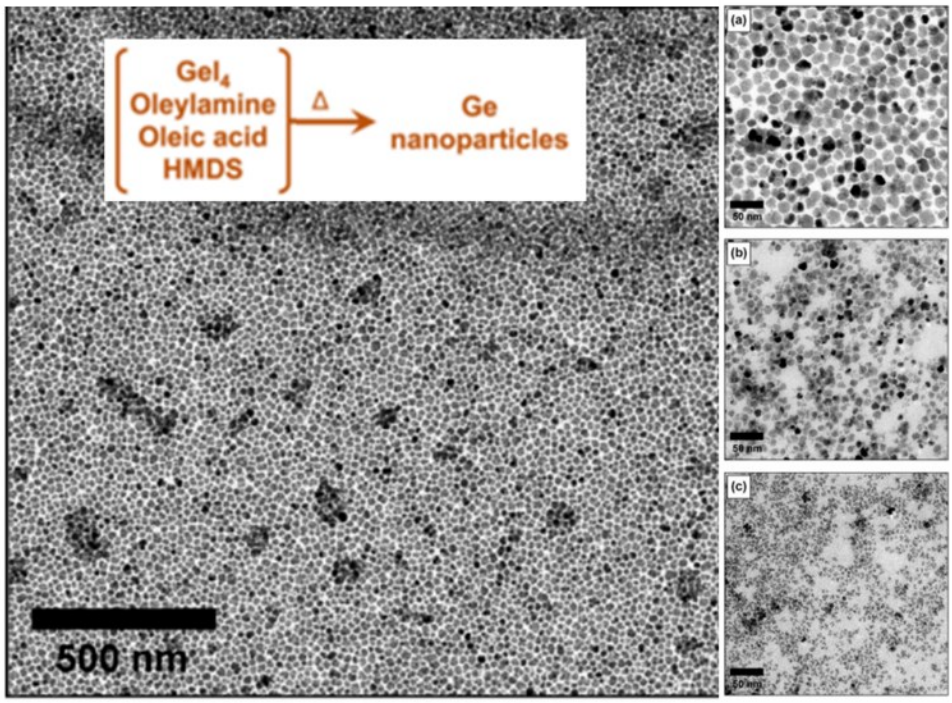

Figure 1-11. Representative Ge nanoparticles made by Schaak *et al.*[100] GeNCs with average sizes of (a) 22 ± 4 nm, (b) 12 ± 2 nm, and (c) 6 ± 1 nm.

Recently, Purkait *et al.* reported a one pot synthesis of GeNCs *via* microwave assisted heating of a Ge(II) dihydride precursor.[20] The microwave-initiated method offers *in-situ* hydrogermylation of alkenes/alkynes onto the surface of GeNCs and it is particularly advantageous as it provides access to GeNCs of different sizes by using different concentrations of precursor (Figure 1-12).

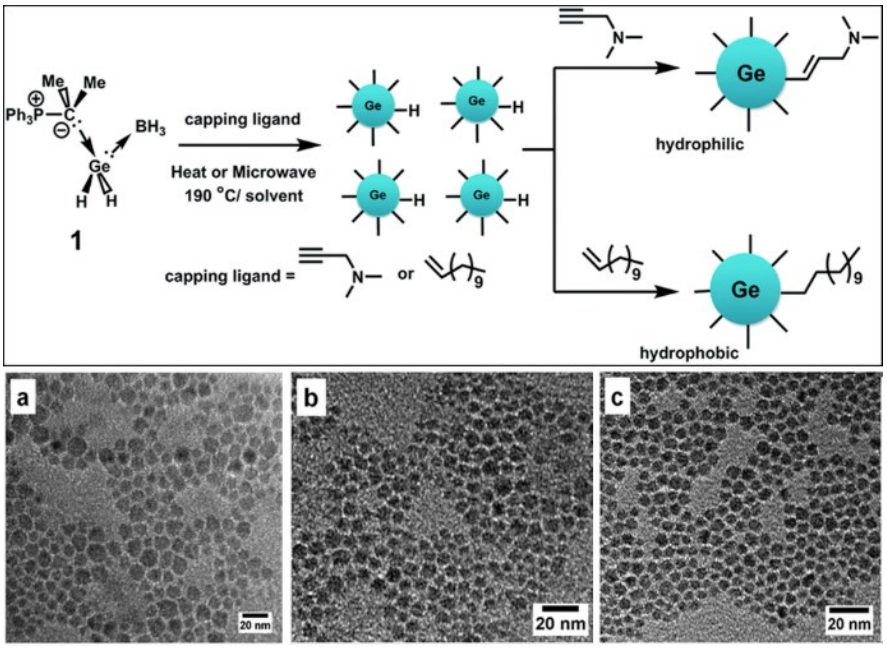

Figure 1-12. Synthesis and *in situ* functionalization of GeNCs upon thermal or microwave irradiation induced decomposition of $Ph_3PCMe_2 \cdot GeH_2 \cdot BH_3$. Representative TEM evaluation of GeNCs obtained from decomposition of the precursor. [20]

B) Hot-Injection Methods

Despite the abundance of single pot heating methods, hot-injection methods are more usual in this category because they yield more monodisperse particles with faster nucleation and shorter growth times. Indeed, hot-injection preparation of GeNCs was proposed before the single pot heating method. Boyle and co-workers reported the synthesis of GeNCs *via* injection of a

solution of germanium (II) bis[bis(trimethylsilyl)amide] ($Ge(N(SiMe_3)_2)$) and oleylamine into octadecene that was preheated to 285 ºC. By thermally decomposing the $Ge[N(SiMe_3)_2]$ complex, GeNCs with a relatively poor size distribution of about 7 ± 4 nm were produced.[103]

Zaitseva *et al.* investigated germanium nanostructure (GeNCs[101] and nanowires[102]) synthesis from differently substituted Ge precursors through hot injection. They reported GeNCs with sizes from 1 to 15 nm prepared by injection of organogermane precursors like trichlorogermane, tetramethylgermane, tetraethylgermane, and tetrabutylgermane into pre-heated organic solvents such as trioctylamine, squalene, and octacosane. These solvents have boiling points in the temperature range from 380 to 429 °C. Trichlorogermane and tetramethylgermane showed the lowest and highest decomposition temperatures, respectively. Figure 1-13 shows a representative image of spherical GeNCs produced from the thermal decomposition of tetrabutylgermane in squalene at 410 °C.[101,102]

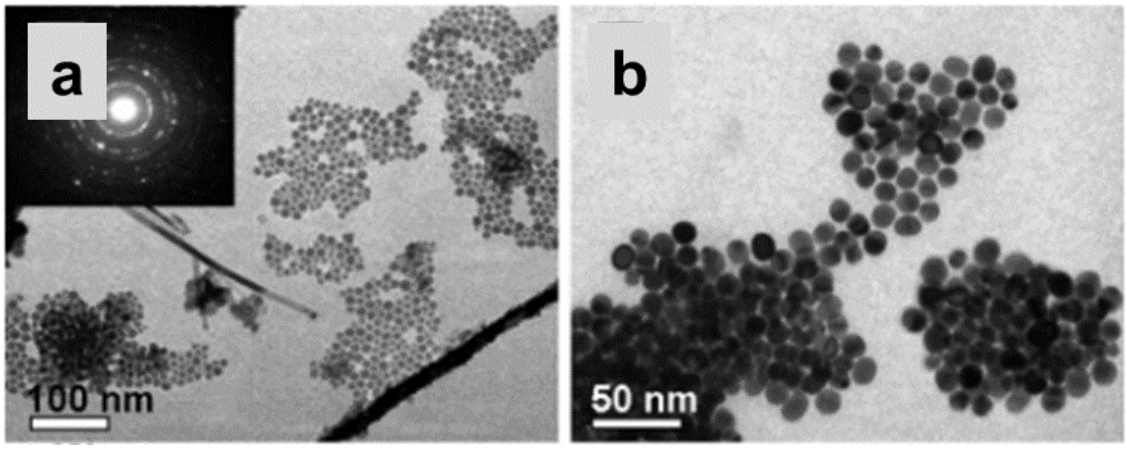

Figure 1-13. TEM images of GeNCs obtained through variation of precursors, solvents, and reaction times:[101] (a) 0.6 mL of TBG in squalene at 410 °C for 35 min; (b) 0.05 weight fraction of dichlorobenzene added to the TBG-squalene precursor mixture.

C) Supercritical Fluids Procedure

This protocol involves using solvents at high temperature and pressure and the injection of pre-heated (not decomposed) Ge precursor solution. As an example, Korgel *et al.* have reported the preparation of GeNCs with sizes from 2 to 70 nm by injecting diphenylgermane and tetraethylgermane into supercritical hexane and octanol at 400-550 °C and 20.7 MPa in a continuous flow reactor.[105] Octanol is added to control particle growth, appearing to serve as a capping ligand that binds to the particle surface through an alkoxide linkage. Although they reported PL for particles around 3-4 nm which was blue-shifted by approximately 1.7 eV relative to the band-gap of bulk Ge, the surface chemistry of the final particles and origin of PL was still complicated.

The above approaches were successful in making uniform GeNCs, but they suffer from drawbacks such as identifying suitable precursors, requiring high temperatures to induce crystallization, low yield, non-predictable (*i.e.,* complex) surface chemistry and limited control on the morphology of final NCs.

1.2.2.4. Solid-state thermal decomposition and reduction methods

Solid-state approaches are less commonly used than solution-based methods for making free-standing GeNCs. The chemistry behind these approaches is not as well developed as other methods. Classically, these methods have been utilized for making oxide-embedded GeNCs that have important potential applications in the electronics industry (*e.g.,* complementary metal-oxide-semiconductors (CMOS) and non-volatile memories (NVMs)).[76,106–108]

Covering all of the methods used for making oxide-embedded GeNCs like chemical vapour deposition,[109] ion implantation,[110] co-sputtering,[111] *etc.* is outside the scope of this Thesis. Our interests lie in the preparation of oxide-embedded GeNCs *via* sol-gel approaches. Sol-gel chemistry can offer facile control over precursor composition and ultimately over morphology of GeNCs by simply altering reaction conditions like temperature, reaction time and concentration of reagents (see Appendix A of this Thesis for further details).[112,113] In this regard, different sol-gel precursors have been used, being prepared by co-hydrolysis and co-condensation of Si sol-gel precursors like tetraethoxysilane (TEOS), tetraethoxygermane (TEOG), tetrachlorogermane ($GeCl_4$) or carboxyethyl trichlorogermane (Cl_3-Ge-C_2H_4-CO_2H).

Nogami *et al.* presented one of the earliest examples in this area.[114] They reported sol-gel preparation of silica glass containing 7 wt % Ge, produced by the sol-gel reaction of TEOS and $GeCl_4$ – simply the hydrolysis of a mixture of TEOS and $GeCl_4$ and the thermal reduction of the sol-gel product in a H_2/N_2 mixture at 400–700 °C (Figure 1-14).[114] They made GeNCs with diameters of ~5 nm that showed photoluminescence with emission peaks at 2.32, 2.17, and 2.0 eV. They also reported large Ge crystals made by heating the sol-gel product at 800 °C. These showed no photoluminescence.

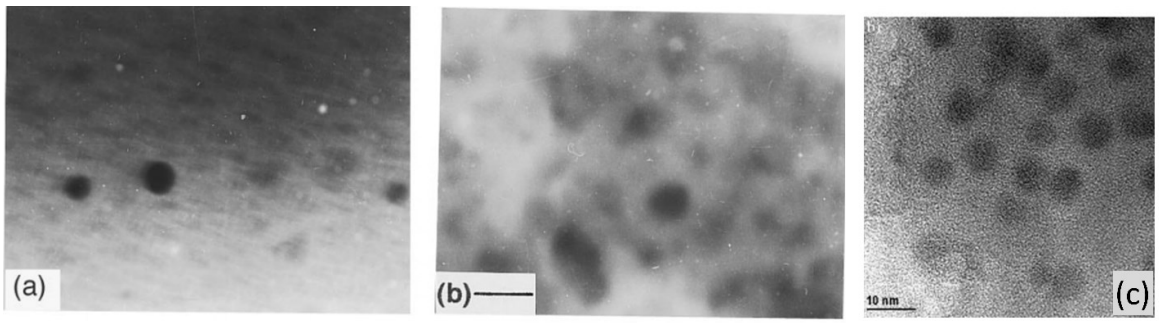

Figure 1-14. a) and b) TEM of 7 wt % Ge containing SiO_2 glasses made from $GeCl_4$ sol-gel.[114] Prepared by heating at 500 °C in air, followed by heating in H_2 / N_2 gas at 700 °C for a) 2 h and b) 5 h. c) TEM of SiO_2 embedded GeNCs made from carboxyethyl trichlorogermane sol-gel polymer.[115]

The high hydrolysis rate of $GeCl_4$ in comparison to TEOS[113,116] led to difficulties in producing a homogeneous solid-state precursor and then uniform GeNCs with narrow size distributions. This was why later works focused on controlling the hydrolysis rate of Ge sol-gel precursors by replacing $GeCl_4$ with carboxyethyl trichlorogermane (Cl_3-Ge-C_2H_4-CO_2H).[115,117] Comparing part c of Figure 1-14 with parts a or b, demonstrates that the results of changing the precursor in making uniform GeNCs were promising.[115–118]

Ozin *et al.* used TEOG as a Ge sol-gel precursor with a low TEOG/TEOS ratio to compensate for the hydrolytic rate differences of these reagents.[113] Annealing the sol-gel derived oxide at 700 ºC in 5 % H_2 / 95% Ar crystallizes the germanium to make SiO_2-embedded GeNCs. The authors also continued to liberate GeNCs from the embedding oxide matrix and make free-standing GeNCs. They removed the SiO_2 matrix with HF etching and the final GeNCs were dispersible in ethanol (Figure 1-15).[113]

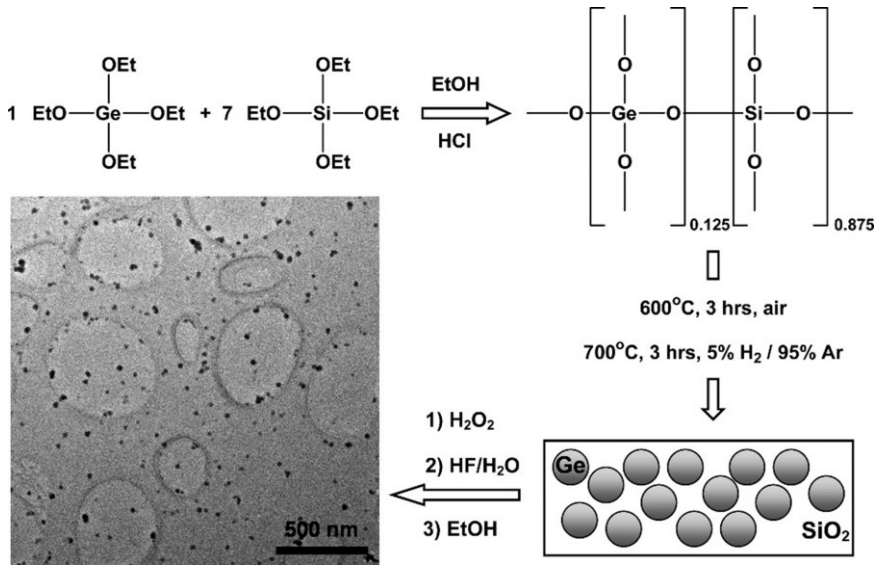

Figure 1-15. GeNCs synthesis from thermally treated $[(GeO_2)_{0.125}(SiO_2)_{0.875}]_n$ sol-gel copolymer made with acid-catalyzed hydrolysis and co-condensation of TEOG and TEOS.[113]

In our group, the solid-state preparation of Si and GeNCs embedded in an oxide matrix *via* disproportionation and/or reduction of substoichiometric oxides (RMO_x, 0<x<2, M: Si or Ge) has been demonstrated.[17,119–123] Upon disproportionation, the substoichiometric oxide undergoes a series of reactions to form the thermodynamically favoured products, which are elemental Si or Ge and form NCs, and the corresponding stoichiometric oxides (*i.e.,* SiO_2 and GeO_2) which act as an embedding matrix for the NCs. In this regard, our group reported a robust method for making SiNCs by reductive thermal processing of hydrogen silsesquioxane (HSQ, $Si_8O_{12}H_8$) or similar polymers $(HSiO_{1.5})_n$.[17,119] However, following the same procedure for making GeNCs is not possible because of the lack of the HSQ precursor equivalent or similar polymer for Ge. It was revealed, though, that thermal processing of organic functionalized germanium rich oxides [$(RGeO_{1.5})_n$] was a means of obtaining oxide-embedded GeNCs.[122] Therefore, our group concentrated on making GeNCs embedded in GeO_2 by the thermal processing of the polymer obtained from a sol-gel reaction of related precursors (see Figure 1-16).

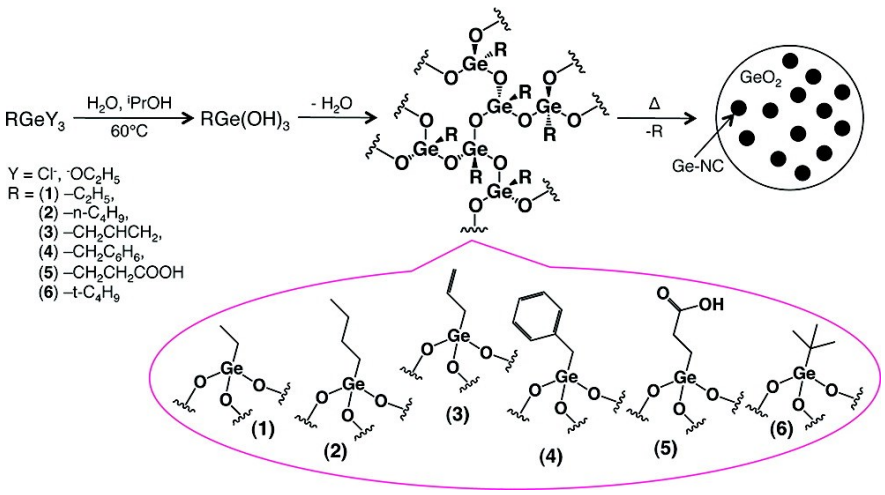

Figure 1-16. Formation of GeNCs embedded in GeO_2 from thermolysis of $(RGeO_{1.5})_n$ prepared by the sol-gel reaction of chloride- or alkoxy-substituted precursors.[121]

Phenyl-substituted sol-gel polymer [$(PhGeO_{1.5})_n$] was thermally processed at different temperatures under reducing conditions to yield GeNCs embedded in GeO_2.[122] As a result of two separate pathways for preparing GeNCs (*i.e.,* uniform disproportionation and non-uniform surface reduction), the final NCs showed poor monodispersity (Figure 1-17).[121–123]

GeNCs have been liberated from GeO_2 composite powders by direct dissolution of the oxide matrix in warm water. Although this straightforward method yielded GeNCs, due to lack of surface functionalization the final particles were suspected to have oxidized (Figure 1-17 A and B) and oxide impurities in the final NCs (which are suspected to show optical responses; *vide infra*) have not been explored.[122]

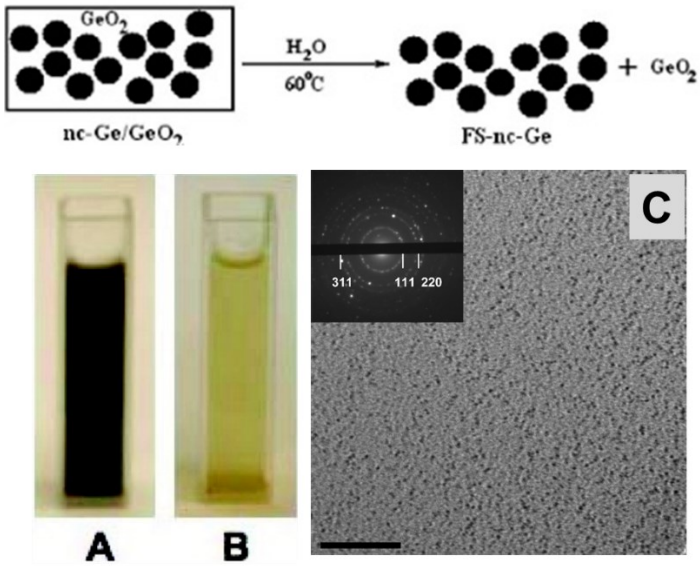

Figure 1-17. Liberation of GeNCs from a GeO_2 matrix *via* warm water washing. A) and B): Suspensions of GeNC/GeO_2 composite in warm water after 30 min and 20 hr, respectively. C) TEM images of GeNCs after 30 min in warm water, made by Veinot *et al.*[122]

Later on, the effect of different organic substituents like ethyl, n-butyl, allyl, benzyl, carboxyethyl, and t-butyl were investigated to determine the minimum temperature at which

disproportionation would occur while remaining below the thermal reduction threshold of GeO_2, effectively removing the reduction pathway.[121] This produced poor monodispersity in final NCs. However, a more drastic problem for all kinds of organic substituted germanium rich oxides ($RGeO_{1.5}$) was the relatively high carbon content in the composite after thermal processing. Carbon impurities cannot be removed by HF etching because of the strong covalent Ge-C bond and this leads to difficulty in liberation of GeNCs from the embedding oxide layer.[121]

1.2.3. Photoluminescence of GeNCs

While nanostructures of Group 14 semiconductors (*i.e.,* Si and Ge nanoparticles) are attractive because of their interesting and potentially applicable optoelectronic properties, Ge is particularly of interest for several reasons:

Ge nanostructures exhibit a large Bohr-exciton radius, which makes it possible to see quantum confinement in wider size ranges of GeNCs. The globally accepted excitonic Bohr radius of Ge (24.3 nm) is five times larger than that of Si (4.9 nm) and CdSe (5.6 nm).[67,70,124,125]

IR-emitting agents (QDs or molecular materials) are very useful for research and technological applications. For example, in bio-imaging applications, it is best to have IR-emitting cell labels because live tissues are more transparent for these wavelength ranges and an improved signal-to-noise ratio is thus achieved.[126] The bulk band-gap of Ge (0.66 eV at 300 K) is smaller compared to Si (1.1 eV) or CdSe.[69,125,127] So Ge-based nanostructure are expected to show opto-electrical properties in the comparatively lower energy regions of electromagnetic spectrum (mostly NIR and IR).

Although, as mentioned previously, bulk germanium shows an indirect band-gap at 0.66 eV, Ge nanostructures have potential behaviour as direct or quasidirect band-gap materials.[128–130]

Moreover, the energy levels in the band structure are strongly dependent on lattice deformation. For example, uniaxial tension along the <111> direction of Ge can lead to a change from an indirect to a direct band-gap.[129] In addition, besides the indirect band-gap at 0.66 eV, germanium also has a direct band-gap at 0.8 eV (Figure 1-18).[128,129,131,132] A combination of possible transitions in the emission process, shown in Figure 1-18, can strongly enhance light-emission efficiency.[128,130,133]

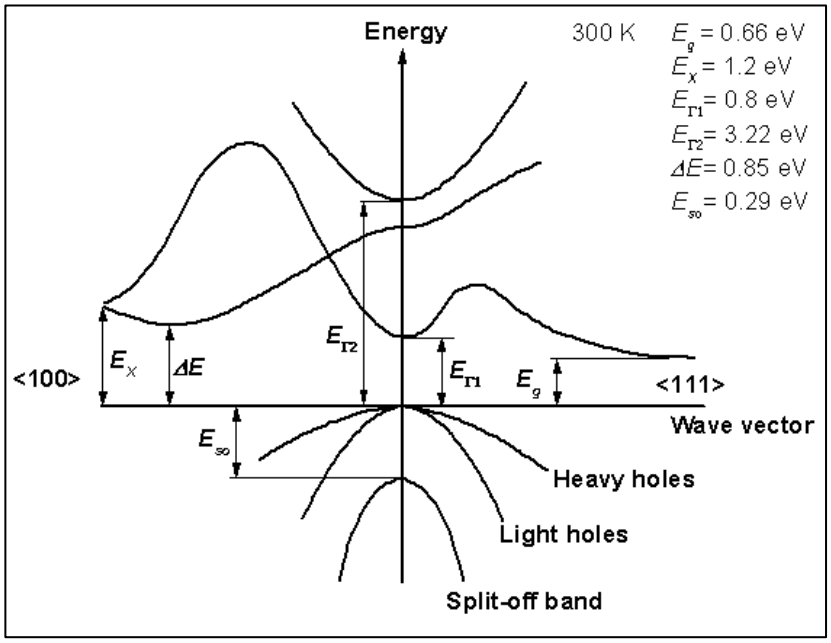

Figure 1-18. Energy band structure and density of states of elemental germanium.[132]

According the band-gap diagram of Ge shown in Figure 1-18, Ge has several gaps between valence bands and conduction bands with various energies. Thus, its nanostructures can absorb light over a broad range of spectral region.[80] Also, by definition, the absorption coefficient is stated as the fraction of the light intensity absorbed per unit length in the media and is totally dependent on the wavelength of incident light.[134] According to Figure 1-19, the Ge bulk optical

absorption spectrum in the energy range from 0.5 to 5 eV samples a large part of the Brillouin zone. In this context, Ge shows a large absorption coefficient (*ca.* 2×10^5 cm^{-1} at 2 eV).[133]

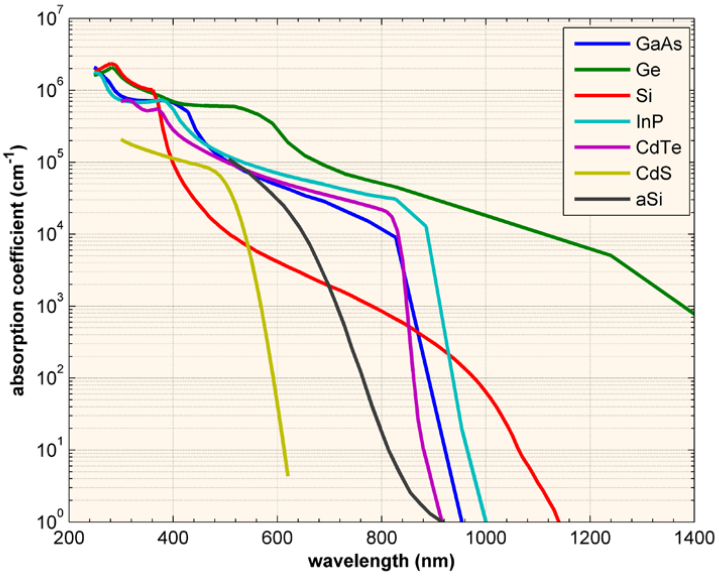

Figure 1-19. The absorption coefficient, α, in a variety of semiconductor materials at 300K as a function of the wavelength of the light.[80]

Despite all of these favorable optoelectronic properties of GeNCs and the various preparation methods (*vide supra*), PL originating from GeNCs remains the subject of some scientific controversy. Reports are often contradictory about the source of PL, the critical size of NCs (Bohr-exciton radius), the expected PL wavelength, determining quantum yield, the effect of oxide and other surface impurities.[18,89,121,122,130] To add to this complexity, it should be mentioned that germanium oxide moieties usually show optical responses in the visible region and thus may cause more misinterpretation.[70,135] For example, many research groups have reported the PL responses of GeNCs made by physical deposition approaches as ranging from 2.1-2.4 eV and arising from the quantum confinement effect of GeNCs from 2-15 nm.[67,70,109]

However, careful follow-up studies demonstrated that the high energy PL (*ca.* 2.0 eV) previously attributed to GeNC emission was in fact the result of surface oxide impurities.[136–138]

A seminal work about the nature of quantum confinement in GeNCs has been reported recently.[139] Veinot *et al.* employed scanning tunneling spectroscopy to directly evaluate the quantum confinement effect in single isolated GeNCs (Figure 1-20).

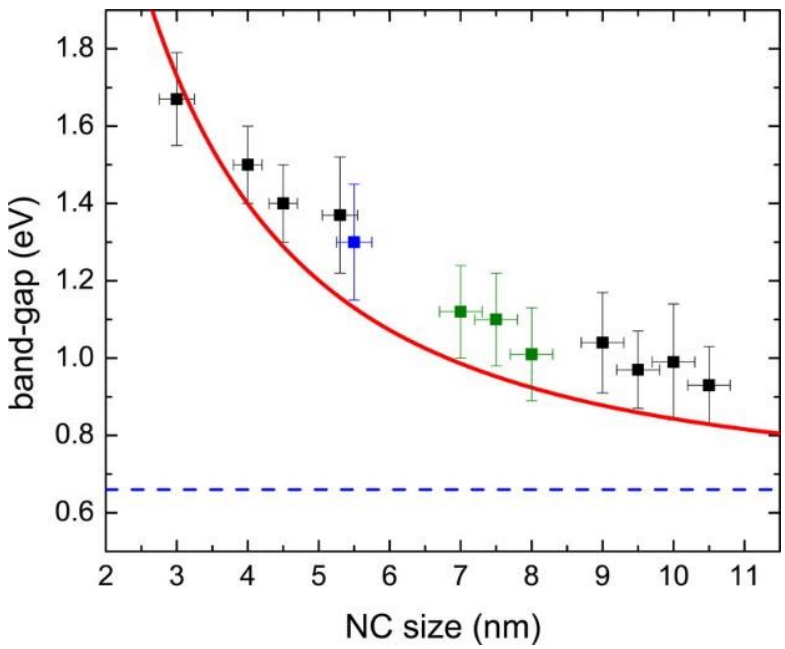

Figure 1-20. Band-gaps of GeNCs as a function of size. Experimental data (dots with error bar) as reported by Veinot *et al.*[139] *vs.* theoretical data (red line) obtained from Lannoo *et al.*[140].

According to Figure 1-20, isolated individual GeNCs exhibit the quantum confinement effect. In fact, the band-gap of NCs increases from 0.97 to 1.67 eV for GeNC sizes in the measured range of 10.5 to 3.0 nm,

Figure 1-20 reveals that GeNCs should theoretically and experimentally show optoelectronic responses in the NIR and IR regions as was discussed at the beginning of this section. Despite considerable research showing UV-Vis emitting GeNCs (which are mostly due

to other sources rather than quantum confinement from GeNCs), there is a surprising paucity of examples of GeNCs showing size-dependent NIR or IR photoluminescence. The first example was discovered in 1998 by Fujii *et al.*, who measured near-infrared optical responses from GeNCs embedded in SiO_2 matrices.[136] They reported PL peaks of 0.88-1.54 eV (1400-800 nm) for 5.3-0.9 nm diameter particles. This group used a calculation study that related the mole fraction of Ge to the size of GeNCs embedded in SiO_2. Due to the indirect size measurement of the GeNCs, particularly for smaller particles (*i.e.,* 0.9 nm), and embedding in silica matrices, obtaining a comprehensive conclusion from this work was not possible.

Synthesis of free-standing IR-emitting GeNCs did not happen until 2010, when Klimov *et al.* showed the first colloidal GeNCs derived from the solution reduction of germanium halides. These exhibited photoluminescence in the infrared spectral region *via* a band-gap transition.[18] These authors also showed the size dependent properties arising from quantum confinement in different NC sizes, reporting PL peaks ranging from 980-1140 nm (1.26-1.09 eV) for 3.2-4.0 nm diameter particles.[18]

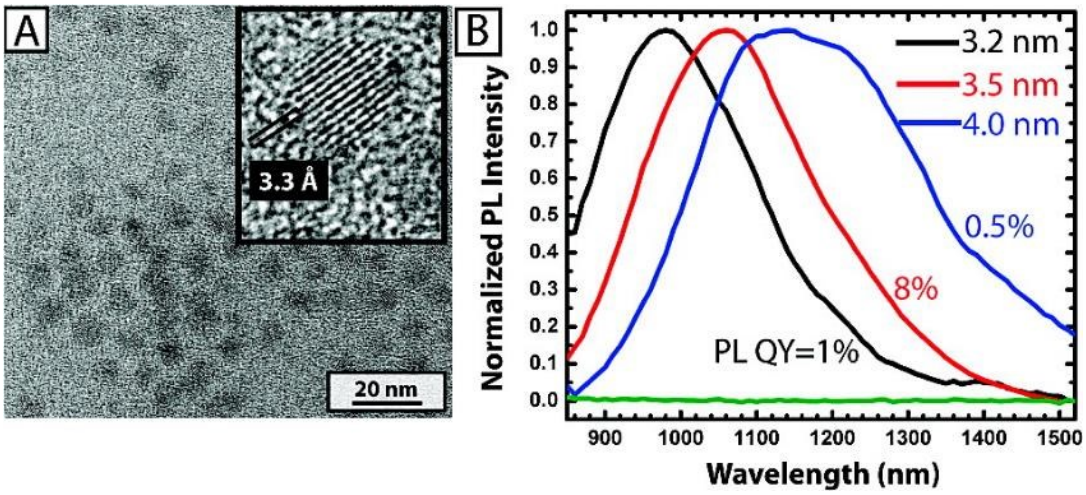

Figure 1-21. (A) TEM and HRTEM images of Ge NCs (4.0 ± 1.7 nm) with a PL peak at 1160 nm (blue curve in part B) reported by Klimov *et al.*[18]

However, follow-up work by Neal *et al.* showed that the PL quantum yield (up to 8%) (shown in Figure 1-21) was somehow due to an error in data interpretation.[130] They then reported that PL Quantum Yield (QY) values for the 2.3, 3.8, and 4.7 nm GeNCs were less than 0.1% in all cases. These low PL QY in GeNCs are classically believed to be the result of non-radiative centres such as surface defects or unsaturated germanium species (*e.g.,* Ge=Ge) acting as trap states that cause thermal energy loss instead of band-gap recombination (*i.e.,* PL).[130,141,142]

Despite the extent of these advanced efforts in the synthesis and characterization of GeNCs, developing methods affording well-defined GeNCs as well as analyzing optoelectrical properties attributed to these nanoscale semiconductors, remain important targets for investigation.

1.3. Scope of this Thesis

The main theme of the current Thesis is Ge-based nanomaterials. In the first two Chapters (Chapters two and three), we have taken advantage of well-established Ge and Si sol-gel chemistry to prepare different morphologies of GeO_2 as well as GeO_2@SiO_2 core-shell nanoparticles. The surfactant-free synthesis of GeO_2 nano-cubes and nano-eggs has been achieved by applying simple alterations to the composition of the reaction mixture (*i.e.,* ammonia and water content). These well-defined GeO_2 nano-cubes and nano-eggs, with narrow size distributions, have been characterized using different techniques such as SEM, TEM, HRTEM, and XRD.

Despite the facile control over GeO_2 NP morphology discussed in Chapter two, hydrogen thermal reduction of these NPs to elemental Ge nanomaterials was not possible without significant morphological damage due to aggregation of NPs. Therefore, in the third Chapter, a

protective shell of SiO_2 around the GeO_2 NPs (nano-eggs and nano-cubes) was produced to make GeO_2@SiO_2 core-shell nano-cubes or nano-eggs. Afterwards, the core and shell were selectively reduced by 5% H_2/95% Ar or elemental magnesium to yield Ge@SiO_2 and Ge@Si core-shell NPs, respectively.

Synthesis and surface functionalization of GeNCs with radii smaller than the Ge Bohr-exciton radius (*i.e.,* 24 nm) are the main subjects of Chapters four and five. We have developed a method for high-yield preparation of hydride-terminated GeNCs (H-GeNCs) *via* disproportionation of a 'Ge$(OH)_2$' precursor. It has been found that Ge$(OH)_2$ is able to undergo an internal oxidation-reduction reaction to form GeNCs embedded in a GeO_2 matrix. These GeNCs can be liberated from the GeO_2 matrix using HF etching to yield H-GeNCs. However, obtaining uniformly sized GeNCs was not possible without modifying the 'Ge$(OH)_2$' precursor. In this context, white, yellow, orange and brown 'Ge$(OH)_2$' precursors have been prepared and it has been found that the brown precursor is most suitable for making nearly monodisperse GeNCs with well-defined surface chemistry. This study clarified some chemistry regarding the 'Ge$(OH)_2$' precursor, as well.

After preparing H-GeNCs, which will be discussed in the fourth Chapter, surface functionalization of GeNCs is the subject of Chapter five. In this context, a series of hydrogermylation approaches (*i.e.*, thermally-activated, radical-initiated, and borane-catalyzed) has been performed. Our results have proven that surface functionalization occurs under all functionalization protocols with some differences regarding surface coverage as well as the degree of ligand oligomerization on the surfaces of GeNCs.

Although Ge is the main subject of the current Thesis, Chapter six explores the fabrication of Si-amide-Fe_3O_4 multi-functional nano-hybrids, indicating that similar chemistry is

possible for GeNCs as well (see future directions in Chapter seven). Si-amide-Fe_3O_4 nano-hybrids are promising materials for use in biological systems due to the biocompatibility and fairly low toxicity of Si compared to typical quantum dots such as CdSe. We have prepared these nano-hybrids *via* N,N'-Dicyclohexylcarbodiimide (DCC) coupling of undecanoic acid-functionalized SiNCs to APTM-coated Fe_3O_4 super-paramagnetic NPs. We have also performed confocal cell imaging and cytotoxicity evaluation of these novel magnetic hybrid NPs. Chapter seven will summarize the results and propose some possible directions for pursuing.

Chapter 2:

Surfactant-free Synthesis of GeO_2 Nanocrystals with Controlled Morphologies*

* A version of this Chapter has been published:

Javadi, M.; Yang, Z.; Veinot, J. G. C. *Chem. Commun. (Camb).* **2014**, *50*, 6101–6104.

2.1. Introduction

Germanium dioxide (GeO_2) is a high-k dielectric[67,143] and its phase stability below 425 °C[144] makes it an ideal system for the electronics industry.[145,146] In addition, photoluminescence (PL) from GeO_2 nanostructures (*e.g.*, nanowires) has been demonstrated with peak energies at *ca.* 3.1 eV (400 nm) and 2.2 eV (563.6 nm).[67,70,147,148] The origin of this PL has been attributed to oxygen vacancies, or other surface defects.[148–151] However, this intriguing property remains the subject of extensive study. Much of the curiosity directed toward GeO_2 nanostructures arises from how it differs from its Si counterpart (*i.e.*, SiO_2); for example, in addition to its higher dielectric constant (*i.e.*, ε_{GeO2} = 14.5 *vs.* ε_{SiO2} = 3.9),[121,143,146] it also has a higher refractive index (η_{GeO2} = 1.6-1.65 *vs.* η_{SiO2} = 1.45),[152,153] wider optical transparency window between 280 and 5000 nm (*i.e.*, from UV to near IR region),[154] and a higher linear coefficient of thermal expansion.[155] All of these properties make germanium dioxide nanostructures appealing for a wide range of applications including, optical waveguides,[156] connections in optoelectronic communications,[157,158] photosensors,[159] among others.[87,160,161]

GeO_2 nanostructures have been synthesized *via* sol-gel reactions using tetraethoxygermane (TEOG)[162] or tetrachlorogermane ($GeCl_4$).[154,163,164] Unlike the analogous reactions of tetraethoxysilane used to prepare Stöber silica, direct sol-gel reactions using TEOG or $GeCl_4$ are rapid and difficult to control/study.[152] As a result, when GeO_2 nanostructures of tailored size and/or morphology are targeted, it is necessary to include substantial quantities of capping agents (*i.e.*, surfactants) to achieve the desired product.[152,163,165–169] Table 2-1 shows a summary of literature reporting different shapes of GeO_2 nanoparticles (NPs). According to this table, usually large quantities of templating agents (*e.g.*, surfactants) are required to obtain GeO_2 nanoparticles of tailored morphology.

Table 2-1. Summary of methods reported in recent references using surfactant approaches to yield GeO_2 NPs

Ref	GeO_2 particles Precursor	Surfactant System	Solvent + Other additives	Nanoparticles form
Kawai et al, *Coll. & Surf.*, **1999**	$Ge(OEt)_4$ (~4×10^{-4} mol)	Sodium bis(2-ethylhexyl) sulfosuccinate (AOT) reversed micelles (~1 g)	2,2,4-Trimethylpentane (~30 mL)	Nanocubes
Wu et al, Chem. Mater. **2006**	$GeCl_4$ (~10^{-3} mol)	Cetyltrimethylammonium (CTAB) reversed micelles (~5 g)	Heptane (~80 mL) Pentanol (~9 mL) Oleylamine(~5 mL) THF (~2 mL)	Nanocubes + spindle-shape
Wang et al, *J. Phys.: Condens. Matter* 18, **2006**	$GeCl_4$ (~10^{-3} mol)	Cetyltrimethylammonium (CTAB) reversed micelles (~5 g)	Heptane (~80 mL) Pentanol (~9 mL) Oleylamine(~5 mL) THF (~2 mL)	Nanocubes
Chen et al, *Materials Letters* **2007**, *61*, 535–537.	$GeCl_4$ (~2×10^{-4} mol)	Sodium bis(2-ethylhexyl) sulfosuccinate (AOT) reversed micelles (~0.88 g)	Isooctane (40 mL)	Nanocubes
Davis et al, *Langmuir* **2007**	$Ge(OEt)_4$ (~10^{-3} mol)	Lysine* (~0.9 g)/9500H_2O/240Ethanol *(S)-2,6-Diaminocaproic acid	Water & Ethanol	Nanocubes
Li et al, *Applied Physics Letters* 91, **2007**	$GeCl_4$ (~10^{-3} mol)	Cetyltrimethylammonium (CTAB) reversed micelles (~5 g)	Heptane (~80 mL) Pentanol (~9 mL) Oleylamine(~5 mL) THF (~2 mL)	Nanocubes
Chiu et al, *J. Phys. Chem.*, **2009**	$Ge(OEt)_4$ (~3×10^{-4} mol)	of Triton X-100 (4-octylphenol poly-ethoxylate, J. T. Baker) (1.56 g)	Cyclohexane (5.60 mL) n-hexanol (1.48 mL)	Hexabranched GeO_2 (spindle-shape)
Wang et al, *Mater. Sci. Forum*, **2011**	$GeCl_4$ (~10^{-3} mol)	Cetyltrimethylammonium (CTAB) reversed micelles (~5 g)	Heptane (~80 mL) Pentanol (~9 mL) Oleylamine(~5 mL) THF (~2 mL)	Nanocubes
Wang et al, *Nanotechnology* 22, **2011**	$GeCl_4$ (~10^{-3} mol)	Cetyltrimethylammonium (CTAB) reversed micelles (~1.25 g)	Octane (~5 mL) Pentanol (~1.8 mL) Oleylamine(~0.7 mL) THF (~0.5 mL) formaldehyde water solution (0.5 ml)	Nanocubes
This work	$Ge(OEt)_4$ (4.48×10^{-4} mol)	-	Water & Ethanol	Small NPs, Egg-shape. Spindle-like and perfect nanocubes

While the addition of surfactants facilitates some shape control, these additives are often costly, toxic, can influence reaction pathways, and complicate material purification. Furthermore, if the GeO_2 nanostructures are intended as precursors for other nanomaterials (*e.g.*, Ge NPs)[162] even traces of these seemingly inert impurities could lead to contamination. In this regard, a surfactant-free synthetic approach to well-defined GeO_2 nanostructures of tailored morphologies is clearly appealing.

Herein, we report a straightforward method for forming GeO_2 NPs of controlled size and shape. Our approach does not require addition of any templating agents or surfactants, and achieves morphological tailoring yielding small pseudospherical nanoparticles, nanoeggs, spindles, and nanocubes of GeO_2.

2.2. Experimental

The synthetic methods employed for all of the presented materials generally involve controlled hydrolysis and condensation of TEOG. Briefly, addition of TEOG to a water/ethanol solution of ammonium hydroxide with rapid stirring yields a cloudy white suspension. Following aging the resulting white product was isolated *via* centrifugation, washed repeatedly with anhydrous ethanol, and dried in vacuo at 110 °C for 12 hours. Defining the water/ethanol ratio, ammonium hydroxide concentration, as well as reaction time and temperature yields different particle morphologies and assemblies. The following discussion focuses on the influences of these parameters on the evolution of the GeO_2 particles.

2.3. Reagents and Materials

Tetraethoxygermane (TEOG, 99.99%) was purchased from Gelest, stored in an argon-filled glovebox and used as received. Anhydrous ethanol and ammonium hydroxide (29.3 wt% NH_3 in

water) were purchased from Sigma-Aldrich and used as received. High-purity DI water (18.2 MΩ/cm) was obtained from a Barnstead Nanopure Diamond purification system.

2.3.1. Synthesis of GeO_2 Nanocubes and Nanoeggs

For a typical synthesis, TEOG (100 µL, 0.113 g, 0.45 mmol) was added dropwise with rapid stirring to 1.0 ml of a water/ethanol solution (2-100 vol. % water) of appropriate ammonium hydroxide concentration. A white precipitate forms at rates dependent upon the reaction mixture water content. Stirring was continued for 24 hours to ensure complete hydrolysis and condensation. Finally, the white precipitate was isolated *via* centrifugation (3000 rpm), washed with anhydrous ethanol (three times), and dried in a vacuum oven at 110 °C for 12 hours.

2.3.2. Material Characterization

Electron Microscopy. Bright field Transmission Electron Microscopy **(**TEM) and Energy Dispersive X-ray Spectroscopy (EDX) analyses were performed using a JEOL 2010 (LaB_6 filament) electron microscope with an accelerating voltage of 200 keV. Samples were by drop coating ethanol suspensions of GeO_2 nanoparticles onto carbon-coated 200-mesh Cu grids. TEM images were processed using Gatan ImageJ software (version 1.46r) and particles size distributions were obtain by measuring *ca.* 300 particles.

High resolution (HR) TEM images were obtained from Hitachi-9500 electron microscope with an accelerating voltage of 300 kV and were processed using Gatan ImageJ software (version 1.46r). Samples were prepared by drop coating solutions of GeO_2 nanoparticles dispersed in ethanol onto a holey carbon coated copper grid (400 mesh). High-resolution TEM (HRTEM) and Selected Area Electron Diffraction (SAED) were obtained from Hitachi-9500 electron microscope with an accelerating voltage of 300 kV.

Scanning electron microscopy (SEM) images were obtained by using a JEOL 6301F field-emission scanning electron microscope with an acceleration voltage of 5 kV. Samples were prepared by drop casting GeO_2 nanoparticles from ethanol suspensions onto a clean (sonicated in ethanol for >10 min) Si (100) wafer.

X-ray Diffraction (XRD) and FT-IR. XRD was performed using an INEL XRG 3000 X-ray diffractometer equipped with a Cu Kα radiation source (λ = 1.54 Å). Crystallinity of all samples was mounted on a low-intensity background Si (100) holder. Approximately 0.1 g of finely ground powders have been placed on holder and run for >6 hr acquisition time. Fourier-Transform Infrared Spectroscopy (FT-IR) of powders of isolated particles was performed on a Nicolet Magna 750 IR spectrophotometer. Finely ground powders were pressed into KBr pellets and measured in reflectance mode.

2.4. Results and Discussion

2.4.1. The Influence of Water/Ethanol Ratio

The dependence of GeO_2 NP morphology on the reaction media water/ethanol ratio for reactions catalyzed by 10^{-3} M ammonium hydroxide is illustrated well in the scanning and transmission electron microscopy evaluation of the isolated products (See Figures 1 and 2). Small (13 nm ± 21%) pseudospherical GeO_2 NPs are obtained when the volume percent (vol. %) of water is 10 (Figure 2-1 A, B and Figure 2-2 A, B). These small particles are agglomerated, consistent with the present reaction conditions that do not involve the addition of surface capping agents. We have hypothesized that, the condensation reaction of alkoxy and/or hydroxy groups on the surface of freshly formed GeO_2 particles leads to this agglomeration. Increasing the water content to 30 vol. % yields nanoegg-shaped (length = 525 nm ± 9%; width = 325 nm ± 13%,

Figure 2-1 C, D and Figure 2-2 C, D) assemblies of the small particles noted in Figure 2-1 A. GeO_2 spindles (length = 250 nm ± 23%; width = 175 nm ± 18%, Figs. 1E, F and Figure 2-2 E, F) with rough surfaces are obtained when reactions are performed at 50 vol. % water. These spindles are similar to those prepared using reverse micelle templates by Jiang *et al.*[165] and Kawai *et al.*[166] Interestingly, contrast in the transmission electron microscopy images is consistent with the present spindles being hollow (Figure 2-1 F, Figure 2-2 E). The exact mechanism for the formation of these hollow structures remains unclear and is the subject of ongoing study in our laboratory. Finally, upon addition of sufficient water (*i.e.*, > 70 vol. %), well-defined GeO_2 nanocubes with edge dimensions of 314 nm ± 10% are obtained (Figure 2-1G, H).

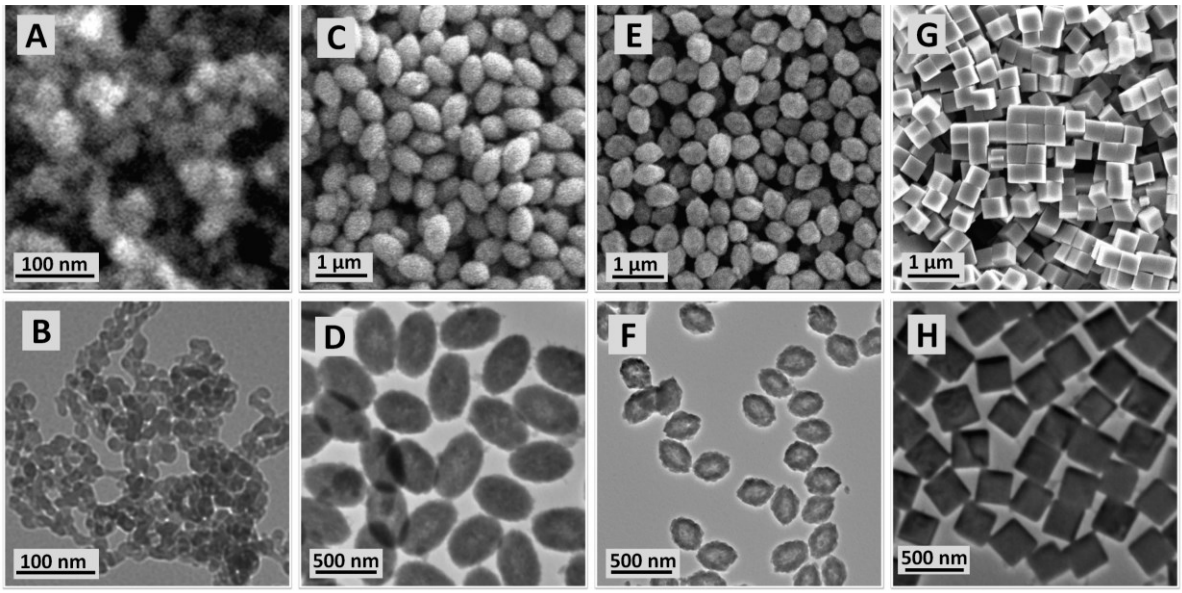

Figure 2-1. SEM (top row) and bright field TEM (bottom row) images of GeO_2 NPs prepared using indicated water/ethanol ratios: A, B) Small pseudospherical NPs (10 vol. % H_2O); C, D) Nanoeggs (30 vol. % H_2O); E, F) Spindles (50 vol. % H_2O); G, H) Nanocubes (>70 vol. % H_2O).

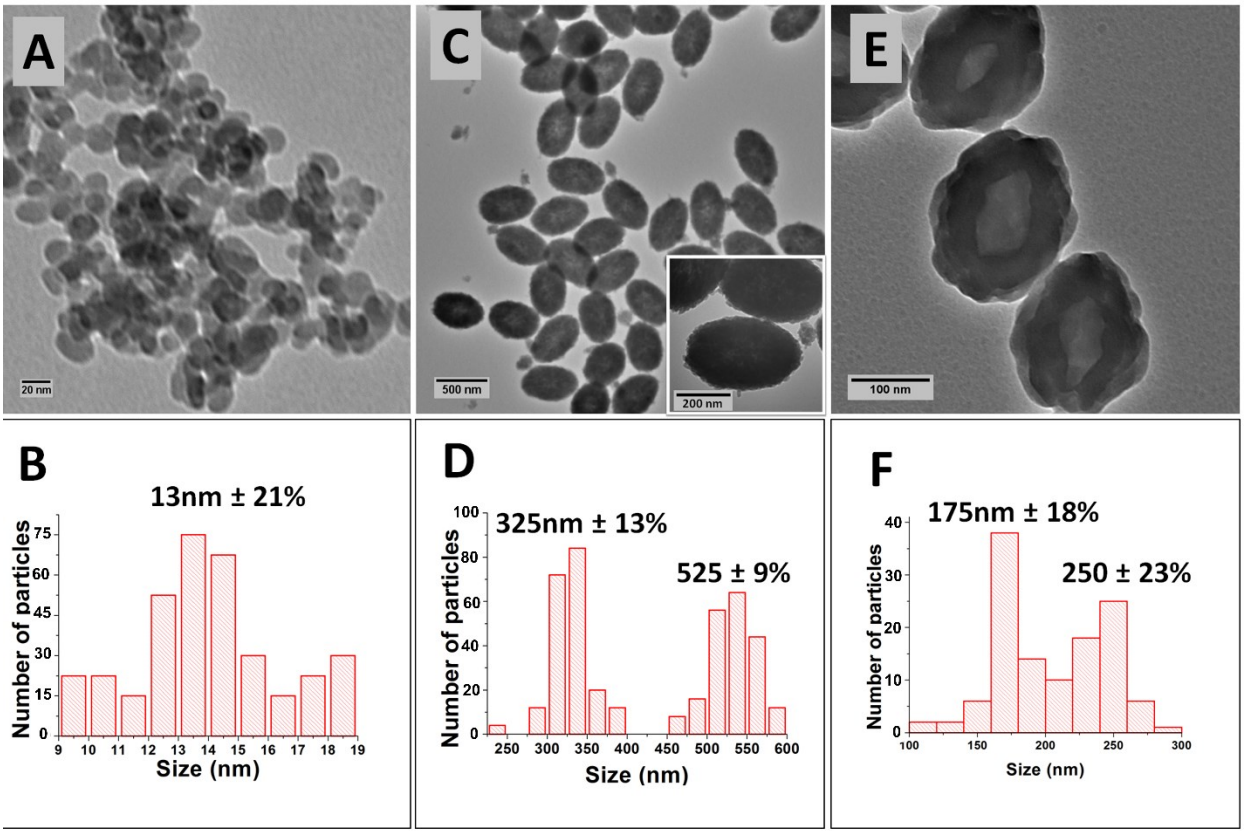

Figure 2-2. TEM analysis of GeO_2 NPs prepared in different water/ethanol ratios: A,B) Pseudospherical NPs (10 vol. % H_2O); C,D) Nanoeggs (30 vol. % H_2O), Rough surfaces of GeO_2 nanoeggs (inset) are because of agglomeration of small particles; E,F) Spindles (50 vol. % H_2O). Particles size distributions shown in D and F highlight distributions of the widths and lengths of the presented asymmetric GeO_2 nanoeggs and spindles.

Scheme 2-1 summarizes the influence of the vol. % H_2O in the reaction mixture on GeO_2 NP shape when the reaction is catalyzed by 10^{-3} M aqueous ammonium hydroxide. The observed evolution of particle morphology may be understood in the context of TEOG hydrolysis and condensation, combined with a general nucleation and growth mechanism.[104] According to *Eq.* 2-1, hydrolysis of TEOG begins with the formation of $Ge(OC_2H_5)_{4-x}(OH)_x$. The exact product distribution obtained from this reaction will depend upon the water/ethanol ratio (*i.e.*, vol. % H_2O). With increasing vol. % H_2O, "x" will tend toward 4 resulting in $Ge(OH)_4$ being the

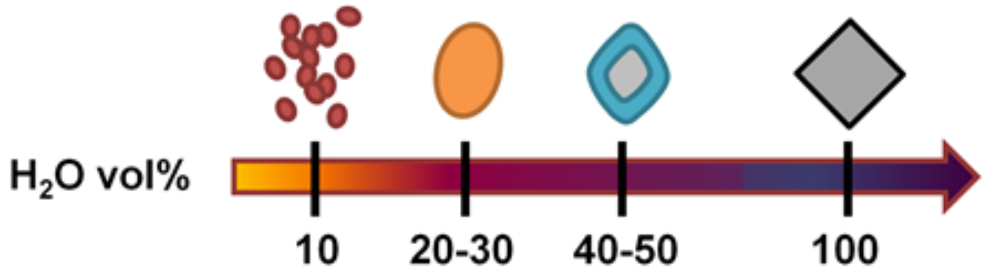

Scheme 2-1. A schematic summary of the morphological evolution of GeO_2 NPs resulting from changes in the water/ethanol ratio for the sol-gel reaction of TEOG when catalyzed by 10^{-3} M ammonium hydroxide.

dominant product. The hydrolysis product mixture (*i.e.*, $Ge(OC_2H_5)_{4-x}(OH)_x$; x = 1, 2, 3, 4) subsequently participates in condensation reactions (*Eq.* 2-2) and yields materials whose properties (*i.e.*, morphology) are expected to depend upon the original hydrolysis product distribution.

$$Ge(OC_2H_5)_4 + xH_2O \rightleftharpoons Ge(OC_2H_5)_{4-x}(OH)_x + xC_2H_5OH \qquad \textit{Eq.}\ 2\text{-}1$$
$$Ge(OC_2H_5)_{4-x}(OH)_x \rightleftharpoons Ge(OC_2H_5)_{4-x}(O)_{x/2} + (x/2)H_2O \qquad \textit{Eq.}\ 2\text{-}2$$

At low vol. % water, it is reasonable that x<<4. Under these conditions there are few reactive sites where condensation can occur and particle formation/growth will proceed slowly. This is consistent with our experimental observation that *ca.* 2 hours is required for a cloudy suspension to form when the reaction mixture vol. % water = 10. In this context, it is reasonable to expect the particle size to be limited by reaction time and available water; small particles will result. When the vol. % water approaches 30, small GeO_2 colloids form more rapidly because more sites are available for condensation reactions to occur. Under these conditions it is reasonable that particles will come together forming loosely agglomerated assemblies that subsequently crosslink through further surface-surface condensation reactions. This process will yield covalently linked aggregate particle assemblies like those shown in Figs. 1C and D. A

similar process is expected to occur at higher vol. % water (*i.e.*, 50%) to yield bonded structures (see Figure 2-1E, F). At vol. % water greater than 70 well-defined crystalline GeO_2 nanocubes are formed. The formation and characterization of these nanocubes will be the subject of the following discussion.

IR spectra of all GeO_2 morphologies are nearly identical (See Figure 2-3) with a strong absorption at *ca.* 895 cm^{-1} that is readily attributed to vibration modes of GeO_4 tetrahedra.[159]

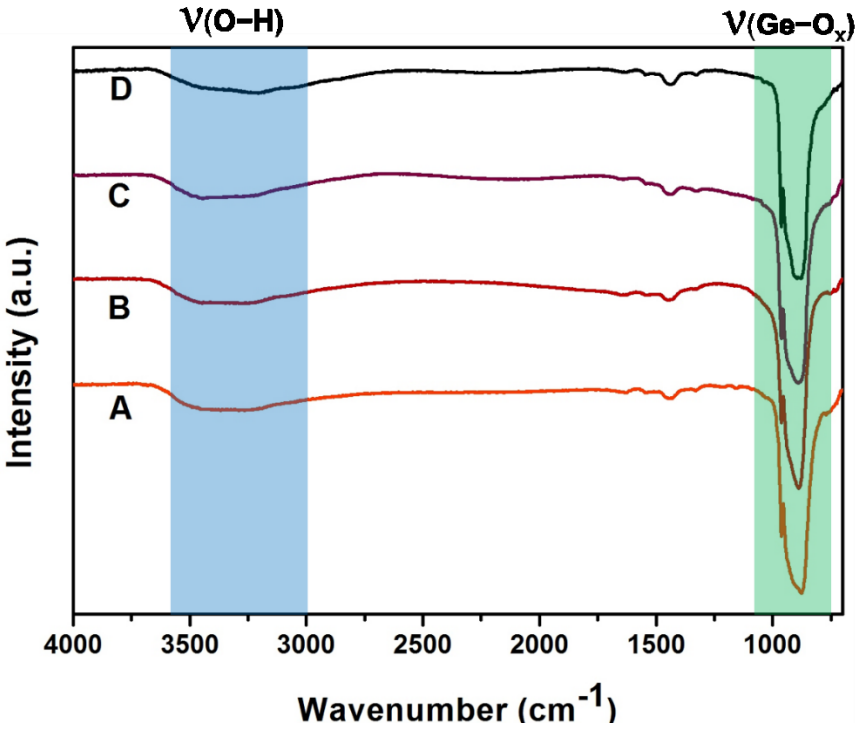

Figure 2-3. Typical IR spectra of GeO_2 nanoparticles: A) nanocubes; B) spindles; C) nanoeggs; D) pseudospherical NPs.

Representative energy dispersive X-ray (EDX) analysis shown in Figure 2-4 confirms the presence of germanium and oxygen in all NPs presented here. Interestingly, no nitrogen is detected at the sensitivity of EDX (± 1-2% atomic % depending on Z)[170] indicating negligible

ammonium hydroxide contamination. X-ray powder diffraction (XRD, Figure 2-4) confirms the nanoparticles, regardless of size or morphology, exhibit the hexagonal GeO_2 (α-GeO_2) crystal structure [PDF #04-0498].[171] Peak broadening in the XRD patterns of small nanoparticles, nanoeggs and spindles (which are assemblies of small particles) is consistent with small crystalline domains. Nanocubes show sharp intense signals consistent with their comparatively large size determined using electron microscopy. Electron diffraction of a single nanocube (Figure 2-4 C) shows a pattern consistent with a single crystal domain. It has previously been reported that the most thermodynamically stable crystal planes of α-GeO_2 are (1-11), (011) and (10-1).

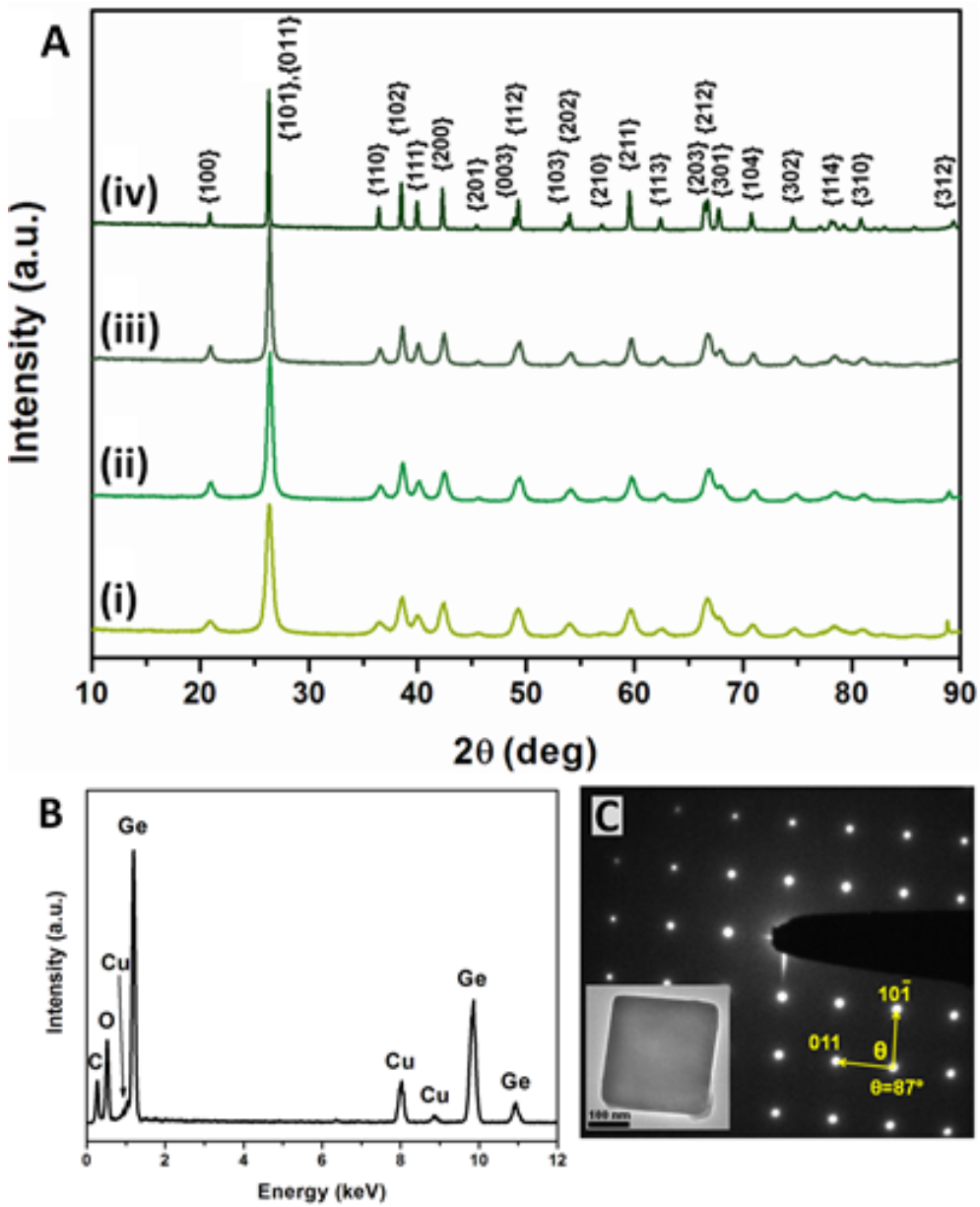

Figure 2-4. A) XRD patterns of different GeO_2 NPs morphologies. **i.** pseudospherical particles, **ii.** Nano-eggs, **iii.** Spindles, and **iv.** Nano-cubes; B) A representative EDX spectra for all GeO_2 NPs morphologies; C) A representative Selected Area Electron Diffraction (SAED) pattern of a single GeO_2 nano-cube (inset).

In this context, cube-like nanocrystals terminated by these faces are reasonable.[165] Representative high-resolution transmission electron microscopy (HRTEM) analysis of a single

nanocube (Figure 2-5) shows lattice fringes separated by 0.34 nm consistent with the α-GeO_2 (10-1) and (011) planes.[171]

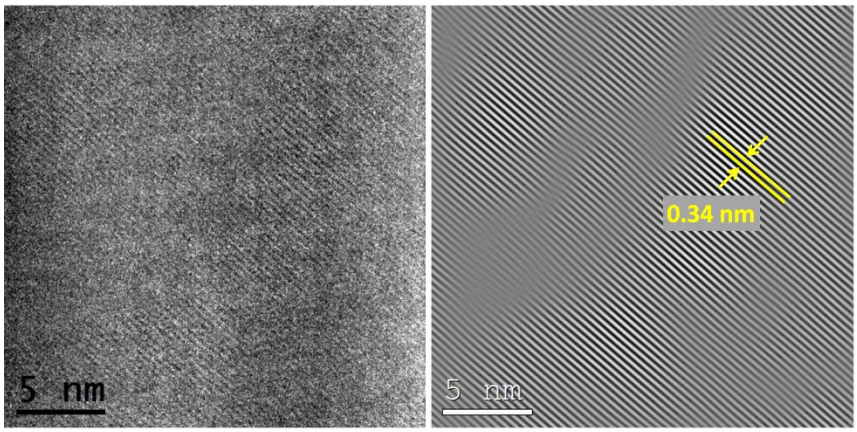

Figure 2-5. A) High resolution transmission electron microscopy (HRTEM) image of GeO_2 nanocubes; B) Fourier transformed image of (A) done by ImageJ software, showing lattice spacing = 0.34 nm consistent with the α-GeO_2 (10-1) and (011)] planes.

2.4.2. The Influence of Ammonium Hydroxide and TEOG Concentration.

Having established the optimum vol. % water for the formation of GeO_2 crystalline nanocubes (*i.e.*, 100%), we turn our attention to the ammonium hydroxide concentration while maintaining the water content and TEOG concentration constant. Figure 2-6 shows the influence of NH_4OH concentration on GeO_2 nanocube morphology. For 0.003 M NH_4OH, polydisperse GeO_2 nanocubes (edge = 350 nm ± 18%, Figure 2-6 A) are obtained. For 0.01 M NH_4OH the product is dominated by well-defined GeO_2 nanocubes (*i.e.*, 314 nm ± 10%: Figs. 6B, C, E). Increasing the NH_4OH to 0.03 M provides polyhedral particles and nanocubes that appear fused presumably because of surface-surface condensation reactions noted above (Figure 2-6D).

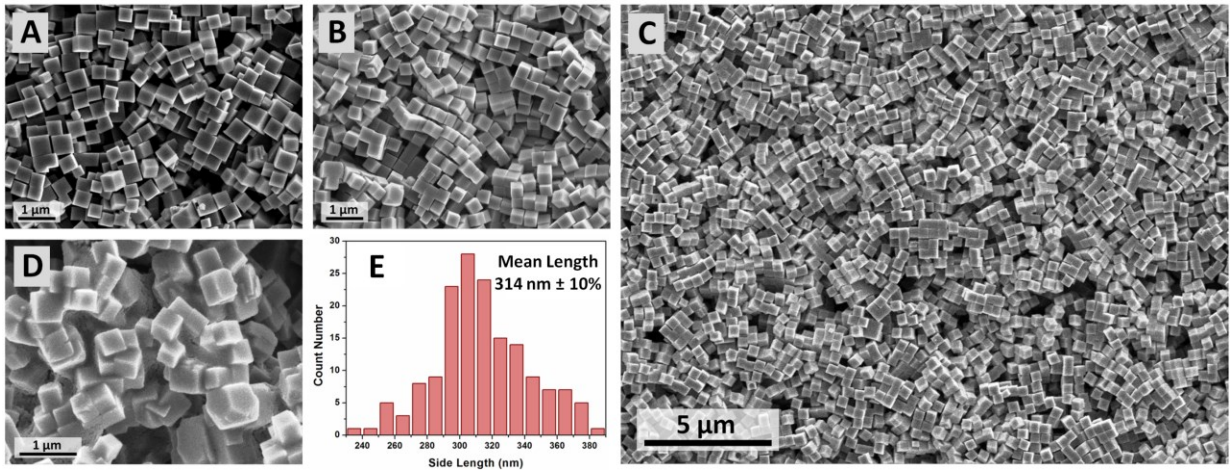

Figure 2-6. Morphological changes of GeO_2 nanocubes as a function of ammonium hydroxide concentration. A) 0.003 M, 350 nm ± 18%; B,C,E) 0.011 M, 314 nm ± 10%, and D: 0.03 M, 287 nm ± 33%.

Recall, that under the presented conditions TEOG is expected to be completely converted to $Ge(OH)_4$ (*vide supra*). In this context, ammonium hydroxide impacts the acid/base equilibria of $Ge(OH)_4$ as outlined in *Eqs.* 2-3 and 2-4.[172]

$$Ge(OH)_4 + H_2O \rightleftharpoons Ge(OH)_3O^- + H_3O^+ \quad pK_{a1} = 9.3 \quad \textit{Eq.}\ 2\text{-}3$$

$$Ge(OH)_3O^- + H_2O \rightleftharpoons Ge(OH)_2O^{2-} + H_3O^+ \quad pK_{a2} = 12.4 \quad \textit{Eq.}\ 2\text{-}4$$

The present observations indicate ammonium hydroxide concentration influences particle shape, but elucidating the exact sol-gel mechanism of particle formation/evolution is difficult given the constantly evolving distribution of germania sources (*e.g.*, $Ge(OH)_4$, $Ge(OH)_3O^-$, $Ge(OH)_2O_2^-$, *etc.*) that results from numerous combinations of hydrolysis and condensation reactions. Complicating interpretation, these reactions will also induce changes in the pH of the reaction media, which are known to impact sol-gel processes.[173]

Considering the equilibrium presented in *Eq.* 2-3 and the initial pH of the reaction media (*i.e.*, pH >10), it is expected that all of the $Ge(OH)_4$ will be deprotonated to form $Ge(OH)_3O^-$.

According to *Eq.* 2-4 negligible $Ge(OH)_3O^-$ will be converted to $Ge(OH)_2O_2^-$. Well-studied base catalyzed silicon sol-gel processes suggest it is reasonable the present Ge-O based gels will exhibit branched structures (See Appendix A of current Thesis for further details).[174] Upon aging, condensation reactions involving the remaining Ge-OH moieties are expected form 'GeO_4' tetrahedra as noted in the IR spectra. While elucidating the mechanism for the formation of crystalline GeO_2 structures is difficult, and perhaps even impossible to conclusively identify, it is reasonable that a combination of the established solubility (albeit low) of "GeO_2-like" species in basic water and the stabilization afforded by the lattice energy of α-GeO_2 (*i.e.*, 12828 $kJ \bullet mol^{-1}$)[175] will lead to the reorganization of the 'GeO_4' tetrahedra and the formation of the thermodynamically favorable crystalline structures presented.

Based upon these relationships, the reactive species (and by extension the morphology of GeO_2 NPs) varies upon changing the pH of the system; this is achieved by controlling the ammonium hydroxide and TEOG concentrations. These equilibria, combined with that described earlier in *Eq.* 2-2, explain how higher concentrations of ammonium hydroxide leads to the consumption of $Ge(OH)_4$ (*i.e.*, *Eq.* 2-3 and 4) and shifts the equilibrium described in *Eq.* 2-2 to the left and ultimately dissolving more GeO_2 (which is not happening here due to lower base concentration). To further support this proposal, we prepared GeO_2 nanoparticles from different concentrations of TEOG to ammonium hydroxide followed by simultaneous monitoring the pH of solution (Figure 2-7).

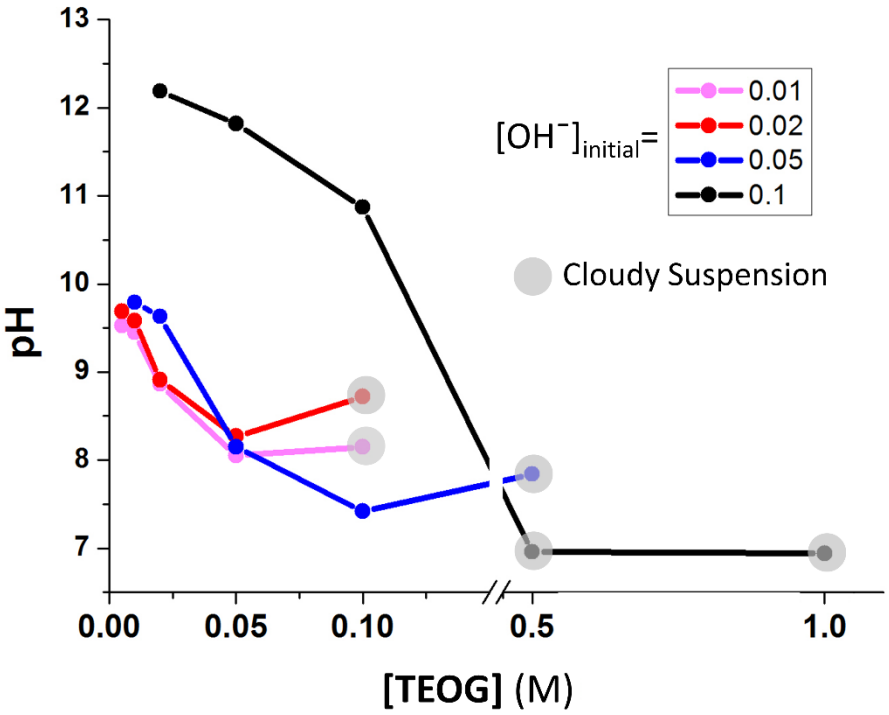

Figure 2-7. Relationship between reaction pH and the concentration of TEOG needed for forming GeO_2 nanocubes (the gray circles show the appearance of precipitate in the reaction solution).

Figure 2-7 shows the relationship between TEOG concentration, reaction pH and the appearance of GeO_2 precipitate (*i.e.*, GeO_2 nanocubes in this case). According to this Figure 2-7, for the solutions with higher initial pH (higher amount of base), higher amounts of TEOG needed to show the GeO_2 perception (nanoparticle forming, shown by gray circles in the Figure 2-7). After consuming of $Ge(OH)_4$ in acid-base reactions in *Eqs.* 2-3 and 2-4, pH of reaction mixture stays constant and leftover $Ge(OH)_4$ starts forming nanoparticles according to *Eq.* 2-2 (*i.e.*, pH reaches gray circles in the Figure 2-7).

2.4.3. The Effect of Reaction Time and Temperature

The effect of reaction time and temperature were also investigated. Not surprisingly, based upon isolated yield increasing the temperature pushes the reaction to completion (See Figure 2-8).

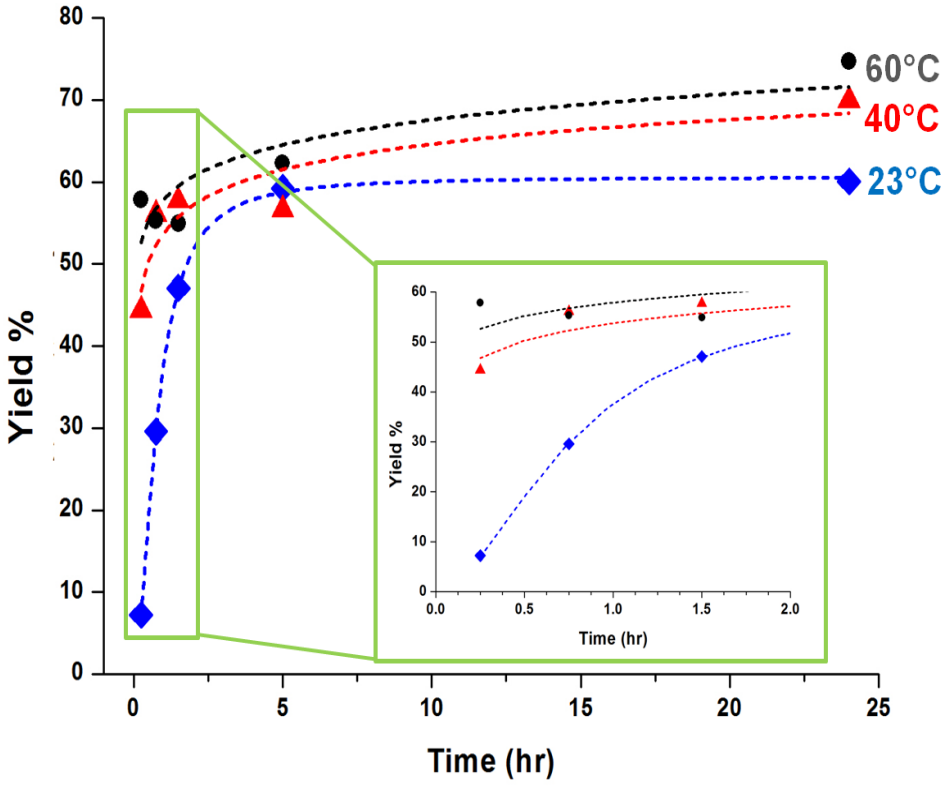

Figure 2-8. Influence of reaction time and temperature on the yield of GeO_2 NPs. Uncertainty of yield for each point is *ca.* ± 5%.

These observations may be understood in the context of the equilibrium summarized in *Eq.* 2-2. These reactions form GeO_2-like sol-gel products that in turn evolve (*vide supra*) to form crystalline GeO_2 nanocubes. Nanostructures obtained within a short time (0 -2 h for 23 °C, 0 -15 minutes for 60 °C) of adding TEOG are faceted and clearly based upon a "cube-like" structural motif (See Figure 2-9 A).

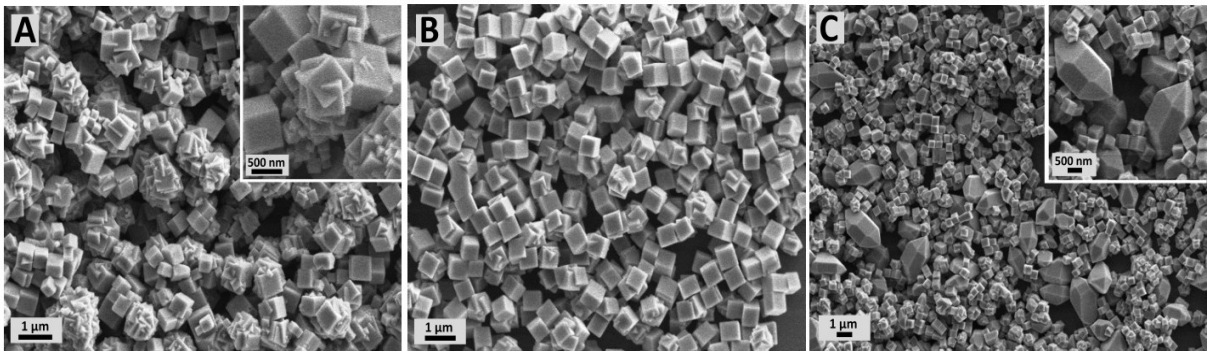

Figure 2-9. Dominant morphologies of GeO_2 NPs synthesized at different times and temperatures: A) 23 °C (0-2 h), 60 °C (0-15 minutes) B) 23 °C (2-20 h), 60 °C (0-15min) C) 23 °C (>24 h), 60 °C (>6 h).

Upon solution aging (2-20 h for 23 °C or 15 min^{-2} h for 60 °C) in the reaction mixture, nanoparticle shapes evolve to form well-defined cubes (See Figure 2-s 9 B, 1G, and H). Again, the limited water solubility of GeO_2 plays a role and is expected to lead to the selective dissolution of high surface energy facets on the randomly shaped structures. Consistent with an Ostwald ripening like process,[173] we also note the appearance of large (edge dimension *ca.* 5 µm) faceted structures and an apparent shrinkage of the cubes (See Figure 2-9 C) after extended solution aging (>24 h for 23 °C or >6 h at 60 °C).

2.5. Conclusions

In conclusion, we have reported a facile method for preparing GeO_2 NPs of tailored shape without the use of surfactants. The morphologies, (*i.e.*, pseudospherical particles, nanoeggs, spindles, and nanocubes) were readily tailored by changing water/ethanol ratios during the hydrolysis of TEOG. Uniform GeO_2 nanocubes with narrow size distribution were obtained by optimizing the concentration of the ammonium hydroxide catalyst.

Chapter 3:

Synthesis and Characterization of GeO_2@SiO_2 Core-Shell Nanoparticles and Selective Reduction of Core and the Shell

3.1. Introduction

Semiconductor-based nanostructures of Group 14 elements (*i.e.,* Si, Ge, Si_xGe_{1-x}, corresponding oxides, *etc.*) have been subject to extensive studies based on their well-established applications in electronic, optoelectronic and size-dependent optical properties.[66] Although Ge-based nanostructures such as GeO_2 and Ge nanoparticles (NPs) show unique properties and applications, they have not been studied as widely as their Si counterparts. Unlike silica, an attractive property of germania (GeO_2) is its green-blue photoluminescence (PL) with peak energies at approximately 3.1 eV (400 nm) and 2.2 eV (563.6 nm).[70,147,148] This optical response has been attributed to oxygen vacancies and other surface defects.[149–151,176] Compared to silica, germania has higher dielectric constant[143,121] and refractive index (η_{GeO2} = 1.6-1.65 *vs.* η_{SiO2} = 1.45),[152,153] lower optical dispersion (higher transparency) in the near-IR region,[154] and higher linear coefficient of thermal expansion.[155,177] Therefore, germania is an attractive material for making wide-angle camera and optical microscope lenses,[178] infrared devices for night-vision technology,[179] infrared photosensors,[159] optical waveguides,[156] optical fibers and nano-connections in optoelectronic communications,[157,158] sealers in vacuum technology;[180] it also has extensive potential applications in the electronics industry and integrated circuits.[145,146]

Important differences also exist when comparing elemental germanium and silicon. For example, Ge exhibits a smaller band-gap (0.67 eV *vs.* 1.1 eV at 300 K),[69] larger Bohr-exciton radius (24.3 nm *vs.* 4.9 nm),[67,70] higher electron and hole mobility (≤3900 $cm^2/V\cdot s$ *vs.* ≤1500 $cm^2/V\cdot s$),[71] as well as greater capacity for and diffusivity of ions (*e.g.,* Li^+).[72] The properties of Ge are also expected to be impacted more substantially by quantum confinement effects; this could provide a photoluminescence response extending well into the near-IR region that may

provide potential applications for Ge-based nanostructures as in biological imaging,[73,74] Bragg reflectors,[18] light-emitting diodes,[181,182] and non-volatile memory devices,[75–79] and many others.[183–185] There are numerous synthetic approaches for making GeNPs such as solution-phase reduction of Ge(II) and Ge(IV) precursors,[19,82,83] metathesis of Ge-based Zintl salts,[97–99,186] and thermal decomposition of organogermane precursors.[101,102,105] Hydrogen thermal reduction of germanium-oxides or germanium rich sol-gel products is an efficient way to produce well-defined Ge nanostructures in high yield.[114,117,120–122,187,188] Unlike silica, germania can be converted to germanium under a slightly reducing atmosphere (5% H_2 / 95% Ar) at relatively low temperatures (*ca.* 600 ˚C, *Eq.* 3-1)[123,162]

$$GeO_2 + 2\ H_2 \longrightarrow Ge + 2\ H_2O \qquad \textit{Eq. 3-1}$$

However, the hydrogen thermal reduction of germanium-oxides suffers from two main drawbacks: loss of Ge content (as the forms of GeO or simply Ge vapor) and the morphological damages of nanostructure due to diffusion and agglomeration of Ge atoms.

At the temperatures commonly used for hydrogen reduction of GeO_2, germanium monoxide (GeO) can form at the interface of Ge and GeO_2 (*Eq.* 3-2). [189–193]

$$Ge + GeO_2 \longrightarrow GeO \qquad \textit{Eq. 3-2}$$

One can envision, GeO being produced by following sub-reactions (*Eq.* 3-3)[121]

$$GeO_2 + \tfrac{1}{2}\ H_2 \longrightarrow GeO_{3/2} + \tfrac{1}{2}\ H_2O$$

$$GeO_{3/2} + \tfrac{1}{2}\ H_2 \longrightarrow GeO + \tfrac{1}{2}\ H_2O \qquad \textit{Eq. 3-3}$$

$$GeO + \tfrac{1}{2}\ H_2 \longrightarrow GeO_{1/2} + \tfrac{1}{2}\ H_2O$$

$$GeO_{1/2} + \frac{1}{2} H_2 \longrightarrow Ge + \frac{1}{2} H_2O \qquad \textit{Eq. 3-4}$$

Regardless of the mechanism of formation, GeO is volatile and will lead to the loss of germanium at temperatures higher than *ca.* 425 ˚C.[194–197]

During the thermal processing, Ge atoms formed as a result of the reduction reaction (*Eq.* 3-4) diffuse and randomly agglomerate to yield nanostructures with ill-defined morphology. This highlights the importance of preparing GeNPs embedded in protective matrices. For example, Guo *et al.* prepared GeO_2 nano-cubes (*via* the method we developed in the second Chapter of this Thesis), and used these NPs to obtain high performance anodes for lithium ion battery applications.[198] GeO_2 nano-cubes have been coated with carbon layers *via* carbonization of acetylene and reduced to elemental Ge, subsequently. The authors hypothesized carbonaceous coating prevents the aggregation of the GeO_2 nano-cubes during the reduction, and also it provides space for the volume expansion of the Ge NPs during lithiation.[198]

GeO_2/Ge@SiO_2 core-shell nanostructures, on the other hand, are extremely important materials in optical applications.[199–202] While many studies have appeared that focus on the preparation of GeO_2/Ge@SiO_2 core-shell nanowires, similar core-shell nanoparticles have not been studied extensively. In one of the few examples, Liu *et al.* have prepared GeO_2@SiO_2 core-shell/mixed NPs (50-200 nm) by vapor deposition and *in-situ* flame oxidation and/or hydrolysis of the corresponding halides (*i.e.,* $GeCl_4$ and $SiCl_4$).[199] However, the formation of GeO_2 is complex and challenging through this method. Lee *et al.* used a similar procedure (*i.e.,* vapor deposition) to make Ge/SiO_2 core/shell NPs.[200] $GeCl_4$ and $SiCl_4$ were used as source gases for making Ge-doped SiO_2 hollow spheres. An extra growth time of these hollow spheres, yielded freestanding Ge@SiO_2 NPs (*ca.* 50 nm).[200] Despite these advances, there are still challenges in

controlling the morphology of GeO_2/Ge@SiO_2 core-shell NPs. In this Chapter we report a straight-forward sol-gel-based method for preparing GeO_2@SiO_2, Ge@SiO_2, as well as Ge@Si/SiO_2 core-shell NPs.

The previous Chapter outlines a facile approach for preparing GeO_2 NPs with morphologies and narrow size distribution *via* a surfactant-free sol-gel reaction of tetraethoxygermane (TEOG).[112] In this Chapter, we build on these investigations and encapsulating these GeO_2 structures in Stöber silica shells. Subsequently, the core and the shell of these NPs were selectively reduced by 5% H_2 / 95% Ar and magnesium, to yield Ge@SiO_2 and Ge@Si core-shell NPs, respectively (Scheme 3-1).

3.2. Experimental

3.2.1. Reagents and Materials

Tetraethoxygermane (TEOG, 99.99%) was purchased from Gelest. Tetraethoxysilane (TEOS, 99%), ammonium hydroxide (29.3 wt % NH_3 in water), magnesium powder (granular, 20 - 230 mesh, 98%) as well as reagent grade anhydrous ethanol were purchased from Sigma-Aldrich. High-purity DI water (18.2 MΩ/cm) was obtained from a Barnstead Nanopure Diamond purification system. All reagents were used as received unless otherwise specified.

3.2.2. Synthesis of GeO_2@SiO_2 Core-shell NPs

GeO_2 NPs (*i.e.,* 0.03 g, nano-cubes or nano-eggs) obtained from the procedures outlined in section 2.2 in the second Chapter of current Thesis, were dispersed in a mixture of 9.0 mL ethanol and 1.0 mL aqueous concentrated NH_4OH by sonication for <30 seconds. After stirring

for 10 min, TEOS (65 μL, 0.3 mmol) was added dropwise to the suspension. After a predefined time (i.e., 15 min, 30 min, 1 h and 24 h), the stirring was stopped and the white product was separated by centrifugation (3000 rpm, 5 min). Clear, colorless supernatant was discarded and white precipitate vacuum dried at 110°C for 12 h. Typical mass yields were *ca.* 0.035 - 0.045 g.

3.2.3. Selective Reduction of GeO_2 core; Synthesis of Ge@SiO_2 Core-shell NPs

A quartz boat containing *ca.* 0.1 g of GeO_2@SiO_2 NPs obtained from the procedure noted above were placed in a Lindberg Blue tube furnace under a flow of 5% H_2 / 95% Ar (*ca.* 15 mL/min). The temperature was ramped to 600 °C (20 °C/min) and maintained for a predefined time (i.e., 1, 2, 4, 8, 12 and 15 h). Under these conditions, SiO_2 is not reduced; the GeO_2 core is selectively converted to Ge to yield Ge@SiO_2 NPs. The original white GeO_2@SiO_2 core-shell NPs turned dark brown consistent with the reduction of GeO_2 to Ge. The crude dark brown product was collected and mechanically ground in an agate mortar and pestle and stored for further reaction and characterization. Typical mass yield was *ca.* 0.08 g.

3.2.4. Selective Reduction of the SiO_2 Shell; Preparing Ge@Si/SiO_2 Core-shell NPs

In a quartz boat, *ca.* 10 mg of Ge@SiO_2 core-shell NPs were gently mixed with various amounts of fresh Mg powder (5, 10, 20 and 30 mg). The boat was placed in a Lindberg Blue tube furnace and kept under a steady flow of Ar (Praxair, zero 4.3, flow rate of *ca.* 15 mL/min). The temperature was ramped to 600 °C (20 °C/min) and maintained for a predefined time (*i.e.,* 6, 10, 15 and 18 h). Black solid composites were collected and mechanically ground in an agate mortar and pestle. Finally, the finely ground powder was dispersed in 5 mL of water. Hydrochloric acid (2 mL, 1 M) was slowly dropped into the mixture to remove unreacted Mg as well as MgO by-

product (*Caution: This reaction is extremely exothermic*). After 30 minutes of stirring, the black powder was separated from solution by centrifugation (3000 rpm, 5 min) and vacuum dried at *ca.* 70°C for 2 h. A typical mass yield was *ca.* 7 – 10 mg of Ge@Si/SiO_2 core-shell NPs.

3.2.5. Characterization

Bright field Transmission Electron Microscopy (BF-TEM) and energy dispersive X-ray (EDX) analyses were performed using a JEOL 2010 electron microscope equipped with a LaB_6 filament working on 200 keV accelerating voltage. Anhydrous ethanol was used for dispersing NPs (*ca.* 1 mg/mL) and dropping onto carbon-coated 200-mesh Cu grids (Electron Microscopy Science) placed on a piece of filter paper. Excess solvent was absorbed to the filter paper and the residual solvent was removed *in vacuo*. High resolution Transmission Electron Microscopy (HRTEM) images were obtained using a Hitachi-9500 electron microscope with an accelerating voltage of 300 kV and processed using Gatan ImageJ software (version 1.46r). HRTEM samples were prepared as described for BF-TEM by placing 1-3 drops of ethanol/NPs dispersion (*ca.* 1 mg/mL) onto a holey carbon coated copper grid (400 mesh, Electron Microscopy Science). Secondary electron scanning electron microscopy (SE-SEM) images were obtained by using a JEOL 6301F field-emission scanning electron microscope with an acceleration voltage of 5 kV. Samples were prepared by drop-casting of an ethanol dispersion of NPs (*ca.* 1 mg/mL) onto a of Si surface wafer.

X-ray Diffraction (XRD) of samples were performed using an INEL XRG 3000 X-ray diffractometer equipped with a Cu Kα radiation source (λ = 1.54 Å) and CPS-120 detector. Crystallinity of all samples was evaluated for finely ground powders mounted on a low-intensity background Si (100) holder.

3.3. Results and Discussion

3.3.1. Hydrogen thermal reduction of GeO_2 NPs

The thermal reduction of GeO_2 nano-cubes and nano-eggs (without silica shells) were studied to evaluate morphological changes resulting from the reduction procedure. Electron micrographs of GeO_2 nano-cubes and nano-eggs have been shown in Chapter 2 of current Thesis (Figure 2-1). Figure 3-1 A and B show BF-TEM and SE-SEM images of GeO_2 nano-cubes and nano-eggs after exposure to a flow of 5% H_2 / 95% Ar at 600 °C for 2 h. The related XRD patterns (shown in Figure 3-1 E and F) display α-GeO_2 reflections along with the characteristic peaks at 2θ = 27.3°, 45.3°, 53.7°, 66.1°, 72.9° and 83.8° which were assigned to diamond Ge crystalline domains (indexed to {111}, {220}, {311}, {400}, {331}, and {422}, respectively).[203] The presence of both sets of reflections (*i.e.*, the remaining α-GeO_2 along with diamond Ge) evidences incomplete thermal reduction. An inspection of the morphologies of nano-cubes and nano-eggs after annealing for 2 h (Figure 3-1 A and B) reveals catastrophic morphological changes even in case of incomplete reduction (*i.e.*, 2 h at 600 °C). According to Figures 3-1 C and D, particles become rounded and aggregated upon heating for 2 h at 600 °C under 5% H_2 / 95% Ar, and this change is more pronounced for the nano-cubes.

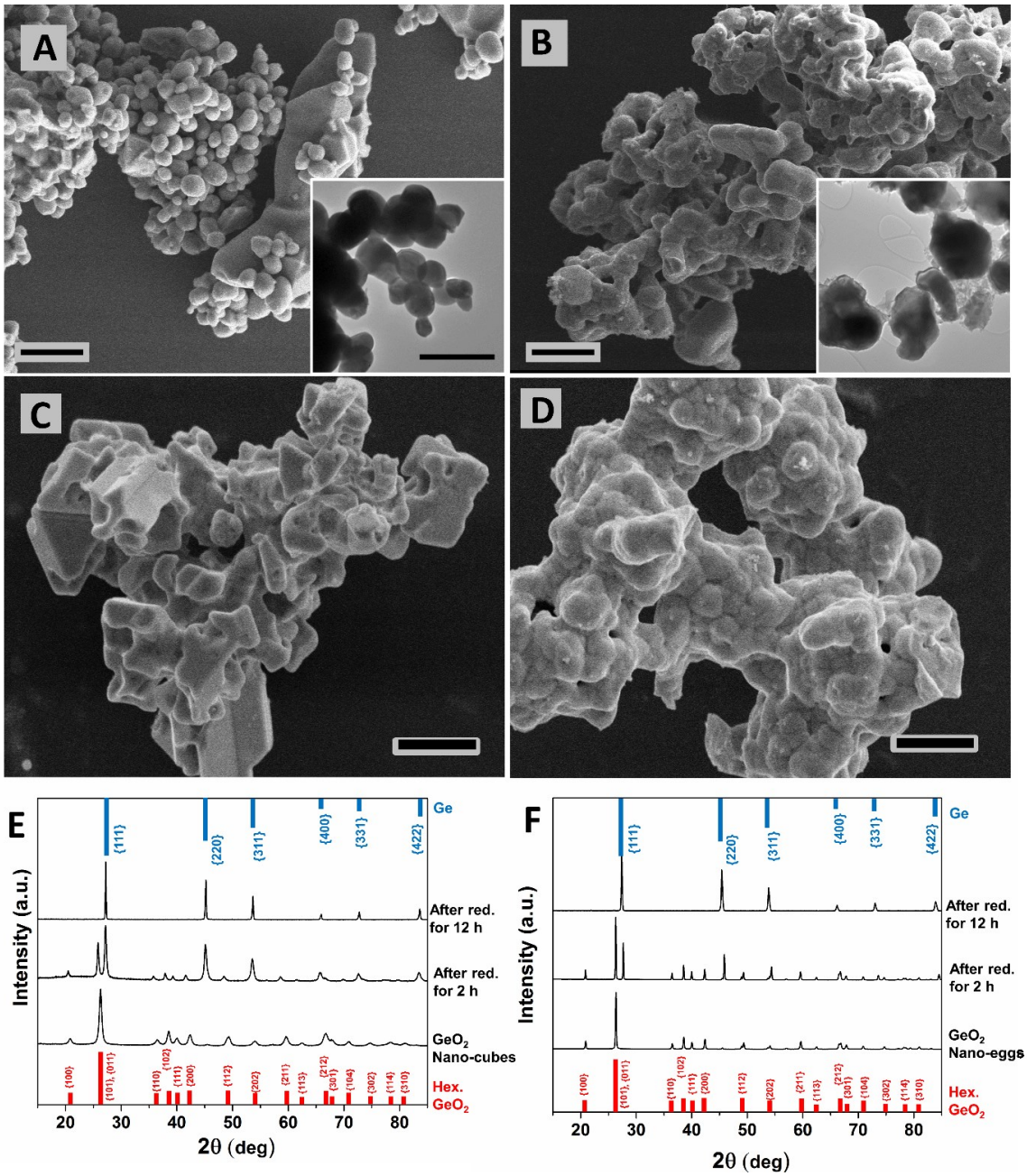

Figure 3-1. A,B) SE-SEM and BF-TEM (inset) images of partially reduced (A) nano-cubes and (B) nano-eggs (in both cases, partially reducing obtained after 2 h annealing in 600°C under 5% H_2 / 95% Ar. Scale bars are 1μm). C, D) SE-SEM images completely reduced (C) nano-cubes and (B) nano-eggs after heating for 12 h in 600°C under 5% H_2 / 95% Ar (Scale bars are 1μm) E, F) Comparing XRD patterns of GeO_2 nano-cubes and nano-eggs before and after partial as well as complete reduction compared to standard reflections of diamond Ge and hexagonal α-GeO_2.

Complete reduction of GeO_2 NPs by annealing GeO_2 NPs for longer times (*i.e.*, 12 h), is not possible without extensive loss of parent particles morphology. Figure 3-1 C and D shows the SE-SEM images of GeO_2 nano-cubes and nano-eggs after complete reduction to Ge by exposing them to a flow of 5% H_2 / 95% Ar at 600 °C for 12 h. Completion of the reduction process has also been supported with XRD analyses (Figure 3-1 E and F). The SE-SEM images indicate that GeO_2 NPs entirely lose their morphology upon complete reduction. We have also observed initial weight losses of 44% for nano-cubes and 61% for nano-eggs. The expected weight loss value for converting GeO_2 to Ge is ~30% (GeO_2 M_w=104.64 g•mol^{-1} *vs.* Ge M_w=72.64 g•mol^{-1}). These experimental values appear higher than the expected weight losses and can be accounted for by the evaporation of Ge and/or GeO (*vide supra*).

Generally, hydrogen thermal reduction of GeO_2 NPs, is not possible without morphological damage due to melting or softening of elemental Ge, migration of Ge atoms, aggregation of particles and evaporation of Ge content.[113] Therefore, making a protective shell of SiO_2 around the GeO_2 NPs (nano-eggs and nano-cubes) was pursued as the next logical step in the current work (Scheme 3-1).

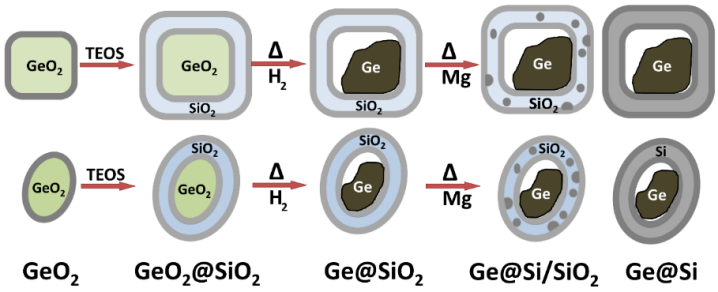

Scheme 3-1. Different GeO_2@SiO_2 core-shell nano-cubes and nano-eggs reported in current Chapter along with the selective reduction of the core and the shell; forming Ge@SiO_2, and Ge@Si core-shell NPs, respectively.

3.3.2. Synthesis of GeO_2@SiO_2 core-shell NPs

A Stöber silica coating around GeO_2 NPs was made *via* the well-known sol–gel processing of silicon alkoxides in an alkaline suspension of particles in ethanol.[204–207] Figure 3-2 shows the BF-TEM image, XRD pattern and energy dispersive X-ray spectra of GeO_2@SiO_2 core-shell NPs. Based on the image contrast in the bright-field BF-TEM images, the darker parts in the center of the core-shell NPs are related to heavier element compounds (*i.e.*, GeO_2) and the brighter regions around the core correspond to lighter elemental combinations (*i.e.*, SiO_2). Moreover, crystalline GeO_2 cores show higher contrast compared to amorphous SiO_2 shells. Figure 3-2 C and D show the XRD patterns of GeO_2@SiO_2 core-shell NPs, which are mainly similar to the reflection patterns of α-GeO_2 crystals (Figure 3-1 E); only a broad reflection is noticed around $2\theta = 25^\circ$ which is related to amorphous SiO_2.[208]

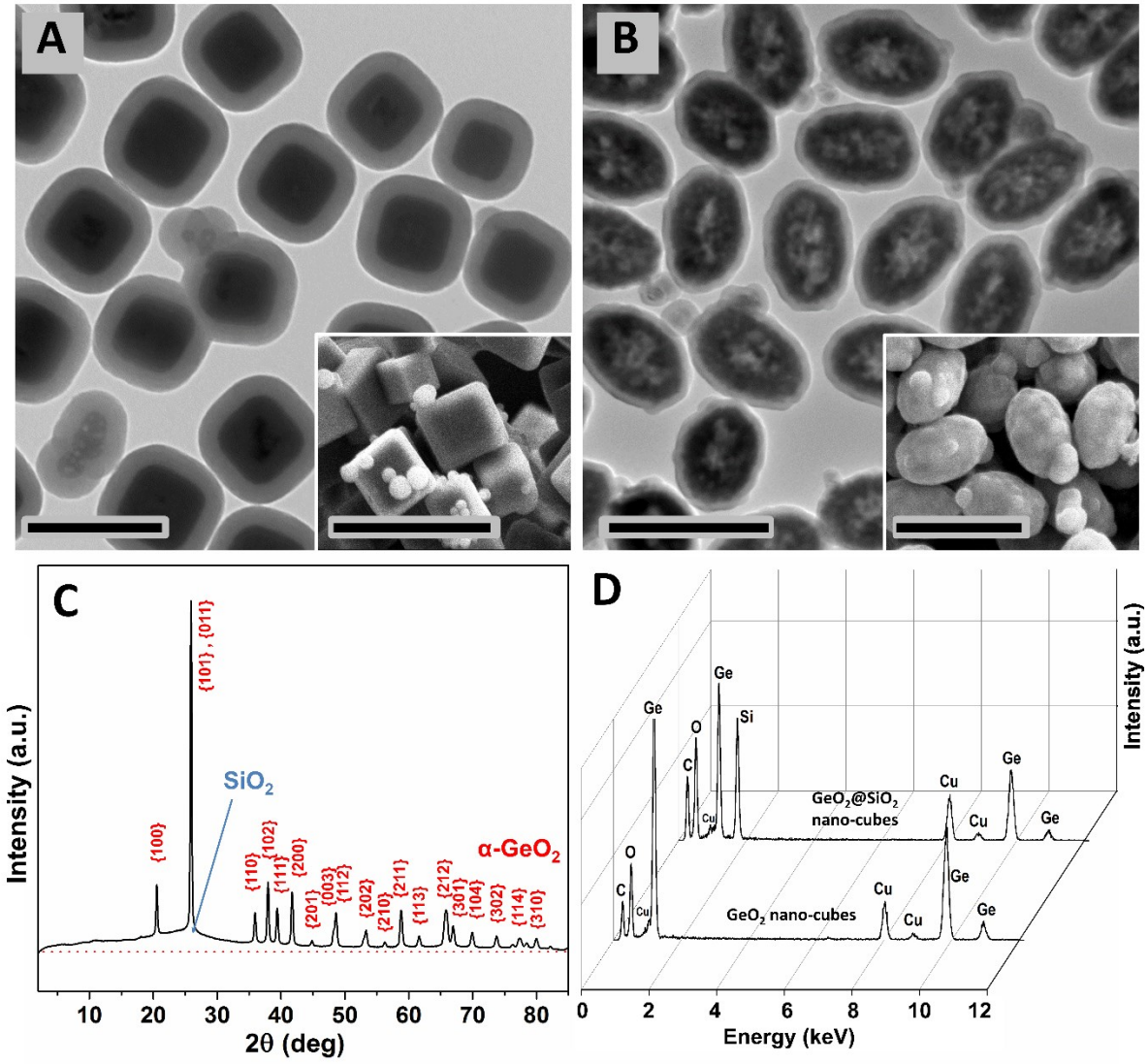

Figure 3-2. A, B) BF-TEM and SE-SEM (inset) images for GeO_2@SiO_2 core-shell nano-cubes (A) nano-eggs (B) (Scale bars are 500 nm). C) XRD patterns of GeO_2@SiO_2 core-shell nano-cubes with broad peak around 2θ = 25˚ related to amorphous SiO_2. D) Comparing EDX spectrum of GeO_2@SiO_2 core-shell nano-cubes with GeO_2 nano-cubes.

EDX analysis of GeO_2@SiO_2 core-shell nano-cubes in Figure 3-2 D also proves the presence of silicon, germanium and oxygen, as expected. The EDX spectrum of GeO_2 NPs show only germanium and oxygen (copper and carbon signals are from the substrate). Comparing the EDX spectra of GeO_2@SiO_2 core-shell nano-cubes with those of GeO_2 nano-cubes, a decrease in

Ge signal intensity is observed upon formation of the silica shell. This observation could be due to embedding of the Ge cores inside shielding silica layers.

The shielding effect of the silica shell can be useful to track its thickness: the thicker the SiO_2 shell, the lower the Ge signal observed in EDX analyses. The silica shell thickness was controlled by stopping the reaction at defined elapsed times from adding TEOS (15 min, 30 min, 1 h and 24 h).

Figure 3-3 shows how shell thickness increases as a function of TEOS sol-gel reaction time. According to BF-TEM images shown in Figure 3-3 A to E, approximately 15 minutes after adding TEOS a thin shell of silica (*ca.* 21 ± 6 nm) is distinguished around the GeO_2 nano-cubes (Figure 3-3 B). The shell thickness increased to 39 ± 5 nm, 45 ± 11 nm, and 62 ± 18 nm after 30 min, 1 h and 24 h from adding TEOS, respectively. In addition, it is important to note that shell growth is limited by the amount of available TEOS, as shown in several reports.[204,209] The shell grows rapidly for the first 30 minutes to *ca.* 40 nm and continues to grow up to 60 nm after 24 (Figure 3-3 F). This observation suggests that the majority of TEOS has been consumed in the first 30 min of the reaction, and this limits further growth of the shell.

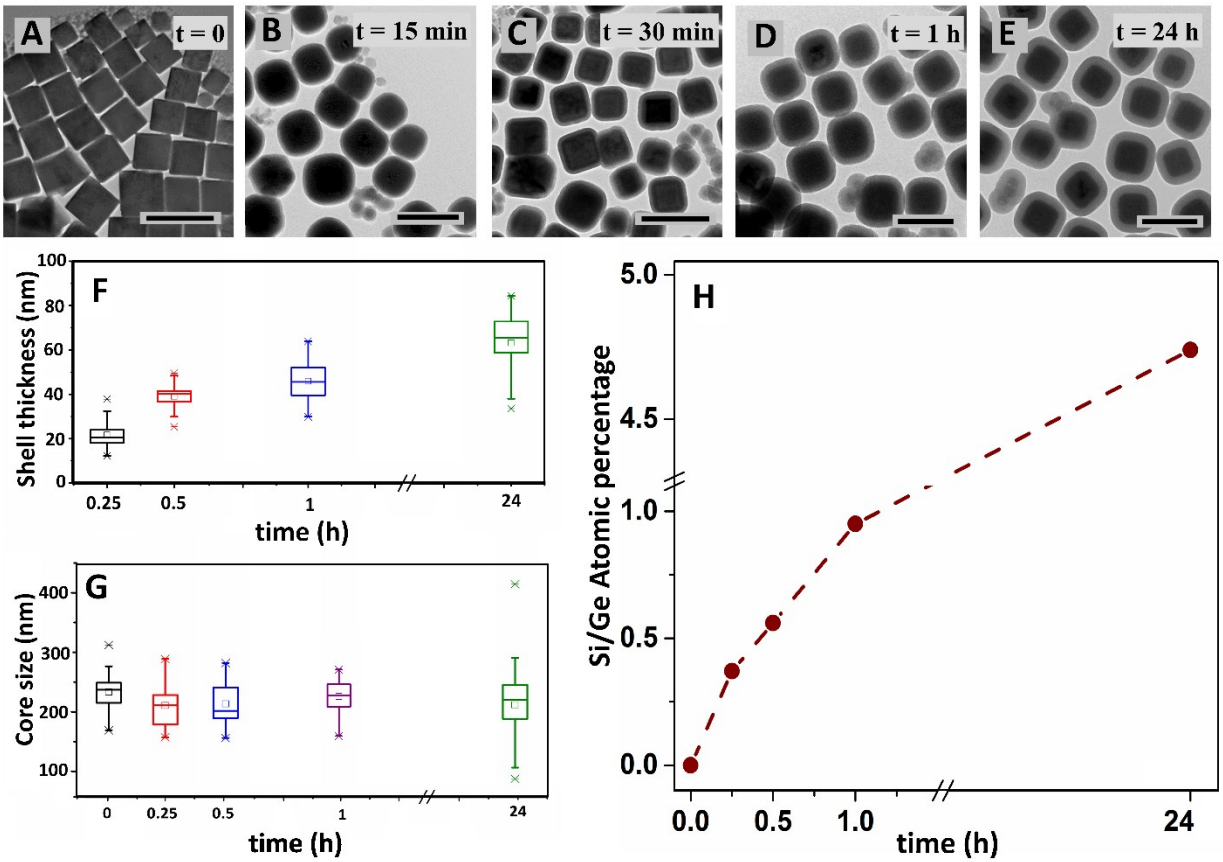

Figure 3-3. BF-TEM images of A) GeO_2 nano-cubes and B-E) GeO_2@SiO_2 core-shell NPs after defined time from adding TEOS (Scale bars are 500 nm). F) Distribution and standard deviations of SiO_2 shell thickness *vs.* reaction time. G) Size distribution and standard deviations of GeO_2 core in GeO_2@SiO_2 core-shell NPs *vs.* reaction time. H) Si/Ge atomic percentage in EDX analyses for GeO_2@SiO_2 core-shell NPs *vs.* reaction time of TEOS.

A similar trend in increasing the shell thickness has been observed for elemental ratios of Si and Ge in EDX analyses of all particles shown in Figure 3-3; for all core-shell samples, the germanium (from the core) and the silicon (from the shell) have been observed together. However, due to the shielding effect of SiO_2, the penetration of EDX electrons into the GeO_2 phase is increasingly limited by greater shell thickness. The Si signal also increases and the Ge signal coming from the GeO_2 core decreases. In this context, the Ge/Si signal ratio changes from

3 to 1.7, 1.0 and finally to 0.5 for samples after 15, 30, 60 min and 24 h, respectively, after adding TEOS (Figure 3-3 H).

3.3.3. Selective reduction of the core; preparing Ge@SiO_2 core-shell NPs

Samples with a shell thickness of 45 ± 11 nm (60 min after adding TEOS) were chosen and reduction was carried out using a flow of 5% H_2 and 95% Ar under constant heating up to 600 °C for a controlled time. This is a typical procedure for the hydrogen thermal reduction of germanium rich oxide sol-gel products.[121,162]

The reduction of GeO_2 to elemental Ge was confirmed by XRD analysis. Figure A and D (A for nano-cubes and D for nano-eggs) shows XRD patterns for GeO_2@SiO_2 core-shell NPs after reduction (600°C under 5% H_2/ 95% Ar) for indicated times. The intensities of the reflections from hexagonal GeO_2 decrease with increasing reduction time. Finally, α-GeO_2 reflections disappear after 12 h for nano-cubes and 15 h for nano-eggs. New reflections appear at 2θ = 28, 46, 54 and 68º, which are assigned to the diamond cubic crystalline Ge;[203] this is evidence for the formation of elemental Ge. This observation supports the complete reduction of GeO_2 to Ge and thus the conversion of GeO_2@SiO_2 core-shell NPs to Ge@SiO_2 core-shell NPs.

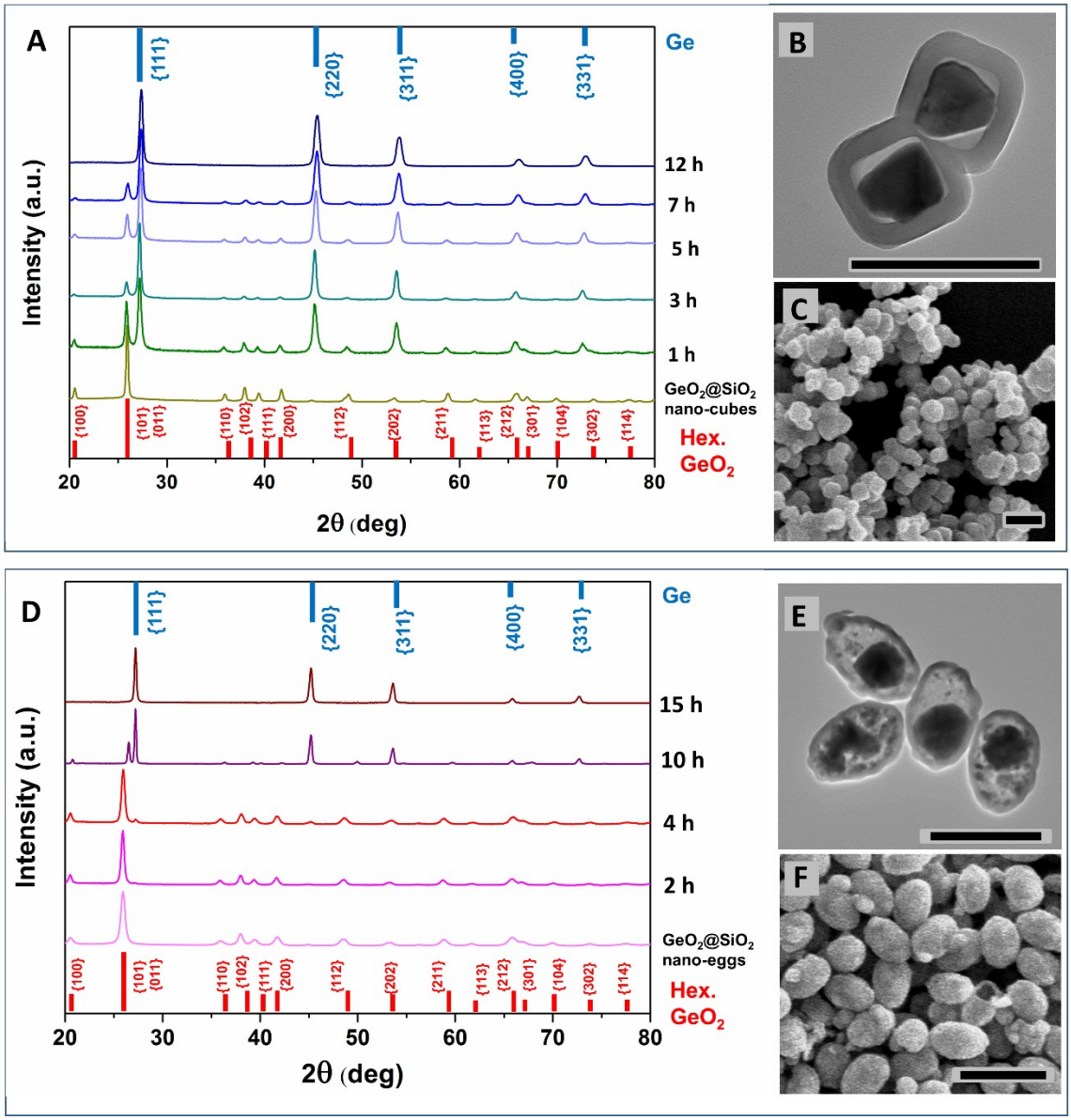

Figure 3-4. A) XRD patterns of GeO_2-SiO_2 core-shell nano-cubes after reducing in 5% H_2 / 95% Ar for indicated times, compared to standard Ge and hexagonal GeO_2 patterns. B) BF-TEM and C) SE-SEM images of Ge@SiO_2 core-shell nano-cubes (reduced for 12 h, scale bars are 500 nm). D) XRD patterns of GeO_2-SiO_2 core-shell nano-eggs after reducing in 5% H_2 / 95% Ar for indicated times, compared to standard Ge and hexagonal GeO_2 patterns. B) BF-TEM and C) SE-SEM images of Ge@SiO_2 core-shell nano-eggs (reduced for 15 h, scale bars are 500 nm).

Figure 3-4 also shows BF-TEM and SE-SEM images of Ge@SiO_2 core-shell NPs (B, C for nano-cubes and E, F for nano-eggs). Based on the BF-TEM images of the same particles (Figure 3-5 B for nano-cubes and E for nano-eggs), no Ge leakage and/ or diffusion through the surrounding shell are observed. Based on SE-SEM images of Ge@SiO_2 core-shell nano-cubes and nano-eggs (Figure 3-4 C and F), there are no melted and/ or agglomerated NPs as there was for the previously reported particles without shells (Figures 3-1). The shape and morphology of the silica shells remained constant during complete annealing (12 h for nano-cubes and 15 h for nano-eggs) for all core-shell NPs. This indicates that the silica shell is rigid and dense enough to keep the NPs separated and prevent aggregation and accumulation. Shrinkage of GeO_2 cores during the reduction process (Figure 3-4 B and E) was not unexpected as the long Ge-O-Ge bond (346 pm, angled bond)[210,211] is reduced to yield the comparatively shorter Ge-Ge bond (241 pm), causing the shrinkage of the core.

3.3.4. Reducing the silica shell of Ge@SiO_2 NPs; Preparing Ge@Si core-shell NPs

In the reduction of GeO_2@SiO_2 core-shell NPs, the conditions used for complete reduction of the GeO_2 cores to Ge (12 h or 15 h at 600 °C under 5% H_2 / 95% Ar) are not sufficient to reduce the SiO_2 shells. With the goal being to ultimately make Ge@Si core-shell NPs, the reduction of silicon oxide to elemental silicon under a slightly reducing atmosphere is not possible unless temperatures higher than *ca.* 1200 °C are used.[212] In the case of GeO_2@SiO_2 core-shell NPs, using such severe conditions is not feasible due to the sensitivity of core-shell structures to high temperatures. Magnesiothermic reduction has recently been presented as an alternative method for preparing Si-based nanomaterials at significantly lower temperatures (*e.g.*,

500 °C).[213,214] Due to the destructive nature of thermal reduction at higher temperatures,[215] magnesiothermic reduction was investigated as a promising method for reprocessing silica with minimal structural damage.[189,216,217] For example, Tolbert *et al.* used magnesiothermic reduction for ordered mesoporous silicon films in which silicon had been prepared through magnesiothermic reduction of polymer templated silica thin films. According to the authors, magnesiothermic reduction conserved the ordered design but replaced the dense silica walls with 10-17 nm silicon crystals.[216]

According to *Eq.* 3-5, during magnesiothermic reduction one mole of silica reacts with two equivalents of magnesium powder to produce elemental silicon and magnesium oxide. The magnesium oxide by-product can be washed off *via* exposure to a dilute acidic solution. Interestingly, using excess magnesium not only fails to bring about reduction but also leads to the formation of impurities such as magnesium silicide (*Eq.* 3-6).[218]

$$SiO_{2(s)} + 2\ Mg_{(s)} \longrightarrow Si_{(s)} + 2\ MgO \qquad \textit{Eq. 3-5}$$

$$2\ Mg_{(s)} + Si_{(s)} \longrightarrow Mg_2Si_{(s)} \qquad \textit{Eq. 3-6}$$

Core-reduced NPs (Ge@SiO_2) were selected for magnesiothermic reduction of the SiO_2 shell. Defining the exact equivalent amount of Mg is not feasible due to uncertainty in the determination of SiO_2 amounts in Ge@SiO_2 core-shell NPs. With respect to the aforementioned critical limitation of magnesiothermic reduction (*i.e.*, the formation of magnesium silicide layers), magnesium amounts have been optimized to reduce the likelihood of forming impurities such as Mg_2Si. In addition, the reaction times were optimized to avoid extended heating periods and possible morphological damage.

3.3.4.1. Optimizing the amount of Mg

For determining the optimum amount of Mg powder, Ge@SiO_2 core-shell NPs were gently mixed with different amounts of Mg powder and the mixture annealed under a flow of Ar. Figure 3-5 shows XRD patterns of Ge@SiO_2 core-shell NPs before and after magnesiothermic reduction using different amounts of Mg powder. According to this figure, the expected MgO by-product is produced in all cases. However, Mg_2Si is only being formed when higher amounts of Mg have been applied for reduction (*i.e.*, 30 mg in sample 5). This observation is consistent with the results expected from *Eqs.* 3-5 and 3-6.

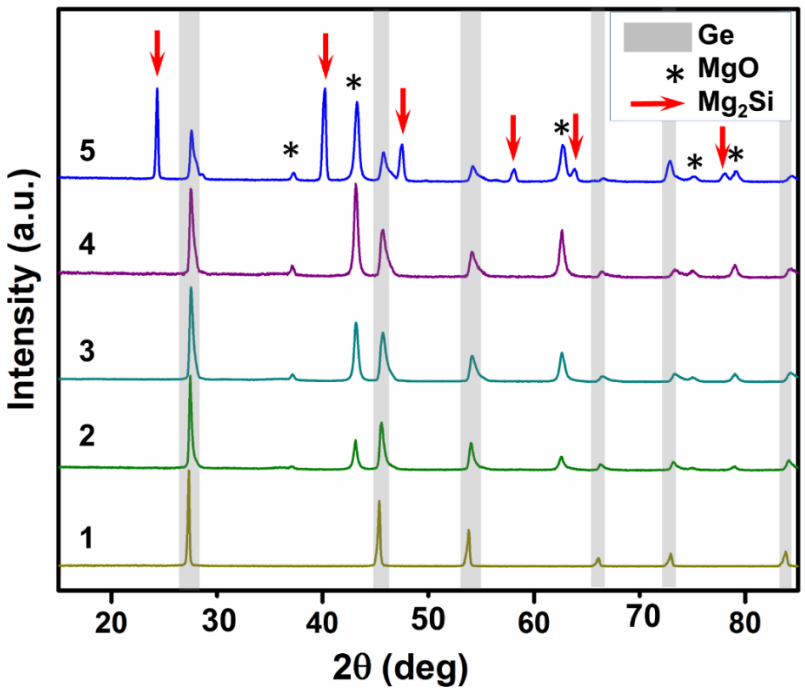

Figure 3-5. XRD pattern of Ge@SiO_2 core-shell NPs before (1) and after (2-5) magnesiothermic reduction by exposing to different amounts of Mg. Number 2-5 are patterns after magnesiothermic reaction of 10 mg Ge@SiO_2 core-shell NPs with 5, 10, 20 and 30 mg Mg powder, respectively. Magnesiothermic reactions were performed at 600 °C under Ar flow for 6 h.

In this context, the highest amount of Mg used without forming Mg_2Si by-product has been identified as the optimum condition for the present study. According to Figure 3-7, using 20 mg of Mg powder for the reduction of 10 mg of Ge@SiO_2 core-shell NPs (sample number 4 in Figure 3-5) has been determined to be the ideal mass ratio of reactants.

It should be noted that all magnesiothermic reactions in Figure 3-7 were performed for 6 h under Ar flow. The appearance of reflections from by-products such as MgO and Mg_2Si are indirect evidence for the reduction of the SiO_2 shell to elemental Si (Figure 3-7). There are also direct indications for the presence of elemental Si, however closer attention is required. According to Table 3-1, the diamond crystal structure of Ge and the diamond crystal structure of Si have similar lattice parameters.[203]

Table 3-1. Values of 2θ for diamond Si compare to similar diamond Ge crystal structures

	{111}	**{220}**	**{311}**	**{400}**	**{331}**	**{422}**
Si	28.43	47.29	56.10	69.11	76.35	88.00
Ge	27.30	45.34	53.74	66.06	72.88	83.76

It is expected that the reflections of Si and Ge crystallographic planes in the XRD pattern of Ge@Si core-shell NPs will appear at similar 2θ values. Looking at Figure 3-6, the broadening of Ge reflections during magnesiothermic reaction can be related to the formation of elemental Si.

3.3.4.2. The effect of time on magnesiothermic reduction

After optimizing the amount of Mg (sample number 4 in Figure 3-5), the effect of prolonged heating times was investigated and showed interesting results. Figure 3-6 demonstrates XRD patterns of Ge@SiO_2 core-shell NPs after magnesiothermic reduction with the optimum amount of Mg for defined times: 10, 15 and 18 h.

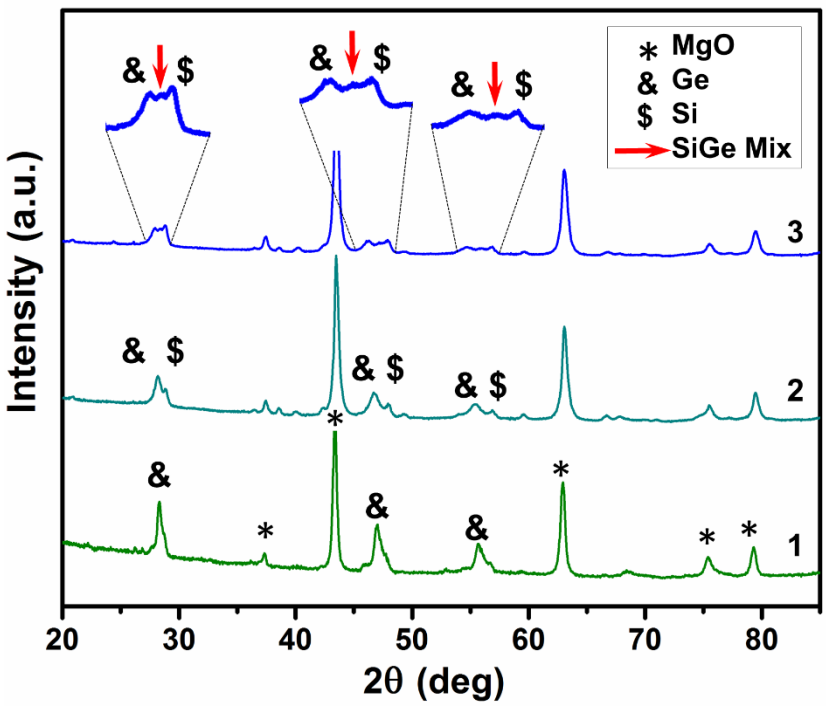

Figure 3-6. XRD patterns of Ge@SiO_2 core-shell NPs after magnesiothermic reduction with optimum Mg amount for: 1) 10 h, 2) 15 h and 3) 18 h

Besides the broadening of Ge reflections due to the production of Si (*vide supra*), other reflections start to appear close to the correlated 2θ values of diamond Ge (shown by a '$' in sample number 2 in Figure 3-7). These new reflections are attributed to crystalline elemental silicon. Further annealing for longer times causes the appearance of a third reflection right

between the other two (shown by a red arrow in sample 3 in Figure 3-6). We believe the new reflection can be attributed to Si_xGe_{1-x} elemental mixture.

The formation of elemental Si in the shell of core-shell NPs has been confirmed by EM imaging as well. According to Figure 3-7, some dark spots appear in the shell of Ge@SiO_2 core-shell NPs after 6 h of magnesiothermic reaction with the optimum Mg amount (Figure 3-7 A, B). These dark spots are attributed to Si nano-domains surrounded by SiO_2 matrices.

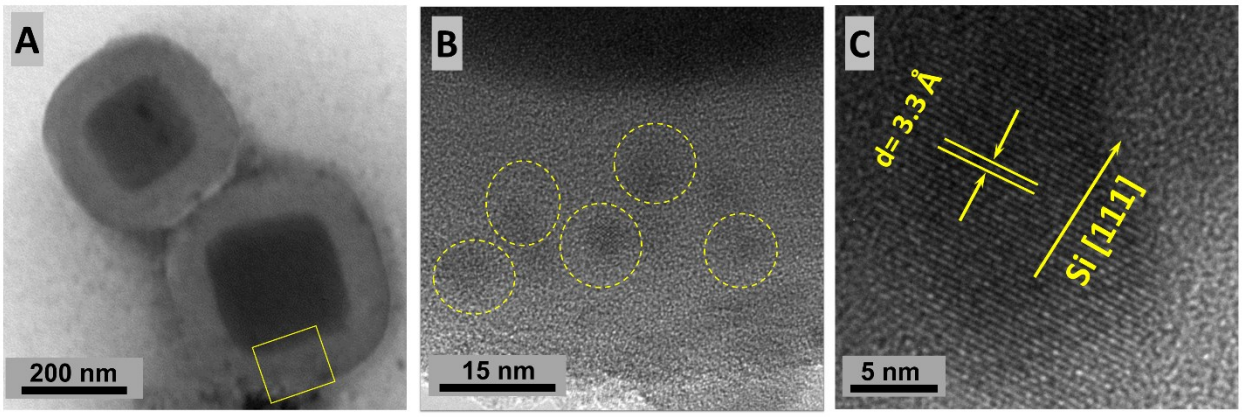

Figure 3-7. A) BF-TEM image of Ge@Si/SiO_2 core-shell after magnesiothermic reduction with optimum Mg amount (600 °C for 6 h under Ar). Dark sports in the shell are related to Si nano-domains. B, C) HRTEM of crystalline silicon domains embedded in SiO_2 matrix in the shell with lattice spacing of 3.3 nm related to Si [111].

Compared to SiO_2 medium, crystalline silicon domains have higher crystallinity and density and therefore show higher contrast in bright field TEM. HRTEM also provides further evidence for Si crystalline domains embedded in SiO_2. Figure 3-7 C shows the characteristic lattice spacing of 3.3 Å for the [111] crystal planes of diamond Si. Although these results are

presenting the reduction of SiO_2 shell to Si crystals embedded in SiO_2, complete reduction of SiO_2 shell to Si shell needs further studies and examinations.

In conclusion, hydrogen thermal reduction of GeO_2 nano-cubes and nano-eggs was not successful without extreme morphological damage to the GeO_2 nanostructures. Therefore, a shell of silica was produced around GeO_2 NPs to make GeO_2@SiO_2 core-shell nano-cubes and nano-eggs. Afterward, selective reductions of the core (*i.e.*, GeO_2) by 5% H_2 / 95% Ar and the shell (*i.e.*, SiO_2) by magnesiothermic reduction were carried out. Consequently, GeO_2@SiO_2 as well as Ge@Si/SiO_2 core-shell nano-cubes and nano-eggs were prepared and subsequently characterized with XRD, TEM, SEM, HRTEM and EDX analyses.

Chapter 4:

Germanium (II) Hydroxide: A Precursor for Facile Preparation of Oxide-Embedded and Freestanding Ge Nanocrystals*

* A version of this Chapter has been published:

Javadi, M.; Picard, D.; Sinelnikov, R.; Narreto, M. A.; Hegmann, F. A.; Veinot, J. G. C *Langmuir* **2017**. Article ASAP, DOI: 10.1021/acs.langmuir.7b00358

4.1. Introduction

Germanium is an interesting case to study in the field of semiconducting materials.[68] It was the first member of Group 14 to be used in semiconductor electronics in the second half of last century.[219,220] Despite the favorable properties of Ge, the chemistry and size dependent properties of GeNCs have not been studied to the same extent as their Si analogues.[89] Presumably, this difference arises because there is a lack of robust synthetic techniques for making GeNCs with well-defined size and surface chemistry.

As outlined in Chapter 1 of this Thesis, GeNCs have been prepared using a variety of different methods including top-down procedures like laser ablation[223] and ball milling,[224] as well as bottom-up techniques such as plasma pyrolysis of GeH_4 in the gas phase,[225] metathesis of Ge Zintl salts,[97–99,186] solution-phase reduction of Ge(II) and Ge(IV) compounds,[19,82,83] and thermal decomposition of organogermane precursors.[101,102,105] While these methods provide some control over the preparation of GeNCs, challenges remain including: limited product yield, size polydispersity, ill-defined shape, complex surface chemistry.

Si and GeNCs have been prepared *via* disproportionation and/or reduction of substoichiometric oxides (RMO_x, $0 < x < 2$, M: Si or Ge) in solid phase.[17,119–122] Upon disproportionation, the substoichiometric oxide undergoes a series of reactions to form elemental nano-domains embedded in the corresponding stoichiometric oxides (*i.e.,* SiO_2 and GeO_2). In this regard, reductive thermal processing of hydrogen silsesquioxane (HSQ, $Si_8O_{12}H_8$) or the similar polymer $(HSiO_{1.5})_n$ has been extensively used for preparing SiNCs.[17,119] A similar procedure for making GeNCs is not readily possible because of the lack of an HSQ equivalent

precursor for Ge. However, thermal processing of organic functionalized germanium rich oxides [$(RGeO_{1.5})_n$] provided a means of obtaining oxide-embedded GeNCs.[119,121,122]

In an earlier investigation from our group, a phenyl substituted sol-gel polymer [$(PhGeO_{1.5})_n$] was thermally processed at different temperatures under reducing conditions to yield GeNCs embedded in GeO_2. It was determined that, during annealing, GeNCs were produced *via* two different pathways: disproportionation of substoichiometric oxides (*Eq.* 4-1), and thermal reduction of stoichiometric oxide (*i.e.,* GeO_2, *Eq.* 4-2). The later pathway occurs preferentially at the surface and as a result, the final NCs were size polydispersed.

$$RGeO_{1.5} \xrightarrow{\Delta} Ge + GeO_2 \quad T > 525\ ^{o}C,\ 5\%\ H_2 / 95\%\ Ar \qquad \textit{Eq. 4-1}$$

$$GeO_2 + H_2 \xrightarrow{\Delta} Ge + H_2O \quad T > 600\ ^{o}C,\ 5\%\ H_2 / 95\%\ Ar \qquad \textit{Eq. 4-2}$$

The effects of the organic substituent (*e.g.,* ethyl, n-butyl, allyl, benzyl, carboxyethyl, and t-butyl) were investigated in attempts to lower the tempertaure at which disproportionation would occur while remaining below the thermal reduction threshold of GeO_2. The goal was to remove the reduction pathway.[121] Unfortunately, polydispersity of GeNCs remained a problem. More importantly, introduction of organic substitution in germanium rich oxides ($RGeO_{1.5}$) resulted in high carbon content in the composite after thermal processing and presented difficulties in the liberation of GeNCs from the embedding oxide matrix.[121]

In this Chapter we introduce a facile method for making carbon-free GeNCs/GeO_2 composites from a partially oxidized form of germanium (*i.e.,* '$Ge(OH)_2$'). We started from an abundant and inexpensive bulk GeO_2 powder followed by reduction in water-based solution. Thermal processing of the resulting '$Ge(OH)_2$' powder under an inert atmosphere (*i.e.,* Ar) with

no reducing gas yielded GeNCs embedded in GeO_2 which can be liberated from the oxide matrix as hydride-terminated NCs which were then functionalized with dodecene.

4.2. Experimental

4.2.1. Reagents and Materials.

Germanium dioxide powder (GeO_2, 99.9%) was purchased from Eagle-Picher. Hypophosphorous acid solution (50 wt. % in H_2O), sodium hydroxide pellets, 1-dodecene (97%), as well as reagent grade methanol, toluene, and ethanol were purchased from Sigma-Aldrich. Electronics grade hydrofluoric acid (HF, 49% aqueous solution) was purchased from J. T. Baker. Hydrochloric acid (36.5 - 38%) and ammonium hydroxide (28 - 30%) were purchased from Caledon Lab. Ultrapure H_2O (18.2 MΩ/ cm) purified in a Barnstead Nanopure Diamond purification system was used in all reactions.

4.2.2. Synthesis of Germanium (II) Hydroxide ('$Ge(OH)_2$').

The synthetic procedure for making '$Ge(OH)_2$' was modified from earlier reports.[226–231] In a typical preparation, 1.0 g of germanium dioxide powder was dissolved in 7.0 mL of a freshly prepared concentrated (~17 M) NaOH aqueous solution. Upon slow addition of 24 mL HCl (6 M) solution over a timeframe of *ca.* 1 min, the GeO_2 powder reprecipitated and then redissolved to give a clear acidic solution of Ge (IV). Subsequently, 7.5 mL of 50 % H_3PO_2 in water was added all at once. The resulting colourless solution was refluxed for 5.5 h under a flowing positive pressure of Ar. The solution was cooled to below *ca.* 5 °C in an ice-salt bath for *ca.* 15 minutes and approximately 10 mL of concentrated NH_4OH solution was added dropwise to yield a yellow precipitate of '$Ge(OH)_2$'. (**Caution:** this reaction is extremely exothermic and care

should be taken to maintain the temperature at *ca.* 5 °C.) The yellow precipitate was recovered by vacuum filtration and washed three times with *ca.* 100 mL of deionized/deoxygenated water. Finally the solid was dried under vacuum for 12 hours and stored in an argon filled glovebox until needed. Typical yields exceed 90%.

In similar way, orange and brown '$Ge(OH)_2$' products were prepared by maintaining the temperatures of Ge(II) solutions at 50 °C and 100 °C, respectively while adding NH_4OH. A white precipitate was also prepared by cooling the Ge(II) solution to <5 °C followed by adding *ca.* 50 mL deionized water (without adding any NH_4OH solution). Isolation, purification and storage of orange, brown and white products are as described above.

4.2.3. Thermal Processing of Germanium (II) Hydroxide.

Thermal processing of the germanium precursors (*i.e.,* yellow, orange and brown '$Ge(OH)_2$') was performed using a Lindberg/Blue tube furnace in flowing argon gas (15 mL/min). Typically, *ca.* 0.5 g of '$Ge(OH)_2$' yellow powder (or white/orange/brown powder) were transferred into a quartz boat, placed in the furnace and heated to a predefined processing temperature at 20 °C/min where it remained for 1 h. After cooling to room temperature a composite of GeNCs in germanium dioxide matrix (GeNCs/GeO_2) was obtained as a black/brown powder. The composite was ground using an agate mortar and pestle and stored under ambient atmosphere for further use and characterization. Typical yields were >0.4 g of GeNCs/GeO_2 composites.

4.2.4. GeNC Isolation.

GeNCs were liberated from the GeO_2 matrix upon etching of GeNCs/GeO_2 composite with alcoholic HF solutions. The finely ground product obtained from thermal processing (~50

mg) was magnetically stirred in 1.0 mL of a 1:1 solution of ethanol and water for *ca.* 10 min in a PET beaker. Subsequently, 0.5 mL of HF (49 % aqueous solution) was added dropwise. (**Caution:** HF must be handled with extreme care.) The effect of etching time was studied by stirring the etching mixture for different times (*i.e.,* 5, 15, 30, 60, and 120 min). After stirring the mixture for the desired time (ideally 15 min), three portions of *ca.* 5 mL toluene were added to extract the GeNCs. The cloudy toluene layer was separated and centrifuged at 3000 rpm to yield a black precipitate. This precipitate was dispersed in toluene containing activated molecular sieves (*ca.* 1 g, 4 Å) and agitated for approximately one minute. The suspension was transferred to centrifuge tubes and the black precipitate (*i.e.,* hydride-terminated GeNCs) was recovered upon centrifuging at 3000 rpm and immediately functionalized as outlined below. Typical yield of hydride-terminated GeNCs was *ca.* 10 mg.

4.2.5. Thermally Induced Hydrogermylation of GeNC.

The black precipitate isolated from the etching of the GeNCs/GeO_2 composite was dispersed in 5.0 mL dodecene, transferred to a Schlenk flask attached to an argon charged double manifold. Three freeze-pump-thaw cycles were performed. Subsequently, the argon filled reaction flask, was heated to 190 °C with stirring. After approximately 12 h the transparent orange-brown suspensions of crude dodecene functionalized GeNCs (dodecyl-GeNCs) were transferred to polypropylene centrifuge tubes and toluene (5 mL) as well as *ca.* 45 mL of a 1:1 ethanol and methanol (v:v) antisolvent were added. The resulting cloudy brown suspension was centrifuged at 12000 rpm for 30 minutes to yield a brown precipitate and transparent colorless supernatant. The supernatant was discarded. The brown precipitate was resuspended with sonication in a minimum volume of toluene (*ca.* 2 ml). Subsequently, methanol (*ca.* 50 mL) was

added to yield a cloudy suspension and the mixture was centrifuged at 12000 rpm for 30 min to yield a brown solid and clear colourless supernatant. The supernatant was decanted and discarded. The suspension/centrifugation procedure was repeated twice after which the precipitate consisting of purified dodecyl-GeNCs was dispersed in *ca.* 5 mL of dry toluene and stored in a vial for material characterization. A typical yield for dodecyl functionalized GeNCs was *ca.* 15 mg from 50 mg of GeNCs/GeO_2 composite. The final dark brown suspension was filtered through a 0.45 µm PTFE syringe filter to give a clear brown suspension.

4.2.6. Material Characterization and Instrumentation.

Fourier-Transform Infrared Spectroscopy (FT-IR) was performed using a Nicolet Magna 750 IR spectrophotometer. Samples were drop cast from a toluene solution/suspension containing GeNCs. X-ray Powder Diffraction (XRD) was performed using an INEL XRG 3000 X-ray diffractometer equipped with a Cu-Kα radiation source (λ = 1.54 Å). Crystallinity of all samples was evaluated for finely ground powders mounted on a low-intensity background Si (100) holder. Bright-field transmission electron microscopy (TEM) and energy dispersive X-ray (EDX) analyses were performed using a JEOL-2010 (LaB6 filament) electron microscope with an accelerating voltage of 200 kV. High resolution TEM (HRTEM) imaging was performed on JEOL-2200FS TEM instrument with an accelerating voltage of 200 kV. TEM samples of GeNCs were prepared by drop-coating 1-3 drops of toluene suspension (*ca.* 1 mg/mL) containing NCs of choice onto a holey carbon coated copper grid (300 mesh, Electron Microscopy Science) and the solvent was removed under vacuum. TEM and HRTEM images were processed using ImageJ software (version 1.48 v). Particles size distributions (PSD) were determined by measuring *ca.* 300 NCs. Raman spectroscopy was performed using a Renishaw in*Via* Raman microscope equipped with a 514 nm diode laser operating at power of 3.98 mW on the sample. Samples were

prepared by mounting the suspension on gold-coated glass. X-ray photoelectron spectra were acquired in energy spectrum mode at 210 W, using a Kratos Axis Ultra X-ray photoelectron spectrometer. X-Ray source was Al Kα line (1486.6 eV) with a probing area of 1 x 2 mm^2. Samples were prepared as films drop-cast from a toluene solution/suspension onto a copper foil substrate. Binding energies were calibrated using the C 1s emission as an internal reference (284.8 eV). CasaXPS Version 2.3.5 software was used to accomplish the Shirley-type background subtraction. The high-resolution Ge 3d region of spectra was collected for all samples and were fit to Ge $3d_{3/2}$/Ge $3d_{5/2}$ partner lines, with spin-orbit splitting fixed at 0.6 eV, and the Ge $3d_{3/2}$/Ge $3d_{5/2}$ intensity ratio was set to 0.67.

4.3. Results and Discussion

Germanium (II) hydroxide, commonly referred to a hydrous germanium (II) oxide, has an uncertain stoichiometry; it is typically represented by formulae such as $Ge(OH)_2$, $Ge(OH)_2 \cdot xH_2O$, $GeO \cdot xH_2O$, *etc.*[227,232] Freshly prepared germanium (II) hydroxide is yellow, however it readily oxidizes to GeO_2 upon aging (*i.e.,* weeks).[226,233] In this context, it is necessary to freshly prepare materials and store them in inert conditions (*i.e.,* argon filled glovebox).

Existing literature is conflicted regarding the nature of '$Ge(OH)_2$'. The resulting solid product can be white, yellow, or brown depending upon the conditions under which it was precipitated from the Ge (II) solution.[227–229,231,232] A white precipitate is formed by simply cooling and adding water; a brown precipitate forms when ammonium hydroxide is added to the boiling solution; a yellow precipitate forms if ammonium hydroxide is added to a chilled

solution.[229] Figure 4-1 a – d, inset pictures, display photographs of materials prepared during the present study and highlight differences in their physical appearances.

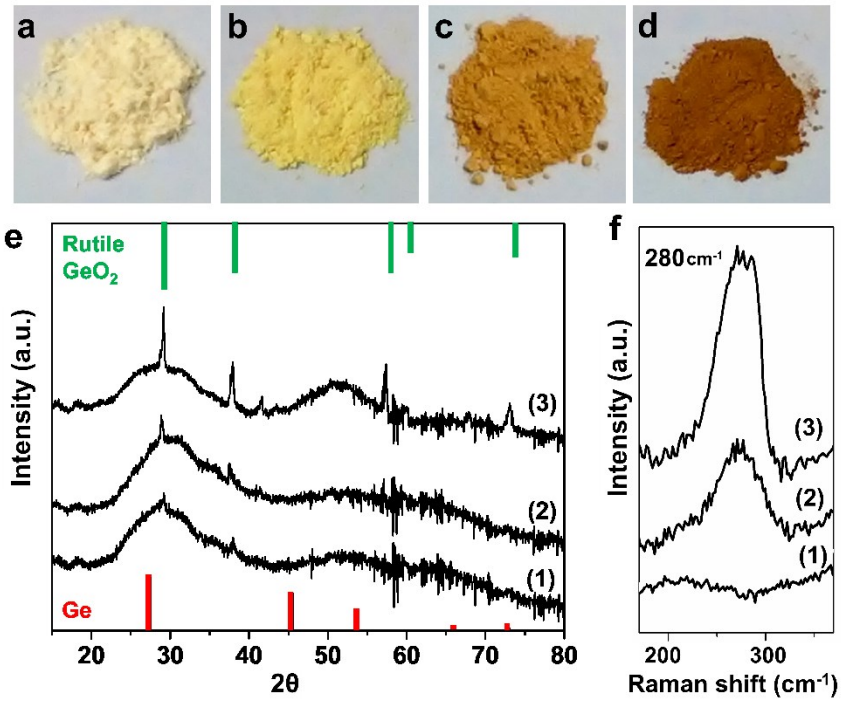

Figure 4-1. Different 'Ge(OH)$_2$' types (a-d) Photographs showing colors and physical appearances for (a) white, (b) yellow, (c) orange, and (d) brown 'Ge(OH)$_2$'. (e) XRD patterns obtained from yellow, orange, and brown 'Ge(OH)$_2$' (1-3, respectively) compared to standard reflections of bulk Ge and rutile GeO_2. (f) Raman spectra for yellow, orange, and brown 'Ge(OH)$_2$' (1-3, respectively).

XRD, XPS, and Raman spectroscopy were used to characterize the white, yellow, orange, as well as brown 'Ge(OH)$_2$'. In contrast with the previous literature reports, we find that the present white, orange, and brown 'Ge(OH)$_2$' do not exhibit element composition ratios that support an empirical formula 'Ge(OH)$_2$'.[227–229,231] For convenience we will confine the present discussion to the yellow, orange, and brown 'Ge(OH)$_2$'. Figure 4-1 e and f show the XRD and

Raman spectra of these materials. In all cases the XRD patterns show broad features at *ca.* 2θ = 25° − 35° and 45° − 50° consistent with the presence of amorphous Ge.[83] Additional sharp reflections at 2θ = 28.7, 37.4, 56.7, 59.3, and 72.3° are assigned to rutile GeO_2 ($P4_2/mnm$ (136)).[159] The brown and orange precursors were precipitated from hot Ge (II) solutions compared to their yellow counterpart. As a result they show more intense XRD features related to Ge and rutile GeO_2 that can be reasonably attributed to solution phase disproportionation of Ge(II) at higher precipitation temperatures.

Raman spectroscopy is a powerful technique that allows detection/identification of Ge-Ge bonds within different '$Ge(OH)_2$' precursors. The proposed disproportionation mechanism of '$Ge(OH)_2$' in solution phase, is further supported by Raman data with the trend observed in the intensity of the Ge-Ge optical phonon feature at *ca.* 280 cm^{-1} (Figure 4-1 f).

Survey XP spectra of the different '$Ge(OH)_2$' materials (Figure B1 in Appendix B) display the presence of germanium and oxygen as expected. Ge LMM signals also are observed at binding energies of 300-600.[20,234] Comparing the deconvolution of the high resolution XP spectra for of Ge 3d spectral region, it is clear the white and yellow '$Ge(OH)_2$' precursors (Figure 4-2) are dominated by a Ge(II) emission. We note more intense features related to intermediate oxides as well as Ge (0) and Ge (IV) in the precursors prepared at higher temperatures (Figure 4-2, orange and brown). This is consistent with the present Raman and XRD data (*vide supra*).

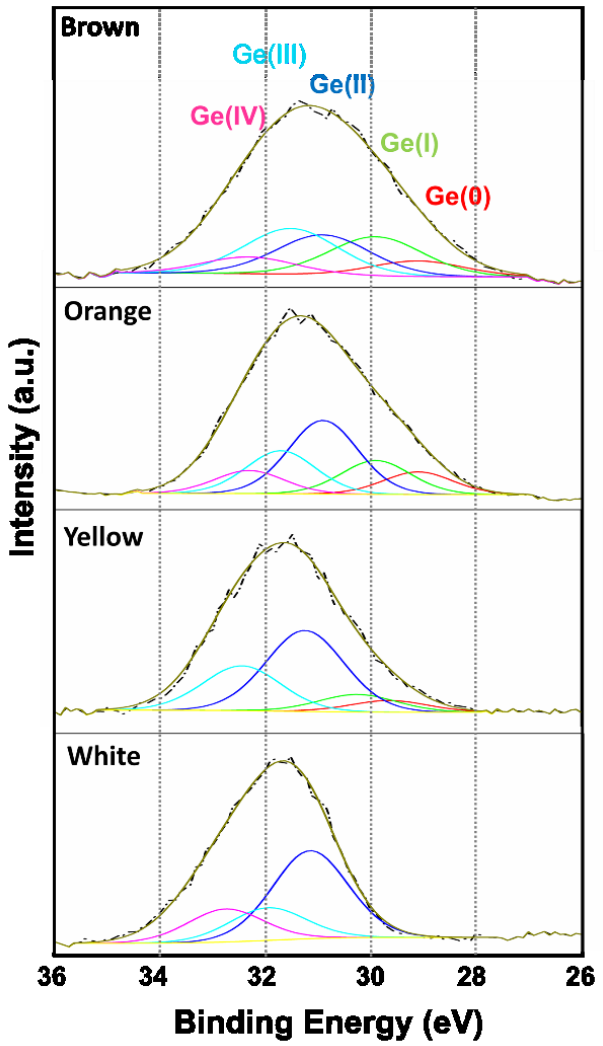

Figure 4-2. High resolution XPS of the Ge 3d region for white, yellow, orange, and brown 'Ge(OH)$_2$', showing Ge 3d$_{5/2}$ contributions. Contributions from Ge 3d$_{3/2}$ have been omitted for clarity.

Heating white, yellow, orange and brown 'Ge(OH)$_2$' at predefined temperatures under Ar produces dark-brown/black powders. Further analyses (XRD, XPS, and Raman) show the dark-brown/black powders produced at all investigated annealing temperatures, contain elemental germanium as well as germanium dioxide.

Figure 4-3 shows XRD patterns obtained for yellow 'Ge(OH)$_2$' before and after thermal processing at the indicated temperatures (for 1 h under Ar). In agreement with literature reports, the parent 'Ge(OH)$_2$' is non-crystalline.[231,235] After heating this solid to the indicated temperatures, broad reflections characteristic of diamond cubic crystalline Ge appear consistent with crystalline nano-domains of germanium (*i.e.,* GeNCs).[203] The breadth of the reflections narrows with increasing processing temperature, presumably as the result of crystalline domains growing.

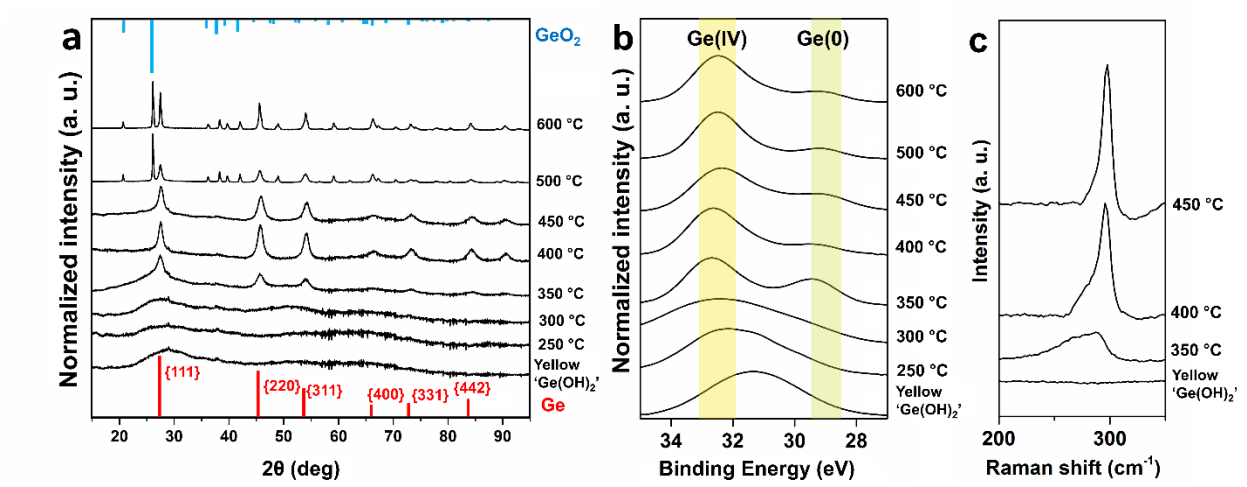

Figure 4-3. (a) XRD patterns obtained from the yellow 'Ge(OH)$_2$' before and after thermal processing at indicated temperatures (for 1 h under Ar) compared to standard reflection of Ge and hexagonal GeO_2. (b) High resolution XPS of the Ge 3d region for yellow 'Ge(OH)$_2$' before and after thermal processing at indicated temperatures (for 1 h under Ar). (c) Raman spectra of yellow 'Ge(OH)$_2$' before and after thermal processing at indicated temperatures (for 1 h under Ar).

Debye-Scherrer analysis of XRD peak broadening (assuming the dimensionless shape factor is 0.94, calculations are provided in Table B1 of Appendix B) indicates that raising the processing temperature through the series of 350, 400, 450, 500 and 600 °C induces growth of

the nanocrystal domains from *ca.* 4.2 to 10.1, 10.3, 15.9 and 23.1 nm, respectively. Moreover, higher temperatures such as 500 or 600 °C are sufficient to also induce crystallization of the germania (GeO_2) matrix. Under these conditions, we have also observed reflections arising from the hexagonal GeO_2, $P3_121$ (152).[135,159] These observations are consistent with the proposal that disproportionation is occurring and amorphous yellow 'Ge(OH)$_2$' is converting into two crystalline materials (GeNCs and GeO_2 matrix) upon thermal processing in an inert atmosphere.

Survey XP spectra of GeNCs/GeO_2 composite obtained from thermal processing of yellow 'Ge(OH)$_2$' at 400 ºC for 1 h under Ar is shown in Figure B2 in Appendix B. The presence of germanium (Ge 3d, 3p and 3s as well as Ge LMM) and oxygen is as expected. High resolution X-ray photoelectron analyses of Ge 3d spectral region, is also consistent with a disproportionation mechanism. Figure 4-3 b shows the high resolution XP spectra of Ge 3d for synthesized yellow 'Ge(OH)$_2$' as well as GeNCs/GeO_2 composites obtained from thermally processed yellow 'Ge(OH)$_2$' at indicated temperatures. The unprocessed yellow 'Ge(OH)$_2$' powder shows a broad range of binding energies from 34 to 28 eV in the Ge 3d region. Upon thermal processing, two broad distinct emissions appear at 29 and 33 eV that are consistent with Ge (0) and Ge (IV), respectively.[121] These two oxidation states are more thermodynamically stable than Ge (II).[236] In this context, the disproportionation of 'Ge(OH)$_2$' to GeNCs and GeO_2 is thermodynamically favorable. The consequence of the results obtained from XRD and XPS analyses clearly indicate the formation of Ge nano-domains inside embedding GeO_2 matrix upon disproportionation of yellow 'Ge(OH)$_2$'.

As it was mentioned previously, Raman spectroscopy can detect Ge-Ge bonds within 'Ge(OH)$_2$' precursor as well as GeNCs/GeO_2 composites. Additionally, the shape and position of

the Raman peak is useful for understanding the size and crystallinity.[80,122,237] For example asymmetric peaks at high frequencies along with small wide shoulders at low frequencies, are routinely attributed more crystalline nanoparticles.[238] Raman spectroscopy also reveals asymmetric peaks at *ca.* 298 cm^{-1} upon thermal processing of yellow 'Ge(OH)$_2$' due to the formation of crystalline Ge domain (*i.e.,* GeNCs).

Orange 'Ge(OH)$_2$' materials have been thermally processed in a similar way. Figure 4-4 a shows XRD patterns obtained for orange 'Ge(OH)$_2$' before and after thermal processing at the indicated temperatures (for 1 h under Ar). From these XRD patterns, it is evident that diamond Ge reflections appears upon thermal processing of orange 'Ge(OH)$_2$'; reflections narrow with increasing processing temperature, as expected. The disproportionation of orange 'Ge(OH)$_2$' to GeNCs and embedding hexagonal GeO_2 is further supported by XPS and Raman analyses (Figure 4-4 b and c).

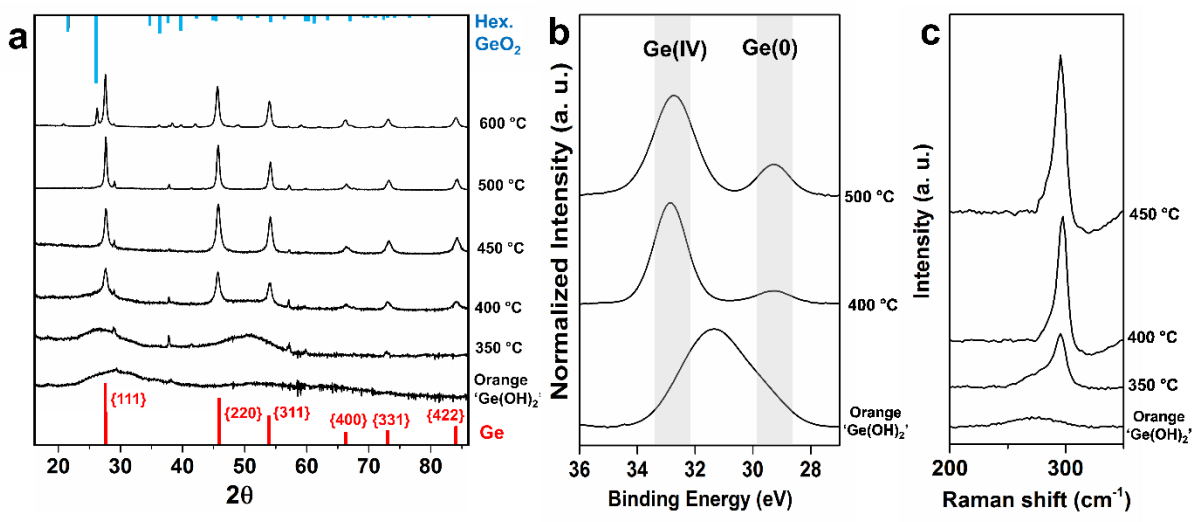

Figure 4-4. (a) XRD patterns obtained from the orange 'Ge(OH)$_2$' before and after thermal processing at indicated temperatures (for 1 h under Ar) compared to standard reflection of Ge and hexagonal GeO_2. (b) High resolution XPS of the Ge 3d region for orange 'Ge(OH)$_2$' before and after thermal processing at indicated temperatures (for 1 h

under Ar). (c) Raman spectra of orange ‘$Ge(OH)_2$’ before and after thermal processing at indicated temperatures (for 1 h under Ar).

Figure 4-5 a shows the XRD patterns of the brown ‘$Ge(OH)_2$’ before and after thermal processing at indicated temperatures (from 250 °C to 600 °C for 1 h under Ar). Following heating of the brown ‘$Ge(OH)_2$’, broad reflections of diamond cubic Ge sharpen and additionally the hexagonal GeO_2 reflections appear at temperatures higher than 500 °C. This observation indicates the disproportionation of brown ‘$Ge(OH)_2$’ to GeNCs and embedding hexagonal GeO_2.[159,203] In this case, the brown ‘$Ge(OH)_2$’ has some unique reflections (*i.e.,* for amorphous Ge nuclei and Rutile GeO_2). Thus the emerging of new reflections for GeNCs and hexagonal GeO_2 finally yields a more crowded pattern. The reflections of GeNCs are wider in composites processed at lower temperatures (*ca.* 350 °C) but sharpen upon thermal processing of composites at higher temperatures. Debye-Scherrer analysis of XRD peak broadening (dimensionless shape factor was assumed 0.94, calculations are provided in Table B2 of Appendix B) shows growing crystal sizes as 6.1, 8.0, 9.4, and 18.2 nm upon the thermal processing of brown ‘$Ge(OH)_2$’ at 400, 450, 500, and 600 °C, respectively.

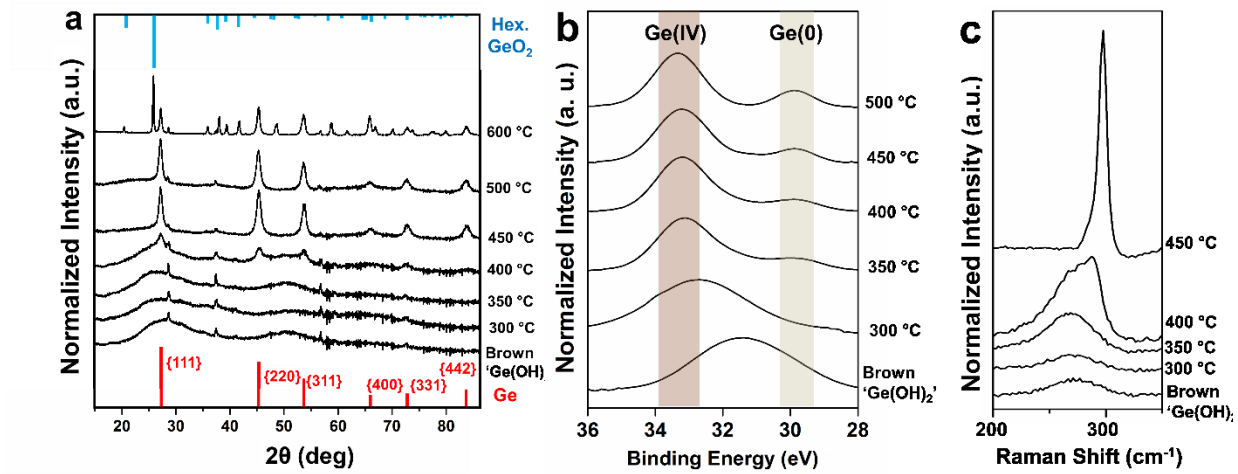

Figure 4-5. (a) XRD patterns obtained from the brown 'Ge(OH)$_2$' before and after thermal processing at indicated temperatures (for 1 h under Ar) compared to standard reflections of Ge and hexagonal GeO_2. (b) High resolution XPS of the Ge 3d region for brown 'Ge(OH)$_2$' before and after thermal processing at indicated temperatures (for 1 h under Ar). (c) Raman spectra of brown 'Ge(OH)$_2$' before and after thermal processing at indicated temperatures (for 1 h under Ar).

Figure B2 in appendix B, shows survey XP spectra of GeNCs/GeO_2 composite obtained from thermal processing of brown 'Ge(OH)$_2$' (at 400 ºC for 1 h under Ar). The presence of germanium (Ge 3d, 3p and 3s as well as Ge LMM) and oxygen is as expected. X-ray photoelectron analyses of Ge 3d spectral region (Figure 4-5 b), is also consistent with the disproportionation of the brown 'Ge(OH)$_2$' to Ge(0) (*i.e.,* GeNCs) and Ge(IV) (*i.e.,* embedding GeO_2 matrix).

In the thermal processing of the brown 'Ge(OH)$_2$', Raman spectroscopy also reveals conversion of amorphous Ge nuclei to crystalline Ge domain (*i.e.,* GeNCs). Shown in Figure 4-5 c, a symmetrical optical phonon is observed at lower energies (*ca.* 280 cm^{-1}) and is related to the smaller size of non-crystalline Ge nuclei. With increasing the processing temperatures, an

asymmetrical peak at high frequencies (*ca.* 298 cm^{-1}) with small wide shoulder appears due to formation of crystalline GeNCs.[237,238]

Finally, thermal processing of white '$Ge(OH)_2$' was investigated in a similar way. White '$Ge(OH)_2$' is less stable than other '$Ge(OH)_2$' species (*i.e.,* yellow, orange, and brown).[228] Our characterization shows the degradation of the white '$Ge(OH)_2$' product (mainly oxidation to GeO_2 or disproportionation to Ge/GeO_2) even in room temperature. This observation is consistent with literature reports.[228,231] XRD characterization of freshly prepared white '$Ge(OH)_2$' shows the material is an amorphous solid with presence of crystalline Ge and hexagonal GeO_2 (Figure 4-6 a). Thermal processing of white '$Ge(OH)_2$' produces elemental Ge, as well as GeO_2 presumably due to disproportionation reaction. Production of GeNCs/GeO_2 has been further proven by XRD, XPS, and Raman analyses (Figure 4-6).

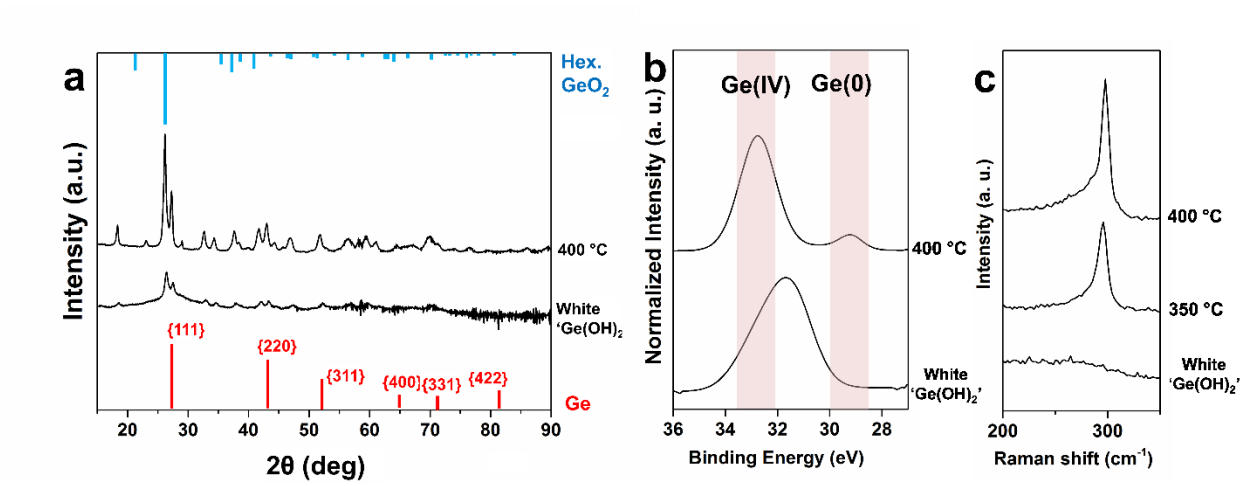

Figure 4-6. (a) XRD patterns obtained from the white '$Ge(OH)_2$' before and after thermal processing at indicated temperatures (for 1 h under Ar) compared to standard reflection of Ge and hexagonal GeO_2. (b) High resolution XPS of the Ge 3d region for white '$Ge(OH)_2$' before and after thermal processing at indicated temperatures (for 1 h under Ar). (c) Raman spectra of white '$Ge(OH)_2$' before and after thermal processing at indicated temperatures (for 1 h under Ar).

Although there are numerous potential applications for GeNCs embedded in GeO_2,[75–79] our interests lie in the preparation of freestanding colloidal GeNCs. In this context, HF etching was employed for selective removing GeO_2; this produces hydride-terminated GeNCs (H-GeNCs)[239] suitable for further functionalization and surface passivation (*e.g.,* hydrogermylation).[19,240,241] Unfortunately, it is not possible to evaluate the morphology of H-GeNCs directly because of solubility limitations. Surface functionalization of GeNCs is necessary for rendering them resistant to deleterious reactions (*e.g.,* oxidation) and compatible with their environment (*e.g.,* solubility).

To evaluate the morphology of the GeNCs formed in thermal processing of different '$Ge(OH)_2$' materials, produces GeNCs/GeO_2 composites were etched to liberated free-standing H-GeNCs. Thermally induced hydrogermylation has been applied to functionalize the GeNCs with alkene groups (*i.e.,* dodecene).

Electron micrographs of dodcyl-GeNCs show there are stark differences in the morphologies of the GeNCs obtained upon thermal processing of each '$Ge(OH)_2$' precursor (*i.e.,* white, yellow, orange, and brown '$Ge(OH)_2$'). Bright field TEM images of dodecene functionalized GeNCs (dodecyl-GeNCs) synthesized from the thermal processing of each precursor upon heating at 400 °C for 1 h in Ar are shown in Figure 4-7 a – d. It is clear from these data and the associated size distributions that in moving from the white through to the brown '$Ge(OH)_2$', the particle size distributions narrow and the GeNCs are more uniform.

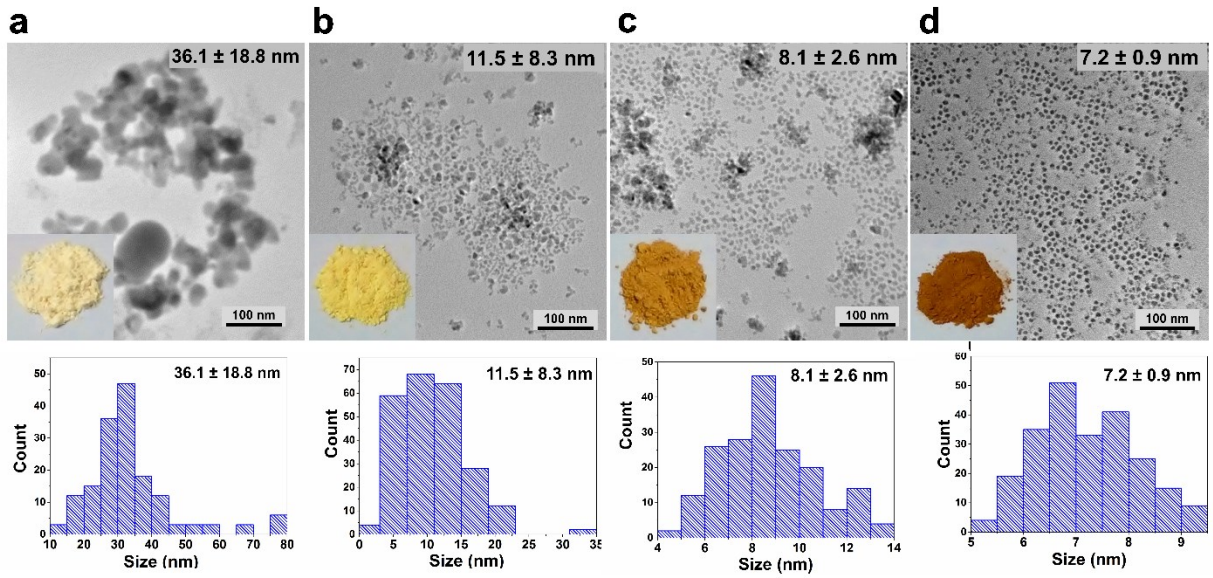

Figure 4-7. Bright-field TEM images of dodecyl-GeNCs synthesized from thermal processing of (a) white, (b) yellow, (c) orange, and (d) brown '$Ge(OH)_2$' along with related particle size distribution. Inset: photographs showing colors and physical appearances for each '$Ge(OH)_2$' material.

From these analyses of the present precursors and a comparison of the GeNCs resulting from thermal processing of them (Figure 4-7 a – d) we propose a NC formation mechanism that is analogous to previous reports involving the preparation of oxide-embedded SiNCs from polymeric precursors.[119] In all cases, the precursors disproportionate producing GeNCs embedded in GeO_2. However, polydispersed NCs are obtained from the white (and to a lesser degree yellow) precursors because unseeded homogeneous nucleation of Ge nano-domains occurs and results in ineffective separation of particle/domain nucleation and growth. For the orange and brown '$Ge(OH)_2$' we note that spectroscopically (XRD, XPS, and Raman) detected Ge seeds are present (*vide supra*). In this context, annealing these precursors could lead to heterogeneous seeded growth of GeNCs, effective separation of particle/domain nucleation and

growth and narrow size distributions GeNCs. We also tentatively speculate that the rutile GeO_2 present in the brown '$Ge(OH)_2$' slows Ge atom diffusion through oxide matrix further controlling domain growth; this aspect of the mechanism is the subject of ongoing studies.

The FT-IR technique provides invaluable information regarding the surface chemistry of colloidal nanoparticles.[121,135] For H-GeNCs (Figure 4-8 a), there are two sharp peaks at *ca.* 2000 and 750 cm^{-1} that are consistent with Ge-H stretching and bending vibrations. After functionalization of H-GeNCs with dodecene, the Ge-H feature decreases in intensity and is replaced by intense absorptions at *ca.* 2850 - 2650 cm^{-1} and *ca.* 1460 cm^{-1} that are attributes C–H stretching and bending on the aliphatic chain.[242] Some germanium oxide is present as evidenced by features at *ca.* 860 cm^{-1} that arise from partial oxidation that occurred during handling/workup. Surface oxidation is further evidenced by the presence of broad O-H stretching feature at *ca.* 3400 cm^{-1}. Finally, the appearance of a Ge-C stretching feature at 700 cm^{-1} confirms the reaction of dodecene with GeNC surfaces.[243]

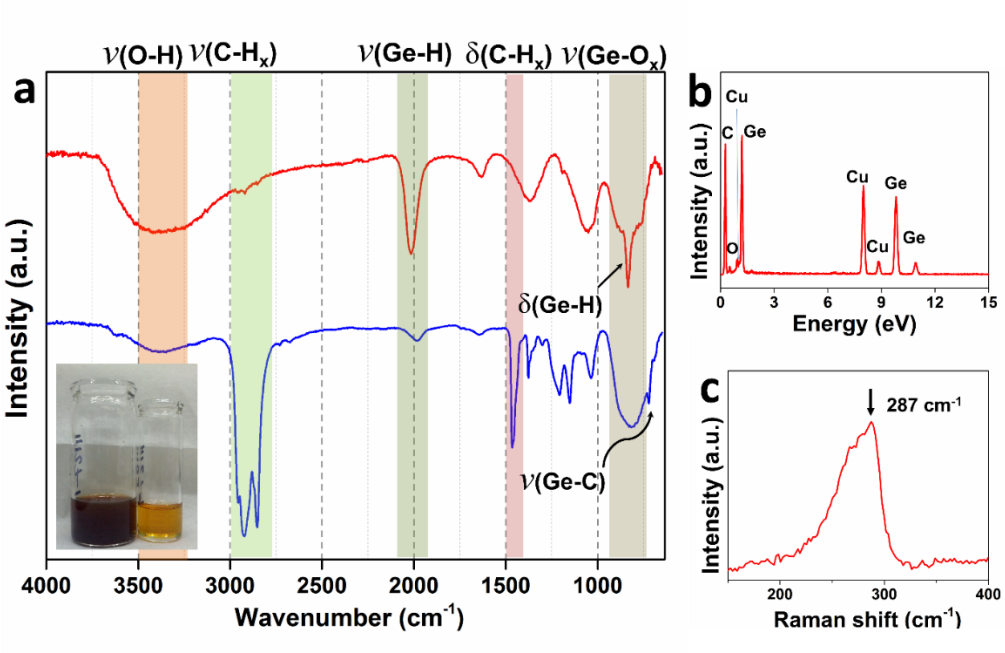

Figure 4-8. (a) FT-IR spectra of dodecyl-GeNCs (blue) compared to H-GeNCs (red). Inset photograph showing the toluene dispersion of dodecyl-GeNCs before (dark color) and after (light color) filtration through a 0.45 μm PTFE syringe. (b) EDX spectrum of dodecyl-GeNCs. (c) Raman spectrum dodecyl-GeNCs.

Energy-dispersive X-ray spectra of these particles (Figure 4-8 b) confirms the presence of germanium and a small amount of oxygen. A representative Raman spectrum of the present dodecyl-GeNCs (Figure 4-8 c), shows an asymmetric feature at 287 cm^{-1} arising from Ge-Ge bonding in crystalline elemental germanium.[237,238] HRTEM imaging (Figure 4-9) shows crystalline nano-domains with a lattice spacing of 0.33 nm corresponding to Ge (111) lattice fringes.

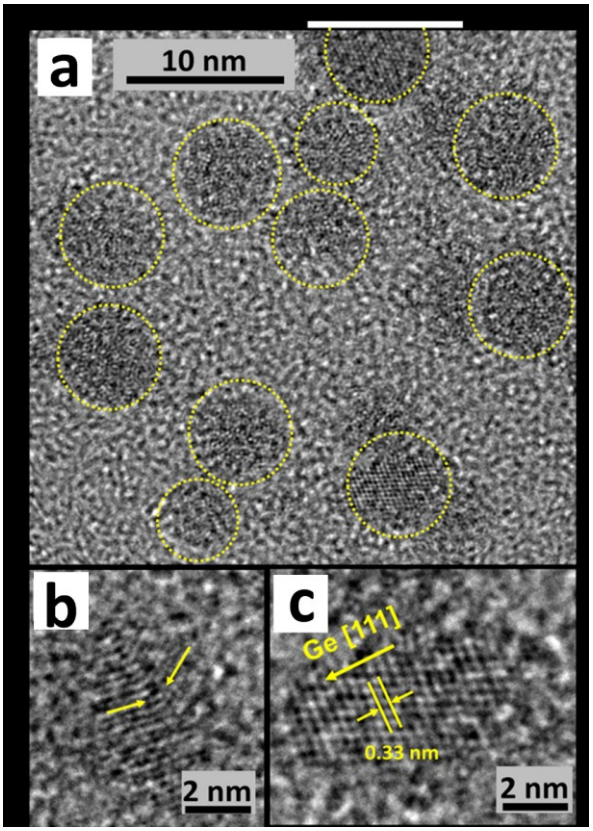

Figure 4-9. (a) HRTEM and image of dodecyl-GeNCs obtained from thermal treatment of 'Ge(OH)$_2$' for 1 h under Ar at 400 °C. (b) Twinned structure in one GeNC. (c) A set of lattice fringes perpendicular to <111> direction.

However, as mentioned previously (Figure 4-7), the brown 'Ge(OH)$_2$' precursor yields more monodispersed GeNCs compared to other 'Ge(OH)$_2$' precursors (*i.e.,* white, yellow and orange 'Ge(OH)$_2$'). The formation of Ge nuclei in the solution (synthesize of the brown 'Ge(OH)$_2$'), followed by growing elemental Ge 'islands' to GeNCs (thermal processing of the brown 'Ge(OH)$_2$') is the key factor for making more monodispersed GeNCs. Further investigations have been done to understand the effect of annealing temperatures on the morphology of GeNCs obtained from thermal treatment of brown 'Ge(OH)$_2$' (*vide infra*).

The TEM images of dodecyl-GeNCs liberated from Ge/GeO_2 composites obtained from thermal processing of brown '$Ge(OH)_2$' at different temperature clearly show the growth of partially larger GeNCs as a result of raised temperature (Figure 4-10). Shown in Figure 4-10 a − d, thermal processing of brown '$Ge(OH)_2$' at 350 °C gives GeNCs with the size range of 5.9 ± 1.2 nm. For similar GeNCs obtained in 400, 450, and 500 °C, particle size distributions are 7.2 ± 0.9, 8.3 ± 1.1, and 10.1 ± 4.3 nm, respectively.

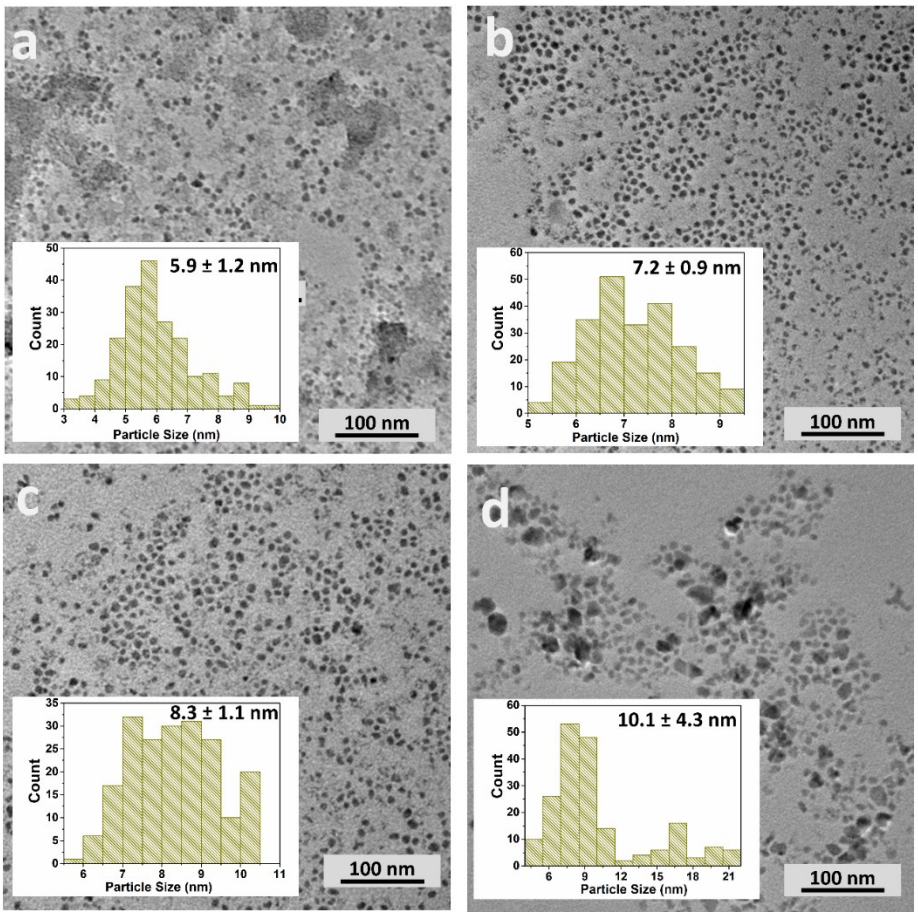

Figure 4-10. Brown '$Ge(OH)_2$' and its thermal processing. (a-d) TEM images and particle size distribution of dodecyl-GeNCs synthesized from thermally processing of the brown compound for 1 h under Ar at 350 °C (a), 400 °C (b), 450 °C (c), and 500 °C (d).

The increasing of the average particle size along with broadening of the size distribution in higher temperature is supported by theory of Ge atoms diffusion in higher rate at raised temperatures (Ostwald ripening).[244] Moreover, the TEM results are consistent with the observation of sharpening peaks in the XRD patterns (Figure 4-8 a) and corroborates the growth of average particle sizes with temperatures. The average size of GeNCs determined from TEM are slightly larger than their crystal sizes calculated by Debye-Scherrer analyses. This is because of the GeNCs formed using current method are mostly poly-crystalline (Twinned structures shown in HRTEM images, Figure 4-7 c) and/or there are amorphous moieties in Ge nanoparticles that are not accounted for by XRD.

The length of etching process was the last factor investigated. According to the details in the experimental section, the effect of etching time was studied to find the best for liberating GeNCs from the oxide layer which they were embedded in. Figure 4-11 shows the TEM images of dodecyl-GeNCs liberated from the same GeNCs/GeO_2 composite (brown '$Ge(OH)_2$' annealed for 1 h at 400 ºC under Ar) after etching with HF acid for predetermined times (5, 30, 60 and 120 min). TEM images of the dodecyl-GeNCs obtained from the same composite after etching for 15 min were already shown in Figure 4-10 b.

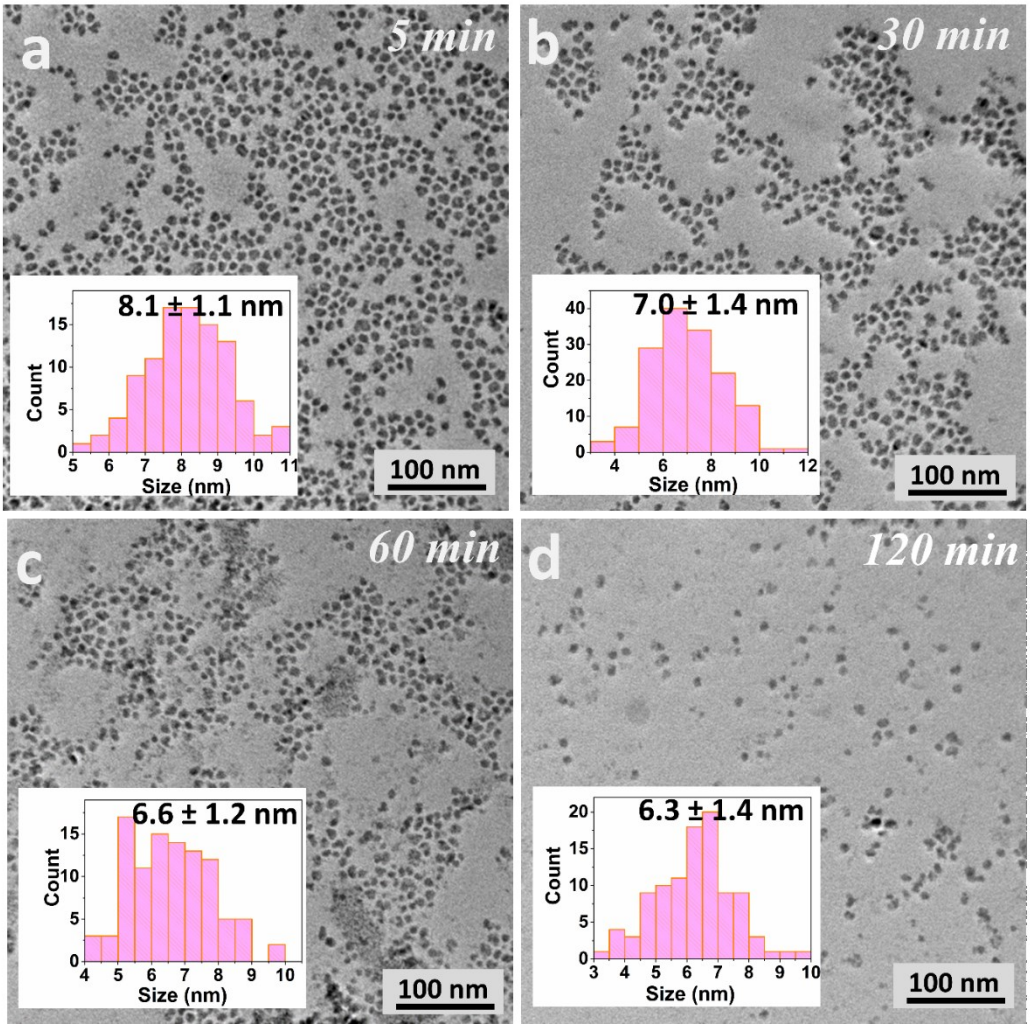

Figure 4-11. (a-d) TEM images and particles size distribution of dodecyl-GeNCs from thermally processed brown '$Ge(OH)_2$' (at 400 °C under Ar for 1 h), liberated from embedding GeO_2 matrix after etching by HF acid for (a) 5 min, (b) 30 min, (c) 60 min and (d) 120 min.

According to Figure 4-11 a, GeNCs are liberated from embedding GeO_2 matrix even after exposing to HF acid for a short time (*i.e.,* 5 min). This was expected because of the higher reactivity of GeO_2 compared to SiO_2.[73,229] However, longer etching times caused minor shrinkages of GeNCs. In this context, particle sizes change from 8.1 ± 1.1 nm for etching time =

5 min to 7.2 ± 0.9 nm for etching time = 15 min (Figure 4-10 b), 7.0 ± 1.4 nm for etching time = 30 min, 6.6 ± 1.2 for etching time = 60 min and finally 6.3 ± 1.4 for etching time = 120 min. Due to the morphological similarity of the final GeNCs obtained from different etching times and in order to avoid any adverse morphological/surface defect from extensively long etching process, 15 min has been chosen as the typical etching time in current work. Precise control over the size distribution as well as morphology of GeNCs through applying different etching times needs further investigations.

4.4. Conclusions

As a summary, GeNCs are an important 21st century technological material that hold potential for far reaching impacts on numerous optoelectronic applications. However few methods exist to prepare large quantities (100s mgs) of well-defined materials. The present investigation demonstrates the effective preparation of a series of 'Ge$(OH)_2$' precursors suitable for large scale preparation of free-standing GeNCs whose surfaces maybe modified through thermally induced hydrogermylation. A detailed comparison of the precursors has also provided insight into, and proposal of a seeded growth mechanism that provides GeNCs exhibiting narrow size distributions. While the present NCs are not photoluminescent, we believe these results from surface defects and is the subject of ongoing investigation.

Chapter 5:

Synthesis and Surface Functionalization of Hydride-terminated Ge Nanocrystals Obtained from the Thermal Treatment of '$Ge(OH)_2$'*

* A version of this Chapter has been published:

Javadi, M.; Picard, D.; Sinelnikov, R.; Narreto, M. A.; Hegmann, F. A.; Veinot, J. G. C *Langmuir* **2017**. Article ASAP, DOI: 10.1021/acs.langmuir.7b00358

5.1 Introduction

General interest in germanium came about with the realization of semiconductor-based electronics in the second half of 20th century.[68] Transistors, which are essential components in the electronic devices upon which modern society relies, were first made using germanium.[219,220] While Ge lost out to ultra-pure silicon, it remains an important material for optoelectronic applications.[68] In the early 1990s the surprising discovery of visible photoluminescence (PL) from silicon and germanium nanostructures opened new possibilities.[66,67] Despite being in Group 14 germanium differs substantially from its more frequently studied periodic congener silicon. Compared to silicon, bulk Ge possesses a smaller band-gap (0.67 *vs.* 1.1 eV at 300 K),[69] larger Bohr-exciton radius (24.3 *vs.* 4.9 nm),[67,70] higher electron and hole mobility (≤3900 *vs.* ≤1500 $cm^2/V\cdot s$),[71] as well as greater capacity for and diffusivity of ions (*e.g.*, Li^+).[72] In the context of these characteristics, comparatively large GeNCs and related structures (*e.g.*, oxide-embedded GeNCs) are expected possess favorable chemical, optical and electronic properties useful in applications such as solar cells,[18] biological imaging,[73,74] Bragg reflectors,[18] light-emitting diodes,[181,182] non-volatile memory devices,[75–79] as well as battery electrode materials.[72,245]

A variety of procedures for preparing GeNCs have appeared; some highlights include: laser ablation[223] and ball milling of bulk Ge,[224] plasma pyrolysis of GeH_4,[225] solution-phase reduction of Ge(II) and Ge(IV) precursors,[19,82,83] metathesis of Ge-based Zintl salts,[97–99,186] and thermal decomposition of organogermane precursors.[101,102,105] While solution-phase reduction protocols using germanium halides have been reported,[89] a ground-breaking report by Klimov *et al.* showed the first example of colloidal GeNCs derived from solution reduction that photoluminesce in the infrared spectral region *via* a band-gap transition.[18] The authors also

effectively showed size dependence of GeNC optical properties that arise from quantum confinement.[18] Despite these important advances, developing methods that afford GeNCs with well-defined surface chemistry remains an important target if their full potential is to be realized.[89]

Solid-state syntheses of oxide-embedded SiNCs *via* thermolysis of substoichiometric oxide-based polymeric precursors have proved very effective.[17,119] These procedures provide control of NC dimension and shape, and afford NCs whose surface chemistry can be tailored subsequent to liberation.[17,246,247] A similar approach using sol-gel derived organic functionalized germanium rich precursors (*i.e.*, $[(RGeO_{1.5})_n]$) showed promise.[122] Specifically, a phenyl substituted sol-gel polymer $[(PhGeO_{1.5})_n]$ was thermally treated to yield GeNCs embedded in GeO_2. This early investigation showed Ge was formed *via* two pathways (*i.e.*, disproportionation of substoichiometric oxides and direct reduction of oxide by hydrogen carrier gas). The GeNCs were freed from the oxide matrix upon etching with warm water, however size distributions were broad.[122] Subsequent investigations aimed at exploring the role of the organic substituents indicated carbon contamination limited the utility this approach.[121]

In the present Chapter a facile method for preparing GeNCs from a carbon-free germanium-rich oxide precursor derived from commercial GeO_2 powder is described. Thermal processing of this precursor in inert atmosphere yields GeO_2-embedded GeNCs that are readily liberated with hydride surfaces (*i.e.*, Ge-H) *via* HF etching and subsequently functionalized *via* hydrogermylation.

5.2 Experimental

5.2.1 Reagents and Materials

Germanium dioxide powder (GeO_2, 99.9%) was purchased from Eagle-Picher. Hydrophosphorous acid (50 wt. % in H_2O), sodium hydroxide pellets, 1-dodecene (97%), Chloroform-d ($CDCl_3$, 99.8 atom % D), 1-dodecene (97%), 2,2'-azobis(2-methylpropionitrile) (AIBN, 98%), benzoyl peroxide (BP, 98%), and borane tetrahydrofuran (BH_3·THF 1M) as well as reagent grade methanol, toluene, and ethanol were purchased from Sigma-Aldrich. Electronics grade hydrofluoric acid (HF, 49% aqueous solution) was purchased from J. T. Baker. Hydrochloric acid (36.5 - 38%) and ammonium hydroxide (28 - 30%) were purchased from Caledon Labs. Ultrapure H_2O (18.2 MΩ/ cm) purified in a Barnstead Nanopure Diamond purification system was used in all reactions. Molecular sieves (type 4 Å) were purchased from Sigma-Aldrich and activated in vacuum oven prior to use. Unless otherwise indicated reagents were used as received.

5.2.2 Synthesis of germanium (II) hydroxide, '$Ge(OH)_2$'

A modified literature procedure was used to prepare '$Ge(OH)_2$'.[226–231] In a typical preparation, 1.0 gram of germanium dioxide powder was dissolved in 7.0 mL of a freshly prepared aqueous NaOH (~17 M). Upon slow addition of 24 mL aqueous HCl (6 M), GeO_2 powder precipitated and then dissolved to give a clear acidic solution. Subsequently, 7.5 mL of aqueous 50 % H_3PO_2 was added all at once and the resulting colourless solution was refluxed under an argon atmosphere. After 5.5 hours the condenser was removed and concentrated aqueous NH_4OH was added dropwise to yield a brown precipitate of '$Ge(OH)_2$' (*Caution: This reaction is extremely exothermic*). The brown precipitate was recovered by vacuum filtration and

washed three times with *ca.* 100 mL of deionized/deoxygenated water. Finally the solid was dried vacuum oven at 50 °C for 12 hours and stored in a vial until needed. Typical mass yields exceed 85%.

5.2.3 Thermal processing of germanium (II) hydroxide

Thermal processing was performed using a Lindberg/Blue tube furnace in flowing argon (15 mL/min). Typically, 0.5 g of '$Ge(OH)_2$' powder was transferred to a quartz reaction boat, placed in the furnace and heated to 400 °C at 20 °C/min where it remained for 60 minutes. A composite of GeNCs in a germanium dioxide matrix (GeNCs/GeO_2) was obtained as a black/brown powder (*ca.* 0.5 g), ground using an agate mortar and pestle (particles size *ca.* 1 μm), and stored under ambient atmosphere for further use and characterization.

5.2.4 Isolation of GeNCs

Hydride-terminated GeNCs (H-GeNCs) were liberated from the oxide matrix upon etching of GeNCs/GeO_2 composite with alcoholic HF. The fine powder obtained from grinding the product of thermal processing (~50 mg) was added to 1.0 mL of 1:1 solution of ethanol and water and stirred for 15 min in a polyethylene terephthalate (PET) beaker to effectively wet the powder. Subsequently, 0.5 mL of HF acid (49% aqueous solution) was added dropwise. *(**Caution!** HF must be handled with extreme care and in accordance with local regulations.)* After stirring the mixture for an additional 15 min, three portions of *ca.* 5 mL toluene were added to extract the H-GeNCs. The cloudy toluene layer was centrifuged at 3000 rpm to yield a black precipitate. This precipitate was dispersed in toluene containing activated 4 Å molecular sieves (*ca.* 1 g) and gently agitated for approximately one minute. The suspension was transferred to

centrifuge tubes and the black precipitate (H-GeNCs) was recovered upon centrifuging at 3000 rpm and immediately functionalized using procedures outlined below.

5.2.5 Thermally induced hydrogermylation of H-GeNC

The black precipitate (*i.e.*, H-GeNCs.) isolated from the etching of the GeNCs/GeO_2 composite (*ca.* 50 mg) was dispersed in 5.0 mL 1-dodecene, transferred to a Schlenk flask attached to an argon charged double manifold and three freeze-pump-thaw cycles were performed. Subsequently, the cloudy deoxygenated reaction mixture was heated to 190 °C with stirring. After approximately 15 h the reaction mixture becomes transparent and takes on an orange-brown appearance. The resulting dodecyl-functionalized GeNCs (dodecyl-GeNCs) were isolated (*ca.* 15 mg) and purified as outlined below. Luminescent dodecyl-GeNCs were prepared by introducing small quantity of I_2 (*ca.* 3 mg) to reaction flask prior to heating.

5.2.6 Radical initiated hydrogermylation of H-GeNC

H-GeNCs (from etching *ca.* 50 mg of GeNCs/GeO_2 composite) were dispersed in 5 ml of 1-dodecene and the radical initiator of choice (*i.e.*, 10 mg AIBN or 15 mg BP) was added. The mixture was transferred to a Schlenk flask attached to an argon charged double manifold and exposed to three freeze-pump-thaw cycles. Subsequently, the argon filled reaction flask was heated (60 °C for AIBN or 85 °C for BP) and stirred for 15 hours to yield an orange-brown transparent suspension of crude dodecyl-GeNCs (*ca.* 15 mg) that were subjected to purification procedures outlined below.

5.2.7 Borane catalyzed surface hydrogermylation

H-GeNCs (from etching *ca.* 50 mg of GeNCs/GeO_2 composite) were dispersed in 5 ml of 1-dodecene. The reaction mixture was transferred to a Schlenk flask attached to an argon charged

double manifold and exposed to three freeze-pump-thaw cycles. Subsequently, 560 μL of BH_3·THF (1M) (*i.e.*, 2.5 mol % of 1-dodecene) was added *via* syringe and the argon filled reaction flask was stirred at room temperature (23 °C) for 15 hours to yield transparent orange-brown suspensions of crude dodecyl-GeNCs (*ca.* 15 mg) that were subjected to purfication procedures outlined below.

5.2.8 Isolation and purification of 1-dodecyl-GeNCs

The same solvent/antisolvent precipitation procedure was used to purify dodecyl-GeNCs obtained from the functionalization procedures noted above. The transparent orange-brown suspensions of crude dodecyl-GeNCs obtained from the functionalization procedures were transferred to a polypropylene centrifuge tubes and toluene (5 mL) as well as *ca.* 45 mL of a 1:1 ethanol and methanol (v:v) antisolvent were added. The resulting cloudy brown suspension was centrifuged at 12000 rpm for 30 minutes to yield a brown precipitate and transparent colorless supernatant. The supernatant was discarded. The brown precipitate was resuspended with sonication in a minimum volume of toluene (*ca.* 2 ml). Subsequently, methanol (*ca.* 50 mL) was added to yield a cloudy suspension and the mixture was centrifuged at 12000 rpm for 30 min to yield a brown solid and clear colourless supernatant. The supernatant was decanted and discarded. The suspension/centrifugation procedure was repeated twice after which the precipitate consisting of purified dodecyl-GeNCs was dispersed in *ca.* 5 mL of dry toluene and stored in a vial for material characterization.

5.2.9 Homo-oligomerization of 1-dodecene

To evaluate the formation of 1-dodecene oligomers during the functionalization procedures investigated in the absence of GeNCs. Samples were prepared by treating 5 mL of

neat 1-dodecene using the identical conditions used for the functionalization protocols of choice (*i.e.*, no GeNCs).

5.2.10 Material Characterization and Instrumentation

Fourier-Transform Infrared Spectroscopy (FT-IR) was performed using a Nicolet Magna 750 IR spectrophotometer. Samples were drop cast from a toluene suspension containing the material in question. X-ray Powder Diffraction (XRD) was performed using an INEL XRG 3000 X-ray diffractometer equipped with a Cu-Kα radiation source (λ = 1.54 Å) and CPS-120 detector. Bright field transmission electron microscopy (TEM) and energy dispersive X-ray (EDX) analyses were performed using a JEOL-2010 (LaB6 filament) electron microscope with an accelerating voltage of 200 kV. High resolution TEM (HRTEM) imaging was performed on JEOL-2200FS TEM instrument with an accelerating voltage of 200 kV. TEM samples of GeNCs were prepared by drop-coating of 1-3 drops of a dilute toluene solution containing GeNCs of choice onto a holey carbon coated copper grid (300 mesh, Electron Microscopy Science) and the solvent was removed *in vacuo*. Bright field TEM and HRTEM images were processed using ImageJ software (version 1.48 v). Particle size distributions were determined using measurements of 200-300 NCs. Raman spectroscopy was performed using a Renishaw in*Via* Raman microscope equipped with a 514 nm diode laser and a power of 3.98 mW on the sample. Samples were prepared by mounting the suspension on gold-coated glass. X-ray photoelectron spectra were acquired in energy spectrum mode at 210 W, using a Kratos Axis Ultra X-ray photoelectron spectrometer. X-Ray source was Al Kα line. Energy is 1486.6 eV. The probing area is about 1 x 2 mm^2. Samples were prepared as films drop-cast from toluene solution/suspension onto a copper foil substrate. Binding energies were calibrated using the C 1s peak as a reference (284.8 eV). CasaXPS Version 2.3.5 software was used to accomplish the

background subtracting and curve fitting. Nanostructured-assisted laser desorption/ionization mass spectroscopy (NALDI-MS) was performed in positive/negative reflection mode using a Bruker Daltonics UltrafleXtreme MALDI TOF/TOF mass spectrometer. Samples were prepared by spotting ~1 μL of GeNC toluene suspension in question onto a Bruker Daltonics NALDI target and air-dried. Nuclear magnetic resonance spectroscopy (NMR) spectra were obtained using a Varian Unity INova Console 500 MHz NMR spectrometer. A concentrated solution (*ca.* 3 mg/mL) of dodecyl-GeNCs in $CDCl_3$ was used to collect the ^{1}HNMR spectra. FID files were processed using Nuts NMR data processing software.

5.2.11 Photoluminescence (PL) Measurements and Instrumentation

An ultrafast laser at 800 nm excitation source with 55 fs pulse width and 1 kHz repetition rate was employed. A fluence of ~340 μJ was used to excite solutions of GeNCs and the PL was collected at the back of the cuvette using lenses and optical fiber onto the entrance slit of the monochromator (Triax 180, Horiba), which has a grating at the NIR region with a blaze at 1500 nm. The output at the exit slit is refocused to a thermoelectronically-cooled InGaAs amplified photodetector (PDA10DT, Thorlabs) which has a wavelength range of 0.9 − 2.57 μm set at 1MHz bandwidth with 70 dB gain. The signal is then processed through a DSP lock-in amplifier (SR830, Stanford Research). The PL spectra were plotted by a Labview program, which also controls the monochromator.

5.3 Results and Discussion

Germanium (II) hydroxide, commonly referred to hydrous germanium (II) oxide, has an uncertain stoichiometry.[227] The ‘$Ge(OH)_2$’ precursor employed herein to prepare GeNCs was precipitated from a hot aqueous Ge(II) solution (Scheme 5-1).[226,229,233]

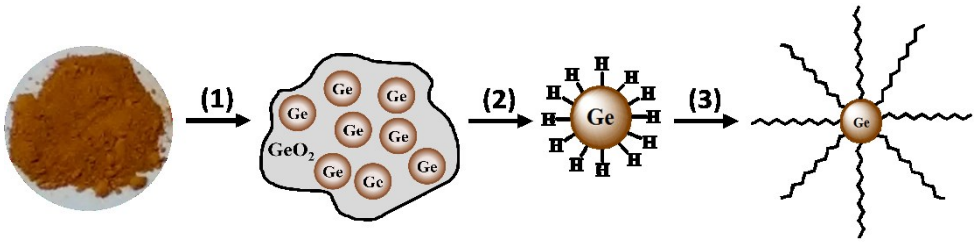

Scheme 5-1. Preparation of dodecane functionalized GeNCs. (1), Thermal processing of ‘$Ge(OH)_2$’ at T = 400 °C in Ar, (2), Liberation of H-GeNCs *via* HF etching, (3), Functionalization/surface modification of GeNCs through thermally-activated, radical-initiated, or borane-catalyzed hydrogermylation.

Figure 5-1 a shows XRD patterns obtained for ‘$Ge(OH)_2$’ and composites prepared upon thermal processing at 400 °C (for 1 h under Ar). The diffraction pattern of the ‘$Ge(OH)_2$’ precursor shows broad features at *ca.* 2θ = 25° - 35° and 45° - 50° consistent with the presence of amorphous Ge.[83] In addition, low intensity, sharp reflections at 2θ = 28.7, 37.4, 56.7, 59.3, and 72.3° appear that are assigned to rutile GeO_2 ($P4_2/mnm$ (136)).[159] Heating the ‘$Ge(OH)_2$’ at 400 °C under Ar provides a dark-brown/black powder the XRD pattern of which (Figure 5-1 a) shows broadened reflections characteristic of diamond cubic crystalline Ge at 27.3, 45.3, 53.7, 66.1, 72.9 and 83.8° consistent with nanocrystalline domains of germanium being present.

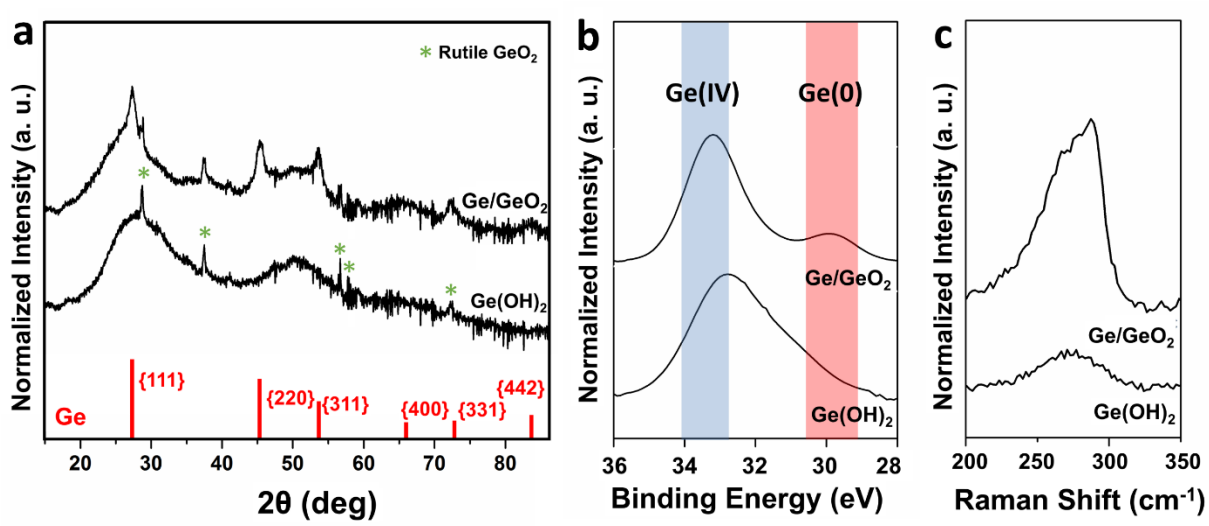

Figure 5-1. Characterization of 'Ge(OH)$_2$' before and after thermal processing at 400°C (for 1 h under Ar) (a) X-ray powder diffraction patterns. Standard reflections of crystalline Ge are provided.[135,159] Rutile GeO_2 reflections are indicated using a *. (b) XP spectra of the Ge 3d spectral region. (c) Raman spectra.

X-ray photoelectron spectroscopy data (Figure 5-1 b) are consistent with a disproportionation process occurring during thermal processing that sees the Ge in 'Ge(OH)$_2$' converted to Ge(0) and Ge(IV) in the GeNC/GeO_2.[248] The spectrum of unprocessed 'Ge(OH)$_2$' (Figure 5-1 b bottom trace) shows a broad emission in the Ge 3d region that is dominated by a Ge(II) emission. After thermal processing (Figure 5-1 b, top trace), two distinct emissions appear at 29 and 33 eV consistent with formation of Ge(0) and Ge(IV), respectively.[236]

Raman spectroscopy allows detection/identification of Ge-Ge bonds. In addition, the shape and position of the Ge-Ge feature provides insight into the size and crystallinity of GeNCs.[80,122,237] Asymmetric peaks at high frequencies featuring shoulders at low frequencies are routinely attributed more crystalline nanoparticles.[238] Raman analyses of 'Ge(OH)$_2$' and GeNC/GeO_2 (Figure 5-1 c) are consistent with amorphous Ge nuclei within the precursor

transforming to nanocrystalline Ge domains with thermal processing. The spectrum of '$Ge(OH)_2$' shows a symmetric optical phonon at *ca.* 280 cm^{-1} that we attribute to small, non-crystalline Ge nuclei while the same analysis of GeNC/GeO_2 shows an asymmetric feature at high frequencies (*ca.* > 290 cm^{-1}) with a shoulder consistent with Ge nanodomain crystallization.

FT-IR analyses provide some limited insight into the bonding within '$Ge(OH)_2$' and GeNC/GeO_2 (Figure 5-2). The spectrum of '$Ge(OH)_2$' shows broad O-H asymmetric/symmetric stretching bands in the range of 2900 to 3700 cm^{-1}, as well as a bending band at 1655 cm^{-1}. In addition, a feature at 755 cm^{-1} is attributed to Ge-O stretching. When comparing the spectra of GeNC/GeO_2 to that of '$Ge(OH)_2$' (Figure 5-2) we note the broad feature at 3400 cm^{-1} is dramatically diminished and the broad Ge-O absorbance at 755 cm^{-1} moves to higher energy (*i.e.*, 860 cm^{-1}) supporting the proposal that a Ge-O-Ge network formed.

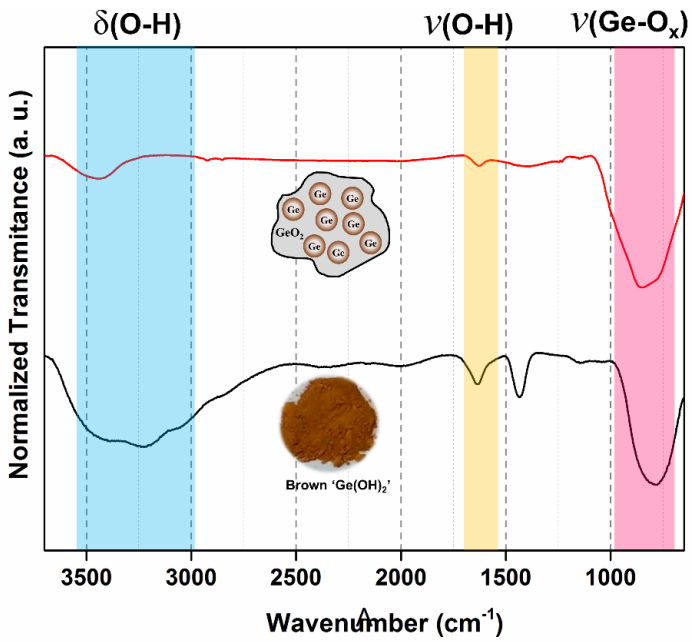

Figure 5-2. FT-IR spectra of '$Ge(OH)_2$' as made (black trace spectrum) and after thermal processing for 1 h in Ar

at 400 °C (red trace spectrum).

While there are numerous potential applications for GeNC/GeO_2 composites,[75–79] the focus of this Chapter lies in the preparation and tailoring surface chemistry of freestanding colloidal GeNCs. Selective removal of the GeO_2 matrix from the present GeNC/GeO_2 composite may be achieved using a variety of chemical etching protocols (*e.g.*, warm water,[122] basic solutions[249]). For the present study HF etching was used because this procedure is expected to yield H-GeNCs that possess surfaces amenable to hydrogermylation.[17] The FT-IR spectrum of the liberated GeNCs (Figure 5-3 a and Figure 5-4) show two sharp features at *ca.* 2000 and 750 cm^{-1} consistent with Ge-H stretching and bending. Of important note, there is negligible indication of surface oxide at the sensitivity of the FT-IR method. Additional characterization of the H-GeNCs was precluded by their limited solvent compatibility and air sensitivity.

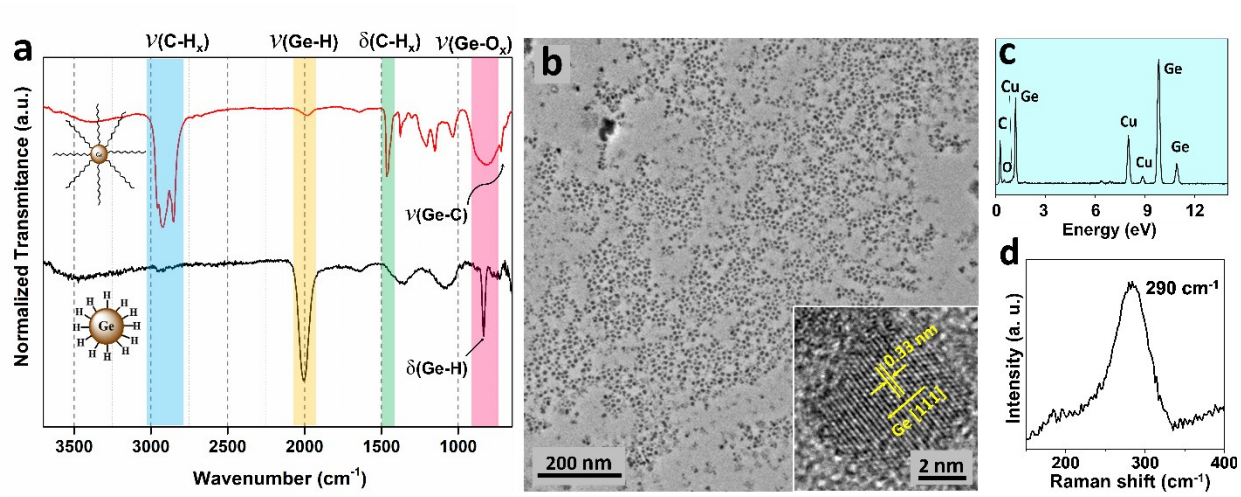

Figure 5-3. Characterization of GeNCs obtained from the thermal treatment of '$Ge(OH)_2$' at 400 °C for 1 h in a flowing Ar atmosphere. (a) FT-IR spectra of hydride-terminated (black trace) and dodecyl-GeNCs obtained from thermal hydrogermylation (red trace). (b) Bright-field TEM micrograph of dodecyl-GeNCs. (c) and (d) EDX and Raman spectra of dodecyl-GeNCs obtained from thermal hydrogermylation.

Three complementary hydrogermylation approaches (*i.e.*, thermally-activated, radical-initiated, and borane-catalyzed) were explored to achieve alkyl surface functionalization of H-GeNCs using 1-dodecene as a model substrate. For convenience the following discussion of alkyl-terminated GeNCs will focus upon those prepared using the thermally initiated reactions. FT-IR spectra of the resulting dodecyl-GeNCs are shown in Figure 5-3 a (thermally-activated) and Figure 5-4 (radical-initiated, borane-catalyzed). In all cases the intensity of the Ge-H diminishes dramatically and intense absorptions at *ca.* 2850 - 2650 and 1460 cm^{-1} appear; we confidently attribute these new features to C–H stretching and bending modes of surface bonded aliphatic chain.[242] Further evidence of alkyl moiety covalent surface attachment is provided by a Ge-C stretching absorption at 700 cm^{-1}.[243] Features at *ca.* 860 cm^{-1} are attributed to Ge-O stretching modes arising from oxidation that presumably occurs during workup following functionalization.

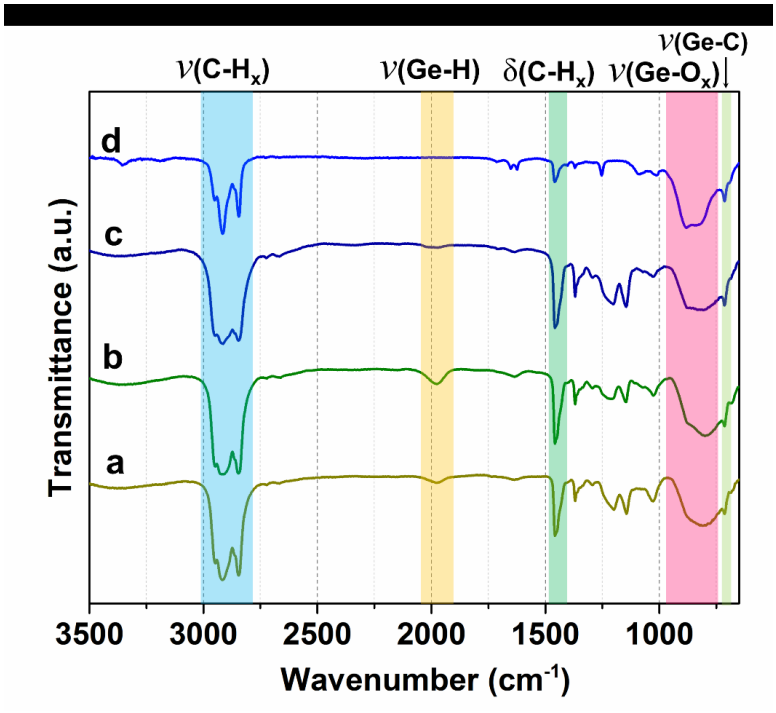

Figure 5-4. FT-IR spectra of dodecyl-GeNCs functionalized *via* different hydrogermylation protocols: a) thermally-activated, b) AIBN radical-initiated, c) BP radical-initiated and d) borane-catalyzed.

Figures 5-3 b and 5-5 show representative bright field transmission electron micrographs of dodecyl-GeNCs. The particles appear pseudospherical with an average diameter of 7.2 ± 0.9 nm. TEM analyses of dodecyl-functionalized GeNCs prepared using radical-initiated, and borane-catalyzed hydrogermylation approaches show similar morphology and size distributions (Figure 5-5). HRTEM imaging (Figure 5-3 b inset, and Figure 5-5) of dodecyl-GeNCs shows crystalline nano-domains with fringes separated by 0.33 nm that correspond to Ge (111) lattice spacing.[250]

Energy-dispersive X-ray analysis (EDX) (Figure 5-3 c) confirms the presence of germanium, carbon and oxygen. Raman spectra (Figure 5-3 d) show an asymmetric feature at

290 cm^{-1} indicating the crystallinity of the germanium nanodomains is maintained throughout the etching of GeNC/GeO_2 composites and functionalization.

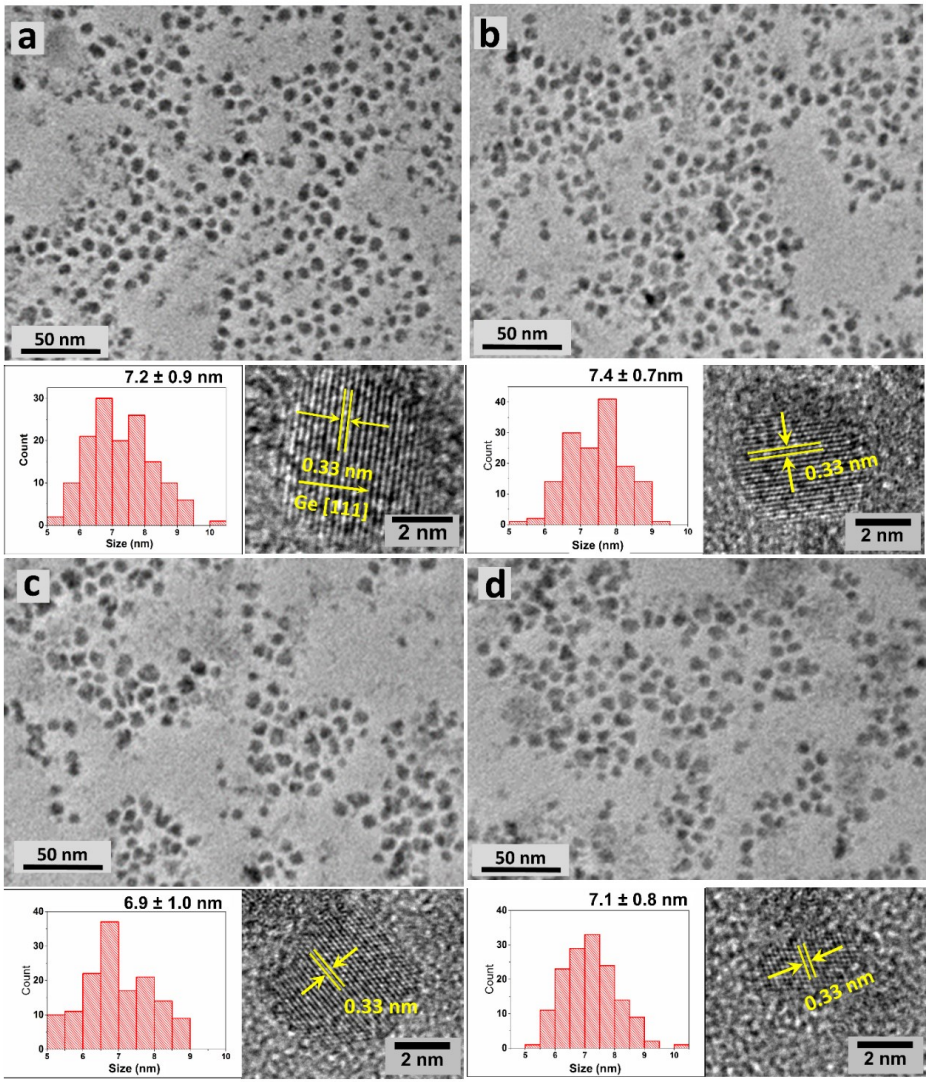

Figure 5-5. Dodecyl-GeNCs obtained from the thermal treatment of brown $Ge(OH)_2$. TEM images with related particles size distribution of dodecyl-GeNCs functionalized *via* different hydrogermylation protocols: a) thermally-activated, b) AIBN radical-initiated, c) BP radical-initiated and d) borane-catalyzed.

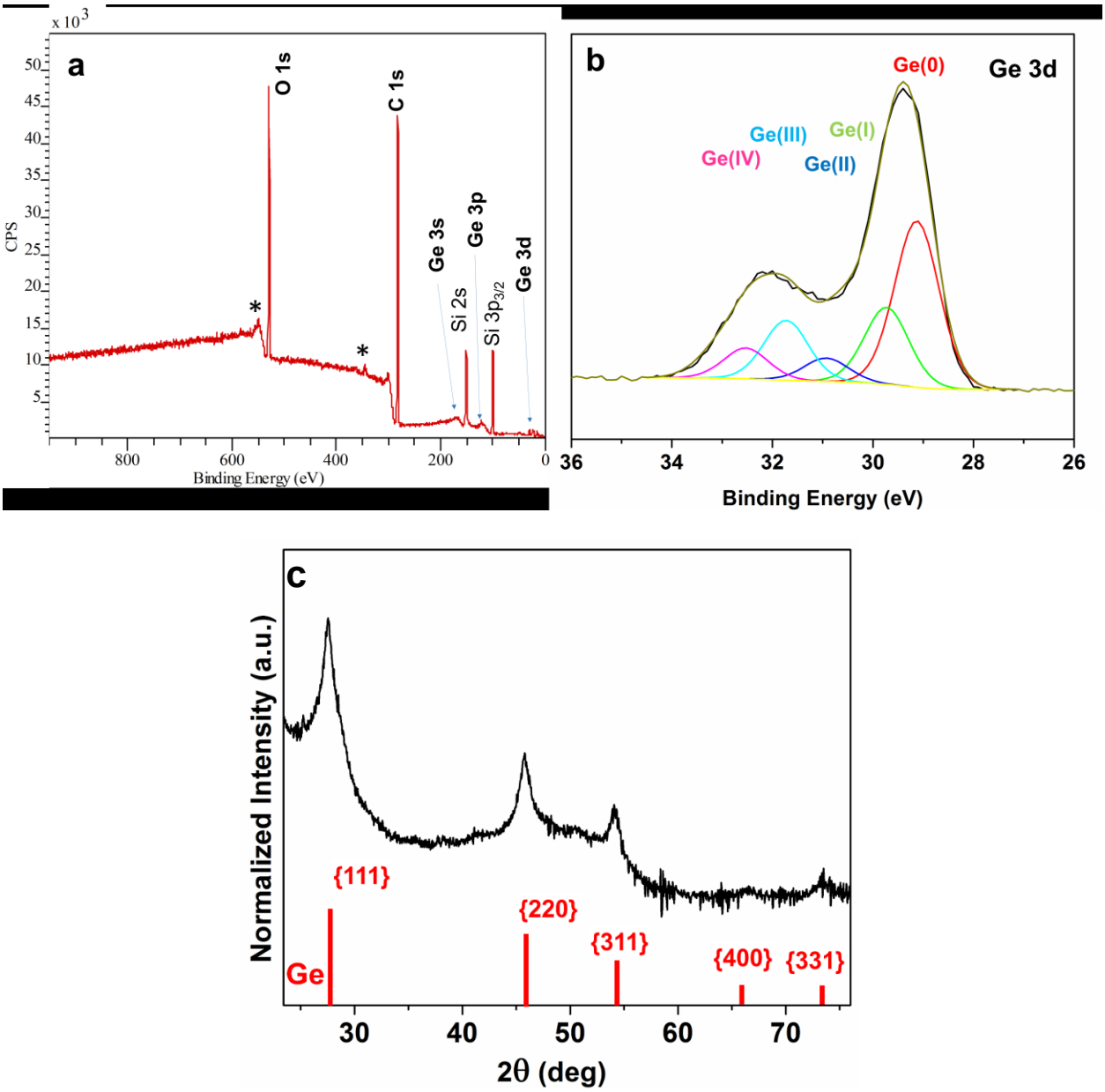

Figure 5-6. Characterization of GeNCs obtained from the thermal treatment of 'Ge(OH)$_2$' at 400 °C for 1 h in a flowing Ar atmosphere. (a) Survey XPS spectrum of dodecyl-GeNCs which is showing Ge, C and O as it is expected. Si signal is coming from silicon wafer used as sample holder. Signals noted by a '*' are related to Ge LMM. (b) Deconvolution of the HR-XP spectra for of Ge 3d spectral region (Figure S3b), shows dodecyl-GeNCs are dominated by elemental Ge along with some Ge(IV) species consistent with partial oxidation. This shows Ge $3d_{5/2}$ contributions. Contributions from Ge $3d_{3/2}$ have been omitted for clarity.

Moreover, dodecyl-functionalized GeNCs were characterized by XPS and XRD (Figure 5-6). Figure 5-6 a shows a representative survey XP spectrum of dodecyl-GeNCs, there are clear peaks corresponding to the binding energies of Ge $3d_{5/2}$, Ge $3p_{3/2}$, C 1s, and O 1s. The XRD pattern of dodecyl-GeNCs in Figure 5-6 b shows a broad reflection from nanocrystalline domains of germanium.

The presented analyses are consistent with surface hydrogermylation proceeding under all conditions explored here; however, investigation of analogous surface hydrosilylation reactions on silicon nanocrystals indicates the nature of surface bonded species and surface coverage are method dependent.[247] In this context, nanostructured-assisted laser desorption/ ionization mass spectroscopy (NALDI-MS) was employed to interrogate the monomeric or oligomeric nature of surface bonded species. To isolate the role of GeNCs NALDI analysis was also performed on product mixtures obtained from the identical reaction conditions used for surface modification - in the absence of GeNCs no high molecular weight fragments were detected (See Figure 5-7).

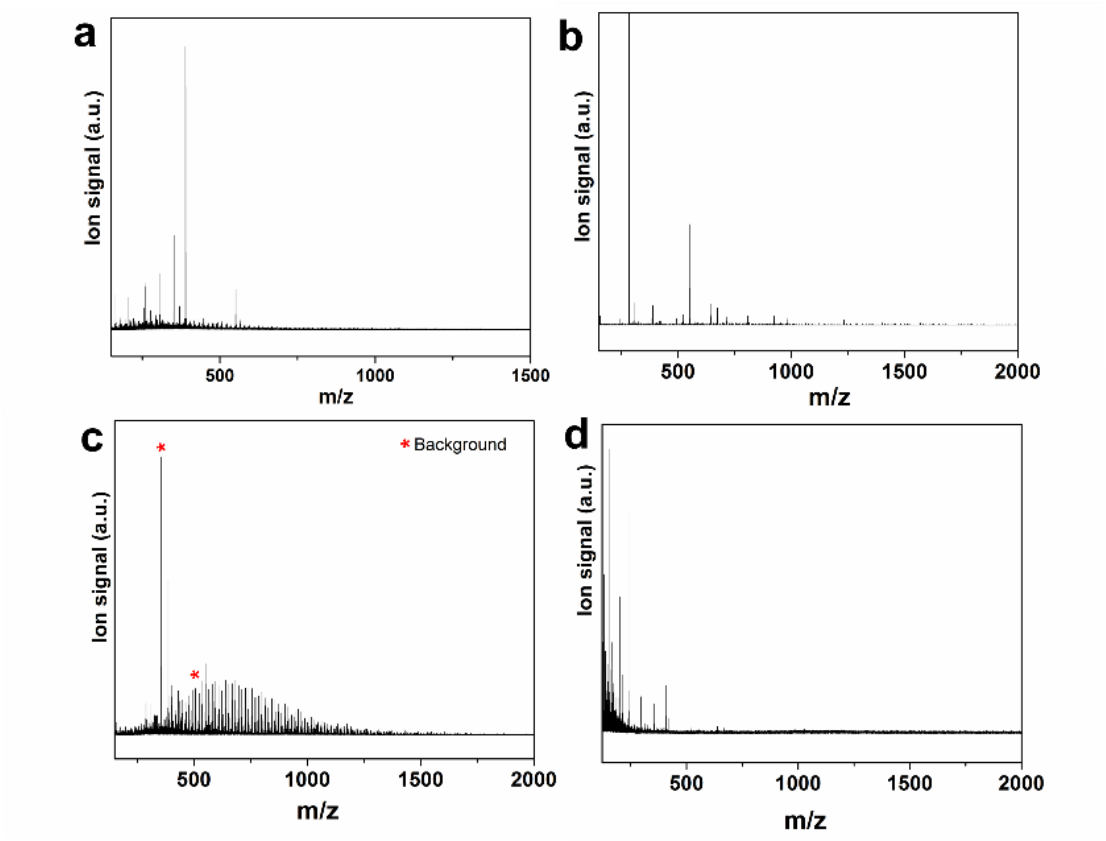

Figure 5-7. NALDI mass spectra of control dodecene solution (no GeNCs) after applying identical condition as a) thermally-activated b) AIBN radical-initiated, c) BP radical-initiated and d) borane-catalyzed hydrogermylation.

In all cases involving GeNCs no fragments corresponding to the molecular weight of 1-dodecene (M_W = 168.3) were detected at the sensitivity of the MS technique consistent with effective purification. The fragmentation patterns obtained for all dodecyl-GeNCs are complex regardless of the functionalization activation method employed (Figures 5-8 a-d). Despite this complexity, insight into the nature of the GeNC surface species can be obtained by considering peak series with mass labels of the same color; these series are separated by the mass of the dodecyl repeat unit (*i.e.*, 168.3 m/z). Similar patterns have been attributed to ligand oligomerization on NC surfaces.[24] Samples prepared using thermally activated hydrogermylation

(Figure 5-8 a) show fragments containing multiple dodecyl repeat units consistent with there being a higher amount of oligomerization occurring on the GeNC surfaces.

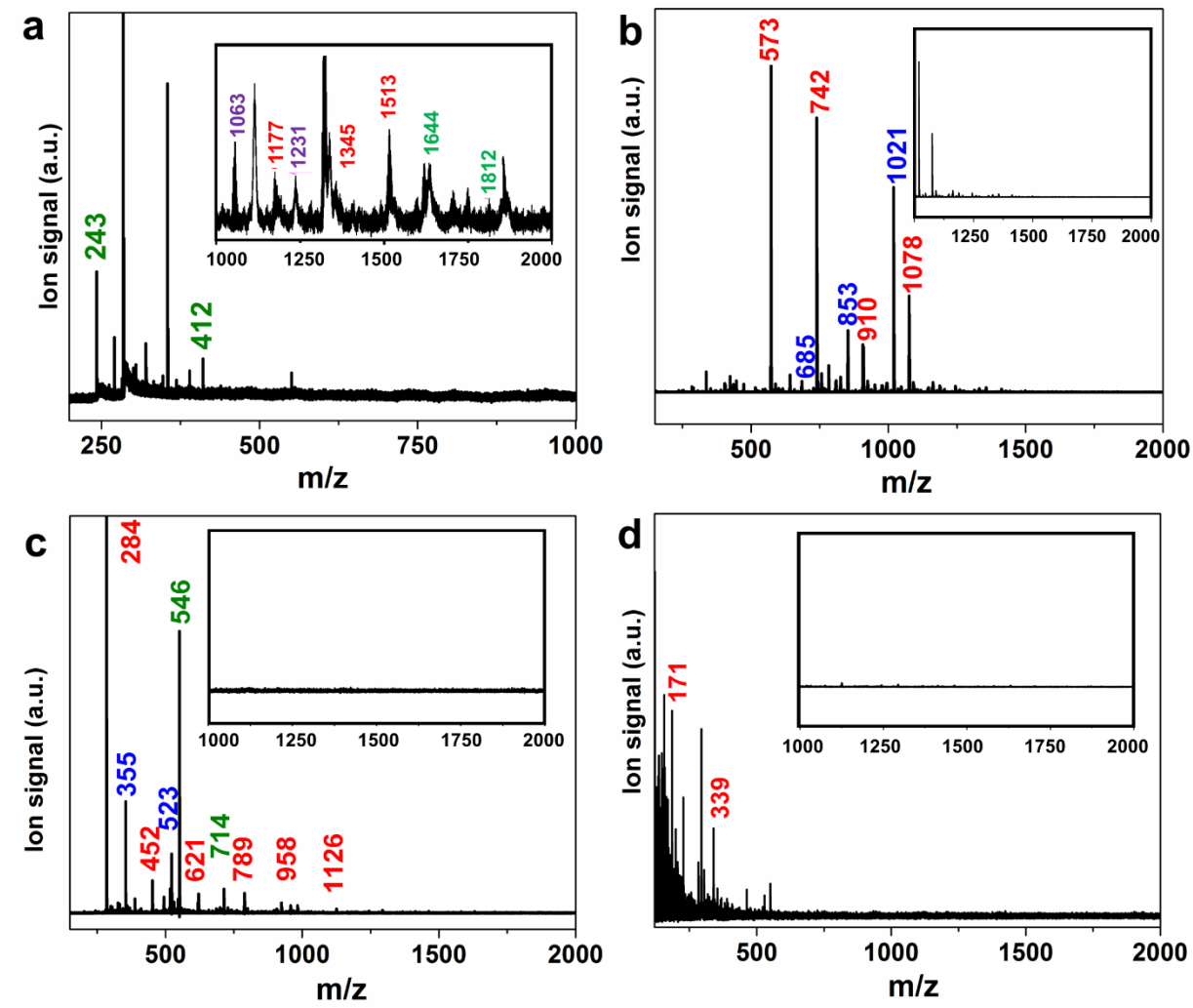

Figure 5-8. Nanoassisted laser desorption ionization mass spectra of dodecyl-GeNCs functionalized using a) thermally-activated (inset: higher m/z showing dodecene repeat units) b) AIBN and c) BP radical-initiated, d) borane-catalyzed hydrogermylation. Inset spectra are higher magnification from larger m/z.

In addition, we note high m/z fragments with the characteristic Ge isotopic signature. Because the Ge-Ge linkage is the weakest of the surface bonds (*i.e.*, Ge-Ge, 190-210; Ge-C, 255;

and C-C, 292-360 KJ·mol^{-1}),[251] it is reasonable it can cleave preferentially to produce high m/z fragments including differing numbers of germanium atoms (Figure 5-9).

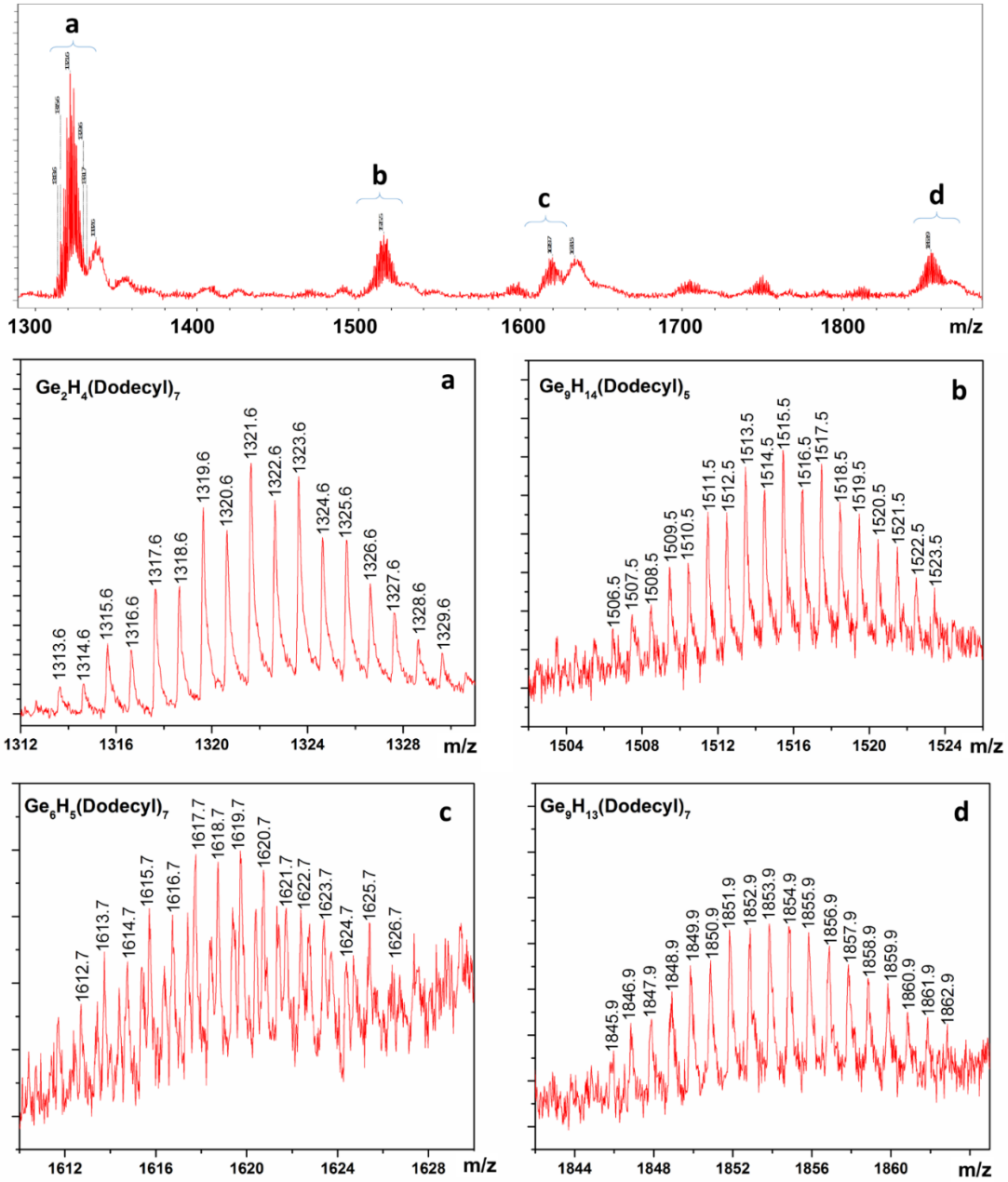

Figure 5-9. NALDI spectrum of dodecyl-GeNCs obtained from thermally-activated hydrogermylation showing the characteristic Ge isotopic pattern.

GeNCs modified using AIBN and BP initiated hydrogermylation (Figure 5-8 b and c) also show fragmentation patterns associated with multiple dodecyl repeat units, and borane catalyzed hydrogermylation (Figure 5-8 d) resulted in the comparatively low m/z (*i.e.*, not exceeding 500 m/z) suggesting limited (even negligible) oligomerization.

Proton nuclear magnetic resonance (^{1}H NMR) spectroscopy provides an alternative method for interrogating surface bonded moieties. Figure 5-10 shows ^{1}H NMR spectrum of dodecyl-GeNCs functionalized *via* thermally-activated hydrogermylation (See Figure 5-11 for ^{1}H NMR spectra of dodecyl-GeNCs obtained using other methods).

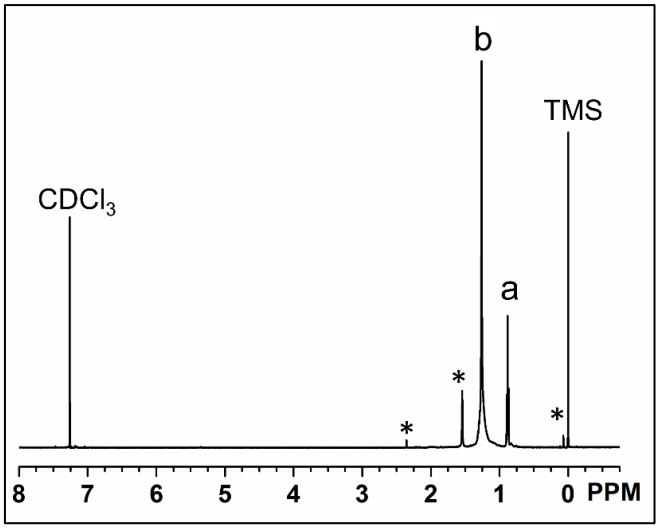

Figure 5-10. ^{1}H NMR spectrum of dodecyl-GeNCs obtained from thermally activated hydrogermylation in $CDCl_3$ containing 0.01% (v/v) TMS. Methyl and chain methylene protons denoted by a and b, respectively. Residual solvent impurities (H_2O or HOD at 1.5 ppm and toluene CH_3 at 2.34 ppm)[252,253] are denoted by (∗).

All dodecyl-GeNCs show the broad resonances arising from terminal methyl protons at *ca.* 0.9 ppm and a broad resonance methylene chain protons in the range of *ca.* 1.1−1.6 ppm. Broad structureless aliphatic CH signals indicative of multiple, surface bonded

environments.[242,254,255] In addition, no features associated with alkene protons are detected at the sensitivity of the ^{1}H NMR method consistent with 1-dodecyl moieties being tethered to the GeNC surfaces.[256]

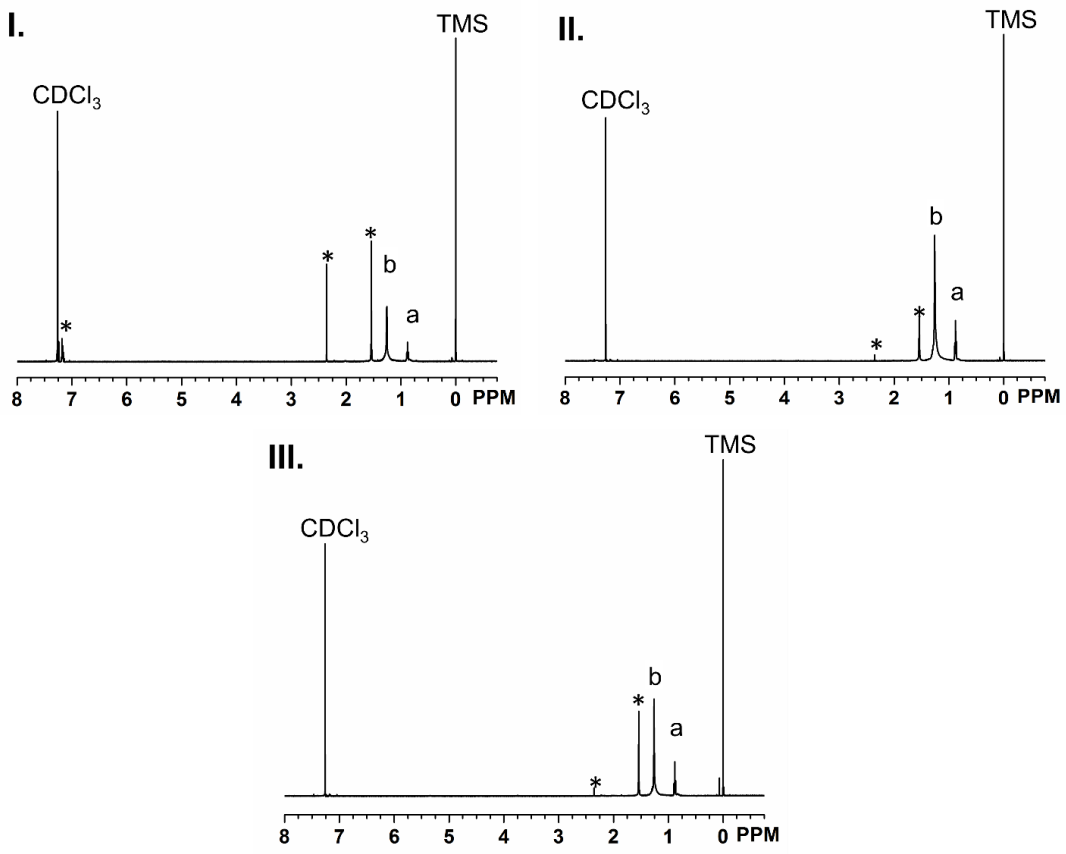

Figure 5-11. ^{1}H NMR spectra of dodecyl-GeNCs in $CDCl_3$ containing 0.01% (v/v) TMS. I) AIBN radical-initiated, II) BP radical-initiated and III) borane-catalyzed hydrogermylation. Dodecyl methyl protons and chain methylene protons denoted by a and b, respectively. Solvent impurities are denoted by an asterisk (∗)

For the present dodecyl-GeNCs, the integration ratios of the methylene (at 1.29) and methyl (at 0.9 ppm) proton signals were determined to be 6.72, 6.09, 6.53 and 6.86 for thermally induced, AIBN initiated, BP initiated and borane catalyzed hydrogermylation, respectively. These values are consistent with the expected surface dodecyl moiety or dodecyl oligomers.[255,257]

^{1}H NMR also offers a method to estimate NC surface coverage. Evaluating a ratio of the integrated peak areas of the surface organic groups and that of an internal standard (*i.e.*, TMS 0.01%) provides an approximation of ligand surface coverage.[255] The results from these calculations (Table 5-1) indicate that, among different hydrogermylation protocols applied here, thermally induced functionalization provide highest degree of surface coverage (207%). AIBN and BP radical initiate reactions, as well as those catalyzed by borane provide lower surface coverage (*i.e.*, 62, 84, and 56 %, respectively).[242,255] These data are consistent with the NALDI-MS analyses noted above that indicated the likelihood of surface oligomerization decreased in the order of thermally activated, radical initiation, and borane catalyzed hydrogermylation (*i.e.*, a higher degree of surface oligomerization will lead to artificially high surface coverage).

Table 5-1. Determination of surface coverage using ^{1}H NMR.

Hydrogermylation Approach	*Ligand methyl to TMS Proton ratio*	*Ligand to TMS mole ratio*	*Moles of ligand*	*Moles of Ge atoms*	*Number of ligands per NC**	*Surface coverage (%)*
***Thermally** activated*	2.11	8.42	6.15×10^{-6}	1.49×10^{-5}	3085	207
***AIBN** radical init.*	0.69	2.74	2.01×10^{-6}	1.60×10^{-5}	930	62
***BP** radical init.*	1.29	5.18	3.78×10^{-6}	2.23×10^{-5}	1261	84
***Borane** catalyst*	0.73	2.94	2.14×10^{-6}	1.91×10^{-5}	838	56

* Number of Ge atoms per GeNCs (d=7 nm) has been estimated to be 7400 with *ca.* 20% on the surface.

Having prepared dodecyl-GeNCs from the thermal processing of '$Ge(OH)_2$', we endeavoured to investigate their optical response (*i.e.,* PL). As a result of the small band-gap of Ge, electron-hole recombination in GeNCs is expected to yield PL in the NIR or IR spectral regions. However, reports are often contradictory regarding the source of PL, critical NC size,

expected PL wavelength, quantum yield, effect of oxides and other impurities.[18,89,121,122,130] Adding further complexity, germanium oxides can often show visible PL.[70,135] There are also numerous examples showing UV-Vis emitting GeNCs,[67,70,109] however it has been suggested that these emitters likely show PL resulting from surface species (*e.g.*, oxides) rather than quantum confinement of GeNCs.[136–138] There are surprisingly few examples of colloidal GeNCs showing NIR or IR PL.[18,130,136]

Despite the average size of the functionalized GeNCs investigated here being smaller than the Bohr-exciton radius of Ge (*i.e.*, 24.3),[67,70] they do not show detectable photoluminescence (PL). We hypothesize this may result from dark surface defects (*e.g.*, impurities, vacancies, surface oxides, dangling bonds *etc.*)[258] arising from the HF liberation protocol that remain after hydrogermylation, that provide non-radiative pathways.[130,141,142]

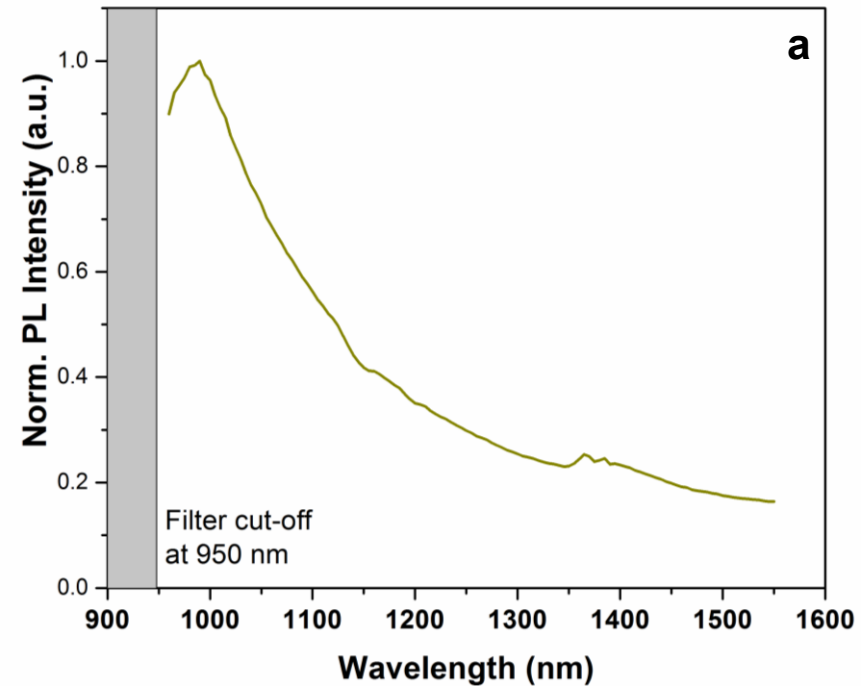

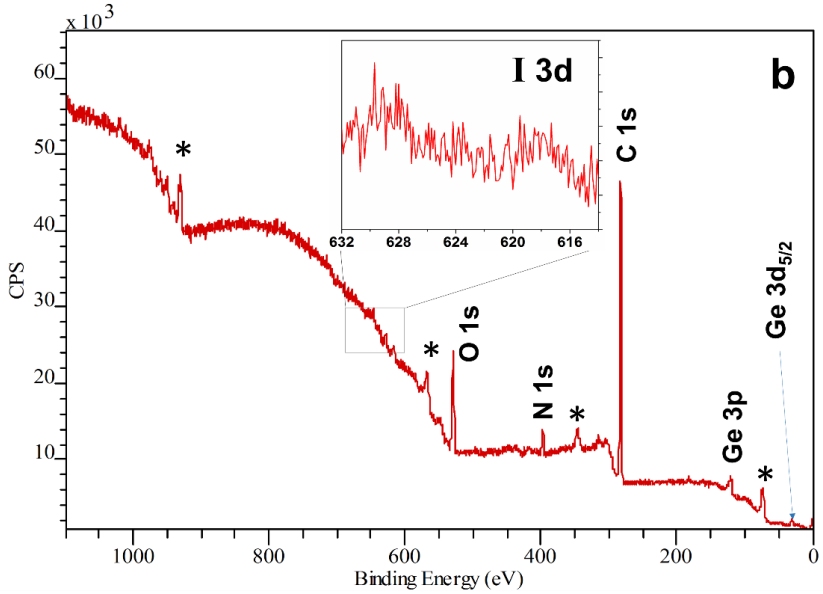

Figure 5-12. (**a**) Photoluminescence spectrum of dodecyl-GeNCs (diameter = 7.2 ± 0.9 nm) prepared in the presence of trace I_2 using thermal functionalization. (**b**) Survey XP spectrum of dodecyl-GeNCs after introducing trace amount of I_2 prior to thermal functionalization. Signals of Ge, C and O were observed as they were expected. The signals which are assigned by a '*' are related to sample holder and copper sample substrate.

In an effort to passivate potential (as of yet unidentified) defects on the GeNC surfaces we introduced a trace quantity of I_2 into the hydrogermylation reaction mixture. GeNCs prepared in this way show PL at 986 nm (See Figure 5-12 a). Survey XP spectra of the resulting dodecyl-GeNCs (Figure 5-12 b) show evidence of only Ge, C and O: no iodine was detected at the sensitivity of the XPS method (ca. 1 – 3 atomic %). At this time, the role of I_2 in inducing PL remains unclear and is the subject of ongoing investigation.

In summary, '$Ge(OH)_2$' was synthesized using a commercial GeO_2 powder and employed as a precursor for H-GeNCs. This procedure exploits a disproportionation reaction to yield GeNCs embedded in a GeO_2 matrix that are readily liberated with hydride surface moieties by HF etching. The resulting H-GeNCs provide a reactive platform that can be further modified using thermal, radical initiated and borane-catalyzed hydrogermylation. NALDI-MS and ^1H

NMR analysis indicated oligomerization and surface coverage occurring by thermally induced method compared to other hydrogermylation procedures. Dodecyl-terminated GeNCs prepared by proper defect removing approach (*i.e.,* introducing I_2), possess optical response in IR region.

Chapter 6:

Cellular Uptake and Cytotoxicity of Photoluminescent Fe_3O_4 Nanoparticle/Si Nanocrystal Hybrids*

* A version of this Chapter has been published:

Javadi, M.; Purkait, T.; Hadidi, L.; Washington, J.; Veinot, J. G. C. *MRS Adv.* **2016**, *1* (33), 2321–2329.

6.1. Introduction

Multi-functional nanomaterials combine various functional groups with potential applications beyond the limitations arising from each individual subunits.[259,260] The design of new hybrid nanomaterials with enhanced functionality and the broad options of applications, can be achieved by combining complementary properties such as light emission and magnetism.[54,261–267] For example, combining a florescent cell-imaging agent label with the property of magnetism would have promising applications in the detection and separation of targeted cell populations as well as medical therapeutic.[262,264,268]

A number of papers have reported the combination of fluorescent molecular dyes with magnetic particles (predominantly iron and its oxides) for the purposes of cell-imaging.[264,269] however, molecular dyes suffer from the combined drawbacks of reduced quantum yield and limited photo-stability particularly at near-infrared (NIR) wavelengths.[55,56,261] Introducing quantum-dots (QDs) as new fluorescent probe was a revolutionary advance in the field of biological imaging.[270,271] QDs overcame and surpassed the aforementioned limitations of organic dyes, by showing size-dependent multiple colours, higher molar absorption coefficient in the NIR region, long-term photo-stability, narrower and symmetric emission bands, and have the capacity to be functionalized with various groups.[54–56]

QD-based magnetofluorescent probes have been made by linking classical QDs (*e.g.,* CdSe) with magnetic NPs using various approaches like high temperature decomposition,[272] doping,[273] crosslinking,[274] encapsulation,[275] nanocomposites[276] and the formation of super-NPs.[277] Bawendi *et al.* prepared super-NPs by co-assembling of Fe_3O_4 NPs 'core' with a 'shell' of fluorescent CdSe@CdS QDs. They also added an exterior silica layer to induce stability of

assemblies, biocompatibility, and surface functionality.[277] The authors used these super-NPs as a dual-mode imaging probe for *in vivo* imaging.[277] Despite these important advances, real world applications involving biological/medical systems for the most well-known QDs (*i.e.,* CdSe) are limited because they contain toxic heavy metals.[51]

The nanostructure of Group 14 semiconductors (*i.e.,* Si, Ge and Si_xGe_{1-x}) have been surprisingly observed to exhibit photoluminescence (PL).[66,67] This observation led to introduction of SiNCs as a new class of QDs which distinguished themselves by their abundance and low toxicity, particularly in compared to classical QD materials (such as CdSe).[51] SiNCs have 10-times less toxicity than the equivalent concentration of Cd based QDs, both *in vitro* and *in vivo*.[278] They have the additional advantage of naturally degrading to silicic acid which is easily excreted.[279] Moreover, the biocompatibility of SiNCs as well as their tunable surface chemistry and optical property (PL response), make them particularly attractive for biological applications.[279,280]

Si-based magnetofluorescent labels have not been investigated for biological imaging purposes as much as other QDs counterparts (*e.g.,* CdSe). However, some examples in literature include, Swihart *et al.* who have developed hydrophobic Si NP nano-probes that are mixed with hydrophobic Fe_3O_4 NPs and encapsulated in phospholipid-polyethyleneglycol micelles.[267] These hydrophilic micelles have a hydrophobic core of NPs and were used for *in vitro* and *in vivo* bio-imaging.[267] In another study, Sailor *et al.* fabricated luminescent microparticles made of porous-Si and loaded with Fe_3O_4 NPs and the anti-cancer drug doxorubicin, in order to target-deliver the drug to human cervical cancer cells *in vitro*.[31] However, there are some concerns with this therapeutic formulation due to bio-incompatibility and toxicity of hydrophobic Fe_3O_4 NPs.[281,282]

In this study we have attempted to combine the optical properties (*i.e.,* visible photoluminescence) of SiNCs with the magnetic response of hydrophilic Fe_3O_4 NPs by covalently linking these materials. Herein, a water-dispersible magnetic-photoluminescent hybrid material has been synthesized *via* the DCC coupling reaction of acid-functionalized SiNCs and hydrophilic amine terminated magnetite (Fe_3O_4) NPs. Moreover, its cytotoxicity and application as a cell-labeling agent have been studied and demonstrated using the rat basophilic leukemia (RBL)-2H3 cell line. RBL-2H3 cells are mast cell-like immune cells and are a commonly used cell model for examination of immune system responses to foreign agents, such as allergens and other contaminants, including NPs.[283–287] Mast cells are located at the interface between the internal and external environments in the mucosal linings of the respiratory and gastrointestinal tracts, in blood vessels and in skin, where they monitor for potential non-self antigens to target and remove. The primary immune function of mast cells is degranulation, a receptor-mediated effector response in which vesicle-stored antimicrobial and inflammatory granules (e.g. histamine) are released in an attempt to destroy foreign antigens.[288] RBL-2H3 cells can also internalize particles using various uptake mechanisms such as phagocytosis.[289] Therefore, since mast cells are early detectors of foreign particles and are likely to encounter infiltrated and circulating NPs, they are ideal cell candidates for determining biocompatibility of novel nanoparticles.

6.2. Experimental

6.2.1. Reagents and Materials.

Hydrogen silsesquioxane (HSQ, trade name Fox-17, sold commercially as a solution in methyl isobutyl ketone) was obtained from Dow Corning Corp. (Midland, MI). Electronics grade

hydrofluoric acid (HF, 49% aqueous solution) was purchased from J. T. Baker. Ferrous chloride tetrahydrate ($FeCl_2 \cdot 4H_2O$ > 99 %), ammonium hydroxide (*i.e.*, 29.3 wt % NH_3 in water), 10-undecenoic acid (98 %), 2,2′-azobis(2-methylpropionitrile) (AIBN, 98 %), (3-aminopropyl) trimethoxysilane (APTMS, 97 %), N,N′-dicyclohexylcarbodiimide (DCC, 99 %), as well as reagent grade of acetone, toluene, ethanol and methanol were purchased from Sigma-Aldrich. Toluene was dried using a Grubbs-type solvent purification system (Innovative Technologies, Inc.) prior to use. Ultrapure H_2O (18.2 MΩ/ cm) was obtained from a Barnstead Nanopure Diamond purification system and used in all reactions/manipulations involving water. Unless otherwise indicated all reagents and solvents were used as received.

6.2.2. Material Characterization and Instrumentation.

Fourier-Transform Infrared Spectroscopy (FT-IR) was performed on a Nicolet Magna 750 IR spectrophotometer by drop casting of a solution/suspension containing desired particles in ethanol (SiNCs) or water (Fe_3O_4 NPs and Si-amide-Fe_3O_4 nano-hybrids) and complete removal of the solvent. Transmission electron microscopy (TEM) and energy dispersive X-ray (EDX) analyses were performed using a JEOL-2010 (LaB6 filament) electron microscope with an accelerating voltage of 200 kV. High resolution TEM (HRTEM) imaging was performed on JEOL-2200FS TEM instrument with an accelerating voltage of 200 kV. TEM samples were prepared by drop-coating of NPs included ethanol dispersion on a holey carbon coated copper grid and the solvent was removed under vacuum. TEM and HRTEM images were processed using ImageJ software (version 1.48 v). Size distribution histograms were determined by measuring *ca.* 300 NPs in each case. Raman spectroscopy was performed using a Renishaw in*Via* Raman microscope equipped with a 514 nm diode laser and a power of 3.98 mW on the

sample. Samples were prepared by drop casting of an ethanol or water suspension on gold-coated glass. X-ray photoelectron spectra were acquired in energy spectrum mode at 210 W, using a Kratos Axis Ultra X-ray photoelectron spectrometer. X-Ray source was Al Kα line. Energy is 1486.6 eV. The probing area is about 1 x 2 mm^2. Samples were prepared as films drop-cast from ethanol/water suspensions onto a copper foil substrate. Binding energies were calibrated using the C 1s peak as a reference (284.8 eV). CasaXPS Version 2.3.5 software was used for Shirley background subtraction and curve fitting. Photoluminescence (PL) spectra for the solution phase samples were acquired using a Varian Cary Eclipse fluorescence spectrometer (λ_{ex} = 350 nm). PL spectra were acquired by illuminating a solution/suspension containing desired particles in ethanol (SiNCs) or water (Fe_3O_4 NPs and Si-amide-Fe_3O_4 nano-hybrids).

6.2.3. Synthesis of Water Dispersible APTMS-capped Fe_3O_4 NPs.

In a typical synthesis, $FeCl_2 \cdot 4H_2O$ (0.62 g; 3.2 mmol) was dissolved in 3.9 ml of ultrapure water to give a clear orange solution. Concentrated aqueous ammonium hydroxide (3.12 ml) was added dropwise with vigorous stirring. The addition of ammonium hydroxide caused the colour of the solution to change from orange to dark blue/green. After vigorous stirring in air for 10 minutes APTMS (1.25 ml, 7.2 mmol) was added dropwise. The reaction mixture was transferred to a 10 ml microwave vessel equipped with a microwave-safe stir bar and sealed. The mixture was irradiated for 1 hour at 134 °C in a *Biotage Initiator* microwave reactor (at *ca.* 100 W and the pressure of *ca.* 7 bar). After cooling to room temperature the reaction vessel was opened and the black suspension of APTMS-capped Fe_3O_4 NPs were transferred to a PTFE centrifuge tube and the tube was filled with *ca.* 45 ml ultrapure water. After centrifuging at 10000 rpm for 15 minutes the clear supernatant was discarded and the black precipitate was re-dispersed in water

and centrifuged (10000 rpm, 15 minutes). Dispersion/separation cycles were repeated for more times twice using water and twice using ethanol. Finally, the black precipitate containing purified APTMS-capped Fe_3O_4 NPs was dispersed in *ca.* 10 mL of water and stored in vial for further analysis using XPS, TEM, EDX, and FTIR. A typical yield of is *ca.* 0.06 g.

6.2.4. Preparation of Hydride-Terminated SiNCs.

Hydride-terminated SiNCs (H-SiNCs) were prepared using well-established procedures developed in the Veinot laboratory.[119] Approximately 3 g of solid HSQ were placed in a zirconia boat, transferred to a Carbolite CTF tube furnace, and heated in a flowing 5 % H_2 / 95 % Ar atmosphere (*ca.* 15 mL/min) at 18 ºC/min to a peak temperature of 1200 ºC where it was maintained for 1 hr. After cooling to room temperature the resulting composite, consisting of oxide-embedded SiNCs, was mechanically ground to a fine powder using an agate mortar and pestle. Subsequently, 0.30 g of the composite powder was transferred to a polyethylene terephthalate beaker and 3 mL each of water, ethanol, and 49 % HF acid were added sequentially with stirring. (Caution: Appropriate safeguards must be implemented when working with hydrofluoric acid.) After stirring for 1 h in ambient light and atmosphere hydrophobic H-SiNCs were extracted into three 15 mL aliquots of toluene. The resulting toluene suspensions were centrifuged at 3000 rpm for 5 minutes to obtain a pellet of H-SiNCs that was re-dispersed in dry toluene and used directly in the functionalization procedure described below. Typical is *ca.* 30 mg.

6.2.5. Preparation of Undecanoic-Acid Functionalized SiNCs.

Undecanoic acid-terminated SiNCs were prepared using established procedures for radical initiated surface hydrosilylation.[242] A 100 ml Schlenk flask was charged with 10-undecenoic acid

(200 mg, 1.1 mmol) equipped with a Teflon-coated magnetic stir bar. The flask was attached to an argon charged double manifold and heated to 70 °C under reduced pressure (*ca.* 2 mbar) for 3 h. After cooling to room temperature a toluene dispersion of H-SiNCs (*ca.* 25 mg SiNCs in 20 mL dry toluene) and AIBN (0.061 mmol) were added to the flask and the mixture was subjected to three freeze-pump-thaw cycles. The cloudy reaction mixture was stirred and heated to, and maintained at 65 °C under an argon atmosphere for at least 15 h. After cooling to room temperature the resulting functionalized particles were isolated by centrifugation (3000 rpm, 10 minutes) and purified by three successive cycles of dispersion/precipitation cycles using methanol/toluene as the solvent/antisolvent mixture. Acid-functionalized SiNCs were dispersible in common polar solvents (*e.g.*, methanol). The resulting products were evaluated using TEM, EDX, XPS, Raman, PL and FT-IR. Typical yield is *ca.* 30 mg.

6.2.6. DCC Coupling of Undecanoic Acid-terminated SiNCs with APTMS-capped Fe_3O_4 NPs.

In a 20 mL glass vial equipped with magnetic stir bar, 100 µL of dicyclohexylcarbodiimide (DCC) in acetone (0.1 M) was mixed with 10 mL of 10-undecenoic acid-functionalized SiNCs in acetone (2 mg/mL). After capping the vial, the solution was stirred for *ca.* 20 minutes followed by sonication (*ca.* 30 s) in a bath sonicator. The magnetic stir bar was removed and 200 µL of APTMS-capped Fe_3O_4 NPs in acetone (20 mg/mL) was added. After capping the vial, it was placed on a vial platform of Orbital Mechanical Shaker at 300 rpm for at least 12 h. The final coupled hybrid NPs were isolated upon exposure to a permanent magnet for at least 30 minutes. The supernatant was removed and the magnetic residue was re-dispersed in acetone (*ca.* 10 mL) and sonicated for minimum 60 s. The magnetic separation cycles were repeated at least four

more times. After magnetic residue was re-dispersed in water (*ca.* 10 mL) and sonicated for minimum 60 s. The magnetic separation cycles were repeated two times for water. Purified coupled magnetic Si-amide-Fe_3O_4 NPs were dispersed in water and stored in vial for further characterization.

6.2.7. Biocompatibility of Si-amide-Fe_3O_4 NPs.

The *in vitro* biocompatibility of Si-amide-Fe_3O_4 NPs was tested using the rat basophilic mast (RBL-2H3) cell line to evaluate the potential for NP cell uptake and effects on cell viability. RBL-2H3 cells were grown to confluence at 37 °C with 5% CO_2 in culture media consisting of Minimal Essential Medium (MEM) with Earle's balanced salt solution (Sigma-Aldrich, Canada) supplemented with 1 % 2 mM L-glutamine, 1% penicillin/streptomycin, and 10 % heat-inactivated FBS as previously described.[290] Cells were passed every third day by harvesting cells in an RBL-2H3 harvest buffer (1.5 mM EDTA, 135 mM NaCl, 20 mM HEPES, 5 mM KCl, pH 7.4) at 37 ºC with 5 % CO_2 for 10 minutes, followed by pipetting to detach cells from cell culture plate (BD Biosciences, Mississauga, Canada). Cells were seeded into new flasks at a sub-cultivation ratio of 1:10.

6.2.8. Effects of Si-amide-Fe_3O_4 NPs on cell viability.

The Annexin V/PI apoptosis assay was used to measure the effects of Si-amide-Fe_3O_4 NPs on cell viability. Annexin V-FITC binds to damaged membranes undergoing early to late apoptosis, while the fluorescent molecule, propridium iodide (PI) penetrates damaged plasma membranes of necrotic and/or late apoptotic cell and intercalates with nucleic acids to enhance its fluorescence. Thus, the balance of fluorescence between Annex V-FITC and PI provides a quantitative measure of cells that are i) viable, ii) early apoptotic, iii) late apoptotic and iv)

necrotic. Cells were grown to confluence over 3 days in RBL-2H3 cell culture media and then harvested as above and enumerated with Trypan Blue staining solution (Sigma Aldrich, Canada) on a haemocytometer to ensure cell cultures had >95% viable cells and to determine cell concentration. Following enumeration, cells were re-suspended in fresh culture media and seeded in 24-well flat-bottom culture plates (Corning Costar, USA) at 2.5 x 10^5 cells per well. Cells were then incubated for 1 h at 37°C to allow for cell attachment to wells. RBL cells were then exposed to Si-amide-Fe_3O_4 NPs at 0, 0.1, 1, 10 and 100 µg/mL for 1 h or 24 h. Vehicle (equivalent H_2O volume), positive (1 % ethanol) and negative (culture media) control treatments were also included.

Following exposure, cell culture media with NPs was removed from wells and cells were washed twice with 1X phosphate buffered saline (PBS; 2.7 mM KCl, 1.5 mM KH_2PO_4, 136.9 mM 148 NaCl, 15.2 mM Na2HPO4; pH 7.0), harvested as above, and transferred to 5 mL polystyrene tubes (Corning Science, Canada) containing 3 mL of PBS supplemented with 0.5 % fetal bovine serum (FBS) (Sigma, Canada) (herein known as PBS-FBS). Cells were centrifuged at 400 x *g* for 7 minutes to pellet cells. The supernatant was decanted and the cell pellet gently disrupted and resuspended in 1 mL of 1x Annexin V binding buffer (BD Biosciences, Canada). Cells were then centrifuged at 400 x *g* for 7 minutes, followed by decanting supernatant and gently disrupting cell pellet. 5 µL of Annexin V-FITC and 4 µL of 1:10 diluted PI (2 µg/mL) were added to each tube and incubated at room temperature in the dark for 15 minutes. Following incubation, an additional 500 µL of Annexin V binding buffer was added to each tube and were centrifuged at 400 x *g* for 7 minutes to wash cells. The supernatant was decanted and cells were resuspended in 500 µL of Annexin V binding buffer and analyzed by flow cytometry

for indications of cell death by monitoring for increases in Annexin V-FITC and PI fluorescence, and for changes in cell profile outputs, relative to unexposed controls.

6.2.9. Uptake of Si-amide-Fe_3O_4 NPs into RBL-2H3 cells.

Confocal microscopy was used to monitor cells for uptake of Si-amide-Fe_3O_4 NPs into cells. Glass slide coverslips (Fisher Scientific) were sterilized with 70 % ethanol, washed with sterile H_2O, UV irradiated and placed into the bottom of 6 well flat-bottom plates (Corning Costar, USA). Cells were seeded overtop of the cover slips, at a density of 1.0 x 10^5 cells in MEM culture media, and incubated for 2 days at 37 °C. Following two days of growth, culture media was removed, cover slips containing adhered cells were washed twice in PBS and then cells exposed for 1 h to Si-amide-Fe_3O_4 NPs suspended in PBS at concentrations of 0, 100, 200, 500, 1000 and 2000 µg/mL. Negative control cells received an equal volume of PBS alone. After exposure, cells were washed twice with PBS-FBS and once with PBS and coverslips were removed from wells and inverted on parafilm containing 1 µg/µL Cholera Toxin B Subunit-FITC GM1 membrane stain (Sigma) and incubated for 20 minutes over ice in the dark. Coverslips were then washed twice with PBS-FBS and fixed at room temperature in the dark with 4% paraformaldehyde, followed by washing with PBS and mounted on glass slides using mounting medium containing DAPI, as a nuclear stain. Fixed cells were imaged with a Zeiss LSCM, LSM 710 AxioObserver Laser Scanning Confocal Microscope (objective 40x 1.3 oil plan-Apochromat, Carl Zeiss Microscopy, Jena, Germany), data collected with Zen 2011 software and processed with LSM Image Browser (v. 4.2.0.121, Carl Zeiss). Three-dimensional z-stack images were surface rendered and then animated using Imaris software (v. 8.1, Bitplane, Zurich, Switzerland) to visualize intracellular uptake of NPs.

6.2.10. Statistical Analysis.

Statistical analyses were performed using the GraphPad 6.0 statistical software program. To investigate effects of NPs on cell viability a one-way analysis of variance (ANOVA) with a pairwise Tukey multiple comparison test was performed for comparisons between treatment groups within a cell death category (*i.e.,* viable, early apoptosis, late apoptosis or necrosis). A probability of $p < 0.05$ was considered significant. Data values are presented as mean ± standard error on the mean (SEM).

6.3. Results and Discussion

Prevailing methods for preparing monodispersed Fe_3O_4 NPs are based on the thermal decomposition of iron precursors in the presence of different surfactants and capping agents such as oleic acid and oleylamine.[291–294] Although these approaches yield a narrow size distribution of magnetite NPs, the bio-incompatibility, toxicity and hydrophobicity of the final Fe_3O_4 particles limit their use for biological imaging and other biomedical purposes.[281,295]

We have chosen to employ an alternative approach involving the microwave assisted *in-situ* hydrothermal synthesis and functionalization of Fe_3O_4 NPs in the presence of excess capping agent (*e.g.,* APTMS).[263,265,281,295–298] The resulting APTMS-capped magnetite NPs form a uniform suspension in water that can be attracted to an external magnetic field (Figure 6-1 a).

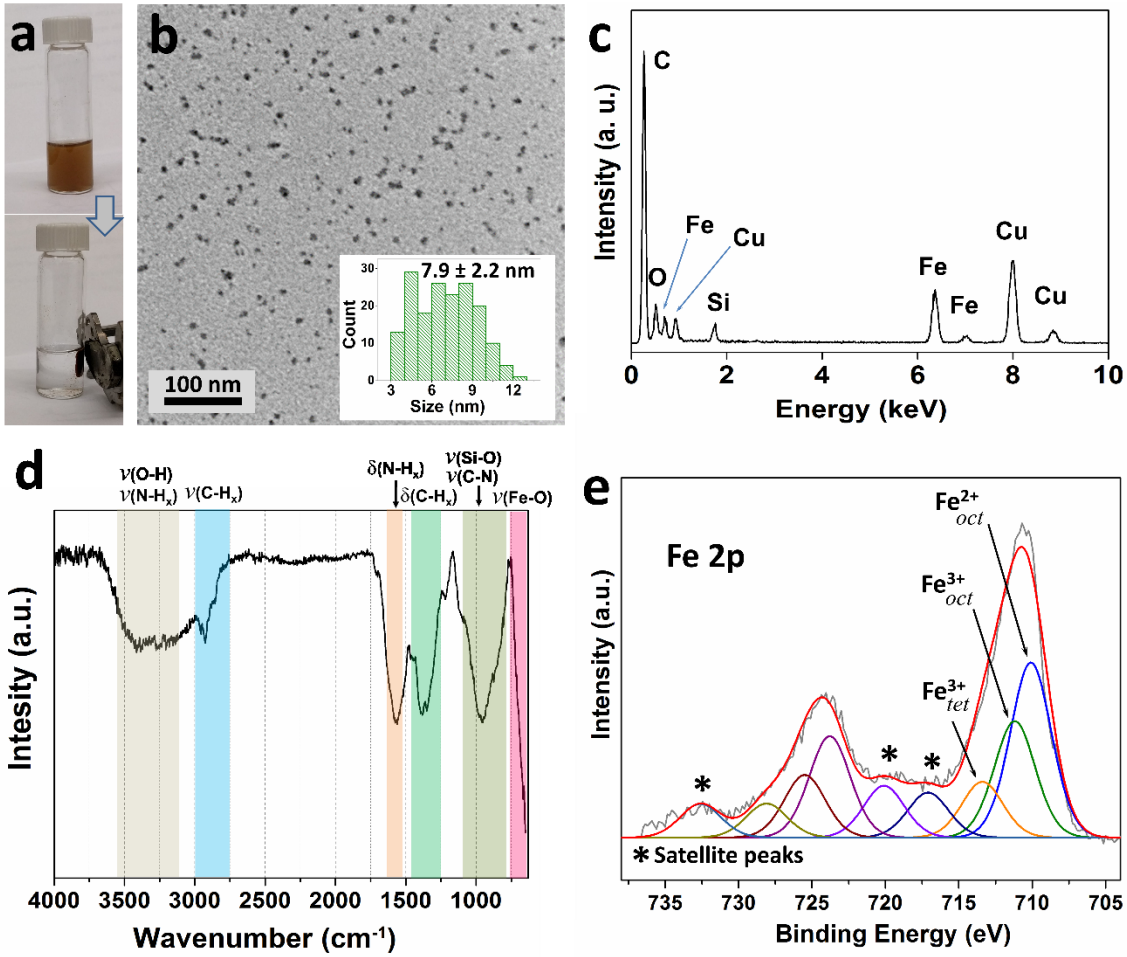

Figure 6-1. Characterization of APTMS-capped Fe_3O_4 NPs: a) A photograph of a water dispersion of APTMS-capped Fe_3O_4 before (left) and after (right) exposure to a permanent magnet. b) A representative bright-field TEM image (Inset: Histogram showing an average diameter = 7.9 ± 2.2 nm). c) EDX, d) FT-IR spectra, and e) The Fe 2p region of the high-resolution XP spectrum with appropriate fitting for Fe^{2+} and Fe^{3+}.[299–304]

TEM analyses of APTMS-capped magnetite particles (Figures 6-1a and 6-2) show NPs with a size distribution of 7.9 ± 2.2 nm (Figure 6-1 a and c). NPs of this size are considerably smaller than the single-domain dimension of bulk Fe_3O_4 (128 nm)[305,306] and are known to exhibit

superparamagnetic behavior.[307] Superparamagnetic particles have no coercivity, hence they will not remain aggregated and freely demagnetize and reorient after removing the magnetic field.[307]

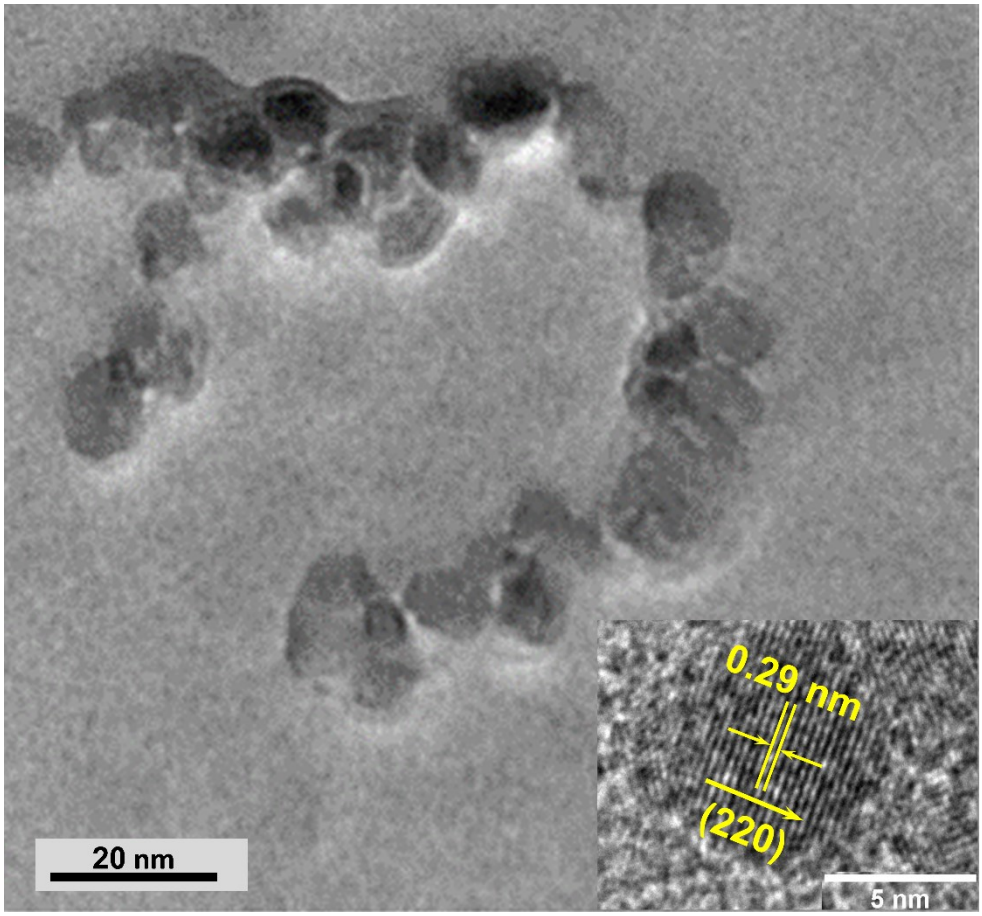

Figure 6-2. Bright-field TEM image of APTMS-capped Fe_3O_4 NPs. Inset: HRTEM image of APTMS-capped Fe_3O_4 NPs. The measured lattice fringe separation of 0.29 nm corresponds to the {220} planes of Fe_3O_4.

HRTEM imaging (Figure 6-2) shows lattice fringes of 0.29 nm that correspond to the {220} planes of bulk Fe_3O_4.[308] The EDX spectrum of APTMS-capped Fe_3O_4 NPs (Figure 6-1 c) indicates the presence of iron, oxygen, silicon and carbon at the sensitivity of the method.

The IR spectrum of APTMS-capped Fe_3O_4 NPs (Figure 6-1 e) shows broad and strong absorption from N-H stretching of the amine functionality at *ca.* 3410 cm^{-1} along with corresponding bending at *ca.* 1580 cm^{-1}. Features associated with aliphatic C-H stretching and bending are noted at 2960 and 1400 cm^{-1}, respectively. In addition, features associated with Si-O (*ca.* 1130 cm^{-1}) and strong Fe-O stretching (ca. 650 cm^{-1}) provide further evidence of APTMS functionalization of the magnetite NP surface.[255,309,310] The XP survey spectrum of magnetite NPs (Figure 6-3) exhibits the expected features arising from Fe_3O_4.[299–303] Figure 6-1 e shows a high resolution XPS of Fe 2p spectral region; three features at binding energies of 710.5, 712.1, and 713.7 eV, corresponding to Fe^{2+}, Fe^{3+} octahedral, and Fe^{3+} tetrahedral. Two other features at 717.6 and 720.7 eV are related to satellite peaks for Fe^{2+} and Fe^{3+} are also noted.[304]

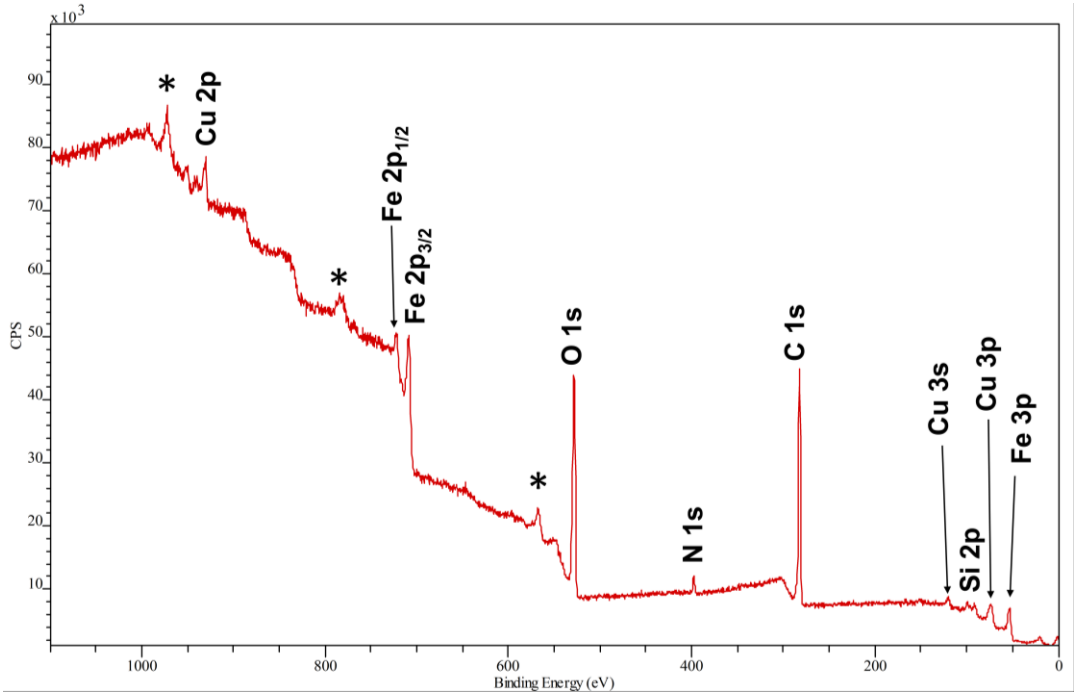

Figure 6-3. Survey XP spectrum of APTMS-capped Fe_3O_4 NPs. Signals of Fe, C, O, N and Si were observed as expected. Cu signals are from sample substrate and the signals which are assigned by a '*' are related to the sample holder.

SiNCs were prepared by the method developed in the Veinot lab based on the reductive thermal processing of a hydrogen silsesquioxane polymer.[17] For the present study, hydride-terminated SiNCs liberated from the oxide matric upon HF etching were functionalized with undecanoic acid moieties using an established radical initiated surface hydrosilylation protocol.[242]

Brightfield TEM imaging of undecanoic acid-functionalized SiNCs (Figure 6-4a) shows pseudospherical SiNCs and a size distribution of 4.6 ± 0.8 nm (Figure 6-4 a, inset), while HRTEM analysis (Figure 6-4 c) shows fringes of 0.33 nm, characteristic of the Si {111} lattice spacing. Furthermore, EDX analysis indicates that the functionalized SiNCs are expectedly composed of silicon, carbon and oxygen (Figure 6-4 b). Consistent with previous reports, the photoluminescence spectrum of SiNCs of these dimensions shows an emission maximum at *ca.* 720 nm upon excitation at 350 nm (Figure 6-4 d and e).[311] The FT-IR spectrum (Figure 6-4 f) clearly shows characteristic features related to surface bonded 10-undecanoic acid (*i.e.,* O-H stretching *ca.* 3400 cm^{-1}, C-H stretching *ca.* 2900 cm^{-1}, C-H bending *ca.* 1400, C=O stretching *ca.* 1708 cm^{-1}). We also note evidence of residual Si-H stretching at *ca.* 2100 cm^{-1} and Si-O-Si at *ca.* 1100 cm^{-1}.

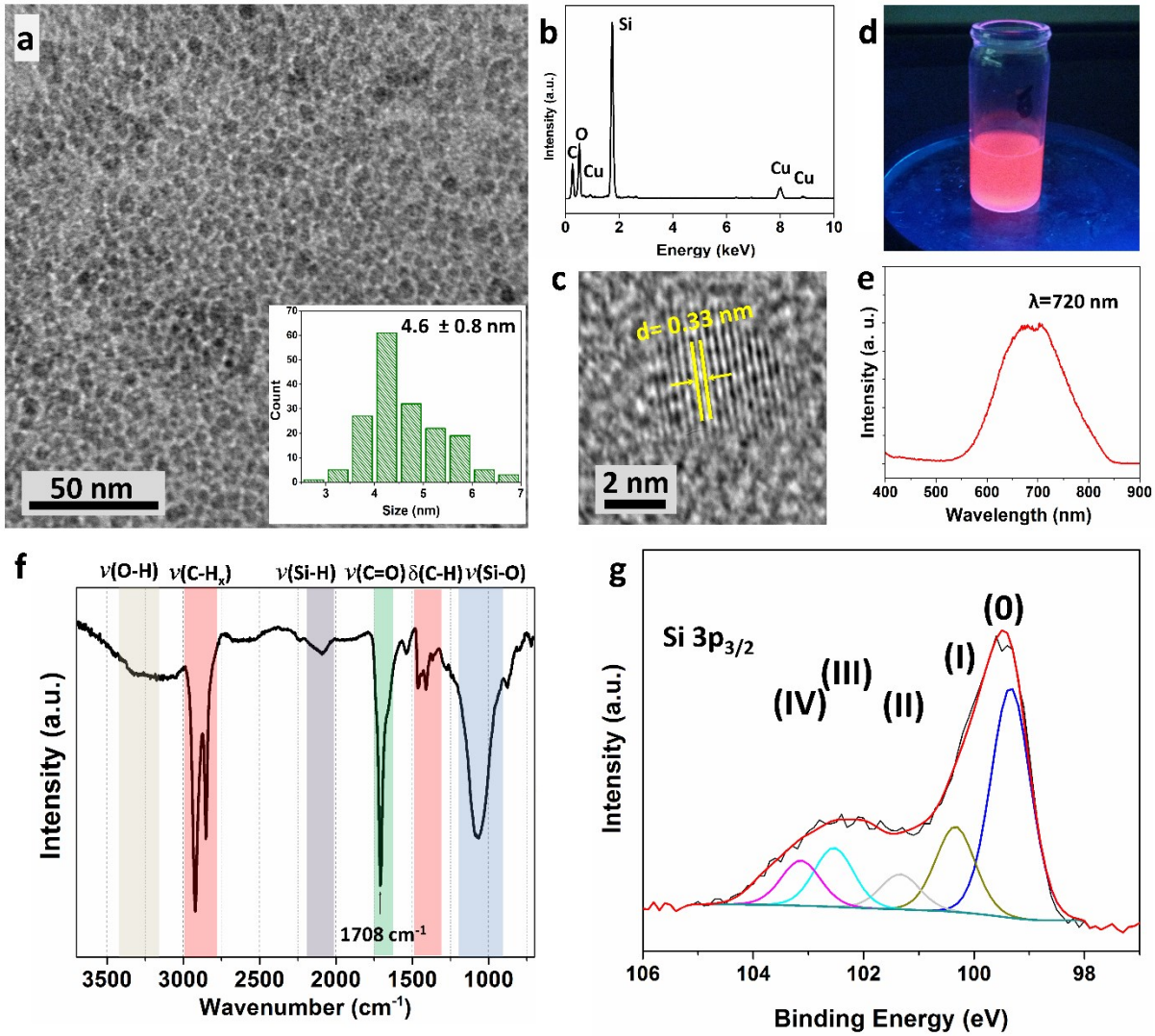

Figure 6-4. a) Bright-field TEM image and size distribution of undecanoic acid-functionalized SiNCs. b) EDX spectrum of undecanoic acid-functionalized SiNCs. c) HRTEM image of a representative SiNCs showing lattice fringes arising from Si [111] planes. d) A photograph of a water dispersion of undecanoic acid-functionalized SiNCs under 350 nm illumination. E) PL spectrum upon excitation at 350 nm. f) FT-IR spectrum. g) Si 2p region of the high-resolution XP spectra of undecanoic acid-functionalized SiNCs showing fitting for the Si $2p_{3/2}$ component. (The Si $2p_{1/2}$ components have omitted for clarity.)

The survey XP spectrum of undecanoic acid-functionalized SiNCs (Figure 6-5) exhibits the expected features arising from SiNCs, while the high resolution scan of the Si spectral region (Figure 6-4 g) is consistent with the present EDX and IR analysis suggesting some surface oxidation.

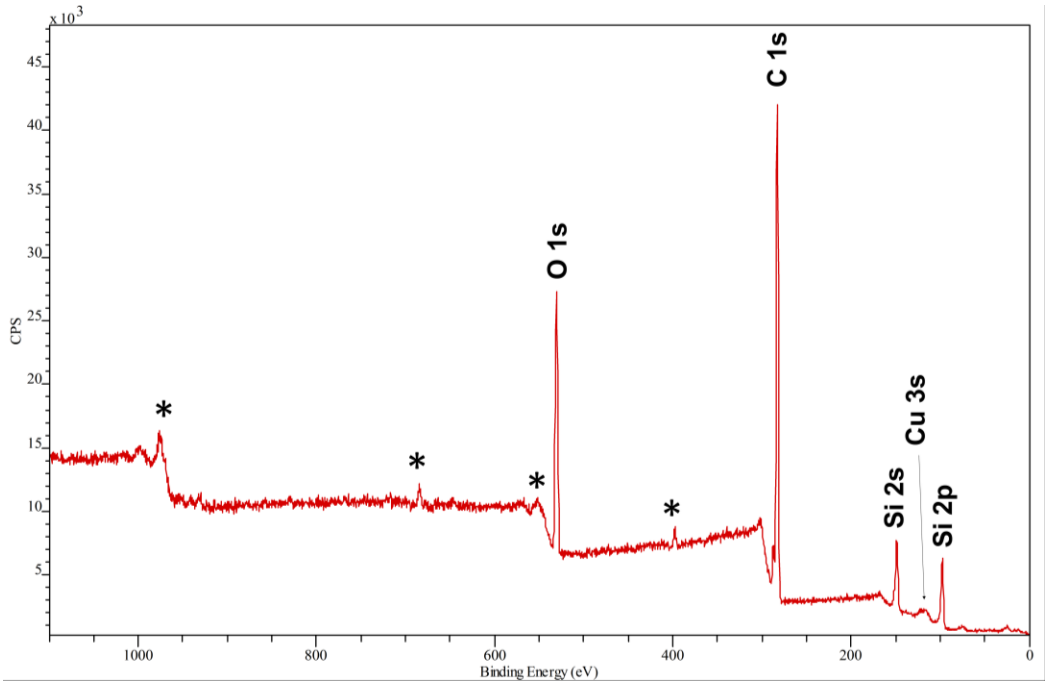

Figure 6-5. Survey XP spectrum of undecanoic acid-functionalized SiNCs. Signals of Si, C, and O were observed as expected. Cu signals are from sample substrate and the signals which are assigned by a '*' are related to sample holder impurity.

With the development of APTMS-capped magnetite and undecanoic acid-functionalized SiNCs, the coupling of these two functional components was achieved using established dicyclohexylcarbodiimide (DCC) mediated coupling (Scheme 6-1).[312,313] Carboxylic acid-terminated SiNCs were first activated with DCC and subsequently exposed to amine-terminated Fe_3O_4 NPs to induce attachment and form amides linkages. The resulting hybrids were freed

from reaction byproducts (*e.g.,* carboxylic acid anhydride, N,N'-dicyclohexylurea) and uncoupled SiNCs, upon repeated isolation by magnetic separation/re-dispersion cycles.

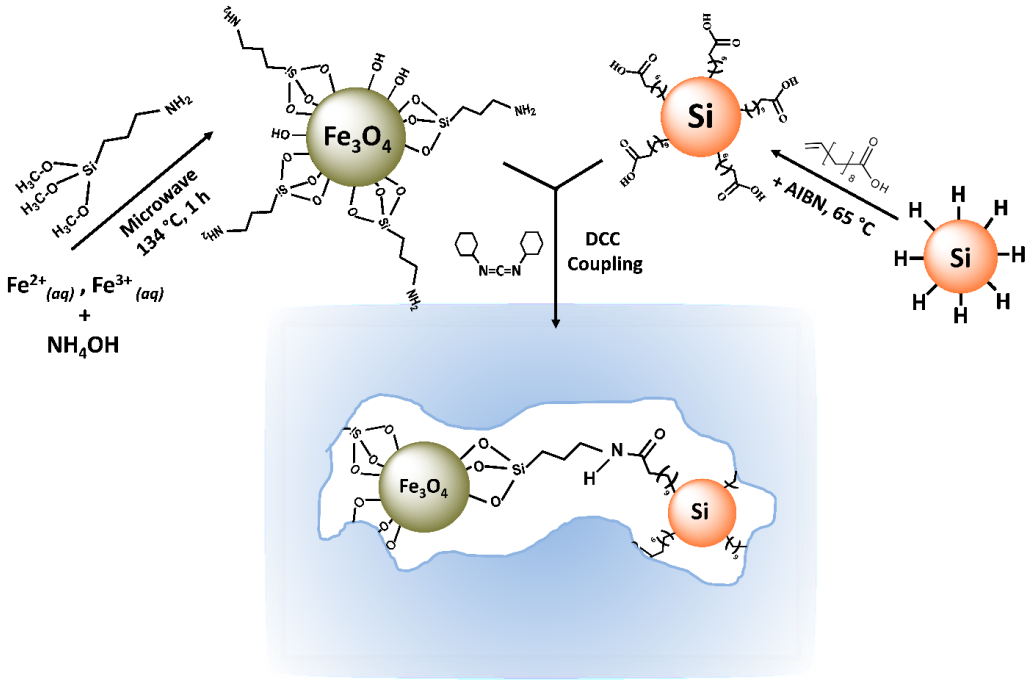

Scheme 6-1. Synthesis of Si-amide-Fe_3O_4 NPs *via* DCC coupling of undecanoic acid-terminated SiNCs and APTMS-capped Fe_3O_4 NPs

Figure 6-6 a shows photographs of a water dispersion of Si-amide-Fe_3O_4 NPs exposed to a benchtop UV light, before, during and after exposure to a permanent magnetic. Qualitative inspection immediately reveals the Si-amide-Fe_3O_4 NPs retain the SiNC optical response – this is also manifested in the PL spectrum (Figure 6-6b) that shows no shift in the PL maximum after the coupling reaction. The response of the Si-amide-Fe_3O_4 NPs upon exposure to a permanent magn*et al*so provides qualitative indication of coupling - the hybrid particles are attracted to the magnet.

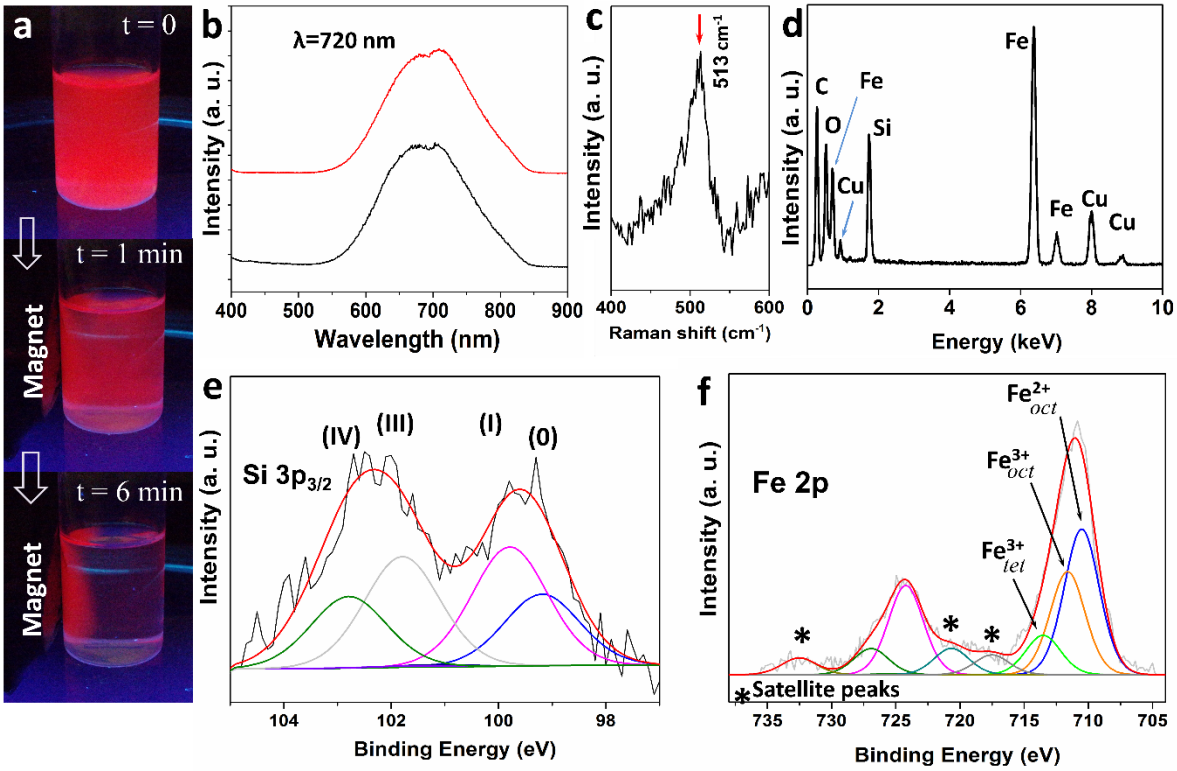

Figure 6-6. a) A photograph of a water suspension of Si-amide-Fe_3O_4 NPs (*ca.* 1 mg/mL) upon exposure to a benchtop UV light and permanent magnet. b) PL spectra of SiNCs (black trace) Si-amide-Fe_3O_4 NPs (red trace) upon excitation at 350 nm. c) Raman spectrum of Si-amide-Fe_3O_4 nano-hybrids. d) EDX spectrum of Si-amide-Fe_3O_4 nano-hybrids. e, f) Si 2p and Fe 2p regions of high-resolution XP spectra Si-amide-Fe_3O_4 nano-hybrids.

Consistent with the integrity of the SiNCs being maintained during coupling Raman spectroscopy shows a feature at 523 cm^{-1} indicative of Si-Si bonding (Figure 6-6c). EDX (Figure 6-6d), XP spectroscopy (Figures 6-6 e and f as well as Figure 6-7) confirms the presence of carbon, oxygen, iron and silicon. Furthermore, the high resolution XP of the Si spectral region (Figure 6-6 e) shows emissions associated with Si(0) as well as Si sub-oxides and the Fe region (Figure 6-6 f) confirms the presence of Fe_3O_4 (*vide supra*).

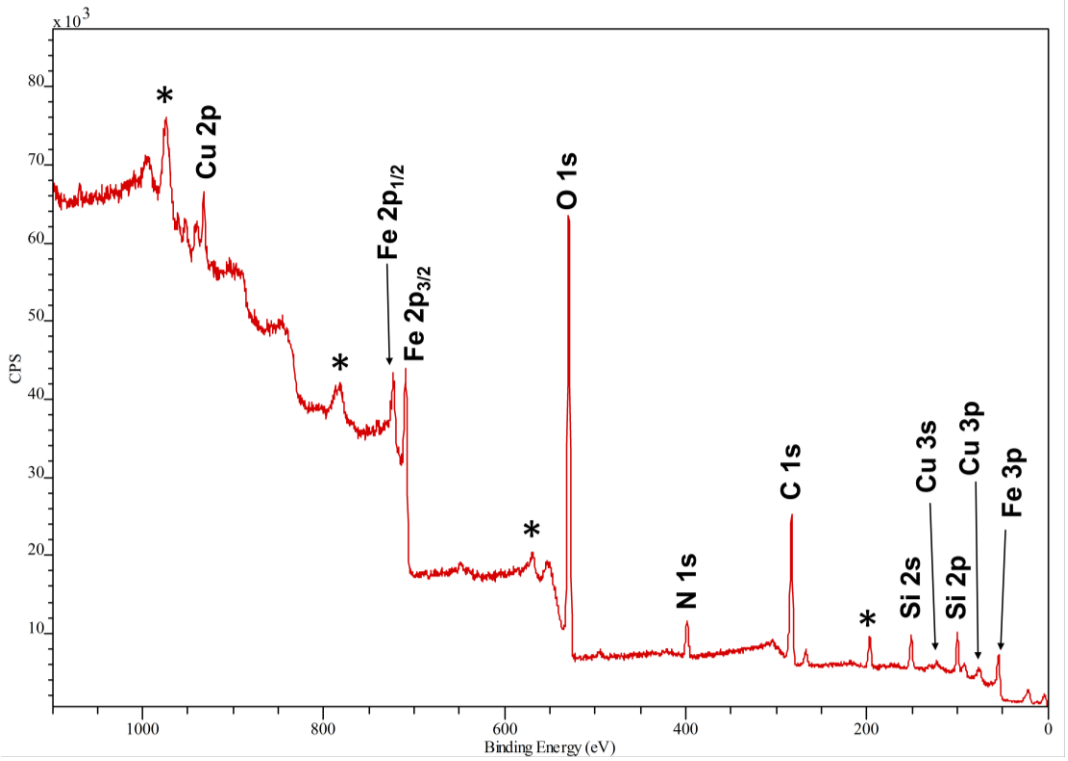

Figure 6-7. Survey XP spectrum of Si-amide-Fe_3O_4 nano-hybrids. Signals of Fe, Si, C, O as well as N were observed as expected. Cu signals are from sample substrate and the signals which are assigned by a '*' are related to the sample holder.

Infra-red spectroscopy (Figure 6-8) further confirms covalent coupling of carboxylic acid functionalized SiNCs with amine termination of APTMS-capped Fe_3O_4 NPs that shows features characteristic of the constituent SiNC and Fe_3O_4 NP components as well as the expected amide linkage (*i.e.,* amide carbonyl stretching at 1643 cm^{-1}).

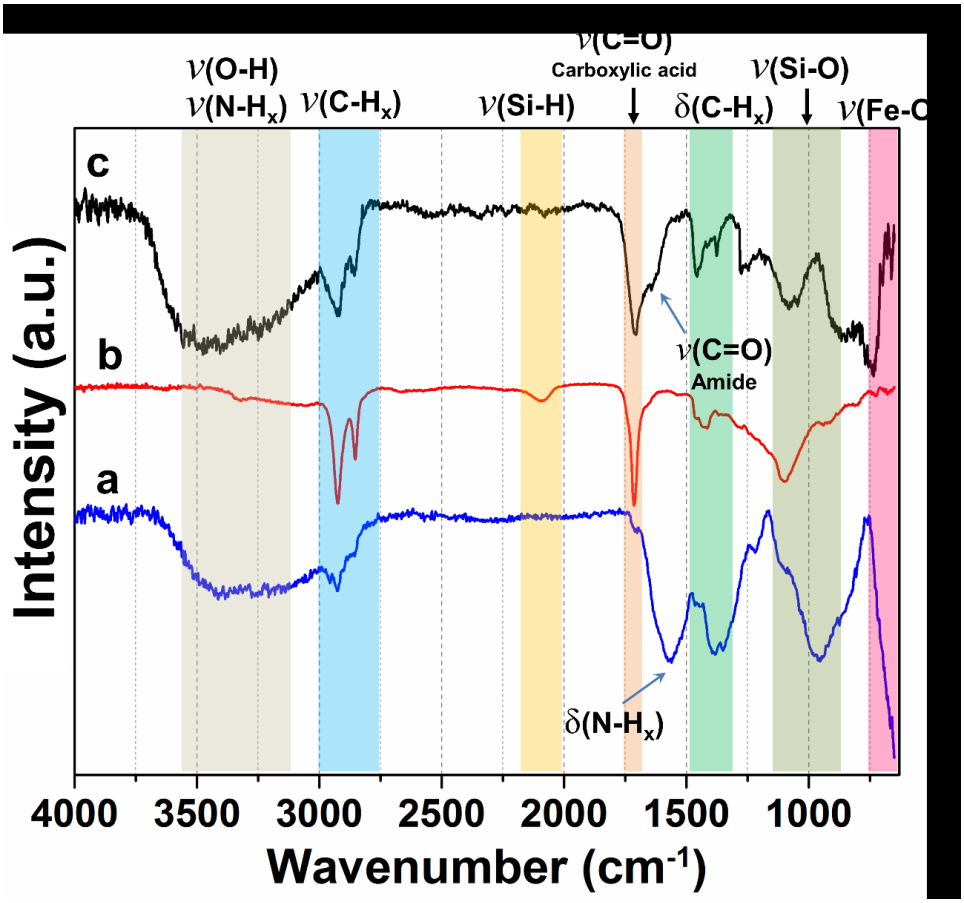

Figure 6-8. FT-IR spectra of APTMS-capped Fe_3O_4 NPs (**a**) undecanoic acid-functionalized SiNCs (**b**) compared to Fe_3O_4 NPs and Si-amide-Fe_3O_4 nano-hybrids (**c**). Stretching for C=O for carboxylic acid shows up at 1708 cm^{-1} while stretching for C=O for amide occurs at 1643 cm^{-1} and bending vibration for N-H is at 1580 cm^{-1}.

Figure 6-9 also shows several bright-field TEM images of Si-amide-Fe_3O_4 nano-hybrids. The aggregated structures shown in these images agree with attaching several Fe_3O_4 NPs (darker spots) to SiNCs (lighter spots). Higher contrast TEM images as well as elemental mapping analysis was not possible due to thick layer of different ligands (*e.g.,* undecenoic acid, APTMS, coupled amide moieties) on the surface of Si-amide-Fe_3O_4 nano-hybrids.

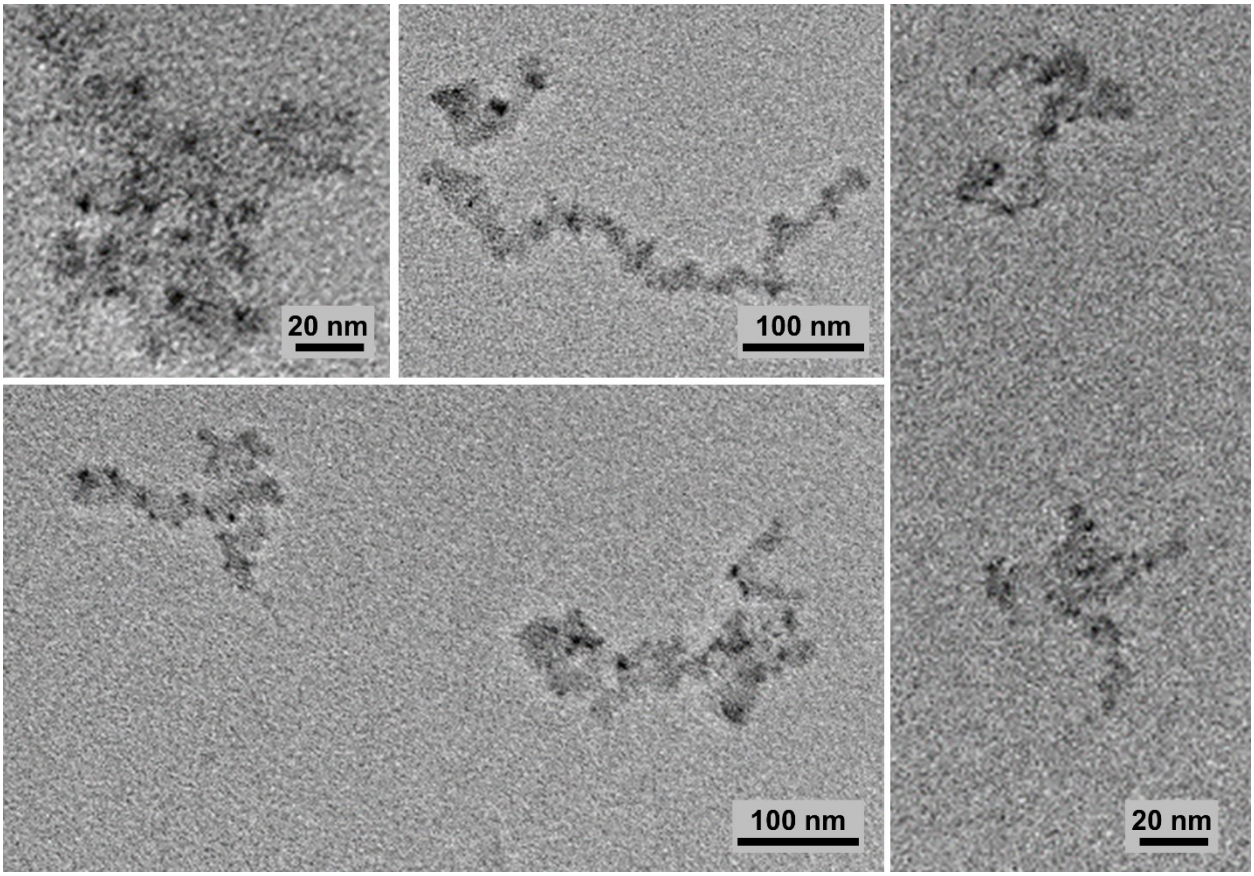

Figure 6-9. Bright-field TEM image of Si-amide-Fe_3O_4 nano-hybrids.

F ollowing the development of stable, magnetic and photoluminescent Si-amide-Fe_3O_4 nano-hybrid NPs, our next objective was to investigate their biocompatibility by measuring the effects of Si-amide-Fe_3O_4 NP exposure on RBL-2H3 cell viability at a range of doses. Results from these tests showed that after 1 h of *in vitro* exposure Si-amide-Fe_3O_4 NPs did not increase apoptosis in RBL-2H3 cells in all doses aside from the highest tested (*i.e.*, 100 µg/mL); under those conditions the percentage of necrotic cells increased significantly (8.2 ± 0.74 %, SEM) compared to the other doses tested, including the control (1.8 ± 0.17%) (Figure 4). However, after a 24 h exposure, the percentage of late apoptotic (0.1 µg/mL: 14.7 ± 2.1%, 1 µg/mL: 13.3 ±

1.2%, 10 μg/mL: 12.8 ± 1.0%, 100 μg/mL: 12.7 ± 1.2%) and necrotic (0.1 μg/mL: 10.9 ± 2.3%, 1 μg/mL: 12.2 ± 0.5%, 10 μg/mL: 10.9 ± 1.1%, 100 μg/mL: 16.8 ± 1.5% SEM) cells increased significantly in all the tested NP doses when compared to vehicle control (6.9 ± 0.4% SEM), but with no difference in the percent increase of late apoptotic and necrotic cells for any of the doses (Figure 4). Despite some decreases in cell viability, when cell death is normalized to vehicle controls over 24 h, the percentage of dead and dying cells in the treatment groups drops to 5-10 % of the cell population. In this context, these results indicate that over a wide range of Si-amide-Fe_3O_4 NP doses, a small population of RBL-2H3 cells are adversely sensitive to Si-amide-Fe_3O_4 NPs, but only after 24 h. Furthermore, given that immune mast cells actively interact with foreign particles and are located at mucosal boundaries with the external environment, means they are likely key targets for NPs and could be increasingly prone to toxicity. Therefore, the low levels of cell death indicate that these Si-amide-Fe_3O_4 NPs are likely highly biocompatible.

Previous biocompatibility studies have shown decreased cell survivability from Fe NPs can be attributed to oxidative stress from the generation of reactive oxygen species when NPs act as catalysts in Fenton reactions.[314] Free radical toxicity is a common mechanism by which many types of NPs can affect cell health, and excessive ROS products can initiate cellular apoptosis by causing excessive damage or changes to the cytoplasmic and/or inner mitochondrial membranes.[315,316] Mitochondrial destabilization results in the loss of mitochondrial transmembrane potential and the downstream activation of the proteolytic caspase cascade that lead to the execution pathway and the final death of the cell.[317] The increase in late apoptosis of a small population of cells after 24 h suggests that these NPs are activating the caspase cascade,

likely through the intrinsic apoptotic pathway which is a known target for free radicals, and are not causing cell death *via* a necrosis, a distinct modality for cell death.[318,319]

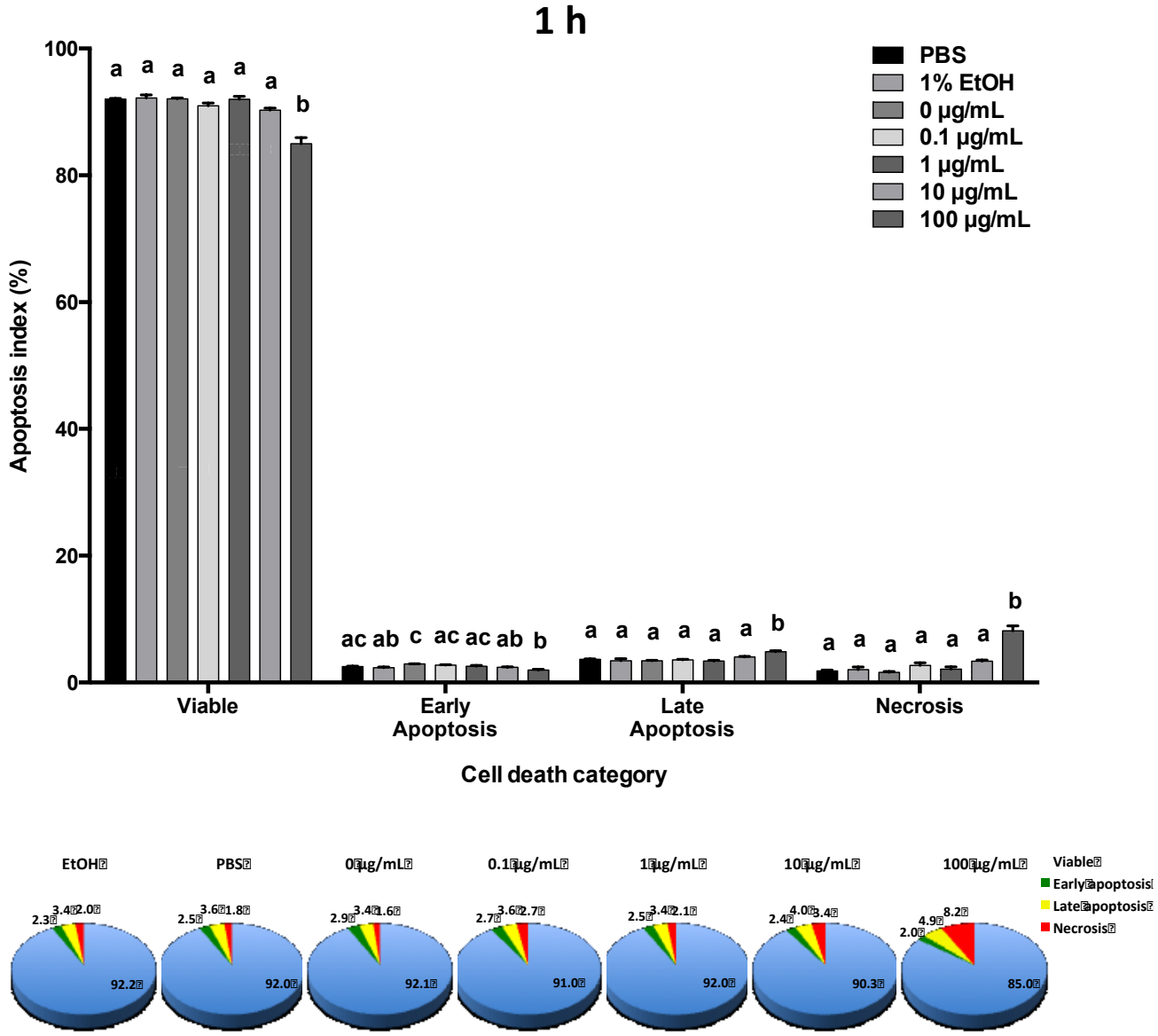

Figure 6-10. RBL-2H3 cell apoptosis results following cell exposure to 0, 0.1, 1, 10, 100 µg/mL Si-amide-Fe_3O_4 NPs, plus negative (PBS) and positive (ethanol) controls for 1 h. Apoptosis is proportioned into: viable, early apoptosis, late apoptosis and necrosis cell death categories as a histogram or into pie charts for each exposure period.

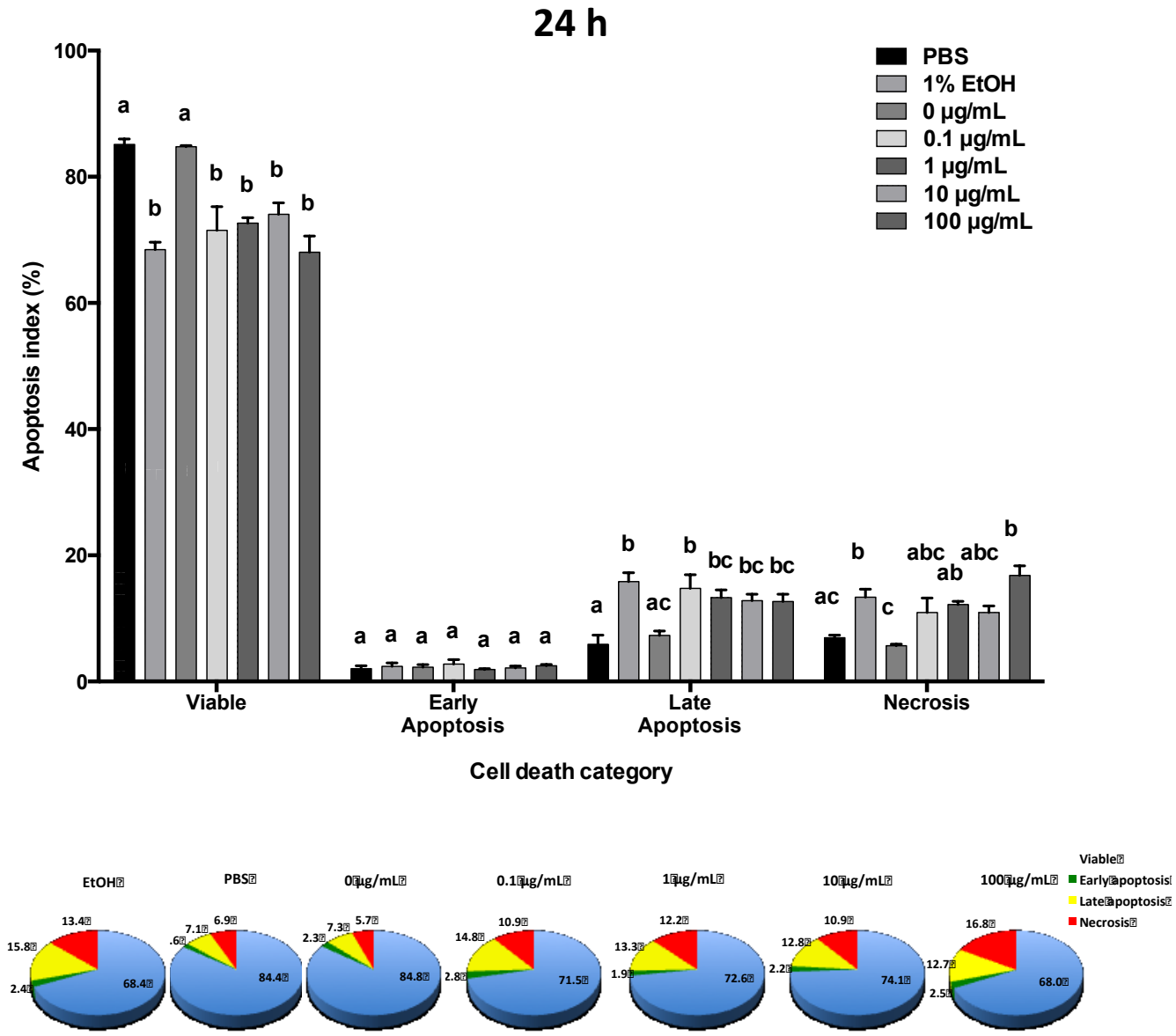

Figure 6-11. RBL-2H3 cell apoptosis results following cell exposure to 0, 0.1, 1, 10, 100 µg/mL Si-amide-Fe_3O_4 NPs, plus negative (PBS) and positive (ethanol) controls for 24 h. Apoptosis is proportioned into: viable, early apoptosis, late apoptosis and necrosis cell death categories as a histogram or into pie charts for each exposure period.

RBL-2H3 cells significantly internalized Si-amide-Fe_3O_4 NPs across a range of NP doses (Figure 6-12). Three-dimensional computer surface rendering of confocal images also confirmed that the NPs had penetrated the plasma membrane and were located mostly in the cytosol, but were also clearly observed inside the nucleus of RBL-2H3 cells (Figure 6-13). The amount of NPs that penetrated the cells also increased dose-dependently. The mechanism by which these NPs can enter cells is unknown, however recent studies have suggested that clathrin receptor-mediated endocytosis is a primary pathway by which NPs can penetrate the plasma membrane.[320] We have also recently shown that when clathrin receptors are pharmacologically antagonized, there is a significant reduction in the amount of NPs that are taken up by the cell (unpublished work). From a biocompatibility perspective, the ability to regulate the amount of NPs that can penetrate a cell presents an interesting opportunity to develop therapeutic NPs that can target various components of the cell. However, uptake into cells may also exacerbate cell death by mechanisms described above and there are several reports that correlate NP uptake and cells death.[286,321] The increased percentage of late apoptotic cells after a 24 h exposure to the highest NP dose (100 μg/mL) may be partially explained by the increased uptake of Si-amide-Fe_3O_4 NPs. Their internal presence may increase the amount of ROS that are generated and trigger apoptotic pathways in the cell.

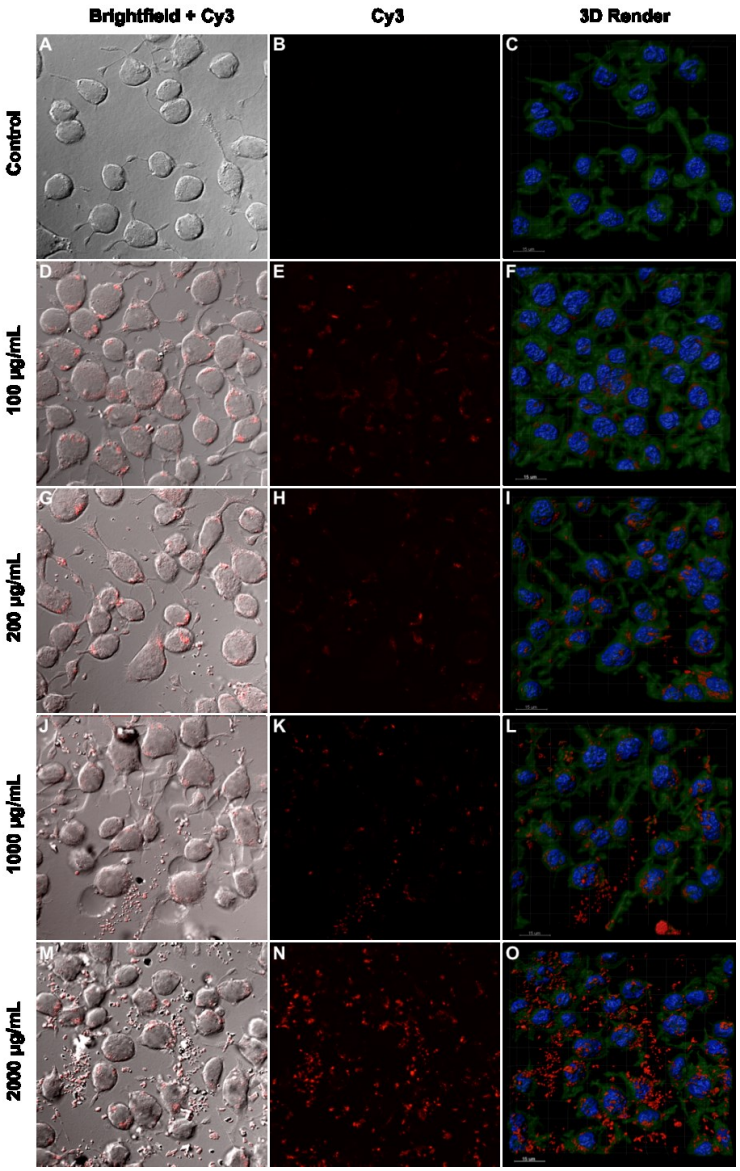

Figure 6-12. Confocal microscopy (Objective 40x, 1.3 oil plan-Apochromat) images of RBL-2H3 cells following exposure to 0, 100, 200, 1000 and 2000 µg/mL Si-amide-Fe_3O_4 NPs for 1 h. Representative bright field micrographs after differential interference contrast (A, D, G, J, M), Cy3 (*i.e.,* red NPs) fluorescence micrographs (B, E, H, K, N) and three-dimensional surface rendering of cells (C, F, I, L, O). DAPI (Blue) and FITC (Green; 75% transparent surface for three-dimensional reconstruction) were used as probes for cell nucleus and plasma membrane, respectively. Scale bars for three-dimensional images are 15 µm, respectively. The cell within white inset box on panel F was selected for single-cell three-dimensional rendering in Figure 6-13.

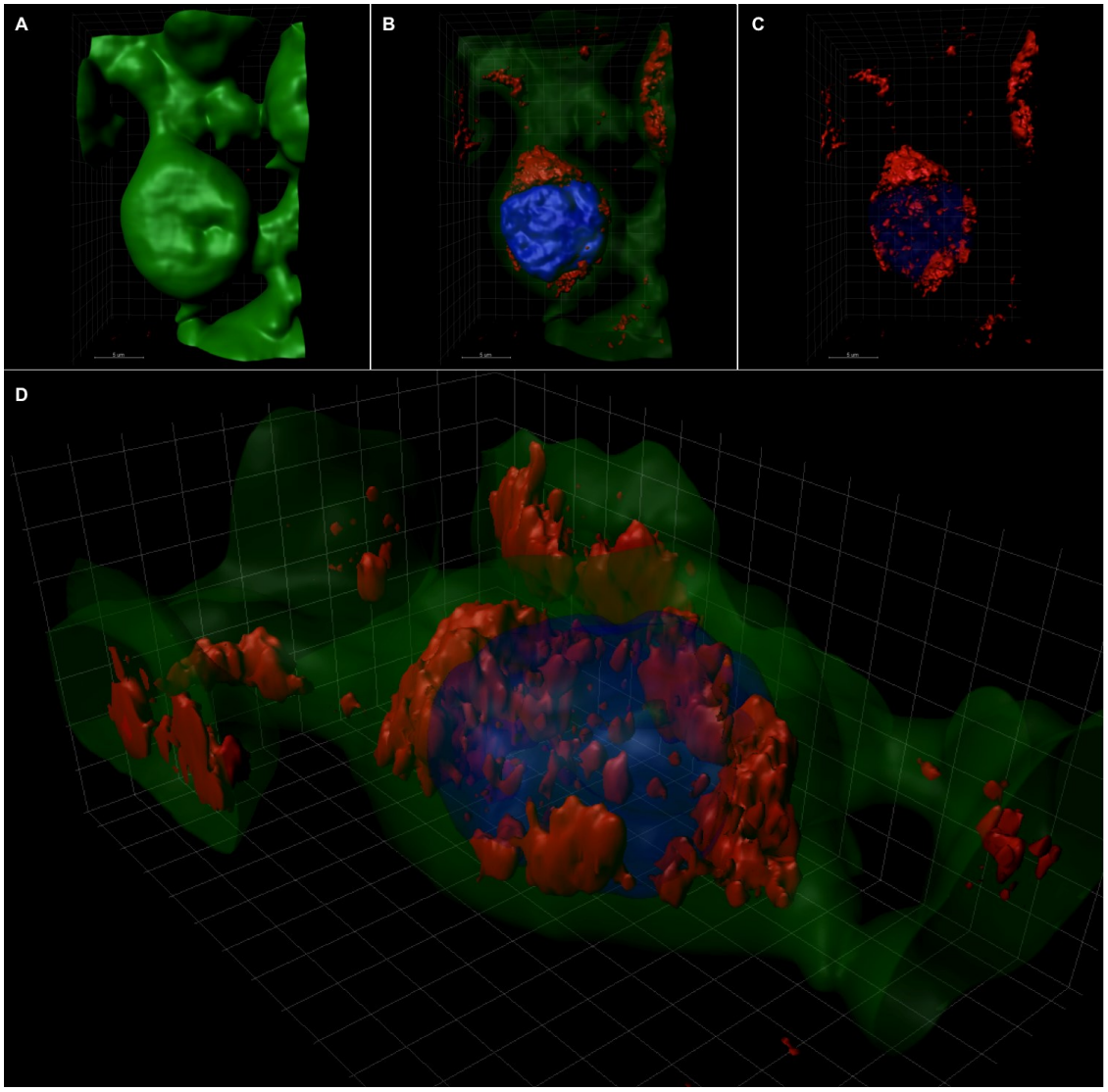

Figure 6-13. Three-dimensional surface rendering of a representative RBL-2H3 cell following exposure to 100 µg/mL Si-amide-Fe_3O_4 NPs (Cy3 red fluorescence) for 1 h. DAPI (Blue) and FITC (Green) were used as probes for cell nucleus and plasma membrane, respectively. Cell with non-transparent plasma membrane (A), cell with 75% transparent plasma membrane (B), cell with 100% transparent plasma membrane and 75% transparent nucleus (C) and cell positioned horizontally with 75% transparent plasma membrane and 75% transparent nucleus (D), clearly show penetration of Si-amide-Fe_3O_4 NPs inside the plasma and nuclear membranes. For a 3D movie animation demonstrating particle localization, please see supplemental information. Scale bars for three-dimensional images are 5 µm, respectively.

6.4. Conclusion

We have shown that nano-hybrids can effectively be prepared by covalent linking carboxylic acid-terminated SiNCs with amine-terminated Fe_3O_4 NPs vial DCC coupling. The resulting nano-hybrids maintain the photoluminescence of the SiNCs and the magnetic response of the Fe_3O_4 NPs. These Si-amide-Fe_3O_4 NPs were also found to be mostly compatible with mast cell-like cells that actively engage with foreign materials. Despite some increased apoptosis after a 24 h exposure period, the cells populations retained high levels of viability, especially when corrected for apoptosis in controls.

Finally, using confocal imaging and 3D surface rendering, the Si-amide-Fe_3O_4 NPs were found to penetrate into the plasma and nuclear membranes of RBL-2H3 cells. Uptake of other fluorescently-labeled NPs has been previously shown,[287,322] however, there are typically issues with bleaching and quenching of fluorescent signals, which can limit their time and the efficacy for visualizing tagged cells. As well, adding fluorescent molecules, such a FITC, to an engineered NP can change the physicochemical properties of that NP and interfere with its proposed use. Here, we have shown that Si-amide-Fe_3O_4 NPs can be used to label cells without altering their intended physicochemical properties, such as their fluorescence, charge or size. This advantage provides better predictability for biological outcomes and allows developers to more easily modify specific NP properties if other intended uses are desired.

Chapter 7:

Conclusions

and

Future Directions

7.1. Conclusion

Quantum dots (QDs) are an important 21st century material that have potential for far reaching impacts and extensive applications in semiconductor and optoelectronic industries.[323] After these semiconductor nanoparticles (mostly direct band-gap) were discovered and quantum confinement theories to explain them were developed,[10] it was difficult to contemplate the possibility of similar phenomena for indirect band-gap materials such as Group 14 semiconductors – namely Si, Ge, Si_xGe_{1-x} – and corresponding compounds. This was until 1990, when Canham observed red photoluminescence (PL) from mesoporous silicon,[66] and closely after that in 1991, when Yoshihito *et al.* reported the same observation (visible photoluminescence) for germanium crystals embedded in silica.[67] These discoveries opened a new window to further investigations of Si and Ge-based nanostructures and demonstrated great potential for their applications. Despite being in Group 14, germanium-based nanostructures such as Ge nanocrystals (GeNCs) and germanium oxide nanoparticles (GeO_2 NPs) differ substantially from their more frequently studied silicon counterparts.

In this context, GeO_2 (the targeted material in the second and third Chapters of the current Thesis) possesses a higher dielectric constant, higher refractive index,[121,143,146,152,153] and wider optical transparency compared to silica.[154] This can be useful in the fabrication of various optical devices.[147,156,157,159,324–326] In Chapter two, we reported a facile method for preparing GeO_2 NPs of tailored shape without the use of surfactants. The morphologies (*i.e.*, pseudospherical particles, nano-eggs, spindles, and nano-cubes) were readily tailored by changing water/ethanol ratios during the hydrolysis of TEOG. Uniform GeO_2 nano-cubes with a narrow size distribution were obtained by optimizing the concentration of the ammonium hydroxide catalyst.

In a follow-up work (third Chapter), shells of silica were produced around GeO_2 nano-cubes and nano-eggs *via* the well-known Stöber process (sol-gel reaction of tetraethoxysilane).[327] This yielded GeO_2@SiO_2 core-shell nano-cubes and nano-eggs. Afterwards, selective reductions of the core (*i.e.*, GeO_2) by 5% H_2 / 95% Ar and the shell (*i.e.*, SiO_2) by magnesium were performed. Consequently, the GeO_2@SiO_2 core-shell nano-cubes and nano-eggs were then characterized with XRD, TEM, SEM, HRTEM, and EDX analyses.

The materials fabricated in Chapters two and three of the current Thesis also show promising results in other investigations. Some examples are "assembling of alkyl monophosphonic acid functionalized GeO_2 nano-cubes" and the "optical response of Cu and Er doped GeO_2 nano-cubes" (results not shown here). Despite these potential uses, our interests for now lie in investigating the optoelectronic properties of GeNCs by themselves. One example is understanding the origin of PL from GeNCs (surface state *vs.* band-gap). Although Ge-based nanostructures show unique properties, they have not been studied as widely as their Si counterparts. Compared to Si, Ge shows a smaller band-gap, larger Bohr-exciton radius and higher electron and hole mobility.[67,69–71] Thus, it is expected that GeNCs with comparatively larger sizes will display the promising optical and electronic properties that will be potentially useful in different optoelectronic applications.[18,73,74] The preparation of colloidal GeNCs is performed *via* solution phase reduction, decomposition and disproportionation of Ge(II) and Ge(IV) precursors.[19,82,83,101,102,105,223,224] Solution-based syntheses also face challenges including identifying suitable precursors, requiring high temperatures to induce crystallization, low yields and developing methods to predictably control surface chemistry.

In this regard, solid-state synthesis of oxide-embedded GeNCs *via* thermolysis of substoichiometric oxide-based molecular precursors has proven very effective.[113,121–123] However, this method also suffers from lack of control on the morphology of the GeNCs and, more importantly, the presence of impurities from the molecular precursors.[121] Therefore, the synthesis of impurity-free GeNCs with well-defined surface chemistry is of considerable interest. In the fourth Chapter of the current Thesis, we demonstrated the effective preparation of a series of "$Ge(OH)_2$" precursors suitable for large scale preparation of free-standing GeNCs, whose surfaces were then modified through thermally induced hydrogermylation. A detailed comparison of the precursors also provided insight into, and proposal of, a seeded growth mechanism that provides GeNCs which exhibit narrow size distributions. While the present NCs are not photoluminescent, we believe that this results from surface defects and is the subject of ongoing investigation.

In Chapter five, we went into the surface chemistry of prepared GeNCs. Modifying and tailoring GeNC surface chemistry provides an avenue by which reactivity, environmental compatibility (*e.g.*, solubility or resistance to oxidation), and electronic properties may be tailored. Hydride-terminated GeNCs (H-GeNCs) are of particular interest because the reactivity of surface Ge-H bonds toward alkenes and alkynes *via* hydrogermylation affords the potential for convenient modification, however these reactions and their scope have not been widely explored. In this context, H-GeNCs provide a reactive platform that can be further modified using thermal, radical initiated and borane-catalyzed hydrogermylation. NALDI-MS and ^{1}H NMR analysis indicated more of both oligomerization and surface coverage occurring with the thermally induced method compared to other hydrogermylation procedures. Dodecane functionalized

GeNCs prepared by the proper defect removal approach (*i.e.*, introducing I_2) possess an optical response in IR region.

The sixth Chapter discussed the predominant potential/actual application of functionalized Si or GeNCs in biological systems. H-GeNCs, like those prepared in Chapters four and five, provide a prodigious possibility for further functionalization on the surfaces of GeNCs. However, these functionalization protocols, as well as size/surface dependent optical responses, are more studied and understood for SiNCs rather than GeNCs. In the sixth Chapter of the current Thesis, we thus presented a promising hybrid nanomaterial that combined the favorable properties (*e.g.*, photoluminescence, biocompatibility, and surface chemistry) of SiNCs with the magnetic characteristics of Fe_3O_4 nanoparticles (NPs). Linking these two complementary nanomaterials *via* DCC coupling yielded a new, advanced hybrid material that possessed the characteristics of its constituents and afforded a photoluminescent system that responded to permanent magnets. We also evaluated the toxicity and demonstrated proof-of-concept confocal cell imaging using these novel hybrid NPs. As will be shown in future work, the chemistry applied step-by-step in Chapter six is applicable for H-GeNCs as well.

7.2. Future Directions

7.2.1. Developing functionalization procedures as well as modifying H-GeNCs with innovative surface functionalities

Finding and understanding various routes as well as numerous bonding groups for surface functionalization of H-GeNCs is possible by considering the well-established reactivity of

similar hydride-terminated surfaces (*i.e.*, Ge or Si wafers; H-SiNCs).[247,251] We have already proven the reactivity of surface Ge-H bonds toward alkenes through a series of hydrogermylation approaches such as thermal activation, radical-initiation, and borane-catalysis (Chapters four and five).

However, there are still many functionalities to be explored and investigated. As just one example, H-GeNCs can be covalently attached to poly (3 – hexylthiophene) polymer (P3HT) following similar chemistry which has been developed for H-SiNCs.[328] In this regard, P3HT functionalized GeNCs are known to be promising materials for solar cell applications[329,330] due to their narrower band-gap and larger exciton-Bohr radius compared to SiNCs, as well as the large absorption coefficient of Germanium by itself (see introduction).[67,69–71]

Apart from different bonding groups, various functionalization procedures can be investigated as well. Again, as one of the many possible cases, surface functionalization of H-GeNCs by xenon difluoride (XeF_2) can be investigated and realized. A recent study of instantaneous functionalization of H-SiNCs at room-temperature by Mobarok *et al*. showed promise.[331] The authors also carried out detailed analysis of the reaction byproducts by in situ NMR spectroscopy and GC-MS.[331] This provided unparalleled insight into SiNC surface composition. In the case of H-GeNCs, using XeF_2 as the functionalization-inducing agent could not only introduce a novel functionalization mechanism but also clarify the surface chemistry of H-GeNCs.

Recently, we have begun thermally induced (*i.e.*, catalyst free) dehydrocoupling of alkyl-silanes and alkyl-germanes onto the surface of H-GeNCs. Our preliminary results show successful functionalization, but the reaction conditions need to be optimized.

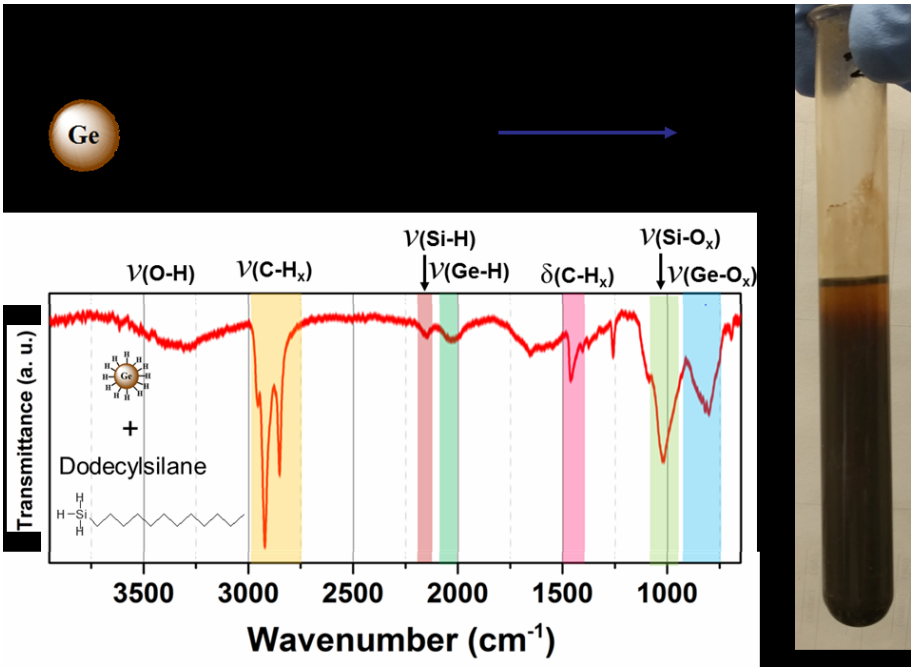

Figure 7-1. Thermally induced (*i.e.*, catalyst free) dehydrocoupling of alkyl-silanes onto the surface of H-GeNCs. Picture and FT-IR spectrum are for GeNCs functionalized with dodecylsilane using aforementioned thermally induced dehydrocoupling

Dehydrogenative coupling has been performed on various hydride-terminated nanostructures but,[332–334] to our knowledge, dehydrocoupling on the surfaces of H-GeNCs has not yet been reported (Figure 7-1).

7.2.2. Studying the effect of halogen additives on optical properties of current GeNCs

The band-gap originating, optoelectronic response from GeNCs remains the subject of some scientific arguments regarding the origin of PL, the exciton-Bohr radius of GeNCs, and the effects of oxides and other surface impurities.[18,89,121,122,130] As observed in Chapter five, dodecyl-functionalized GeNCs do not possess an optical response (*i.e.*, photoluminescence) despite their average size (<10 nm) being smaller than the exciton-Bohr radius of Ge (*i.e.*, 24.3nm).[67,70] We

believe this may result from surface defects (*e.g.*, impurities, vacancies, surface oxides, dangling bonds, *etc.*).[258] However, introducing a trace quantity of I_2 into the thermally induced hydrogermylation reaction mixture led to a PL response of the dodecyl-GeNCs at λ_{max}= 986 nm (Figure 7-2 d).

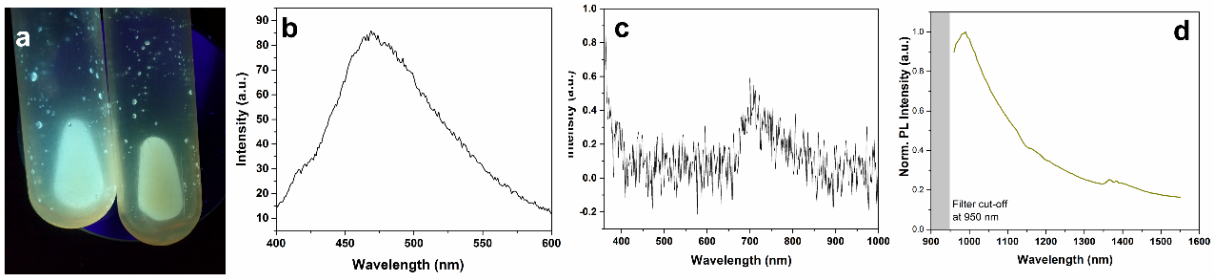

Figure 7-2. a) A photograph of a toluene dispersion of dodecyl-GeNCs functionalized by XeF_2 under 350 nm illumination. b) PL spectrum of dodecyl-GeNCs functionalized by XeF_2 upon excitation at 300 nm. c) PL spectrum of dodecyl-GeNCs functionalized by PCl_5 upon excitation at 320 nm. d) PL spectrum of dodecyl-GeNCs functionalized thermally induced hydrogermylation shown in Chapter five of current Thesis.

In our preliminary results from XeF_2 induced functionalization, GeNCs show visible green-yellow PL (λ_{max} at *ca.* 400 nm; results not shown) after the reaction (Figure 7-2 a, b). We have also observed that chlorine impurity can cause a PL response with λ_{max} around 720 nm (Figure 7-2 c). These observations demonstrate a trend of PL wavelength according to type of halogen and need further investigation.

7.2.3. Magnetite-GeNCs nano-hybrids for biological applications

One of the potential opportunities for the nanostructures of Group 14 semiconductors (particularly Si, SiC and GeNCs) is in biological imaging. This is due to their generally accepted low-toxicity, high-biocompatibility, high-photostability, and wide fluorescence spectral regions

that span from the near-ultraviolet to near-infrared ranges.[280,335] Although there are some concerns regarding the cytotoxicity of germanium nanomaterials,[336] studies still show that GeNCs are less toxic than CdSe NCs at similar concentrations.[90] This gives GeNCs a strong future in biological applications, on which research has been already started by numerous groups.[73,90,91,337]

Moreover, because of the smaller band-gap of Ge compared to Si or CdSe,[69,125] GeNCs are expected to show band-gap correlated PL response at lower energies (*i.e.*, near-IR). In this regard, optical imaging in the NIR region seems promising due to lower interference of NIR wavelengths with the metabolism of targeted cells, lower risk of autofluorescence signals arising from the biological material and deeper penetration of NIR wavelengths due to reduced light scattering and low absorption.[126]

As the next logical step for Chapter six of the current Thesis, undecenoic acid-functionalized GeNCs could be synthesized with a similar radical-initiated method. Subsequently, this ligand could be attached to APTMS-terminated Fe_3O_4 NPs *via* DCC coupling to make magnetite-GeNC nano-hybrids. However, adjusting the PL response of GeNCs (*e.g.*, by adding halogen impurities) needs careful examination.

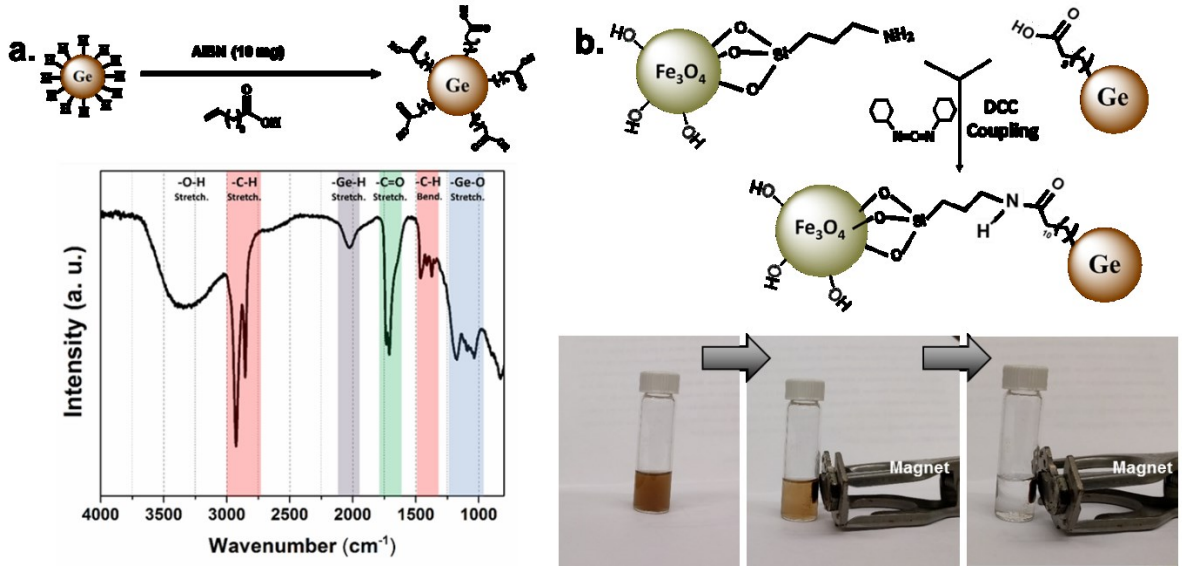

Figure 7-3. a) Synthetic scheme and IR spectra of undecenoic acid-functionalized GeNCs. b) Synthetic scheme of preparing and photographs of showing acetone dispersion of magnetic Fe_3O_4-amide-GeNCs nano-hybrids

7.2.4. Investigating the morphology of GeNCs obtained from thermal treatment of $Ge(OH)_2$

As outlined in Chapter four, $Ge(OH)_2$ is suitable for large scale preparation of oxide-embedded as well as free-standing GeNCs. However, the morphological study of free-standing GeNCs whose surfaces were modified through thermally induced hydrogermylation showed poor monodispersity and ill-defined shapes of GeNCs. A detailed comparison of the yellow, orange and brown precursors also provided insight into, and proposal of, a seeded growth mechanism that provided GeNCs exhibiting narrow size distributions.

It has been shown that the prolonged annealing of well-defined pseudospherical SiNCs embedded in SiO_2 leads to nanocrystal surfaces that thermodynamically self-optimize to yield particles with cubic geometries.[246] Also, Korgel *et al.* have reported SiNCs with uniform

cuboctahedral shape synthesized with reparative heating-cooling cycles of SiNCs/SiO_2.[338] Similar procedures can be examined on the current GeNCs embedded in GeO_2 in order to reach better shape and morphological control.

Bibliography

(1) Goldstein, A. N., C. M. Echer, and A. P. A. Melting in Semiconductor Nanocrystals. *Science (80-.).* **1992**, *256* (5062), 1425–1427.

(2) Ashoori, R. C. Electrons in Artificial Atoms. *Nature* **1996**, *379* (6564), 413–419.

(3) Ashoori, R. C.; Stormer, H. L.; Weiner, J. S.; Pfeiffer, L. N.; Pearton, S. J.; Baldwin, K. W.; West, K. W. Single-Electron Capacitance Spectroscopy of Discrete Quantum Levels. *Phys. Rev. Lett.* **1992**, *68* (20), 3088–3091.

(4) Dabbousi, B. O.; Rodriguez-Viejo, J.; Mikulec, F. V; Heine, J. R.; Mattoussi, H.; Ober, R.; Jensen, K. F.; Bawendi, M. G. (CdSe) ZnS Core-Shell Quantum Dots: Synthesis and Characterization of a Size Series of Highly Luminescent Nanocrystallites. *J. Phys. Chem. B* **1997**, *101* (46), 9463–9475.

(5) Norris, D. J.; Bawendi, M. G. Measurement and Assignment of the Size-Dependent Optical Spectrum in CdSe Quantum Dots. *Phys. Rev. B* **1996**, *53* (24), 16338.

(6) Murray, Cb.; Norris, D. J.; Bawendi, M. G. Synthesis and Characterization of Nearly Monodisperse CdE (E= Sulfur, Selenium, Tellurium) Semiconductor Nanocrystallites. *J. Am. Chem. Soc.* **1993**, *115* (19), 8706–8715.

(7) Ekimov, A. I.; Onushchenko, A. A. Quantum Size Effect in Three-Dimensional Microscopic Semiconductor Crystals. *Jetp Lett* **1981**, *34* (6), 345–349.

(8) Spanhel, L.; Haase, M.; Weller, H.; Henglein, A. Photochemistry of Colloidal Semiconductors. 20. Surface Modification and Stability of Strong Luminescing CdS Particles. *J. Am. Chem. Soc.* **1987**, *109* (19), 5649–5655.

(9) Weller, H.; Schmidt, H. M.; Koch, U.; Fojtik, A.; Baral, S.; Henglein, A.; Kunath, W.; Weiss, K.;

Dieman, E. Photochemistry of Colloidal Semiconductors. Onset of Light Absorption as a Function of Size of Extremely Small CdS Particles. *Chem. Phys. Lett.* **1986**, *124* (6), 557–560.

(10) Brus, L. Electronic Wave Functions in Semiconductor Clusters: Experiment and Theory. *J. Phys. Chem.* **1986**, *90* (12), 2555–2560.

(11) Rossetti, R.; Ellison, J. L.; Gibson, J. M.; Brus, L. E. Size Effects in the Excited Electronic States of Small Colloidal CdS Crystallites. *J. Chem. Phys.* **1984**, *80* (9), 4464–4469.

(12) Alivisatos, A. P. Perspectives on the Physical Chemistry of Semiconductor Nanocrystals. *J. Phys. Chem.* **1996**, *100* (31), 13226–13239.

(13) de Mello Donegá, C. Synthesis and Properties of Colloidal Heteronanocrystals. *Chem. Soc. Rev.* **2011**, *40* (3), 1512–1546.

(14) Smith, A. M.; Nie, S. Semiconductor Nanocrystals: Structure, Properties, and Band Gap Engineering. *Acc. Chem. Res.* **2009**, *43* (2), 190–200.

(15) Brus, L. E. Electron–electron and Electron-hole Interactions in Small Semiconductor Crystallites: The Size Dependence of the Lowest Excited Electronic State. *J. Chem. Phys.* **1984**, *80* (9), 4403–4409.

(16) English, D. S.; Pell, L. E.; Yu, Z.; Barbara, P. F.; Korgel, B. A. Size Tunable Visible Luminescence from Individual Organic Monolayer Stabilized Silicon Nanocrystal Quantum Dots. *Nano Lett.* **2002**, *2* (7), 681–685.

(17) Hessel, C. M.; Henderson, E. J.; Veinot, J. G. C.; Uni, V.; February, R. V; Re, V.; Recei, M.; August, V. A Molecular Precursor for Nanocrystalline Si - SiO2 Composites and Freestanding Hydride-Surface-Terminated Silicon Nanoparticles. *Chem. Mater.* **2006**, *18*, 6139–6146.

(18) Lee, D. C.; Pietryga, J. M.; Robel, I.; Werder, D. J.; Schaller, R. D.; Klimov, V. I. Colloidal

Synthesis of Infrared-Emitting Germanium Nanocrystals. *J. Am. Chem. Soc.* **2009**, *131* (10), 3436–3437.

(19) Fok, E.; Shih, M.; Meldrum, A.; Veinot, J. G. C. C. Preparation of Alkyl-Surface Functionalized Germanium Quantum Dots via Thermally Initiated Hydrogermylation. *Chem. Commun. (Camb).* **2004**, *1* (4), 386–387.

(20) Purkait, T. K.; Swarnakar, A. K.; Glenda, B.; Hegmann, F. A.; Rivard, E.; Veinot, J. G. C. One-Pot Synthesis of Functionalized Germanium Nanocrystals from a Single Source Precursor. *Nanoscale* **2015**, *7* (6), 2241–2244.

(21) Pellegrini, G.; Mattei, G.; Mazzoldi, P. Finite Depth Square Well Model: Applicability and Limitations. *J. Appl. Phys.* **2005**, *97* (7), 073706.

(22) Tan, Z.; Zhang, F.; Zhu, T.; Xu, J.; Wang, A. Y.; Dixon, J. D.; Li, L.; Zhang, Q.; Mohney, S. E.; Ruzyllo, J. Bright and Color-Saturated Emission from Blue Light-Emitting Diodes Based on Solution-Processed Colloidal Nanocrystal Quantum Dots. *Nano Lett.* **2007**, *7* (12), 3803–3807.

(23) Anikeeva, P. O.; Halpert, J. E.; Bawendi, M. G.; Bulović, V. Quantum Dot Light-Emitting Devices with Electroluminescence Tunable over the Entire Visible Spectrum. *Nano Lett.* **2009**, *9* (7), 2532–2536.

(24) Monticone, S.; Tufeu, R.; Kanaev. Complex Nature of the UV and Visible Fluorescence of Colloidal ZnO Nanoparticles. *J. Phys. Chem. B* **1998**, *102* (16), 2854–2862.

(25) Li, H.; Shih, W. Y.; Shih, W.-H. Highly Photoluminescent and Stable Aqueous ZnS Quantum Dots. *Ind. Eng. Chem. Res.* **2009**, *49* (2), 578–582.

(26) Li, L. S.; Pradhan, N.; Wang, Y.; Peng, X. High Quality ZnSe and ZnS Nanocrystals Formed by Activating Zinc Carboxylate Precursors. *Nano Lett.* **2004**, *4* (11), 2261–2264.

(27) Hines, M. A.; Guyot-Sionnest, P. Bright UV-Blue Luminescent Colloidal ZnSe Nanocrystals. *J. Phys. Chem. B* **1998**, *102* (19), 3655–3657.

(28) Jun, Y.; Choi, C.-S.; Cheon, J. Size and Shape Controlled ZnTe Nanocrystals with Quantum Confinement Effect. *Chem. Commun.* **2001**, No. 1, 101–102.

(29) Bang, J.; Park, J.; Lee, J. H.; Won, N.; Nam, J.; Lim, J.; Chang, B. Y.; Lee, H. J.; Chon, B.; Shin, J.; et al. ZnTe/ZnSe (Core/Shell) Type-II Quantum Dots: Their Optical and Photovoltaic Properties. *Chem. Mater.* **2010**, *22* (1), 233–240.

(30) Taylor, P. N.; Schreuder, M. A.; Smeeton, T. M.; Grundy, A. J. D.; Dimmock, J. A. R.; Hooper, S. E.; Heffernan, J.; Kauer, M. Synthesis of Widely Tunable and Highly Luminescent Zinc Nitride Nanocrystals. *J. Mater. Chem. C* **2014**, *2* (22), 4379–4382.

(31) Xu, S.; Ziegler, J.; Nann, T. Rapid Synthesis of Highly Luminescent InP and InP/ZnS Nanocrystals. *J. Mater. Chem.* **2008**, *18* (23), 2653–2656.

(32) Xie, R.; Battaglia, D.; Peng, X. Colloidal InP Nanocrystals as Efficient Emitters Covering Blue to Near-Infrared. *J. Am. Chem. Soc.* **2007**, *129* (50), 15432–15433.

(33) Talapin, D. V; Gaponik, N.; Borchert, H.; Rogach, A. L.; Haase, M.; Weller, H. Etching of Colloidal InP Nanocrystals with Fluorides: Photochemical Nature of the Process Resulting in High Photoluminescence Efficiency. *J. Phys. Chem. B* **2002**, *106* (49), 12659–12663.

(34) Aharoni, A.; Mokari, T.; Popov, I.; Banin, U. Synthesis of InAs/CdSe/ZnSe Core/Shell1/Shell2 Structures with Bright and Stable Near-Infrared Fluorescence. *J. Am. Chem. Soc.* **2006**, *128* (1), 257–264.

(35) Zimmer, J. P.; Kim, S.-W.; Ohnishi, S.; Tanaka, E.; Frangioni, J. V; Bawendi, M. G. Size Series of Small Indium Arsenide−Zinc Selenide Core−Shell Nanocrystals and Their Application to In Vivo

Imaging. *J. Am. Chem. Soc.* **2006**, *128* (8), 2526–2527.

(36) Liu, W.; Chang, A. Y.; Schaller, R. D.; Talapin, D. V. Colloidal InSb Nanocrystals. *J. Am. Chem. Soc.* **2012**, *134* (50), 20258–20261.

(37) Yarema, M.; Kovalenko, M. V. Colloidal Synthesis of InSb Nanocrystals with Controlled Polymorphism Using Indium and Antimony Amides. *Chem. Mater.* **2013**, *25* (9), 1788–1792.

(38) Mićić, O. I.; Ahrenkiel, S. P.; Bertram, D.; Nozik, A. J. Synthesis, Structure, and Optical Properties of Colloidal GaN Quantum Dots. *Appl. Phys. Lett.* **1999**, *75* (4), 478–480.

(39) Fernée, M. J.; Jensen, P.; Rubinsztein-Dunlop, H. Origin of the Large Homogeneous Line Widths Obtained from Strongly Quantum Confined PbS Nanocrystals at Room Temperature. *J. Phys. Chem. C* **2007**, *111* (13), 4984–4989.

(40) Fernée, M. J.; Thomsen, E.; Jensen, P.; Rubinsztein-Dunlop, H. Highly Efficient Luminescence from a Hybrid State Found in Strongly Quantum Confined PbS Nanocrystals. *Nanotechnology* **2006**, *17* (4), 956–962.

(41) Ma, W.; Swisher, S. L.; Ewers, T.; Engel, J.; Ferry, V. E.; Atwater, H. A.; Alivisatos, A. P. Photovoltaic Performance of Ultrasmall PbSe Quantum Dots. *ACS Nano* **2011**, *5* (10), 8140–8147.

(42) Keuleyan, S.; Lhuillier, E.; Guyot-Sionnest, P. Synthesis of Colloidal HgTe Quantum Dots for Narrow Mid-IR Emission and Detection. *J. Am. Chem. Soc.* **2011**, *133* (41), 16422–16424.

(43) Chang, J.-Y.; Wang, G.-Q.; Cheng, C.-Y.; Lin, W.-X.; Hsu, J.-C. Strategies for Photoluminescence Enhancement of AgInS2 Quantum Dots and Their Application as Bioimaging Probes. *J. Mater. Chem.* **2012**, *22* (21), 10609–10618.

(44) Hong, S. P.; Park, H. K.; Oh, J. H.; Yang, H.; Do, Y. R. Comparisons of the Structural and Optical Properties of O-AgInS2, T-AgInS2, and c-AgIn5S8 Nanocrystals and Their Solid-Solution

Nanocrystals with ZnS. *J. Mater. Chem.* **2012**, *22* (36), 18939–18949.

(45) Akkerman, Q. A.; Genovese, A.; George, C.; Prato, M.; Moreels, I.; Casu, A.; Marras, S.; Curcio, A.; Scarpellini, A.; Pellegrino, T.; et al. From Binary Cu2S to Ternary Cu–In–S and Quaternary Cu–In–Zn–S Nanocrystals with Tunable Composition via Partial Cation Exchange. *ACS Nano* **2015**, *9* (1), 521–531.

(46) Zhang, J.; Xie, R.; Yang, W. A Simple Route for Highly Luminescent Quaternary Cu-Zn-In-S Nanocrystal Emitters. *Chem. Mater.* **2011**, *23* (14), 3357–3361.

(47) Nakamura, H.; Kato, W.; Uehara, M.; Nose, K.; Omata, T.; Otsuka-Yao-Matsuo, S.; Miyazaki, M.; Maeda, H. Tunable Photoluminescence Wavelength of Chalcopyrite CuInS2-Based Semiconductor Nanocrystals Synthesized in a Colloidal System. *Chem. Mater.* **2006**, *18* (14), 3330–3335.

(48) Guo, Y.; Rowland, C. E.; Schaller, R. D.; Vela, J.; Cds, G.; Zns, G.; Ii, I. V; Semiconductor, À. V. I.; Guo, Y.; Rowland, C. E.; et al. Near-Infrared Photoluminescence Enhancement in Ge/CdS and Ge/ZnS Core/Shell Nanocrystals: Utilizing IV/II–VI Semiconductor Epitaxy. *ACS Nano* **2014**, *8* (8), 8334–8343.

(49) Groeneveld, E. Synthesis and Optical Spectroscopy of (hetero)-Nanocrystals : An Exciting Interplay between Chemistry and Physics, Utrecht University, 2012.

(50) Koole, R.; Groeneveld, E.; Vanmaekelbergh, D.; Meijerink, A.; de Mello Donegá, C. Size Effects on Semiconductor Nanoparticles. In *Nanoparticles*; Springer, 2014; pp 13–51.

(51) Grim, J. Q.; Manna, L.; Moreels, I. A Sustainable Future for Photonic Colloidal Nanocrystals. *Chem. Soc. Rev.* **2015**, *44* (16), 5897–5914.

(52) Kim, S.; Fisher, B.; Eisler, H.-J.; Bawendi, M. Type-II Quantum Dots: CdTe/CdSe (core/shell)

and CdSe/ZnTe (core/shell) Heterostructures. *J. Am. Chem. Soc.* **2003**, *125* (38), 11466–11467.

(53) Pisanic Ii, T. R.; Zhang, Y.; Wang, T. H. Quantum Dots in Diagnostics and Detection: Principles and Paradigms. *Analyst* **2014**, *139* (12), 2968–2981.

(54) Kolosnjaj-tabi, J.; Wilhelm, C.; Clément, O.; Gazeau, F. Cell Labeling with Magnetic Nanoparticles : Opportunity for Magnetic Cell Imaging and Cell Manipulation. *J. Nanobiotechnology* **2013**, *11* (Suppl 1), S7.

(55) Jin, S.; Hu, Y.; Gu, Z.; Liu, L.; Wu, H. Application of Quantum Dots in Biological Imaging. *J. Nanomater.* **2011**, *2011*, 13.

(56) Resch-genger, U.; Grabolle, M.; Cavaliere-jaricot, S.; Nitschke, R.; Nann, T. Quantum Dots versus Organic Dyes as Fluorescent Labels. *Nat. Methods* **2008**, *5* (9), 763–775.

(57) Nozik, A. J.; Beard, M. C.; Luther, J. M.; Law, M.; Ellingson, R. J.; Johnson, J. C. Semiconductor Quantum Dots and Quantum Dot Arrays and Applications of Multiple Exciton Generation to Third-Generation Photovoltaic Solar Cells. *Chem. Rev.* **2010**, *110* (11), 6873–6890.

(58) Leschkies, K. S.; Divakar, R.; Basu, J.; Enache-Pommer, E.; Boercker, J. E.; Carter, C. B.; Kortshagen, U. R.; Norris, D. J.; Aydil, E. S. Photosensitization of ZnO Nanowires with CdSe Quantum Dots for Photovoltaic Devices. *Nano Lett.* **2007**, *7* (6), 1793–1798.

(59) Caruge, J. M.; Halpert, J. E.; Wood, V.; Bulović, V.; Bawendi, M. G. Colloidal Quantum-Dot Light-Emitting Diodes with Metal-Oxide Charge Transport Layers. *Nat. Photonics* **2008**, *2* (4), 247–250.

(60) Sun, Q.; Wang, Y. A.; Li, L. S.; Wang, D.; Zhu, T.; Xu, J.; Yang, C.; Li, Y. Bright, Multicoloured Light-Emitting Diodes Based on Quantum Dots. *Nat. Photonics* **2007**, *1* (12), 717–722.

(61) Wu, Y.; Li, X.; Steel, D.; Gammon, D.; Sham, L. J. Coherent Optical Control of Semiconductor

Quantum Dots for Quantum Information Processing. *Phys. E Low-dimensional Syst. Nanostructures* **2004**, *25* (2), 242–248.

(62) Jamieson, T.; Bakhshi, R.; Petrova, D.; Pocock, R.; Imani, M.; Seifalian, A. M. Biological Applications of Quantum Dots. *Biomaterials* **2007**, *28* (31), 4717–4732.

(63) Michalet, X.; Pinaud, F. F.; Bentolila, L. A.; Tsay, J. M.; Doose, S.; Li, J. J.; Sundaresan, G.; Wu, A. M.; Gambhir, S. S.; Weiss, S. Quantum Dots for Live Cells, in Vivo Imaging, and Diagnostics. *Science (80-.).* **2005**, *307* (5709), 538–544.

(64) Gao, X.; Cui, Y.; Levenson, R. M.; Chung, L. W. K.; Nie, S. In Vivo Cancer Targeting and Imaging with Semiconductor Quantum Dots. *Nat. Biotechnol.* **2004**, *22* (8), 969–976.

(65) Wu, X.; Liu, H.; Liu, J.; Haley, K. N.; Treadway, J. A.; Larson, J. P.; Ge, N.; Peale, F.; Bruchez, M. P. Immunofluorescent Labeling of Cancer Marker Her2 and Other Cellular Targets with Semiconductor Quantum Dots. *Nat. Biotechnol.* **2003**, *21* (1), 41–46.

(66) Canham, L. T. Silicon Quantum Wire Array Fabrication by Electrochemical and Chemical Dissolution of Wafers. *Appl. Phys. Lett.* **1990**, *57* (10), 1046–1048.

(67) Yazawa, Y.; Maeda, Y.; Tsukamoto, N.; Kanemitsu, Y.; Masumoto, Y.; Yazawa, Y.; Kanemitsu, Y.; Masumoto, Y. Visible Photoluminescence of Ge Microcrystals Embedded in SiO2 Glassy Matrices. *Appl. Phys. Lett.* **1991**, *59* (24), 3168–3170.

(68) Haller, E. E. Germanium: From Its Discovery to SiGe Devices. *Mater. Sci. Semicond. Process.* **2006**, *9* (4–5), 408–422.

(69) Collings, P. J. Simple Measurement of the Band Gap in Silicon and Germanium. *Am. J. Phys* **1980**, *48* (3), 197–199.

(70) Maeda, Y. Visible Photoluminescence from Nanocrystallite Ge Embedded in a Glassy SiO2

Matrix. *Phys. Rev. B* **1995**, *51* (3), 1658–1670.

(71) Cho, S.; Kang, I. M.; Kim, K. R.; Park, B.; Jr, J. S. H.; Cho, S.; Kang, I. M.; Kim, K. R.; Park, B.; Man Kang, I.; et al. Silicon-Compatible High-Hole-Mobility Transistor with an Undoped Germanium Channel for Low-Power Application. *Appl. Phys. Lett.* **2013**, *103* (22), 222102–222105.

(72) Seng, K. H.; Park, M.; Guo, Z. P.; Liu, H. K.; Cho, J. Catalytic Role of Ge in Highly Reversible GeO2/Ge/C Nanocomposite Anode Material for Lithium Batteries. *Nano Lett.* **2013**, *2013* (1), 2–8.

(73) Prabakar, S.; Shiohara, A.; Hanada, S.; Fujioka, K.; Yamamoto, K.; Tilley, R. D. Size Controlled Synthesis of Germanium Nanocrystals by Hydride Reducing Agents and Their Biological Applications. *Chem. Mater.* **2010**, *22* (2), 482–486.

(74) Lambert, T. N.; Andrews, N. L.; Gerung, H.; Boyle, T. J.; Oliver, J. M.; Wilson, B. S.; Han, S. M. Water-Soluble germanium(0) Nanocrystals: Cell Recognition and near-Infrared Photothermal Conversion Properties. *Small* **2007**, *3* (4), 691–699.

(75) Choi, W. K.; Chim, W. K.; Heng, C. L.; Teo, L. W.; Ho, V.; Ng, V.; Antoniadis, D. A.; Fitzgerald, E. A. Observation of Memory Effect in Germanium Nanocrystals Embedded in an Amorphous Silicon Oxide Matrix of a Metal-Insulator-Semiconductor Structure. *Appl. Phys. Lett.* **2002**, *80* (11), 2014–2016.

(76) Kanoun, M.; Busseret, C.; Poncet, A.; Souifi, A.; Baron, T.; Gautier, E. Electronic Properties of Ge Nanocrystals for Non Volatile Memory Applications. *Solid. State. Electron.* **2006**, *50* (7–8), 1310–1314.

(77) Batra, Y.; Kabiraj, D.; Kanjilal, D. Charge Retention and Optical Properties of Ge Nanocrystals Embedded in GeO2 Matrix. *Solid State Commun.* **2007**, *143* (4–5), 213–216.

(78) Das, S.; Manna, S.; Singha, R.; Anopchenko, A.; Daldosso, N.; Pavesi, L.; Dhar, A.; Ray, S. K. Light Emission and Floating Gate Memory Characteristics of Germanium Nanocrystals. *Phys. status solidi* **2011**, *208* (3), 635–638.

(79) Ray, S. K.; Das, K. Luminescence Characteristics of Ge Nanocrystals Embedded in SiO2 Matrix. *Opt. Mater. (Amst).* **2005**, *27* (5), 948–952.

(80) Heath, J. R. J. R.; Shiang, J. J.; Alivisatos, A. P. Germanium Quantum Dots: Optical Properties and Synthesis. *J. Chem. Phys.* **1994**, *101* (2), 1607–1615.

(81) Heath, J. R.; LeGoues, F. K. A Liquid Solution Synthesis of Single Crystal Germanium Quantum Wires. *Chem. Phys. Lett.* **1993**, *208* (3), 263–268.

(82) Kornowski, A.; Giersig, M.; Vogel, R.; Chemseddine, A.; Weller, H. Nanometer-sized Colloidal Germanium Particles: Wet-chemical Synthesis, Laser-induced Crystallization and Particle Growth. *Adv. Mater.* **1993**, *5* (9), 634–636.

(83) Chiu, H. W.; Chervin, C. N.; Kauzlarich, S. M. Phase Changes in Ge Nanoparticles. *Chem. Mater.* **2005**, *17* (19), 4858–4864.

(84) Chiu, H. W.; Kauzlarich, S. M. Investigation of Reaction Conditions for Optimal Germanium Nanoparticle Production by a Simple Reduction Route. *Chem. Mater.* **2006**, *18* (4), 1023–1028.

(85) Lee, H.; Kim, M. G.; Choi, C. H.; Sun, Y.-K.; Yoon, C. S.; Cho, J. Surface-Stabilized Amorphous Germanium Nanoparticles for Lithium-Storage Material. *J. Phys. Chem. B* **2005**, *109* (44), 20719–20723.

(86) Wilcoxon, J.; Provencio, P.; Samara, G. Synthesis and Optical Properties of Colloidal Germanium Nanocrystals. *Phys. Rev. B* **2001**, *64* (3), 1–9.

(87) Wu, H. P. P.; Liu, J. F. F.; Wang, Y. W. W.; Zeng, Y. W. W.; Jiang, J. Z. Z. Preparation of Ge

Nanocrystals via Ultrasonic Solution Reduction. *Mater. Lett.* **2006**, *60* (7), 986–989.

(88) Lu, X.; Korgel, B. A.; Johnston, K. P. High Yield of Germanium Nanocrystals Synthesized from Germanium Diiodide in Solution. *Chem. Mater.* **2005**, *17* (25), 6479–6485.

(89) Vaughn II, D. D.; Schaak, R. E. Synthesis, Properties and Applications of Colloidal Germanium and Germanium-Based Nanomaterials. *Chem. Soc. Rev.* **2012**, *42* (7), 2861–2879.

(90) McVey, B. F. P.; Prabakar, S.; Gooding, J. J.; Tilley, R. D. Solution Synthesis, Surface Passivation, Optical Properties, Biomedical Applications, and Cytotoxicity of Silicon and Germanium Nanocrystals. *Chempluschem* **2017**, *82*, 60–73.

(91) Warner, J. H.; Tilley, R. D. Synthesis of Water-Soluble Photoluminescent Germanium Nanocrystals. *Nanotechnology* **2006**, *17* (15), 3745.

(92) Warner, J. H.; Hoshino, A.; Shiohara, A.; Yamamoto, K.; Tilley, R. D. The Synthesis of Silicon and Germanium Quantum Dots for Biomedical Applications. In *Biomedical Optics 2006*; International Society for Optics and Photonics, 2006; p 609607.

(93) McNaught, A. D.; Wilkinson, A. Compendium of Chemical Terminology. IUPAC Recommendations. **1997**.

(94) Kauzlarich, S. M. Encyclopedia of Inorganic Chemistry. John Wiley & Sons 1994.

(95) Muthuswamy, E.; Zhao, J.; Tabatabaei, K.; Amador, M. M.; Holmes, M. A.; Osterloh, F. E.; Kauzlarich, S. M. Thiol-Capped Germanium Nanocrystals: Preparation and Evidence for Quantum Size Effects. *Chem. Mater.* **2014**, *26* (6), 2138–2146.

(96) Yang, C.; Kauzlarich, S. M.; Wang, Y. C. Synthesis and Characterization of Germanium / Si-Alkyl and Germanium / Silica Core-Shell Quantum Dots. *Chem. Mater.* **1999**, *11* (12), 3666–3670.

(97) Ma, X.; Wu, F.; Kauzlarich, S. M. Alkyl-Terminated Crystalline Ge Nanoparticles Prepared from NaGe: Synthesis, Functionalization and Optical Properties. *J. Solid State Chem.* **2008**, *181* (7), 1628–1633.

(98) Tanke, R. S.; Kauzlarich, S. M.; Patten, T. E.; Pettigrew, K. a.; Murphy, D. L.; Thompson, M. E.; Lee, H. W. H. Synthesis of Germanium Nanoclusters with Irreversibly Attached Functional Groups: Acetals, Alcohols, Esters, and Polymers. *Chem. Mater.* **2003**, *15* (8), 1682–1689.

(99) Taylor, B. R.; Kauzlarich, S. M.; Delgado, G. R.; Lee, H. W. H.; Nanocrystals, L. E. S. Solution Synthesis and Characterization of Quantum Confined Ge Nanoparticles. *Chem. Mater.* **1999**, *11* (9), 2493–2500.

(100) Vaughn, D. D.; Bondi, J. F.; Schaak, R. E. Colloidal Synthesis of Air-Stable Crystalline Germanium Nanoparticles with Tunable Sizes and Shapes. *Chem. Mater.* **2010**, *22* (22), 6103–6108.

(101) Zaitseva, N.; Dai, Z. R.; Grant, C. D.; Harper, J.; Saw, C. Germanium Nanocrystals Synthesized in High-Boiling-Point Organic Solvents. *Chem. Mater.* **2007**, *19* (21), 5174–5178.

(102) Gerion, D.; Zaitseva, N.; Saw, C.; Casula, M. F.; Fakra, S.; Van Buuren, T.; Galli, G. Solution Synthesis of Germanium Nanocrystals: Success and Open Challenges. *Nano Lett.* **2004**, *4* (4), 597–602.

(103) Gerung, H.; Bunge, S. D.; Boyle, T. J.; Brinker, C. J.; Han, S. M. Anhydrous Solution Synthesis of Germanium Nanocrystals from the Germanium (II) Precursor Ge [N (SiMe 3) 2] 2. *Chem. Commun.* **2005**, No. 14, 1914–1916.

(104) Rimer, J. D.; Roth, D. D.; Vlachos, D. G.; Lobo, R. F. Self-Assembly and Phase Behavior of Germanium Oxide Nanoparticles in Basic Aqueous Solutions. *Langmuir* **2007**, *23* (5), 2784–2791.

(105) Lu, X.; Ziegler, K. J.; Ghezelbash, A.; Johnston, K. P.; Korgel, B. a. Synthesis of Germanium Nanocrystals in High Temperature Supercritical Fluid Solvents. *Nano Lett.* **2004**, *4* (5), 969–974.

(106) Peibst, R.; Erenburg, M.; Bugiel, E.; Hofmann, K. R. Effects Influencing Electron and Hole Retention Times in Ge Nanocrystal Memory Structures Operating in the Direct Tunneling Regime. *J. Appl. Phys.* **2010**, *108* (5), 054316.

(107) Liu, H.; Winkenwerder, W.; Liu, Y.; Ferrer, D.; Shahrjerdi, D.; Stanley, S. K.; Ekerdt, J. G.; Banerjee, S. K. Core-Shell Germanium–Silicon Nanocrystal Floating Gate for Nonvolatile Memory Applications. *IEEE Trans. Electron Devices* **2008**, *55* (12), 3610–3614.

(108) Neupane, M. R.; Lake, R. K.; Rahman, R. Electronic States of Ge/Si Nanocrystals with Crescent-Shaped Ge-Cores. *J. Appl. Phys.* **2012**, *112* (2), 024326.

(109) Dutta, A. K. Visible Photoluminescence from Ge Nanocrystal Embedded into a SiO2 Matrix Fabricated by Atmospheric Pressure Chemical Vapor Deposition. *Appl. Phys. Lett.* **1996**, *68* (9), 1189–1191.

(110) Zhang, J.-Y.; Bao, X.-M.; Ye, Y.-H. Synthesis of Ge Nanocrystals in Thermal SiO 2 Films by Ge+ Ion Implantation. *Thin Solid Films* **1998**, *323* (1), 68–71.

(111) Maeda, Y. Visible Photoluminescence from Nanocrystallite Ge Embedded in a Glassy SiO2 Matrix: Evidence in Support of the Quantum-Confinement Mechanism. *Phys. Rev. B* **1995**, *51* (3), 1658–1670.

(112) Javadi, M.; Yang, Z.; Veinot, J. G. C. Surfactant-Free Synthesis of GeO2 Nanocrystals with Controlled Morphologies. *Chem. Commun. (Camb).* **2014**, *50* (46), 6101–6104.

(113) Henderson, E. J.; Seino, M.; Puzzo, D. P.; Ozin, G. a. Colloidally Stable Germanium Nanocrystals for Photonic Applications. *ACS Nano* **2010**, *4* (12), 7683–7691.

(114) Nogami, M.; Abe, Y. Sol-gel Method for Synthesizing Visible Photoluminescent Nanosized Ge-crystal-doped Silica Glasses. *Appl. Phys. Lett.* **1994**, *65* (20), 2545–2547.

(115) Yang, H.; Yang, R.; Wan, X.; Wan, W. Structure and Photoluminescence of Ge Nanoparticles with Different Sizes Embedded in SiO 2 Glasses Fabricated by a Sol–gel Method. *J. Cryst. Growth* **2004**, *261* (4), 549–556.

(116) Yang, H.; Wang, X.; Shi, H.; Xie, S.; Wang, F.; Gu, X.; Yao, X. Photoluminescence of Ge Nanoparticles Embedded in SiO2 Glasses Fabricated by a Sol–gel Method. *Appl. Phys. Lett.* **2002**, *81* (27), 5144–5146.

(117) Yang, H. Q.; Yao, X.; Wang, X. J.; Xie, S. H.; Fang, Y.; Liu, S. X.; Gu, X. X. Sol-Gel Preparation and Photoluminescence of Size Controlled Germanium Nanoparticles Embedded in a SiO2 Matrix. *J. Phys. Chem. B* **2003**, *107* (48), 13319–13322.

(118) Puzzo, D. P.; Bonifacio, L. D.; Oreopoulos, J.; Yip, C. M.; Manners, I.; Ozin, G. A. Color from Colorless Nanomaterials: Bragg Reflectors Made of Nanoparticles. *J. Mater. Chem.* **2009**, *19* (21), 3500–3506.

(119) Hessel, C. M.; Henderson, E. J.; Veinot, J. G. C. An Investigation of the Formation and Growth of Oxide-Embedded Silicon Nanocrystals in Hydrogen Silsesquioxane-Derived Nanocomposites. *J. Phys. Chem. C* **2007**, *111*, 6956–6961.

(120) Kelly, J. a; Henderson, E. J.; Veinot, J. G. C. Sol-Gel Precursors for Group 14 Nanocrystals. *Chem. Commun. (Camb).* **2010**, *46* (46), 8704–8718.

(121) Hoffman, M.; Veinot, J. G. C. Understanding the Formation of Elemental Germanium by Thermolysis of Sol-Gel Derived Organogermanium Oxide Polymers. *Chem. Mater.* **2012**, *24* (7), 1283–1291.

(122) Henderson, E. J.; Hessel, C. M.; Veinot, J. G. C. Synthesis and Photoluminescent Properties of Size-Controlled Germanium Nanocrystals from Phenyl Trichlorogermane-Derived Polymers. *J. Am. Chem. Soc.* **2008**, *130* (11), 3624–3632.

(123) Henderson, E. J.; Hessel, C. M.; Cavell, R. G.; Veinot, J. G. C. How Processing Atmosphere Influences the Evolution of GeO2 -Embedded Germanium Nanocrystals Obtained from the Thermolysis of Phenyl Trichlorogermane-Derived Polymers. *Chem. Mater.* **2010**, *22* (8), 2653–2661.

(124) Wu, Y.; Yang, P. Germanium Nanowire Growth via Simple Vapor Transport. *Chem. Mater.* **2000**, *12* (3), 605–607.

(125) Peyghambarian, N.; Fluegel, B.; Hulin, D.; Migus, A.; Joffre, M.; Antonetti, A.; Koch, S. W.; Lindberg, M. Femtosecond Optical Nonlinearities of CdSe Quantum Dots. *IEEE J. Quantum Electron.* **1989**, *25* (12), 2516–2522.

(126) Martinić, I.; Eliseeva, S. V.; Petoud, S. Near-Infrared Emitting Probes for Biological Imaging: Organic Fluorophores, Quantum Dots, Fluorescent Proteins, Lanthanide (III) Complexes and Nanomaterials. *J. Lumin.* **2016**.

(127) de Oliveira, E. L.; Albuquerque, E. L.; de Sousa, J. S.; Farias, G. a.; Peeters, F. M. Configuration-Interaction Excitonic Absorption in Small Si/Ge and Ge/Si Core/Shell Nanocrystals. *J. Phys. Chem. C* **2012**, *116* (7), 4399–4407.

(128) Sánchez-Pérez, J. R.; Boztug, C.; Chen, F.; Sudradjat, F. F.; Paskiewicz, D. M.; Jacobson, R. B.; Lagally, M. G.; Paiella, R. Direct-Bandgap Light-Emitting Germanium in Tensilely Strained Nanomembranes. *Proc. Natl. Acad. Sci.* **2011**, *108* (47), 18893–18898.

(129) El Kurdi, M.; Fishman, G.; Sauvage, S.; Boucaud, P. Band Structure and Optical Gain of Tensile-Strained Germanium Based on a 30 Band K· p Formalism. *J. Appl. Phys.* **2010**, *107* (1), 013710.

(130) Ruddy, D. A.; Johnson, J. C.; Smith, E. R.; Neale, N. R.; Near-, S. S.; Ruddy, D. A.; Johnson, J. C.; Smith, E. R.; Neale, N. R. Size and Bandgap Control in the Solution-Phase Synthesis of Near-Infrared-Emitting Germanium Nanocrystals. *ACS Nano* **2010**, *4* (12), 7459–7466.

(131) Braunstein, R.; Moore, A. R.; Herman, F. Intrinsic Optical Absorption in Germanium-Silicon Alloys. *Phys. Rev.* **1958**, *109* (3), 695.

(132) Persson, C.; Mirbt, S. Improved Electronic Structure and Optical Properties of Sp-Hybridized Semiconductors Using LDA+ U SIC. *Brazilian J. Phys.* **2006**, *36* (2A), 286–290.

(133) Philipp, H. R.; Taft, E. A. Optical Constants of Germanium in the Region 1 to 10 eV. *Phys. Rev.* **1959**, *113* (4), 1002.

(134) Harris, T. R. Optical Properties of Si, Ge, GaAs, GaSb, InAs, and InP at Elevated Temperatures, DTIC Document, 2010.

(135) Javadi, M.; Yang, Z.; Veinot, J. G. C. Surfactant-Free Synthesis of GeO2 Nanocrystals with Controlled Morphologies. *Chem. Commun. (Camb).* **2014**, *50* (46), 6101–6104.

(136) Takeoka, S.; Fujii, M.; Hayashi, S.; Yamamoto, K. Size-Dependent near-Infrared Photoluminescence from Ge Nanocrystals Embedded in SiO 2 Matrices. *Phys. Rev. B* **1998**, *58* (12), 7921.

(137) Zacharias, M.; Fauchet, P. M. Blue Luminescence in Films Containing Ge and GeO2 Nanocrystals: The Role of Defects. *Appl. Phys. Lett.* **1997**, *71*, 380–382.

(138) Min, K. S.; Shcheglov, K. V; Yang, C. M.; Atwater, H. A.; Brongersma, M. L.; Polman, A. The Role of Quantum-confined Excitons vs Defects in the Visible Luminescence of SiO2 Films Containing Ge Nanocrystals. *Appl. Phys. Lett.* **1996**, *68* (18), 2511–2513.

(139) Millo, O.; Balberg, I.; Azulay, D.; Purkait, T. K.; Swarnakar, A. K.; Rivard, E.; Veinot, J. G. C.

Direct Evaluation of the Quantum Confinement Effect in Single Isolated Ge Nanocrystals. *J. Phys. Chem. Lett.* **2015**, *6* (17), 3396–3402.

(140) Niquet, Y. M.; Allan, G.; Delerue, C.; Lannoo, M. Quantum Confinement in Germanium Nanocrystals. *Appl. Phys. Lett.* **2000**, *77* (8), 1182–1184.

(141) Popescu, D. P.; Eliseev, P. G.; Stintz, A.; Malloy, K. J. Temperature Dependence of the Photoluminescence Emission from InAs Quantum Dots in a Strained GaO.85InO. 15As Quantum Well. *Semicond. Sci. Technol.* **2003**, *19* (1), 33–38.

(142) Nardis, S.; Mandoj, F.; Paolesse, R.; Fronczek, F. R.; Smith, K. M.; Prodi, L.; Montalti, M.; Battistini, G. Synthesis and Functionalization of Germanium Triphenylcorrolate: The First Example of a Partially Brominated Corrole. *Eur. J. Inorg. Chem.* **2007**, *2007* (16), 2345–2352.

(143) Kahan, A. Polarized Reflectivity Spectra of Tetragonal GeO2. *J. Appl. Phys.* **1971**, *42* (11), 4444.

(144) Takeuchi, H.; Wung, A.; Sun, X.; Howe, R. T.; King, T.; Member, S. Thermal Budget Limits of Quarter-Micrometer Foundry CMOS for Post-Processing MEMS Devices. **2005**, *52* (9), 2081–2086.

(145) Hsu, C.-H.; He, Y.-D.; Yang, S.-F. Microstructural, Optical and Electrical Properties of GeO2 Thin Films Prepared by Sol-Gel Method. *Cryst. Res. Technol.* **2011**, *46* (1), 65–68.

(146) Phani, A. R.; Di Claudio, D.; Passacantando, M.; Santucci, S. GeO2 Based High K Dielectric Material Synthesized by Sol–gel Process. *J. Non. Cryst. Solids* **2007**, *353* (5), 692–696.

(147) Yin, Z. Y.; Garside, B. K. Low-Loss GeO2 Optical Waveguide Fabrication Using Low Deposition Rate Rf Sputtering. *Appl. Opt.* **1982**, *21* (23), 4324–4328.

(148) Zacharias, M.; Fauchet, P. M. Light Emission from Ge and GeO2 Nanocrystals. *J. Non. Cryst. Solids* **1998**, *227* (230), 1058–1062.

(149) Wu, X. C.; Song, W. H.; Zhao, B.; Sun, Y. P.; Du, J. J. Preparation and Photoluminescence Properties of Crystalline GeO2 Nanowires. *Chem. Phys. Lett.* **2001**, *349* (3), 210–214.

(150) Zyubin, A. S.; Mebel, A. M.; Lin, S. H. Optical Properties of Oxygen Vacancies in Germanium Oxides: Quantum Chemical Modeling of Photoexcitation and Photoluminescence. *J. Phys. Chem. A* **2007**, *111* (38), 9479–9485.

(151) Peng, M.; Li, Y.; Gao, J.; Zhang, D.; Jiang, Z.; Sun, X. Electronic Structure and Photoluminescence Origin of Single-Crystalline Germanium Oxide Nanowires with Green Light Emission. *J. Phys. Chem. C* **2011**, *115* (23), 11420–11426.

(152) Chiu, Y.; Huang, M. H. Formation of Hexabranched GeO2 Nanoparticles via a Reverse Micelle System. *J. Phys. Chem. C* **2009**, *113*, 6056–6060.

(153) Patwardhan, S. V.; Clarson, S. J. Bioinspired Mineralisation: Macromolecule Mediated Synthesis of Amorphous Germania Structures. *Polymer (Guildf).* **2005**, *46* (12), 4474–4479.

(154) Kitschke, P.; Schulze, S.; Hietschold, M.; Mehring, M. Synthesis of Germanium Dioxide Nanoparticles in Benzyl Alcohols – a Comparison. *Main Gr. Met. Chem.* **2013**, *36* (5-6), 209–214.

(155) Tang, Y. H.; Zhang, Y. F.; Wang, N.; Bello, I.; Lee, C. S.; Lee, S. T. Germanium Dioxide Whiskers Synthesized by Laser Ablation. *Appl. Phys. Lett.* **1999**, *74* (25), 3824.

(156) Hidalgo, P.; Méndez, B.; Piqueras, J. High Aspect Ratio GeO2 Nano- and Microwires with Waveguiding Behaviour. *Nanotechnology* **2007**, *18* (15), 155203–155207.

(157) Viswanathamurthi, P.; Bhattarai, N.; Kim, H. Y.; Khil, M. S.; Lee, D. R.; Suh, E.-K. GeO2 Fibers: Preparation, Morphology and Photoluminescence Property. *J. Chem. Phys.* **2004**, *121* (1), 441–445.

(158) Yantasee, W.; Warner, C. L.; Sangvanich, T.; Addleman, R. S.; Carter, T. G.; Wiacek, R. J.;

Fryxell, G. E.; Timchalk, C.; Warner, M. G. Removal of Heavy Metals from Aqueous Systems with Thiol Functionalized Superparamagnetic Nanoparticles. *Environ. Sci. Technol.* **2007**, *41* (14), 5114–5119.

(159) Atuchin, V. V.; Gavrilova, T. A.; Gromilov, S. A.; Kostrovsky, V. G.; Pokrovsky, L. D.; Troitskaia, I. B.; Vemuri, R. S.; Carbajal-Franco, G.; Ramana, C. V. Low-Temperature Chemical Synthesis and Microstructure Analysis of GeO2Crystals with α-Quartz Structure. *Cryst. Growth Des.* **2009**, *9* (4), 1829–1832.

(160) Khan, M. A.; Hogan, T. P.; Shanker, B. Surface-Enhanced Raman Scattering from Gold-Coated Germanium Oxide Nanowires. **2008**, No. March, 893–900.

(161) Farhan, M.; Khan, M. a.; Hogan, T. P. Large Scale, Low Temperature Hotplate Synthesis of Germanium Dioxide Nanowires. *J. Alloys Compd.* **2010**, *508* (2), L21–L23.

(162) Yang, Z.; Veinot, J. G. C. Size-Controlled Template Synthesis of Metal-Free Germanium Nanowires. *J. Mater. Chem.* **2011**, *21* (41), 16505.

(163) Chen, X.; Cai, Q.; Zhang, J.; Chen, Z.; Wang, W.; Wu, Z.; Wu, Z. Synthesis and Growth of Germanium Oxide Nanoparticles in AOT Reversed Micelle. *Mater. Lett.* **2007**, *61* (2), 535–537.

(164) Wang, H.; Tao, Y.; Zhang, G. Q.; Xia, Y. P.; Gong, F. H.; Wu, H. P.; Tao, G. L. Germanium Dioxide Nanocubes with Different Size Distributions and Its Gibbs Free Energy Theory. *Mater. Sci. Forum* **2011**, *688*, 135–140.

(165) Wu, H. P.; Liu, J. F.; Ge, M. Y.; Niu, L.; Zeng, Y. W.; Wang, Y. W.; Lv, G. L.; Wang, L. N.; Zhang, G. Q.; Jiang, J. Z. Preparation of Monodisperse GeO2 Nanocubes in a Reverse Micelle System. *Chem. Mater.* **2006**, *18* (7), 1817–1820.

(166) Kawai, T.; Usui, Y.; Kon-no, K. Synthesis and Growth Mechanism of GeO2 Particles in AOT

Reversed Micelles. *Colloids Surfaces A Physicochem. Eng. Asp. 149* **1999**, *149*, 39–47.

(167) Wang, H.; Liu, J. F.; Wu, H. P.; He, Y.; Chen, W.; Wang, Y.; Zeng, Y. W.; Wang, Y. W.; Luo, C. J.; Liu, J.; et al. Phase Transformation in Nanocrystalline α-Quartz GeO2 up to 51.5 GPa. *J. Phys. Condens. Matter* **2006**, *18* (48), 10817–10824.

(168) Davis, T. M.; Snyder, M. a; Tsapatsis, M. Germania Nanoparticles and Nanocrystals at Room Temperature in Water and Aqueous Lysine Sols. *Langmuir* **2007**, *23* (25), 12469–12472.

(169) Kim, Y.; Hwang, H.; Lawler, K.; Martin, S. W.; Cho, J. Electrochemical Behavior of Ge and GeX2 (X = O, S) Glasses: Improved Reversibility of the Reaction of Li with Ge in a Sulfide Medium. *Electrochim. Acta* **2008**, *53* (15), 5058–5064.

(170) Goldstein, J.; Newbury, D. E.; Echlin, P.; Joy, D. C.; Romig Jr, A. D.; Lyman, C. E.; Fiori, C.; Lifshin, E. *Scanning Electron Microscopy and X-Ray Microanalysis: A Text for Biologists, Materials Scientists, and Geologists*; Springer Science & Business Media, 2012.

(171) Glinnemann, J. Erratum: Crystal Structures of the Low-Temperature Quartz-Type Phases of SiO2 and GeO2 at Elevated Pressure. *Zeitschrift für Krist. Mater.* **1992**, *202* (1-4), 269–270.

(172) Pokrovski, G. S.; Schott, J. Thermodynamic Properties of Aqueous Ge (IV) Hydroxide Complexes from 25 to 350 C: Implications for the Behavior of Germanium and the Ge/Si Ratio in Hydrothermal Fluids. *Geochim. Cosmochim. Acta* **1998**, *62* (9), 1631–1642.

(173) Ostwald, W. Lehrbuch Der Allgemeinen Chemie, Vol. 2, Part 1. Engelmann, Leipzig, Germany. German 1896.

(174) Schubert, U.; Hüsing, N. *Synthesis of Inorganic Materials*; John Wiley & Sons, 2012.

(175) Ghobadi, E.; Capobianco, J. A. Crystal Properties of α-Quartz Type GeO2. *Phys. Chem. Chem. Phys.* **2000**, *2* (24), 5761–5763.

(176) Zyubin, A. S.; Mebel, A. M.; Lin, S. H. Photoluminescence of Oxygen-Deficient Defects in Germanium Oxides: A Quantum Chemical Study. *J. Chem. Phys.* **2006**, *125* (6), 64701.

(177) Pasricha, A. *Encyclopaedia Eminent Thinkers (vol. 15: The Political Thought Of C. Rajagopalachari)*; Concept Publishing Company, 2008; Vol. 11.

(178) Moskalyk, R. R. Review of Germanium Processing Worldwide. *Miner. Eng.* **2004**, *17* (3), 393–402.

(179) Lippincott, E. R.; Van Valkenburg, A.; Weir, C. E.; Bunting, E. N. Infrared Studies on Polymorphs of Silicon Dioxide and Germanium Dioxide. *J. Res. Natl. Bur. Stand. (1934).* **1958**, *61* (1), 61–70.

(180) Darwish, H.; Salama, S. N.; Salman, S. M. Contribution of Germanium Dioxide to the Thermal Expansion Characteristics of Some Borosilicate Glasses and Their Corresponding Glass-Ceramics. *Thermochim. Acta* **2001**, *374* (2), 129–135.

(181) Saito, S.; Oda, K.; Takahama, T.; Tani, K.; Mine, T. Germanium Fin Light-Emitting Diode. *Appl. Phys. Lett.* **2011**, *99* (24), 241105.

(182) Sun, X. Ge-on-Si Light-Emitting Materials and Devices for Silicon Photonics. Massachusetts Institute of Technology 2009.

(183) Wu, S.; Han, C.; Iocozzia, J.; Lu, M.; Ge, R.; Xu, R.; Lin, Z. Germanium-Based Nanomaterials for Rechargeable Batteries. *Angew. Chemie Int. Ed.* **2016**, *55* (28), 7898–7922.

(184) Isomura, M.; Nakahata, K.; Shima, M.; Taira, S.; Wakisaka, K.; Tanaka, M.; Kiyama, S. Microcrystalline Silicon–germanium Solar Cells for Multi-Junction Structures. *Sol. energy Mater. Sol. cells* **2002**, *74* (1), 519–524.

(185) Sorianello, V.; Colace, L.; Maragliano, C.; Fulgoni, D.; Nash, L.; Assanto, G. Germanium-on-

Glass Solar Cells: Fabrication and Characterization. *Opt. Mater. Express* **2013**, *3* (2), 216–228.

(186) Taylor, B. R.; Kauzlarich, S. M.; Lee, H. W. H.; Delgado, G. R. Solution Synthesis of Germanium Nanocrystals Demonstrating Quantum Confinement. *Chem. Mater.* **1998**, *10* (1), 22–24.

(187) Yang, H.; Yao, X.; Xie, S.; Wang, X.; Liu, S.; Fang, Y.; Gu, X.; Wang, F. Structure and Photoluminescence of Ge Nanoparticles Embedded in SiO2 Gel Glasses Fabricated at Different Temperatures. *Opt. Mater. (Amst).* **2005**, *27* (4), 725–730.

(188) Shi, R.; Zhang, R.; Chen, X.; Yang, F.; Zhao, Q.; Yu, J.; Zhao, H.; Wang, L.; Liu, B.; Bao, L.; et al. Controllable Growth of GeO2 Nanowires with the Cubic and Hexagonal Phases and Their Photoluminescence. *J. Cryst. Growth* **2011**, *336* (1), 6–13.

(189) Oh, J.; Campbell, J. C. Thermal Desorption of Ge Native Oxides and the Loss of Ge from the Surface. *J. Electron. Mater.* **2004**, *33* (4), 364–367.

(190) Wang, S. K.; Kita, K.; Lee, C. H.; Tabata, T.; Nishimura, T.; Nagashio, K.; Toriumi, A. Desorption Kinetics of GeO from GeO2/Ge Structure. *J. Appl. Phys.* **2010**, *108* (5), 054104.

(191) Oh, J.; Campbell, J. C. Thermal Desorption of Ge Native Oxides and Loss of Ge from the Surface. *Mater. Sci. Semicond. Process.* **2010**, *13* (3), 185–188.

(192) Prabhakaran, K.; Maeda, F.; Watanabe, Y.; Ogino, T. Thermal Decomposition Pathway of Ge and Si Oxides: Observation of a Distinct Difference. *Thin Solid Films* **2000**, *369* (1-2), 289–292.

(193) Kita, K.; Suzuki, S.; Nomura, H.; Takahashi, T.; Nishimura, T.; Toriumi, A. Direct Evidence of GeO Volatilization from GeO2 /Ge and Impact of Its Suppression on GeO2 /Ge Metal–Insulator–Semiconductor Characteristics. *Jpn. J. Appl. Phys.* **2008**, *47* (4), 2349–2353.

(194) Prabhakaran, K.; Maeda, F.; Watanabe, Y.; Ogino, T. Distinctly Different Thermal Decomposition Pathways of Ultrathin Oxide Layer on Ge and Si Surfaces. *Appl. Phys. Lett.* **2000**, *76* (16), 2244–

2246.

(195) Jolly, W. L.; Latimer, W. M. The Equilibrium Ge (s)+ GeO2 (s)= 2GeO (g). The Heat of Formation of Germanic Oxide. *J. Am. Chem. Soc.* **1952**, *74* (22), 5757–5758.

(196) Law, J. T.; Meigs, P. S. Rates of Oxidation of Germanium. *J. Electrochem. Soc.* **1957**, *104* (3), 154–159.

(197) Zhang, X.; Xue, G.; Agarwal, A.; Tsu, R.; Hasan, M.; Greene, J. E.; Rockett, A. Thermal Desorption of Ultraviolet–ozone Oxidized Ge (001) for Substrate Cleaning. *J. Vac. Sci. Technol. A* **1993**, *11* (5), 2553–2561.

(198) Li, D.; Wang, H.; Liu, H. K.; Guo, Z. A New Strategy for Achieving a High Performance Anode for Lithium Ion Batteries—Encapsulating Germanium Nanoparticles in Carbon Nanoboxes. *Adv. Energy Mater.* **2016**, *6* (5), 1501666 – n/a.

(199) Cheng, S. C.; Liu, J. TEM Investigation of GeO2 Concentration Profiles in GeO2-SiO2 Soot Particles from Preforms of Outside Vapor Deposition. *Microsc. Microanal.* **2005**, *11* (S02), 2000–2001.

(200) Park, K.-T.; Um, H.-D.; Jee, S.-W.; Jung, J.-Y.; Park, Y. C.; Yang, J. M.; Lee, J.-H. Freestanding Ge/SiO2 Core/shell Nanoparticles Formed via Metastable SiO2 Hollow Nanospheres on a Si Wafer. *Chem. Vap. Depos.* **2008**, *14*, 331–333.

(201) Dianov, E. M.; Mashinsky, V. M. Germania-Based Core Optical Fibers. *J. Light. Technol.* **2005**, *23* (11), 3500.

(202) Kirkbir, F.; Chaudhuri, S. R. Optical Fibers from Sol-Gel-Derived Germania-Silica Glasses. In *San Diego'92*; International Society for Optics and Photonics, 1992; pp 160–172.

(203) Downs, R. T.; Bartelmehs, K. L.; Gibbs, G. V; Boisen, M. B.; Grnns, G. V; Borsnn, M. B.

Interactive Software for Calculating and Displaying X-Ray or Neutron Powder Diffractometer Patterns of Crystalline Materials. *Am. Mineral.* **1993**, *78* (9-10), 1104–1107.

(204) Kobayashi, Y.; Katakami, H.; Mine, E.; Nagao, D.; Konno, M.; Liz-Marzán, L. M. Silica Coating of Silver Nanoparticles Using a Modified Stober Method. *J. Colloid Interface Sci.* **2005**, *283* (2), 392–396.

(205) Ung, T.; Liz-marza, L. M. Controlled Method for Silica Coating of Silver Colloids . Influence of Coating on the Rate of Chemical Reactions. **1998**, *7463* (10), 3740–3748.

(206) Liz-marza, L. M.; Mulvaney, P. The Assembly of Coated Nanocrystals. *J. Phys. Chem. B* **2003**, *107* (30), 7312–7326.

(207) Liz-marza, L. M.; Giersig, M.; Mulvaney, P. Synthesis of Nanosized Gold - Silica Core - Shell Particles. **1996**, *7463* (5), 4329–4335.

(208) Pothirat, T.; Jongsomjit, B.; Praserthdam, P. Effect of Zr-Modified SiO2-Supported metallocene/MAO Catalyst on Copolymerization of ethylene/1-Octene. *Catal. Letters* **2008**, *121* (3-4), 266–273.

(209) Graf, C.; Dembski, S.; Hofmann, A.; Rühl, E. A General Method for the Controlled Embedding of Nanoparticles in Silica Colloids. *Langmuir* **2006**, *22* (13), 5604–5610.

(210) Drewitt, J. W. E.; Salmon, P. S.; Barnes, A. C.; Klotz, S.; Fischer, H. E.; Crichton, W. A. Structure of GeO2 Glass at Pressures up to 8.6 GPa. *Phys. Rev. B* **2010**, *81* (1), 14202.

(211) Dawson, C. J.; Sanchez-Smith, R.; Rez, P.; O'Keeffe, M.; Treacy, M. M. J.; Kee, M. O.; Treacy, M. M. J. Ab Initio Calculations of the Energy Dependence of Si–O–Si Angles in Silica and Ge–O–Ge Angles in Germania Crystalline Systems. *Chem. Mater.* **2014**, *26* (4), 1523–1527.

(212) Han, G.; Sohn, H. Y. Kinetics of the Hydrogen Reduction of Silica Incorporating the Effect of

Gas-Volume Change upon Reaction. *J. Am. Ceram. Soc.* **2005**, *88* (4), 882–888.

(213) Dasog, M.; Yang, Z.; Veinot, J. G. C. Size-Controlled Solid State Synthesis of Luminescent Silicon Nanocrystals Using Stöber Silica Particles. *CrystEngComm* **2012**, *14* (22), 7576.

(214) Dasog, M.; Smith, L. F.; Purkait, T. K.; Veinot, J. G. C. Low Temperature Synthesis of Silicon Carbide Nanomaterials Using a Solid-State Method. *Chem. Commun. (Camb).* **2013**, *49* (62), 7004–7006.

(215) Nagamori, M.; Malinsky, I.; Claveau, A. Thermodynamics of the Si-CO System for the Production of Silicon Carbide and Metallic Silicon. *Metall. Trans. B* **1986**, *17* (3), 503–514.

(216) Richman, E. K.; Kang, C. B.; Brezesinski, T.; Tolbert, S. H. Ordered Mesoporous Silicon through Magnesium Reduction of Polymer Templated Silica Thin Films. *Nano Lett.* **2008**, *8* (9), 3075–3079.

(217) Cai, Y.; Allan, S. M.; Sandhage, K. H.; Zalar, F. M. Three-Dimensional Magnesia-Based Nanocrystal Assemblies Via Low-Temperature Magnesiothermic Reaction of Diatom Microshells. *J. Am. Ceram. Soc.* **2005**, *88* (7).

(218) Kim, K. H.; Lee, D. J.; Cho, K. M.; Kim, S. J.; Park, J.-K.; Jung, H.-T. Complete Magnesiothermic Reduction Reaction of Vertically Aligned Mesoporous Silica Channels to Form Pure Silicon Nanoparticles. *Sci. Rep.* **2015**, *5*.

(219) Patton, G. L.; Iyer, S. S.; Delage, S. L.; Tiwari, S.; Stork, J. M. C. Silicon-Germanium Base Heterojunction Bipolar Transistors by Molecular Beam Epitaxy. *IEEE Electron Device Lett.* **1988**, *9* (4), 165–167.

(220) Weiner, C. How the Transistor Emerged. *IEEE Spectr.* **1973**, *10* (1), 24–33.

(221) Vörös, M.; Wippermann, S.; Somogyi, B.; Gali, A.; Rocca, D.; Galli, G.; Zimanyi, G. T.

Germanium Nanoparticles with Non-Diamond Core Structures for Solar Energy Conversion. *J. Mater. Chem. A* **2014**, *2* (25), 9820–9827.

(222) Lu, P.; Yang, P. Poly (3, 4-Ethylenedioxythiophene)/germanium Organic–inorganic Hybrid Thin Films: Substrate-Induced Synthesis, Enhanced Photoelectrochemical and Photocatalytic Properties. *RSC Adv.* **2016**, *6* (1), 601–606.

(223) Riabinina, D.; Durand, C.; Chaker, M.; Rowell, N.; Rosei, F. A Novel Approach to the Synthesis of Photoluminescent Germanium Nanoparticles by Reactive Laser Ablation. *Nanotechnology* **2006**, *17* (9), 2152–2155.

(224) Giri, P. K. Strain Analysis on Freestanding Germanium Nanocrystals. *J. Phys. D. Appl. Phys.* **2009**, *42* (24), 245402.

(225) Gorla, C. R. Silicon and Germanium Nanoparticle Formation in an Inductively Coupled Plasma Reactor. *J. Vac. Sci. Technol. A Vacuum, Surfaces, Film.* **1997**, *15* (3), 860.

(226) Jolly, W. L.; Latimer, W. M. The Solubility of Hydrous Germanous Oxide and the Potential of the Germanous Oxide-Germanic Oxid Couple. *J. Am. Chem. Soc.* **1952**, *74*, 5751–5752.

(227) Yang, D. J.; Jolly, W. L.; O'Keefe, A. Conversion of Hydrous germanium(II) Oxide to Germynyl Sesquioxide (HGe)2O3. *Inorg. Chem.* **1977**, *16* (11), 2980–2982.

(228) Dennis, L. M.; Hulse, R. E. Germanium XXXV. Germanium Monoxide. Germanium Mono Sulfide. *J. Am. Chem. Soc.* **1930**, *52*, 3553–3556.

(229) Gayer, K. H.; Zajicek, O. T. The Solubility of Germanium (II) Hydroxide in Perchloric Acid and Sodium Hydroxide at 25 °C. *J. Inorg. Nucl. Chem.* **1964**, *26*, 2123–2125.

(230) Babich, O. A.; Ghosh, M. C.; Gould, E. S. Preparation of Aqueous Solutions of Hypovalent Germanium; Reactions Involving Germanium-(II) and -(III). *Chem. Commun.* **2000**, No. 11, 907–

908.

(231) Terrey, H.; Everest, D. A.; Terrey, H. *Germanous Oxide and Sulphide*; Royal Society of Chemistry, 1950.

(232) Sun, W.; Zhong, G.; Kübel, C.; Jelle, A. A.; Qian, C.; Wang, L.; Ebrahimi, M.; Reyes, L. M.; Helmy, A. S.; Ozin, G. A. Size-Tunable Photothermal Germanium Nanocrystals. *Angew. Chemie* **2017**, *129*, 6426–6431.

(233) Rochow, E. G.; Abel, E. W. *The Chemistry of Germanium: Tin and Lead*; Elsevier, 2014; Vol. 14.

(234) Kuhn, W. K. Zinc Germanium Phosphide by XPS. *Surf. Sci. Spectra* **1994**, *3* (2), 93–99.

(235) Yang, D. J.; Jolly, W. L.; O'Keefe, A. Conversion of Hydrous Germanium (ii) Oxide to Germynyl sesquioxide,(Hge) 2O3. *Inorg. Chem.* **1977**, *16* (11), 2980–2982.

(236) Strahlenchemie, B.; Heights, Y.; Heights, Y.; Schmeisser, D.; Schnell, R. D.; Bogen, A.; Himpsel, F. J.; Rieger, D.; Landgren, G.; Morar, J. F. Surface Oxidation States of Germanium. *Surf. Sci.* **1986**, *172* (2), 455–465.

(237) Fujii, M.; Hayashi, S.; Yamamoto, K. Growth of Ge Microcrystals in SiO2 Thin Film Matrices. A Raman and Electron Microscopic Study. *Japanese J. Appl. Physics, Part 1 Regul. Pap. Short Notes Rev. Pap.* **1991**, *30*, 687–694.

(238) Karavanskii, V. A.; Lomov, A. A.; Sutyrin, A. G.; Bushuev, V. a.; Loikho, N. N.; Melnik, N. N.; Zavaritskaya, T. N.; Bayliss, S. Raman and X-Ray Studies of Nanocrystals in Porous Stain-Etched Germanium. *Thin Solid Films* **2003**, *437* (1-2), 290–296.

(239) Trucks, G. W.; Raghavachari, K.; Higashi, G. S.; Chabal, Y. J. Mechanism of HF Etching of Silicon Surfaces: A Theoretical Understanding of Hydrogen Passivation. *Phys. Rev. Lett.* **1990**, *65* (4), 504.

(240) Choi, H. C.; Buriak, J. M. Preparation and Functionalization of Hydride Terminated Porous germaniumElectronic Supplementary Information (ESI) Available: FTIR Thermal Stability Measurements and SEM Images. See Http://www. Rsc. org/suppdata/cc/b0/b004011h. *Chem. Commun.* **2000**, No. 17, 1669–1670.

(241) Buriak, J. M. Organometallic Chemistry on Silicon and Germanium Surfaces. *Chem. Rev.* **2002**, *102* (5), 1271–1308.

(242) Yang, Z.; Gonzalez, C. M.; Purkait, T. K.; Iqbal, M.; Meldrum, A.; Veinot, J. G. C. Radical Initiated Hydrosilylation on Silicon Nanocrystal Surfaces: An Evaluation of Functional Group Tolerance and Mechanistic Study. *Langmuir* **2015**, *31* (38), 10540–10548.

(243) Fuchs, R.; Moore, L.; Miles, D.; Gilmak, H. Some Symmetrical Tetraalkyl- and Tetraaralkyl-Germanes. *J. Org. Chem.* **1956**, 1113–1117.

(244) Ostwald, W. *Lehrbuch Der Allgemeinen Chemie*; W. Engelmann: Leipzig, 1896.

(245) Seng, K. H.; Park, M.-H.; Guo, Z. P.; Liu, H. K.; Cho, J. Self-Assembled Germanium/carbon Nanostructures as High-Power Anode Material for the Lithium-Ion Battery. *Angew. Chem. Int. Ed. Engl.* **2012**, *51* (23), 5657–5661.

(246) SI Yang, Z.; Dobbie, A. R.; Cui, K.; Veinot, J. G. C.; Yang, Z.; Dobbie, A. R.; Cui, K.; Veinot, J. G. C. A Convenient Method for Preparing Alkyl-Functionalized Silicon Nanocubes. *J. Am. Chem. Soc.* **2012**, *134* (34), 13958–13961.

(247) Yang, Z.; Iqbal, M.; Dobbie, A. R.; Veinot, J. G. C. Surface-Induced Alkene Oligomerization: Does Thermal Hydrosilylation Really Lead to Monolayer Protected Silicon Nanocrystals? *J. Am. Chem. Soc.* **2013**, *135* (46), 17595–17601.

(248) Reisman, A.; Alyanakyan, S. A. Thermodynamic Analyses of Open Tube Germanium

Disproportionation Reactions. *J. Electrochem. Soc.* **1964**, *111* (10), 1154–1164.

(249) Gayer, K. H.; Zajicek, O. T. The Solubility of Germanium (IV) Oxide in Aqueous NaOH Solutions at 25°C. *J. Inorg. Nucl. Chem.* **1964**, *26* (6), 951–954.

(250) Sun, X. H.; Didychuk, C.; Sham, T. K.; Wong, N. B. Germanium Nanowires: Synthesis, Morphology and Local Structure Studies. *Nanotechnology* **2006**, *17* (12), 2925.

(251) Buriak, J. M. Organometallic Chemistry on Silicon and Germanium Surface. *Chem. Rev.* **2002**, *102* (5), 1271–1380.

(252) Gottlieb, H. E.; Kotlyar, V.; Nudelman, A. NMR Chemical Shifts of Common Laboratory Solvents as Trace Impurities. *J. Org. Chem.* **1997**, *62* (21), 7512–7515.

(253) Fulmer, G. R.; Miller, A. J. M.; Sherden, N. H.; Gottlieb, H. E.; Nudelman, A.; Stoltz, B. M.; Bercaw, J. E.; Goldberg, K. I. NMR Chemical Shifts of Trace Impurities: Common Laboratory Solvents, Organics, and Gases in Deuterated Solvents Relevant to the Organometallic Chemist. *Organometallics* **2010**, *29* (9), 2176–2179.

(254) Cheng, X.; Lowe, S. B.; Ciampi, S.; Magenau, A.; Gaus, K.; Reece, P. J.; Gooding, J. J. Versatile "Click Chemistry" Approach to Functionalizing Silicon Quantum Dots: Applications toward Fluorescent Cellular Imaging. *Langmuir* **2014**, *30* (18), 5209–5216.

(255) Purkait, T. K.; Iqbal, M.; Wahl, M. H.; Gottschling, K.; Gonzalez, C. M.; Islam, M. A.; Veinot, J. G. C. Borane-Catalyzed Room-Temperature Hydrosilylation of Alkenes/Alkynes on Silicon Nanocrystal Surfaces. *J. Am. Chem. Soc.* **2014**, *136* (52), 17914–17917.

(256) Clayden, J.; Greeves, N.; Warren, S. G. *Organic Chemistry.*; Oxford ; New York : Oxford University Press, 2012., 2012.

(257) Hua, F.; Swihart, M. T.; Ruckenstein, E. Efficient Surface Grafting of Luminescent Silicon

Quantum Dots by Photoinitiated Hydrosilylation. *Langmuir* **2005**, *21* (13), 6054–6062.

(258) Weber, J. R.; Janotti, A.; Van de Walle, C. G. Defects in Germanium. In *Photonics and Electronics with Germanium*; Wiley-VCH Verlag GmbH & Co. KGaA, 2015; pp 1–23.

(259) Bigall, N. C.; Parak, W. J.; Dorfs, D. Fluorescent, Magnetic and plasmonic—Hybrid Multifunctional Colloidal Nano Objects. *Nano Today* **2012**, *7* (4), 282–296.

(260) Suh, W. H.; Suh, Y.-H.; Stucky, G. D. Multifunctional Nanosystems at the Interface of Physical and Life Sciences. *Nano Today* **2009**, *4* (1), 27–36.

(261) Mahajan, K. D.; Fan, Q.; Ruan, G.; Winter, J. O. Magnetic Quantum Dots in Biotechnology – Synthesis and Applications. **2013**, 1424–1434.

(262) Mahmoudi, M.; Shokrgozar, M. A. Multifunctional Stable Fluorescent Magnetic Nanoparticles. *Chem. Commun.* **2012**, *48* (33), 3957–3959.

(263) Yang, W. J.; Lee, J. H.; Hong, S. C.; Lee, J.; Lee, J.; Han, D.-W. Difference between Toxicities of Iron Oxide Magnetic Nanoparticles with Various Surface-Functional Groups against Human Normal Fibroblasts and Fibrosarcoma Cells. *Materials (Basel).* **2013**, *6* (10), 4689–4706.

(264) Corr, S. A.; Rakovich, Y. P.; Gun'ko, Y. K. Multifunctional Magnetic-Fluorescent Nanocomposites for Biomedical Applications. *Nanoscale Res. Lett.* **2008**, *3* (3), 87–104.

(265) Hu, F. Q.; Wei, L.; Zhou, Z.; Ran, Y. L.; Li, Z.; Gao, M. Y. Preparation of Biocompatible Magnetite Nanocrystals for In Vivo Magnetic Resonance Detection of Cancer. *Adv. Mater.* **2006**, *18* (19), 2553–2556.

(266) Quarta, A.; Corato, R. Di; Manna, L.; Ragusa, A.; Pellegrino, T. Fluorescent-Magnetic Hybrid Nanostructures : Preparation , Properties , and Applications in Biology. **2007**, *6* (4), 298–308.

(267) Oxide, I. I. I. I.; Erogbogbo, F.; Yong, K.-T.; Hu, R.; Law, W.; Ding, H.; Chang, C.; Prasad, P. N.;

Swihart, M. T. Biocompatible Magnetofluorescent Probes: Luminescent Silicon Quantum Dots Coupled with Superparamagnetic Iron(III) Oxide. *ACS Nano* **2010**, *4* (9), 5131–5138.

(268) Budde, M. D.; Frank, J. A. Magnetic Tagging of Therapeutic Cells for MRI. *J. Nucl. Med.* **2009**, *50* (2), 171–174.

(269) Kim, J.; Lee, J. E.; Lee, J.; Yu, J. H.; Kim, B. C.; An, K.; Hwang, Y.; Shin, C.-H.; Park, J.-G.; Kim, J. Magnetic Fluorescent Delivery Vehicle Using Uniform Mesoporous Silica Spheres Embedded with Monodisperse Magnetic and Semiconductor Nanocrystals. *J. Am. Chem. Soc.* **2006**, *128* (3), 688–689.

(270) Weller, H. Quantum Size Colloids: From Size-Dependent Properties of Discrete Particles to Self-Organized Superstructures. *Curr. Opin. Colloid Interface Sci.* **1998**, *3* (2), 194–199.

(271) Alivisatos, P. The Use of Nanocrystals in Biological Detection. *Nat Biotech* **2004**, *22* (1), 47–52.

(272) Murrag, C. B.; Norris, D. B.; Bawendi, M. G. 'Synthesis and Characterization of Nearly Monodisperse CdE (E= S, Se, Te) Semiconductor Nanocrystallite. *J. Am. Chem. Soc* **1993**, *115* (19), 8706–8715.

(273) Wang, S.; Jarrett, B. R.; Kauzlarich, S. M.; Louie, A. Y. Core/shell Quantum Dots with High Relaxivity and Photoluminescence for Multimodality Imaging. *J. Am. Chem. Soc.* **2007**, *129* (13), 3848–3856.

(274) Veiseh, O.; Sun, C.; Gunn, J.; Kohler, N.; Gabikian, P.; Lee, D.; Bhattarai, N.; Ellenbogen, R.; Sze, R.; Hallahan, A. Optical and MRI Multifunctional Nanoprobe for Targeting Gliomas. *Nano Lett.* **2005**, *5* (6), 1003–1008.

(275) Ruan, G.; Vieira, G.; Henighan, T.; Chen, A.; Thakur, D.; Sooryakumar, R.; Winter, J. O. Simultaneous Magnetic Manipulation and Fluorescent Tracking of Multiple Individual Hybrid

Nanostructures. *Nano Lett.* **2010**, *10* (6), 2220–2224.

(276) Ang, C. Y.; Giam, L.; Chan, Z. M.; Lin, A. W. H.; Gu, H.; Devlin, E.; Papaefthymiou, G. C.; Selvan, S. T.; Ying, J. Y. Facile Synthesis of Fe2O3 Nanocrystals without Fe(CO)5 Precursor and One-Pot Synthesis of Highly Fluorescent Fe2O3–CdSe Nanocomposites. *Adv. Mater.* **2009**, *21* (8), 869–873.

(277) Chen, O.; Riedemann, L.; Etoc, F.; Herrmann, H.; Coppey, M.; Barch, M.; Farrar, C. T.; Zhao, J.; Bruns, O. T.; Wei, H.; et al. Magneto-Fluorescent Core-Shell Supernanoparticles. *Nat. Commun.* **2014**, *5*, 5093.

(278) Fujioka, K.; Hiruoka, M.; Sato, K.; Manabe, N.; Miyasaka, R.; Hanada, S.; Hoshino, A.; Tilley, R. D.; Manome, Y.; Hirakuri, K. Luminescent Passive-Oxidized Silicon Quantum Dots as Biological Staining Labels and Their Cytotoxicity Effects at High Concentration. *Nanotechnology* **2008**, *19* (41), 415102.

(279) Park, J.-H.; Gu, L.; Von Maltzahn, G.; Ruoslahti, E.; Bhatia, S. N.; Sailor, M. J. Biodegradable Luminescent Porous Silicon Nanoparticles for in Vivo Applications. *Nat. Mater.* **2009**, *8* (4), 331–336.

(280) Bimbo, L. M.; Sarparanta, M.; Santos, H. A.; Airaksinen, A. J.; Mäkilä, E.; Laaksonen, T.; Peltonen, L.; Lehto, V.-P.; Hirvonen, J.; Salonen, J. Biocompatibility of Thermally Hydrocarbonized Porous Silicon Nanoparticles and Their Biodistribution in Rats. *ACS Nano* **2010**, *4* (6), 3023–3032.

(281) Ge, S.; Shi, X.; Sun, K.; Li, C.; Uher, C.; Baker, J. R.; Banaszak Holl, M. M.; Orr, B. G.; Baker Jr, J. R.; Banaszak Holl, M. M.; et al. Facile Hydrothermal Synthesis of Iron Oxide Nanoparticles with Tunable Magnetic Properties. *J. Phys. Chem. C* **2009**, *113* (31), 13593–13599.

(282) Gonzales, M.; Mitsumori, L. M.; Kushleika, J. V; Rosenfeld, M. E.; Krishnan, K. M. Cytotoxicity

of Iron Oxide Nanoparticles Made from the Thermal Decomposition of Organometallics and Aqueous Phase Transfer with Pluronic F127. *Contrast Media Mol. Imaging* **2010**, *5* (5), 286–293.

(283) Palmer, R. K.; Hutchinson, L. M.; Burpee, B. T.; Tupper, E. J.; Pelletier, J. H.; Kormendy, Z.; Hopke, A. R.; Malay, E. T.; Evans, B. L.; Velez, A. Antibacterial Agent Triclosan Suppresses RBL-2H3 Mast Cell Function. *Toxicol. Appl. Pharmacol.* **2012**, *258* (1), 99–108.

(284) Ortega, V. A.; Ede, J. D.; Boyle, D.; Stafford, J. L.; Goss, G. G. Polymer-Coated Metal-Oxide Nanoparticles Inhibit IgE Receptor Binding, Cellular Signaling, and Degranulation in a Mast Cell-like Cell Line. *Adv. Sci.* **2015**, *2* (11).

(285) Chen, S.; Gong, J.; Liu, F.; Mohammed, U. Naturally Occurring Polyphenolic Antioxidants Modulate IgE-mediated Mast Cell Activation. *Immunology* **2000**, *100* (4), 471–480.

(286) Feltis, B. N.; Elbaz, A.; Wright, P. F. A.; Mackay, G. A.; Turney, T. W.; Lopata, A. L. Characterizing the Inhibitory Action of Zinc Oxide Nanoparticles on Allergic-Type Mast Cell Activation. *Mol. Immunol.* **2015**, *66* (2), 139–146.

(287) Ede, J. D.; Ortega, V. A.; Boyle, D.; Beingessner, R. L.; Hemraz, U. D.; Fenniri, H.; Stafford, J. L.; Goss, G. G. Rosette Nanotubes Alter IgE-Mediated Degranulation in the Rat Basophilic Leukemia (RBL)-2H3 Cell Line. *Toxicol. Sci.* **2015**, kfv166.

(288) Gilfillan, A. M.; Tkaczyk, C. Integrated Signalling Pathways for Mast-Cell Activation. *Nat. Rev. Immunol.* **2006**, *6* (3), 218–230.

(289) Massol, P.; Montcourrier, P.; Guillemot, J.; Chavrier, P. Fc Receptor-mediated Phagocytosis Requires CDC42 and Rac1. *EMBO J.* **1998**, *17* (21), 6219–6229.

(290) Cortes, H. D.; Montgomery, B. C.; Verheijen, K.; García-García, E.; Stafford, J. L. Examination of the Stimulatory Signaling Potential of a Channel Catfish Leukocyte Immune-Type Receptor and

Associated Adaptor. *Dev. Comp. Immunol.* **2011**.

(291) Sun, S.; Zeng, H.; Robinson, D. B.; Raoux, S.; Rice, P. M.; Wang, S. X.; Li, G. Monodisperse MFe2O4 (M= Fe, Co, Mn) Nanoparticles. *J. Am. Chem. Soc.* **2004**, *126* (1), 273–279.

(292) Bao, N.; Shen, L.; Wang, Y.; Padhan, P.; Gupta, A. Ref 27-A Facile Thermolysis Route to Monodisperse Ferrite Nanocrystals. *J. Am. Chem. Soc.* **2007**, *129* (41), 12374–12375.

(293) Sun, S.; Zeng, H. Size-Controlled Synthesis of Magnetite Nanoparticles. *J. Am. Chem. Soc.* **2002**, *124* (28), 8204–8205.

(294) Pavía-Sanders, A.; Zhang, S.; Flores, J. a; Sanders, J. E.; Raymond, J. E.; Wooley, K. L. Robust Magnetic (SI)/Polymer Hybrid Nanoparticles Designed for Crude Oil Entrapment and Recovery in Aqueous Environments. *ACS Nano* **2013**, No. Xx, 1–6.

(295) Shen, M.; Cai, H.; Wang, X.; Cao, X.; Li, K.; Wang, S. H.; Guo, R.; Zheng, L.; Zhang, G.; Shi, X. Facile One-Pot Preparation, Surface Functionalization, and Toxicity Assay of APTS-Coated Iron Oxide Nanoparticles. *Nanotechnology* **2012**, *23* (10), 105601.

(296) Hu, F.; Li, Z.; Tu, C.; Gao, M. Preparation of Magnetite Nanocrystals with Surface Reactive Moieties by One-Pot Reaction. *J. Colloid Interface Sci.* **2007**, *311* (2), 469–474.

(297) Xie, J.; Chen, K.; Lee, H.-Y.; Xu, C.; Hsu, A. R.; Peng, S.; Chen, X.; Sun, S. Ultrasmall c(RGDyK)-Coated Fe3O4 Nanoparticles and Their Specific Targeting to Integrin αvβ3-Rich Tumor Cells. *J. Am. Chem. Soc.* **2008**, *130* (24), 7542–7543.

(298) Mohapatra, S.; Pramanik, N.; Mukherjee, S.; Ghosh, S. K.; Pramanik, P. A Simple Synthesis of Amine-Derivatised Superparamagnetic Iron Oxide Nanoparticles for Bioapplications. *J. Mater. Sci.* **2007**, *42* (17), 7566–7574.

(299) Eltouny, N.; Ariya, P. A. Competing Reactions of Selected Atmospheric Gases on Fe 3 O 4

Nanoparticles Surfaces. *Phys. Chem. Chem. Phys.* **2014**, *16* (42), 23056–23066.

(300) Wilson, D.; Langell, M. A. XPS Analysis of Oleylamine/oleic Acid Capped Fe3O4 Nanoparticles as a Function of Temperature. *Appl. Surf. Sci.* **2014**, *303*, 6–13.

(301) Fan, T.; Pan, D.; Zhang, H. Study on Formation Mechanism by Monitoring the Morphology and Structure Evolution of Nearly Monodispersed Fe3O4 Submicroparticles with Controlled Particle Sizes. *Ind. Eng. Chem. Res.* **2011**, *50* (15), 9009–9018.

(302) Eltouny, N. A.; Ariya, P. A. Fe 3O 4 Nanoparticles and Carboxymethyl Cellulose: A Green Option for the Removal of Atmospheric Benzene, Toluene, Ethylbenzene, and O -Xylene (BTEX). *Ind. Eng. Chem. Res.* **2012**, *51* (39), 12787–12795.

(303) Poulin, S.; França, R.; Moreau-Bélanger, L.; Sacher, E. Confirmation of X-Ray Photoelectron Spectroscopy Peak Attributions of Nanoparticulate Iron Oxides, Using Symmetric Peak Component Line Shapes. *J. Phys. Chem. C* **2010**, *114* (24), 10711–10718.

(304) Descostes, M.; Mercier, F.; Thromat, N.; Beaucaire, C.; Gautier-Soyer, M. Use of XPS in the Determination of Chemical Environment and Oxidation State of Iron and Sulfur Samples: Constitution of a Data Basis in Binding Energies for Fe and S Reference Compounds and Applications to the Evidence of Surface Species of an Oxidized Py. *Appl. Surf. Sci.* **2000**, *165* (4), 288–302.

(305) Laurent, S.; Forge, D.; Port, M.; Roch, A.; Robic, C.; Vander Elst, L.; Muller, R. N. Magnetic Iron Oxide Nanoparticles: Synthesis, Stabilization, Vectorization, Physicochemical Characterizations, and Biological Applications. *Chem. Rev.* **2008**, *108* (6), 2064–2110.

(306) Lu, A.; Salabas, E. emsp14L; Schüth, F. Magnetic Nanoparticles: Synthesis, Protection, Functionalization, and Application. *Angew. Chemie Int. Ed.* **2007**, *46* (8), 1222–1244.

(307) Huber, D. L. Synthesis, Properties, and Applications of Iron Nanoparticles. *Small* **2005**, *1* (5), 482–501.

(308) Xu, H.; Zhu, X.; Sun, K.; Liu, Y.; Xie, X. Elaborately Designed Hierarchical Heterostructures Consisting of Carbon-Coated TiO2 (B) Nanosheets Decorated with Fe3O4 Nanoparticles for Remarkable Synergy in High-Rate Lithium Storage. *Adv. Mater. Interfaces* **2015**, *2* (15).

(309) Chen, Z.; Hu, J.; Lu, Z.; He, X. Low-Temperature Preparation of Lanthanum-Doped BiFeO 3 Crystallites by a Sol–gel-Hydrothermal Method. *Ceram. Int.* **2011**, *37* (7), 2359–2364.

(310) Bordbar, A. K.; Rastegari, A. A.; Amiri, R.; Ranjbakhsh, E.; Abbasi, M.; Khosropour, A. R. Characterization of Modified Magnetite Nanoparticles for Albumin Immobilization. *Biotechnol. Res. Int.* **2014**, *2014*.

(311) Dasog, M.; Yang, Z.; Regli, S.; Atkins, T. M.; Faramus, A.; Singh, M. P.; Muthuswamy, E.; Kauzlarich, S. M.; Tilley, R. D.; Veinot, J. G. C. Chemical Insight into the Origin of Red and Blue Photoluminescence Arising from Freestanding Silicon Nanocrystals. *ACS Nano* **2013**, *7* (3), 2676–2685.

(312) Sheehan, J. C.; Hess, G. P.; Lerner, A. B.; Lee, T. E. H. H. A New Method of Forming Peptide Bonds. *J. Am. Chem. Soc.* **1955**, *77* (4), 1067–1068.

(313) Neises, B.; Steglich, W. Simple Method for the Esterification of Carboxylic Acids. *Angew. Chemie Int. Ed. English* **1978**, *17* (7), 522–524.

(314) Wilkinson, K.; Ekstrand-Hammarström, B.; Ahlinder, L.; Guldevall, K.; Pazik, R.; Kępiński, L.; Kvashnina, K. O.; Butorin, S. M.; Brismar, H.; Önfelt, B. Visualization of Custom-Tailored Iron Oxide Nanoparticles Chemistry, Uptake, and Toxicity. *Nanoscale* **2012**, *4* (23), 7383–7393.

(315) AshaRani, P. V; Low Kah Mun, G.; Hande, M. P.; Valiyaveettil, S. Cytotoxicity and Genotoxicity

of Silver Nanoparticles in Human Cells. *ACS Nano* **2008**, *3* (2), 279–290.

(316) Sharma, J.; Rocha, R. C.; Phipps, M. L.; Yeh, H.-C.; Balatsky, K. A.; Vu, D. M.; Shreve, A. P.; Werner, J. H.; Martinez, J. S. A DNA-Templated Fluorescent Silver Nanocluster with Enhanced Stability. *Nanoscale* **2012**, *4* (14), 4107–4110.

(317) Elmore, S. Apoptosis: A Review of Programmed Cell Death. *Toxicol. Pathol.* **2007**, *35* (4), 495–516.

(318) Kroemer, G.; Galluzzi, L.; Vandenabeele, P.; Abrams, J.; Alnemri, E. S.; Baehrecke, E. H.; Blagosklonny, M. V; El-Deiry, W. S.; Golstein, P.; Green, D. R. Classification of Cell Death: Recommendations of the Nomenclature Committee on Cell Death 2009. *Cell Death Differ.* **2009**, *16* (1), 3–11.

(319) Galluzzi, L.; Vitale, I.; Abrams, J. M.; Alnemri, E. S.; Baehrecke, E. H.; Blagosklonny, M. V; Dawson, T. M.; Dawson, V. L.; El-Deiry, W. S.; Fulda, S. Molecular Definitions of Cell Death Subroutines: Recommendations of the Nomenclature Committee on Cell Death 2012. *Cell Death Differ.* **2012**, *19* (1), 107–120.

(320) Kou, L.; Sun, J.; Zhai, Y.; He, Z. The Endocytosis and Intracellular Fate of Nanomedicines: Implication for Rational Design. *Asian J. Pharm. Sci.* **2013**, *8* (1), 1–10.

(321) Ede, J. D.; Ortega, V. A.; Boyle, D.; Beingessner, R. L.; Hemraz, U. D.; Fenniri, H.; Stafford, J. L.; Goss, G. G. The Effects of Rosette Nanotubes with Different Functionalizations on Channel Catfish (Ictalurus Punctatus) Lymphocyte Viability and Receptor Function. *Environ. Sci. Nano* **2016**, *3* (3), 578–592.

(322) Felix, L. C.; Ortega, V. A.; Ede, J. D.; Goss, G. G. Physicochemical Characteristics of Polymer-Coated Metal-Oxide Nanoparticles and Their Toxicological Effects on Zebrafish (Danio Rerio) Development. *Environ. Sci. Technol.* **2013**, *47* (12), 6589–6596.

(323) Claeys, C.; Simoen, E. *Germanium-Based Technologies: From Materials to Devices*; Elsevier, 2011.

(324) Wu, X. C. Preparation and Photoluminescence Properties of Crystalline GeO2 Nanowires. **2001**, *349* (November), 210–214.

(325) Madsen, H. E. L.; Boistelle, R. Solubility of Octacosane and Hexatriacontane in Different N-Alkane Solvents. *J. Chem. Soc. Faraday Trans. 1 Phys. Chem. Condens. Phases* **1978**, *75*, 1254–1258.

(326) Werner, M. J.; Friberg, S. R. Phase Transitions and the Internal Noise Structure of Nonlinear Schrödinger Equation Solitons. *Phys. Rev. Lett.* **1997**, *79* (21), 4143.

(327) Stöber, W.; Fink, A.; Bohn, E. Controlled Growth of Monodisperse Silica Spheres in the Micron Size Range. *J. Colloid Interface Sci.* **1968**, *26* (1), 62–69.

(328) Islam, M. A.; Purkait, T. K.; Mobarok, M. H.; Hoehlein, I.; Sinelnikov, R.; Iqbal, M.; Azulay, D.; Balberg, I.; Millo, O.; Rieger, B. Grafting Poly (3-hexylthiophene) from Silicon Nanocrystal Surfaces: Synthesis and Properties of a Functional Hybrid Material with Direct Interfacial Contact. *Angew. Chemie Int. Ed.* **2016**, *55* (26), 7393–7397.

(329) Cosentino, S.; Torrisi, G.; Raciti, R.; Zimbone, M.; Crupi, I.; Mirabella, S.; Terrasi, A. Growth Kinetics of Colloidal Ge Nanocrystals for Light Harvesters. *RSC Adv.* **2016**, *6* (44), 38454–38462.

(330) Xue, D.; Wang, J.; Wang, Y.; Xin, S.; Guo, Y.; Wan, L. Facile Synthesis of Germanium Nanocrystals and Their Application in Organic–inorganic Hybrid Photodetectors. *Adv. Mater.* **2011**, *23* (32), 3704–3707.

(331) Mobarok, M. H.; Purkait, T. K.; Islam, M. A.; Miskolzie, M.; Veinot, J. G. C. Instantaneous Functionalization of Chemically Etched Silicon Nanocrystal Surfaces. *Angew. Chemie* **2016**, *128*.

(332) Yang, Z.; Wahl, M. H.; Veinot, J. G. C. Size-Independent Organosilane Functionalization of Silicon Nanocrystals Using Wilkinson's Catalyst. *Can. J. Chem.* **2014**, *92* (10), 951–957.

(333) Azpeitia, S.; Fernández, B.; Garralda, M. A.; Huertos, M. A. Dehydrogenative Coupling of a Tertiary Silane Using Wilkinson's Catalyst. **2016**, *2*, 2891–2895.

(334) Li, Y.-H.; Buriak, J. M. Dehydrogenative Silane Coupling on Silicon Surfaces via Early Transition Metal Catalysis. *Inorg. Chem.* **2006**, *45* (3), 1096–1102.

(335) Fan, J.; Chu, P. K. Group IV Nanoparticles: Synthesis, Properties, and Biological Applications. *Small* **2010**, *6* (19), 2080–2098.

(336) Ma, Y.-H.; Huang, C.-P.; Tsai, J.-S.; Shen, M.-Y.; Li, Y.-K.; Lin, L.-Y. Water-Soluble Germanium Nanoparticles Cause Necrotic Cell Death and the Damage Can Be Attenuated by Blocking the Transduction of Necrotic Signaling Pathway. *Toxicol. Lett.* **2011**, *207* (3), 258–269.

(337) Lambert, T. N.; Andrews, N. L.; Gerung, H.; Boyle, T. J.; Oliver, J. M.; Wilson, B. S.; Han, S. M. Water-Soluble Germanium (0) Nanocrystals: Cell Recognition and Near-Infrared Photothermal Conversion Properties. *Small* **2007**, *3* (4), 691–699.

(338) Yu, Y.; Lu, X.; Guillaussier, A.; Voggu, V. R.; Pineros, W.; de la Mata, M.; Arbiol, J.; Smilgies, D.-M.; Truskett, T. M.; Korgel, B. A. Orientationally Ordered Silicon Nanocrystal Cuboctahedra in Superlattices. *Nano Lett.* **2016**, *16* (12), 7814–7821.

(339) Brinker, C. J.; Scherer, G. W. *Sol-Gel Science: The Physics and Chemistry of Sol-Gel Processing*; Academic press, 2013.

(340) Levy, D.; Zayat, M. *The Sol-Gel Handbook: Synthesis, Characterization and Applications, 3-Volume Set*; John Wiley & Sons, 2015.

(341) Yeh, J.; Huang, K.; Dai, C.; Chand, B. G.; Weng, C. Organic-acid-catalyzed Sol–gel Route for

Preparing Poly (methyl Methacrylate)–silica Hybrid Materials. *J. Appl. Polym. Sci.* **2008**, *110* (4), 2108–2114.

(342) Scherrer, P. Bestimmung Der Inneren Struktur Und Der Größe von Kolloidteilchen Mittels Röntgenstrahlen. In *Kolloidchemie Ein Lehrbuch*; Springer, 1912; pp 387–409.

Appendix A:

Sol-gel Chemistry

As was mentioned in the Introdcution Chapter of current Thesis, solid-state thermal decompostion and reduction for making GeNCs, is predominanted by Ge-based sol-gel reaction. In this section we will turn our attention to the sol-gel reaction itself.

Sol-gel is a wet-chemical technique that uses a solution to make a colloidal suspension (*i.e.,* sol). The sol acts as a precursor to produce an integrated network of metal-oxide (*i.e.,* gel). Colloid is defined as a homogeneous suspension in which the dispersed phase contain partilces in nanoscale size (1-1000 nm) with negligible gravitational forces acting upon them. The intra-particle interactions are dominanted by short-range forces such as van der Waals attraction and surface charges.[339] Therefore a "sol" can be defined as the colloidal nano-scale size solid particles in a liquid. On that note, "aerosol" is a colloid containing nano-scale size solid particles in a gas and an "emulsion" is a colloid nano-scale size liquid drops inside another liquid.[339,340]

Alkoxide and metal chloride are precursors typical of those which have been used to form sol. They undergo reactions which can be divided into two main steps: 1) "hydrolysis" and 2) "condensation". However, two steps of hydrolysis and condensation are not separate and most of time there are happening simultaneously (Figure A-1).

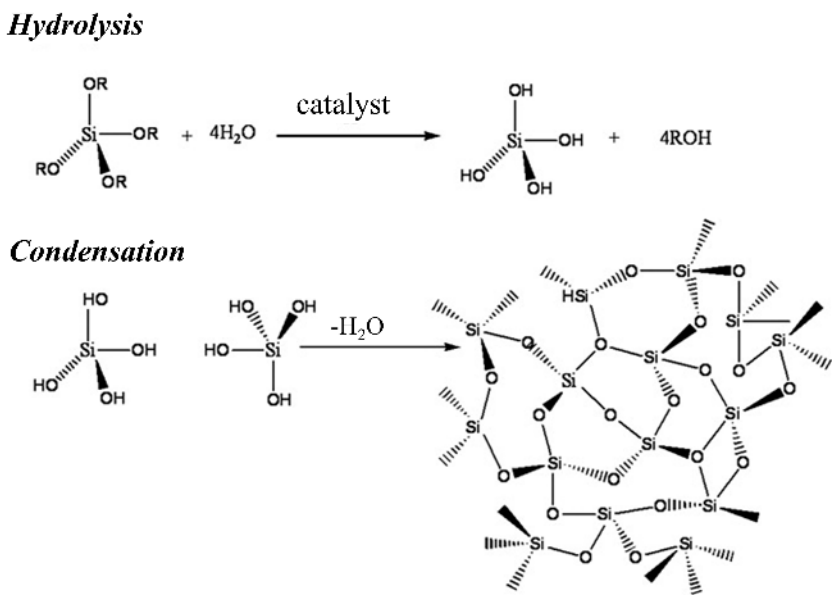

Figure A-1. Hydrolysis and condensation for the sol–gel reaction of TEOS.[341]

A classic example of alkoxide, which has been extensively studied by Werner Stöber *et al.*, is hydrolysis and condensation of tetraalkoxysilane [$Si(OR)_4$] and mainly tetraethoxysilane [$Si(OC_2H_5)_4$].[327] In this regard, hydrolysis is the attachment of hydroxyl groups from solvent (*i.e.,* H_2O) to silicon atom (Figure A-1). Complete hydrolysis requires excess water and the presence of catalyst (usually H^+ or OH^- ions). Condensation occurs followed by hydrolysis (either complete or non-complete). Condensation is the reaction of alkoxyl or hydroxyl groups on one Si center with the ones from another Si center, forming a network of Si–O–Si bonds (and ultimately SiO_2). ROH and H_2O are also produced during the condensation step (Figure A-1).

The sol-gel reaction is an extremely useful procedure for making numerous variety of metal-oxide structures. A simple change to the experimental conditions can lead to significant variation in the morphology of the produced metal-oxide network. The second Chapter of current Thesis presents a revealing example of the changing of the morphology of resulting oxide by

altering the reaction condition (see Chapter two). Variations can be acheived by changing the temperature of sol-gel reaction, reaction time, solvent composition and more interestingly, the pH of the reaction itself.[340]

As previously mentioned, the presence of acid or base can change the rate of hydrolysis (role of catalyst). In another interesting result, H^+ or OH^- ions can act as structure-directing agents by producing chain-like or granular sol-gel product, respectively. In this instance, at the pH < 3, H^+ protonated the oxygen atoms of Si-OR or Si-OH groups. This protonation produces good leaving groups (*i.e.,* water and ROH). It also decreases the electron density and facilitates nucleophilic attack of water (during hydrolysis) or silanol groups (during condensation) on the central Si atom. The latter forms a Si-O-Si bond with the reduced electron density on the central Si.

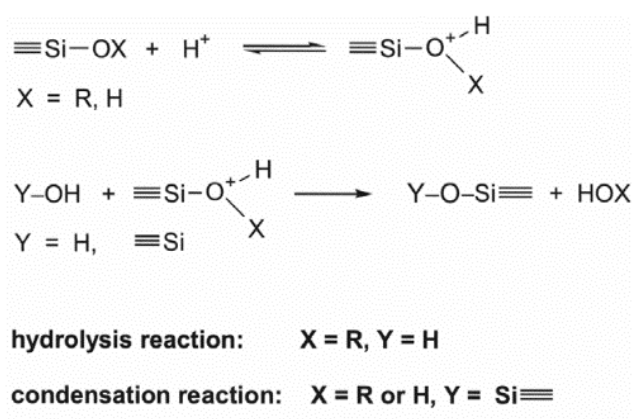

Eq. A-1

Eq. A-2

General sol-gel reaction under acidic conditions[340]

Moreover, Si with higher electron density has higher rate for hydrolysis and condensation (*i.e.,* higher probability of the adjacent O atom to be protonated). *Eq.* A-3 shows the trend for changing electron density on the central Si atom.

≡Si-R > ≡Si-OR > ≡Si-OH > ≡Si-O-Si *Eq.* A-3

According to this trend, Si-OR and Si-OH have higher electron density on the central Si atom in compared to Si-O-Si. This phenomenon causes a growing network from terminal Si atoms (not from the central Si atom) and produces chain-like structures.

In contrast, base-catalyzed sol-gel reactions, can end with producing branched networks. In this context, at the pH > 3, the central Si atom undergoes a nucleophilic attack by hydroxide ions (OH^-, during hydrolysis) or silanoate ions (≡Si-O^-, during condensation) through an S_N2-type mechanism which creates a five-coordinated transition state. Later on, OR^- (for hydrolysis) or OH^- (for condensation) leaves the transition state complex. The nucleophilic attack which follows, occurs on the central Si atom (not on the terminal Si atoms) because it has the lowest electron density (*Eq.* A-4). This results in the formation of branched/granular structures at the end.

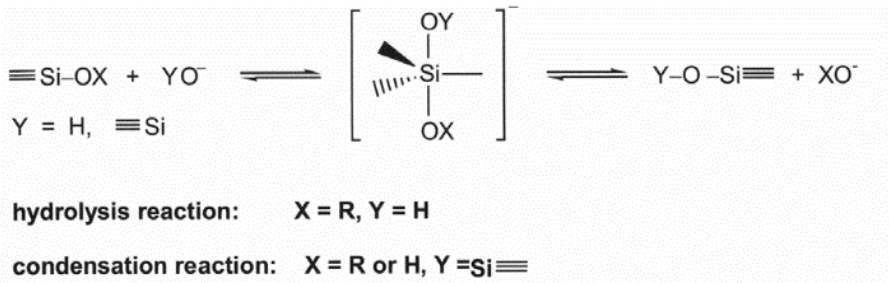

Eq. A-4

General sol-gel reactions under basic conditions[340]

Appendix B:

Supplementary information for Chapter 4

and

Debye-Scherrer analysis

Debye-Scherrer analysis of XRD peak broadening:

Proposed by P. Debye and P. Scherrer, this method is a straightforward (but rough estimating) analysis to understand the crystal size of NCs based on the broadening of XRD peaks.[342] Debye-Scherrer equation is shown as:

$$t = \frac{K\lambda}{B\cos\theta_B}$$

Where

- t is the crystal sizes of the NCs,
- K is dimensionless shape factor and is mainly depended on the shape of the NCs. Usually for spherical and pseudospherical shapes of NCs, where the size of nanoparticles is same in all directions, K set as 0.94 and it is independent from *hkl* of the planes chosen for calculation.
- B is the Full Width at Half Maximum (FWHM) of the peak (in radians), obtained according to Table B1 and B2 by Gaussian and Lorentzian line shapes fitted to {111} peaks of Ge.
- θ is the Bragg angle (in radians); in current contribution, Scherrer analysis has been done based on the {111} crystallographic planes (peak with the highest intensity), 2θ = 27.28°, cos θ (in radians) = 0.9718).
- λ is the X-ray wavelength; in current contribution Cu-Kα radiation source with λ = 0.154 nm.

This equation explains peak width of XRD diffractions varies inversely with crystallite size; as the crystallite size gets smaller, the XRD peak gets broader.

Table B1. Debye-Scherrer analysis results for GeNCs diameters obtained from thermal processing of yellow $Ge(OH)_2$ at indicated temperature

Annealing Temp. (°C)	FWHM (starting-deg)	FWHM (ending-deg)	FWHM B (deg)	B (Radian)	t (nm)
350	28.36	26.33	2.03	0.0354	4.2
400	27.95	27.11	0.84	0.0147	10.1
450	28.01	27.18	0.83	0.0145	10.3
500	27.71	27.17	0.54	0.0094	15.9
600	27.61	27.24	0.37	0.0065	23.1

Table B2. Debye-Scherrer analysis results for GeNCs diameters obtained from thermal processing of brown $Ge(OH)_2$ at indicated temperature

Annealing Temp. (°C)	FWHM (starting-deg)	FWHM (ending-deg)	FWHM B (deg)	B (Radian)	t (nm)
400	26.73	28.12	1.39	0.0243	6.1
450	27.61	28.68	1.07	0.0187	8.0
500	27.2	28.11	0.91	0.0159	9.4
600	27.3	27.77	0.47	0.0082	18.2

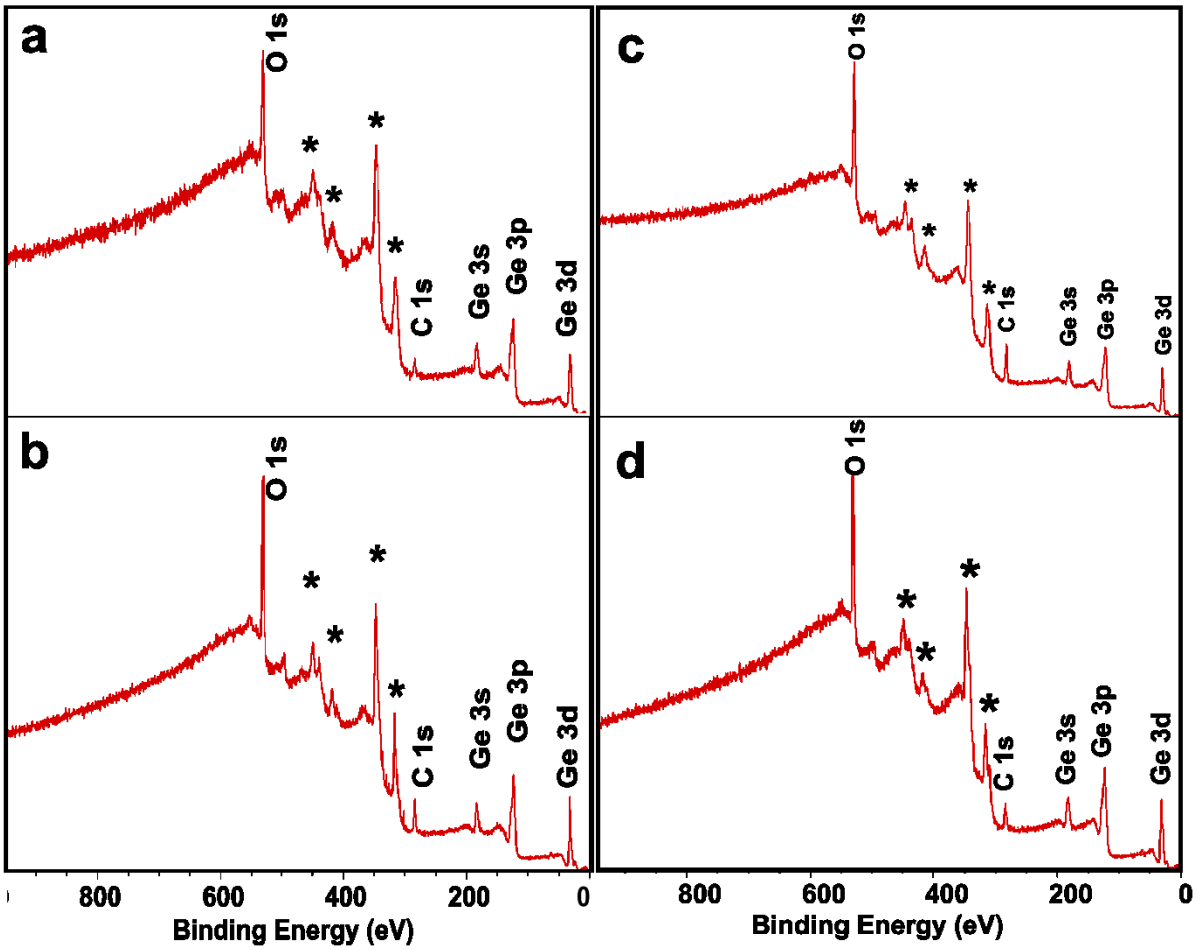

Figure B-1. Survey XP spectra of (a) yellow 'Ge(OH)$_2$' and (b) brown 'Ge(OH)$_2$'. Signals of Ge, C and O, were observed as expected. Signals assigned by a '*' are related to Ge LMM.[20,234]

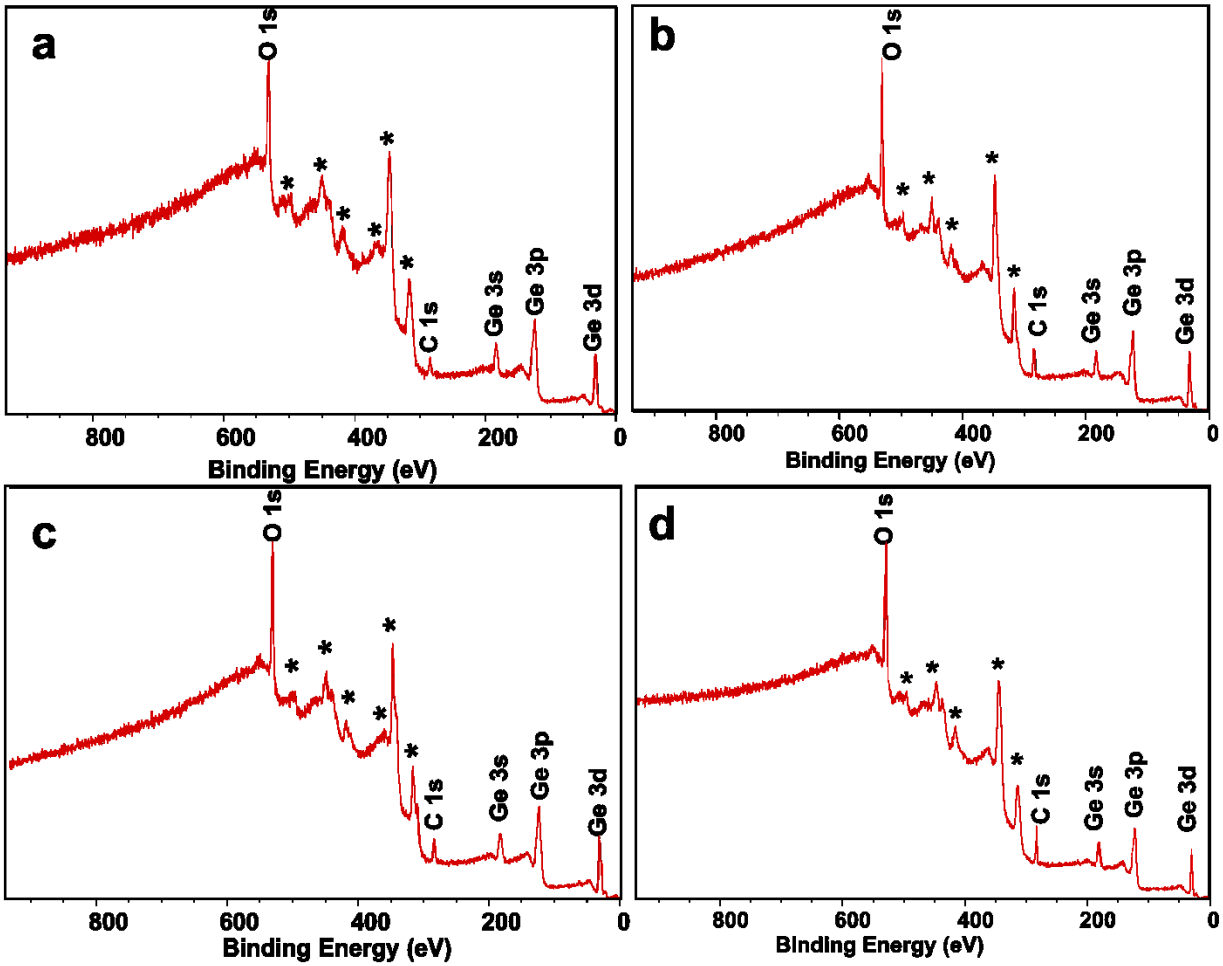

Figure B-2. Survey XP spectra of Ge/GeO_2 composite obtained from thermal treatment of (a) yellow '$Ge(OH)_2$' and (b) brown '$Ge(OH)_2$' at 400 °C for 1 h under Ar. Signals of Ge, C and O, were observed as expected. Signals assigned by a '*' are related to Ge LMM.[20,234]